Challenges of Planet Formation: Insights from Global Modelling and Population Synthesis

Inaugural dissertation
of the Faculty of Science,
University of Bern

presented by

Andrin Kessler

Supervisor of the doctoral thesis:

Prof. Dr. Yann Alibert
Physics Institute of the University of Bern

Challenges of Planet Formation: Insights from Global Modelling and Population Synthesis

Inaugural dissertation
of the Faculty of Science,
University of Bern

presented by

Andrin Kessler

Supervisor of the doctoral thesis:

Prof. Dr. Yann Alibert
Physics Institute of the University of Bern

Accepted by the Faculty of Science.

Bern, 27th of February 2025

The Dean
Prof. Dr. Jean-Louis Reymond

Für aui wos interessiert.

Acknowledgements

I would like to express my gratitude to my advisor, Yann, for your vision, guidance, and supervision throughout my PhD. Thank you, especially, for your interest and support regarding my post-doctorate future. To Joanna, thank you for your precise feedback and for taking the time to evaluate this thesis. To Christoph, thank you for repeatedly offering your insight and support, which you did not have to, over four years. I have greatly enjoyed working with you, also in various capacities outside of research such as teaching, organising a retreat, and acting in university committees. I would also like to thank the extremely helpful administrative staff, Agnès, Leonore, Deon, Tina, and Dora, for your vital support.
To all past, current, and visiting members of the TAPS group, I thank you for the countless stimulating presentations and discussions we had. The weekly TAPS meeting was without a doubt my favourite part of the scientific life as a PhD and has greatly improved my understanding and intuition of Physics. To my office mates who have practically started and ended their PhDs in parallel and co-inhabited office 008 for four years, Jo Ann, Nicolas, and Jeanne, thank you for the serious, procrastination-free, and totally efficient work environment I was able to share with you. In all seriousness, thank you for the infinitely many little scientific and non-scientific exchanges and for the comfortable and supportive life you enabled, also beyond the office walls. A rough start in a peculiar time, overshadowed by a pandemic, was made easier and enjoyable by a great many people who have enriched my work and social life since. I would like to specially thank Kathryn, Tobias, Chloe, Marit, Clémence, and Daniel, for immediately welcoming me with open arms and becoming great friends. To everyone I was able to share many activities outside of work with, I am truly thankful for everything, be it Friday beers at Unsinkbar (RIP) or the Grosse Schanze, enjoying the Aare at the Marzili, skiing and hiking all over Switzerland, or having one too many at certain Triple-T events. Shout-out to the bois, Beni, Jesse, and Jesse, with whom good times are always guaranteed, both at and outside of work. To the whole diverse community at the university of Bern over the last four years, I thank you for enriching my life.

To the Zmittägler, Nafie, Nöms, Mättu, Beni, Alex, and Sebi, you are the real ones without whom I would not be a physicist, much less a PhD physicist. Beyond the simple lunch, I am truly grateful for your friendship, the time we spend together, and the people you brought into my life. To many more retreats, LANs,

and other shenanigans.
To my parents, Flurina and Martin, and my brother, Nicolas, I sincerely thank you for everything you have done and still do for me. I greatly value your perspectives, opinions, and company. I cannot thank you enough for your continued support in all aspects of life, setting me up for happiness. To my orange flatmate, Filou, thank you for only being annoying occasionally (at least once a day). You are lucky you are cute.
Finally, to my partner and companion, Naomi, you are my best friend and I wholeheartedly thank you for sharing life with me.

Contents

1 Introduction

The confirmed existence of planets, both within our Solar System as well as around thousands of other stars, raises the fundamental question about how they form. This is not only a profound inquiry about our own origins but also an intriguing multi-disciplinary scientific problem. Our foundational understanding of planetary properties is driven by observations of Earth and its neighbours, as well as planets outside of the Solar System. It is the challenge of planet formation theory to make sense of the planets we see and their diverse characteristics. Addressing this requires identifying the key physical processes driving planet formation and understanding how these processes interplay to shape fundamental planetary properties, such as mass and orbital distance.
In this thesis, I use a global model of planet formation and evolution to examine two current areas of study in the planet formation community. First, I investigate the arising complexity due to two concurrently acting mechanisms for planets to grow (Kessler and Alibert, 2023). In the second work, I revisit the long-standing conundrum of the formation of Uranus and Neptune (Kessler et al., subm.). Both studies highlight the complexity of planet formation, demonstrating the need for, and the value of, global models incorporating the most important physical processes.

The thesis is structured in the following way: in the introductory chapter 1, I give a broad overview of the observational constrains on the planet formation process which is inspired by the recent thorough reviews of Drazkowska et al. (2022) and Miotello et al. (2022). The current state of our knowledge about the outcome of planet formation – the planets we can see today – is covered in chapters 1.1 and 1.2. In chapter 1.3, I give an overview of our observational understanding of the initial conditions that set the stage for planet formation. In chapter 1.4, I provide a qualitative picture of how planets are believed to form, and finally in chapter 1.5, I present the modelling approach employed in the two main works. In chapter

2, I introduce the most important physical processes for the formation of planets. The global model used in this thesis, which incorporates most of these physics, is introduced in chapter 3. In chapters 4 and 5, I present the two main works of the thesis Kessler and Alibert (2023) and Kessler et al., (subm.), respectively. Finally, I conclude the thesis with an outlook in the context of my work in chapter 6.

1.1 The Solar System

The Solar System hosts (at least) eight planets. Four so-called *terrestrial* planets in the inner parts of the system which mostly consist of solid rock and other heavy elements such as iron: Mercury, Venus, Earth, and Mars. The four planets in the outer system are Jupiter, Saturn, Uranus, and Neptune. They are much more massive and gas-rich than the planets in the inner Solar System. Jupiter and Saturn are dominated in mass by hydrogen and helium (henceforth H-He) and are colloquially known as *gas giants*. Uranus and Neptune are believed to bear 8-25% of their mass in H-He (Helled et al., 2011; Nettelmann et al., 2013) and are called *ice giants* due to their large orbital distance to the Sun. To compare, the Earth's atmosphere only makes up for about a millionth of the total mass of the planet. The masses and semi-major axes of the Solar System planets are listed in Table 1.1. There are many more well-studied characteristics of these planets such as their radii, composition, surface properties, moons, etc., as well as groups of smaller bodies such as the asteroid belt between the orbits of Mars and Jupiter, and the so-called trans-Neptunian objects beyond Neptune's orbit. A discussion of all these components of the Solar System is beyond the scope of this thesis but the planets and the system architecture already pose challenging questions about the formation history of the Solar System. A by no means exhaustive list of fundamental questions reads: 'Why is Mars substantially less massive than Earth and Venus?', 'Why is Saturn much less massive than Jupiter despite their otherwise similar nature?', 'How come Mercury is much more dense than the other terrestrial planets?', 'How can Uranus and Neptune form so far away from the Sun?'. There exist various studies and hypotheses on all of these topics (see e.g. Walsh et al., 2011; Helled, 2023; Chau et al., 2018; Tsiganis et al., 2005; Lambrechts et al., 2014). I investigate the last question about the formation of the Solar System ice giants Uranus and Neptune in Chapter 5 (Kessler et al., subm.).

Planet	Mass [M_E]	Semi-major axis [au]
Mercury	0.055	0.39
Venus	0.815	0.72
Earth	1	1
Mars	0.107	1.52
Jupiter	317.8	5.20
Saturn	95.2	9.58
Uranus	14.5	19.22
Neptune	17.1	30.05

TABLE 1.1: The masses and semi-major axes of the Solar System planets, given in relative units with respect to Earth. One M_E corresponds to one Earth mass and one astronomical unit au is almost exactly the average distance between the Earth and the Sun.

It remains a key objective of planet formation theory to explain the formation of the Solar System. Currently, we are far from providing a complete picture. Although fundamentally, the formation of the Solar System planets must be a possible outcome of a valid theory of planet formation, it is a priori unclear whether the Solar System represents a common or a special occurrence. As such, the Solar System only provides incomplete information about the outcome of the planet formation process. In order to learn more, we must look further.

1.2 Exoplanets and extra-solar systems

In 1995, the first planet which orbits a different main-sequence star than the Sun, namely *51 Pegasi*, was discovered (Mayor and Queloz, 1995). The Jupiter-mass planet *51 Pegasi b* was found to orbit its host star so closely that it would be well inside Mercury's orbit in the Solar System. Such planets outside the Solar System are called *exoplanets*. For the study of planet formation, the discovery of the first exoplanet marked the beginning of a new era and the significance of this finding was recognized with the Nobel Prize in physics in 2019. Already the very first discovered exoplanet revealed that the Solar System planets represent only a subset of possible planet formation outcomes, as our own Jupiter is on a much wider orbit than 51 Pegasi b. The prospect of more exoplanet discoveries opens

up the possibility to compare predictions from planet formation theory against a much larger, more diverse, population of planets than the Solar System. Indeed, the 'exoplanet revolution' is in full swing. Currently, we have discovered 5811 exoplanets according to the NASA Exoplanet Archive (as of 03.01.2025). It turns out that the formation of planets is not a rarely occurring phenomenon. From the observed population of exoplanets it is estimated that around 50-60% of Sun-like stars host at least one planet (Mulders et al., 2018; Zhu et al., 2018; He et al., 2019, 2021). Furthermore, at least half of the known exoplanets are part of a multi-planetary system (Lissauer et al., 2011). In order to understand this vast population of planets, it is crucial to understand how exoplanets are discovered, what planetary properties can be measured or inferred, and what the observational biases are.

1.2.1 Exoplanet detection

It is beyond the scope of this thesis to give a detailed description of all the exoplanet detection methods. The aim of this simple overview of the two most important exoplanet detection methods, the radial velocity and the transit method, is to allow a reasonable understanding of the bulk of the exoplanet population presented in Chapter 1.2.2. It should be mentioned that there are other detection methods, such as microlensing and direct imaging, which are not as successful in finding new exoplanets yet. However, the sensitivity to low mass planets at larger distances of the microlensing method, as well as the powerful characterisation capabilities of giant planets on very long orbits via direct imaging, provide valuable extensions of the known exoplanet parameter space. Note that I also omit a discussion on the vast amount of observational facilities and instruments, both ground and space-based, which are involved with exoplanet detection and characterisation, as well as missions exploring the Solar System.

Radial velocity

The 1995 discovery was made using the so-called radial velocity method. This method relies on the mutual gravitational interaction of the star and the companion which causes both objects to orbit the centre of mass of the System. Unless we are observing the system face-on (an inclination of 0°), a part of this periodic motion of the star takes place in the line of sight. This radial velocity away/towards the

observer results in a Doppler red/blue shift of the incident stellar light. Using a high precision spectrograph, this shift can be measured and translated into a radial velocity signal. The amplitude of the radial velocity depends, among other parameters, on the mass of the companion and the inclination i. By measuring the amplitude and the orbital period, the minimum mass of the planet, $M_p \sin(i)$, can be calculated if the mass of the star is known. The true planetary mass M_p can not be inferred, since the inclination is unknown from radial velocity measurements alone.
This exoplanet detection method is biased towards massive companions on short orbital periods as they lead to a larger radial velocity signal. Similarly, a planet of a given mass is more easily detectable if the host star mass is lower. Fundamentally, the observed star also needs to be sufficiently bright in order to be observable. The main limitation for precise radial velocity measurements are signals due to stellar activity phenomena which can mimic and/or mask the planetary signal (Dumusque, 2016). Currently, we are just about able to detect an Earth-twin around a Sun-like star using the radial velocity method. Nevertheless, it is a hugely successful method of exoplanet detection responsible for 1096 exoplanet discoveries up to now.

Transit

The so-called transit method is by far the most successful way of detecting planets which has lead to the discovery of 4329 exoplanets. It uses the fact that a planet partly obscures the stellar light as it crosses ('transits') in front of the star in the line of sight of the observer. This is not the case for every planet as it relies on a suitable observation geometry, disqualifying all planets which do not transit from the point of view of the observer. Planets on close-in orbits are much more likely to cross in front of the star than planets on longer orbits which makes the detection of longer period planets unlikely and impractical using this method. The transit method has been successfully applied for the first time in 1999 on the already known planet *HD 209458 b* which was first detected using the radial velocity method (Henry et al., 1999; Charbonneau et al., 2000). The main observational quantity is the transit depth, the maximum extent by which the planet reduces the apparent brightness of the star. The depth is directly related to the ratio of the planetary to stellar radius. Since a deeper transit is easier to detect, small planets are more readily detected around smaller stars. Additionally to the

radius, the orbital characteristics can be constrained from the shape, timing, and duration of the measured transit lightcurve. If the orbits in exoplanetary systems are co-planar, as is the case in the Solar System, and a single transiting planet is found, the probability of the other planets in the system transiting as well is high. From variations in the transit timing due to the mutual gravitational interactions among the planets in a multi-planetary system, it is even possible to infer the masses of the planets. The most famous example of a multi-exoplanetary system is the *TRAPPIST-1* system which is hosting seven known terrestrial exoplanets (*TRAPPIST-1 b* through *h*), which were all found using the transit method (Gillon et al., 2016, 2017).
Since the transit and radial velocity methods are both biased towards edge-on (inclination of 90°) orbits with respect to the observer, many planets discovered by radial velocity are transiting and many exoplanets discovered with the transit method can be followed up with radial velocity measurements. The simultaneous measurement of the planetary mass as well as the radius using both methods constrains the bulk density of the planet. This allows us to roughly characterise exoplanets in terms of their composition. However, the interior structure of planets remains a highly degenerate problem and requires advanced methods in order to be constrained (e.g. Egger et al., 2024).
As for the radial velocity method, stellar activity related signals are a major source of noise. For instance, colder regions on the stellar surface can cause a transit-like dip in the total brightness as the star rotates. Nevertheless, it is possible to detect exoplanets smaller than Earth around sufficiently bright Sun-like stars using the transit method (e.g. Fressin et al., 2012).

1.2.2 The exoplanet population

In Figure 1.1, the population of known planets with both an existing mass and semi-major axis estimate is shown. The lower detection limit around one Earth mass discussed in the previous chapter is clearly visible. As seen by the colour of the points, the transiting exoplanet population is biased towards small separations and the radial velocity population extends further out for more massive planets. Outside of 10 au, only planets more massive than Jupiter can be detected by radial velocity and direct imaging. For reference, the Solar System planets are indicated by black crosses highlighting our current inability to detect a twin-system to our own.

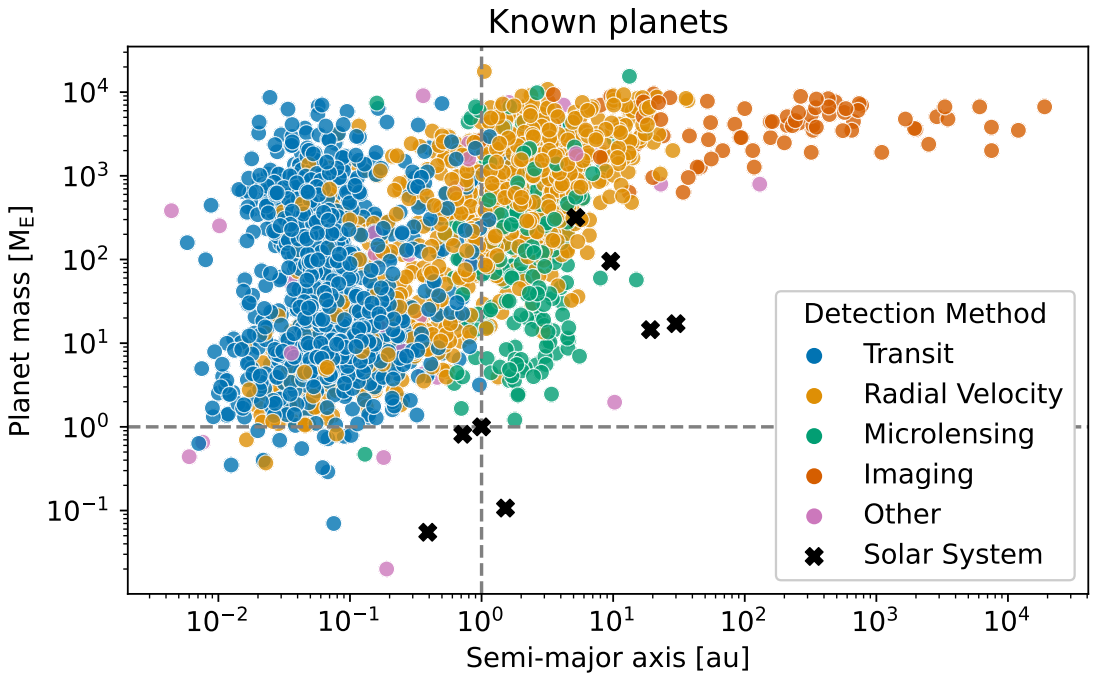

FIGURE 1.1: All known planets for which a mass and semi-major axis estimate exists as of 03.01.2025. The colour of the points indicates the discovery method used for each exoplanet. The black crosses represent the Solar System planets and the grey dashed lines highlight the Earth's location at one au and one M_E.

The exoplanet population provides a much wider perspective on the possible planet formation outcomes but it remains restricted by the current observational limits. Since the known exoplanet population clearly shows a large diversity, different from the Solar System, planets are loosely grouped into categories.

Super-Earths and sub-Neptunes

The most common detectable planets are the so-called *super-Earths* and *sub-Neptunes*. They are, generally, in the mass range between Earth and Neptune but are technically defined according to their radius, ranging from 1-3 R_E (Earth radii). For reference, Neptune's radius is 3.88 R_E. The transit and radial velocity method are perfectly suited to probe this mass range for orbits within one au, however, the ubiquity of these planets is not an artifact of the observational biases. Even after bias correction, more than every second Sun-like star is found to host at least one super-Earth or sub-Neptune, and often more than one (Mulders et al., 2018; Hsu et al., 2019; Kunimoto and Matthews, 2020).
The planets in the 1-3 R_E range are bi-modally distributed in terms of radii with a minimum occurrence rate around 1.7 R_E, which is commonly referred to as the *radius valley* (Fulton et al., 2017; Fulton and Petigura, 2018; Ho and Van Eylen, 2023). This separates two populations, the super-Earths with radii below $\sim$1.7 R_E and the sub-Neptunes with radii above $\sim$1.7 R_E. Since both the mass and the radius is known for many super-Earths and sub-Neptunes, their bulk density can be inferred. This allows to constrain the bulk composition of these planets. The super-Earth population with radii below $\sim$1.6 R_E is found to be consistent with terrestrial planets composed primarily of silicates and iron whereas planets with radii above $\sim$1.6 R_E, including the sub-Neptune population, likely have substantial volatile atmospheres (Rogers, 2015).
There are two main hypotheses for the emergence of the radius valley in the context of planetary formation and evolution. If the planets consist mainly of silicate and iron cores with H-He dominated atmospheres, the radius valley could be carved due to atmospheric escape of H-He, shaping the terrestrial super-Earth population (Lopez and Fortney, 2013; Jin et al., 2014; Owen, 2019; Ginzburg et al., 2016; Gupta and Schlichting, 2019; Rogers et al., 2021). A discussion on the long term evolution of planets due to atmospheric escape processes is presented in Chapter 2.8. The radius distribution can also be explained if the sub-Neptune population is rich in water (mass fractions of several tens of percent) while the

super-Earths are dry (Zeng et al., 2019; Mousis et al., 2020; Aguichine et al., 2021). This idea is consistent with water fraction predictions from planet formation models and tentatively supported by observations of planets around M-dwarfs (stars less massive than the Sun) (Mordasini et al., 2009a; Venturini et al., 2020; Luque and Pallé, 2022). However, it depends on how the water is mixed in the atmosphere, and atmospheric escape remains a key factor in shaping the radius valley assuming water-rich sub-Neptunes (Burn et al., 2024). Using the recently commissioned *James Webb Space Telescope* (JWST), we are for the first time able to characterise the composition of sub-Neptune atmospheres. Recently, a water-rich atmosphere has been detected on a 1.98 R_E sub-Neptune (Piaulet-Ghorayeb et al., 2024). Although it remains difficult to confidently link the observed spectral data to the atmospheric water abundance and even moreso to the bulk water content of a planet, this is an important development in the context of the radius valley. If the water-rich nature of close-in sub-Neptunes can be corroborated on a statistical level in future observations, this represents a fundamental success of predictive planet formation theory.
Above radii of $\sim$3 R_E, beyond the sub-Neptune population, the planet occurrence rate drops off steeply, which is sometimes referred to as the *radius cliff* (Youdin, 2011; Howard et al., 2012; Mulders et al., 2015a). This is thought to be related to the sequestration of hydrogen in the molten surface of the planet, stalling the radial growth of the atmosphere when more gas is accreted onto the planet (Kite et al., 2019).

Giant planets

Giant planets are loosely defined as planets above roughly 30 M_E ($\sim$0.1 Jupiter masses) and below the brown dwarf limit of about 4,000 M_E ($\sim$13 Jupiter masses). Giant planets are expected to contain increasing amounts of H-He the more massive the planet is. Sufficiently massive giants are predominantly composed of H-He with mass fractions well beyond 90%. For reference, Jupiter is estimated to get more than 87% of it's mass from H-He (Vazan et al., 2018; Ni, 2019).
Giant planets are found from very close to their parent star, out to about 30 au by radial velocity, and much further out by direct imaging. The very close-in giant planets, called *hot Jupiters*, are over-represented in the exoplanet population due to the fact they are comparatively easy to detect. In reality, the hot Jupiters are estimated to represent only about 0.5-1% of giant planets (Wright et al., 2012;

Howard et al., 2012; Fressin et al., 2013). Outside of the very short orbits, the intrinsic occurrence rate of giant planets increases with distance to the star, with most of them orbiting between 1-10 au (Cumming et al., 2008; Mayor et al., 2011; Fernandes et al., 2019; Fulton et al., 2021). Beyond 10 au, giant planets become increasingly more rare and outside of the radial velocity limit of about 30 au, only planets more massive than Jupiter, so-called *super-Jupiters*, can be detected by direct imaging. The occurrence rate of super-Jupiters is estimated to be on the order of 5% in the 10-100 au range (Nielsen et al., 2019; Vigan et al., 2021). Exoplanetary counterparts to the Solar System ice giants Uranus and Neptune are currently clearly out of reach observationally.

System architectures

The architecture of observed multi-planetary systems can be broadly divided into systems with and systems without giant planets. In the absence of giant planets, the properties of planets in the same system tend to be similar. The typical multi-planet system found in the *Kepler* transit survey hosts planets that are similar in size, regularly spaced, and co-planar (Ballard and Johnson, 2016; Millholland et al., 2017; Weiss et al., 2018; Gilbert and Fabrycky, 2020). Although some of these correlations could be explained by observational biases, they are consistent with predictions from planet formation models (He et al., 2019; Mishra et al., 2021; Emsenhuber et al., 2023b). A common occurrence in planet formation simulations are so-called orbital resonances, which arise when the orbital period ratios of successive planets are integer-valued (e.g. Emsenhuber et al., 2021b). One of the most famous examples of orbital resonances are Jupiter's moons Io, Europa, and Ganymede. For every one orbital revolution of Ganymede, Europa orbits Jupiter twice and Io four times. The majority of observed exoplanet systems, however, are not in orbital resonances. It has been proposed that orbital resonances are broken after the planets have formed in order to explain this discrepancy (Izidoro et al., 2017).

The architecture of systems with at least one giant planet are significantly different. Hot Jupiters are only very rarely accompanied by other planets within about 50 au, while companions at larger distances are common (Ngo et al., 2016). The planet multiplicity of systems with giant planets at larger distances is not as well constrained due to the observational limitations, however, super-Earths have been found to be often accompanied by an outer giant (Zhu et al., 2018; Bryan

et al., 2019; Rosenthal et al., 2022; Huang et al., 2016). This is consistent with the emerging architectures in planet formation simulations (Emsenhuber et al., 2023b).

Dependence on the host star

We detect planets around stars with different masses, compositions, and ages. Since the stellar properties are thought to be representative of the environment from which a planetary system formed and evolved in over billions of years, an imprint of stellar properties on the exoplanet population is expected. Most fundamentally, environments which lead to the formation of a low mass star are also thought to provide less material for planet formation. Similarly, the relative abundance of heavy elements (everything except H-He) with respect to H-He, is commonly assumed to be the same in the host star and the matter from which the planets form. Therefore, it is expected that the properties of planetary systems and the individual planets correlate with stellar mass and the so-called *metallicity*, which is a proxy for the heavy element abundance given by the iron to hydrogen ratio normalised by the Sun's values. Consistent with this idea, the planetary population around M-dwarfs ($<$0.6 M_{Sun}) is dominated by planets which are smaller than $\sim$3 R_E and orbit closer to the star compared to Sun-like systems (Howard et al., 2012; Dressing and Charbonneau, 2013, 2015; Morton and Swift, 2014; Mulders et al., 2015a; Hsu et al., 2020). The typical super-Earth mass in a system is found to scale roughly linearly with stellar mass (Wu, 2019; Pascucci et al., 2018). Giant planets, both hot-Jupiters and more distant giants, are much rarer around M-dwarfs than Sun-like stars (Mulders et al., 2015b; Hsu et al., 2020; Johnson et al., 2010; Fulton et al., 2021).
There is a well-established positive correlation of giant planet occurrence and host star metallicity (Santos et al., 2004; Fischer and Valenti, 2005; Fulton et al., 2021) and a weak positive metallicity dependence for larger planets (2-4 R_E) (Petigura et al., 2018). A similar correlation for super-Earths is much weaker or perhaps even absent (Wang and Fischer, 2014; Mulders et al., 2016; Kutra et al., 2021).

A perhaps surprising fact is that roughly half of Sun-like stars are found to have at least one stellar companion. For M-dwarfs the multiplicity fraction is about 20% (Offner et al., 2022). Clearly, multi-stellar systems are not a rare

occurrence. Nevertheless, planet formation is typically studied considering single-star systems, not just because of the search for a Solar System twin but also for simplicity. The presence of a secondary star is an additional source of energy and tidal forces which are not negligible in the planet formation and evolution process. For these reasons, planet formation is solely discussed in the context of a single central star in this thesis.

1.3 The protoplanetary disk

In order to study planet formation, apart from looking at outcomes of this process, we must also understand the environment in which it takes place. To do this, we go back in time to when the host star itself formed, as we believe the leftovers of this process provide the material planets form out of. The birthplace of stars are so-called molecular clouds. Molecular clouds are huge collections of very low-density gas, spanning hundreds of lightyears and containing up to millions of solar masses of mostly molecular hydrogen. Filaments, which are substructures of varying density, are ubiquitous in molecular clouds. Sufficiently dense filaments can fragment into gravitationally bound objects which collapse further into stellar nebulae, finally evolving into stars (see e.g. Kippenhahn and Weigert, 1990). When a so-called protostar forms, the increasingly dense gas revolves around the central protostar according to the total angular momentum of the nebula. As the nebula shrinks further, it speeds up due to the conservation of angular momentum and flattens into a thin circumstellar disk. Conceptually, this is assumed to be the starting point of planet formation where the refractory components in the disk start to accumulate and grow into planets. Therefore, planet-forming circumstellar disks are also referred to as *protoplanetary disks*. Typically, the heavy-element contribution to the total disk mass is assumed to be on the order of one percent – the rest is H-He. The refractory components in the disk, e.g. silicate and water ice grains, are commonly referred to as *dust*, while the rest is aptly called gas.

Protoplanetary disks are historically detected and classified by spectrography of the combined light of the young star and the disk, which is in this context often called a *young stellar object* (YSO). If a disk is present, there is an excess flux in the infrared range compared to the spectrum of the star alone, which is accurately modelled as a blackbody. The infrared excess stems from the dust component

in the disk, which is heated up by the stellar irradiation and re-emitting in the infrared. The distribution of the spectral energy, given by the wavelength λ multiplied by the incident flux at this wavelength F_λ, as a function of the wavelength in the infrared range, provides a way of classifying YSOs. Four classes are defined according to the slope of the distribution, given as $\alpha = \frac{\mathrm{d}\log \lambda F_\lambda}{\mathrm{d}\log \lambda}$ (Williams and Cieza, 2011; Armitage, 2020):

- **Class 0**: undefined α due to missing infrared emission,
- **Class I**: $\alpha > 0.3$,
- **Class II**: $-1.6 < \alpha < -0.3$,
- **Class III**: $\alpha < -1.6$.

This classification of YSOs follows the temporal evolution of the protostar and the surrounding material. The physical interpretation of a class 0 and I YSO is that the stellar light is heavily obscured by the disk which is still forming and being fed by infalling material from the surrounding cloud. Class II objects have cleared the majority of the enveloping gas and dust with a thin disk remaining. This is the stage where it is commonly assumed that planet formation takes place. As the gas disk dissipates, a class III YSO showing close to no infrared excess is left behind. Since most YSOs are found to be of class II, most of the circumstellar disk lifetime consists of star-disk systems which have largely cleared the surrounding cloud material (Evans et al., 2009). Comparing disk occurrence rates in star forming regions of different estimated ages, allows to constrain the expected lifetime of protoplanetary disks, albeit with large associated uncertainties. Disk lifetimes are expected to be in the range of 1-10 million years with characteristic values around 2.5-5 Myr (Mamajek, 2009; Richert et al., 2018; Michel et al., 2021). The disk lifetime is a fundamental constraint for the formation of planets as well as models of protoplanetary disk evolution.

Although reliant on assumptions regarding the dust sizes, opacity, and temperature, the dust mass in the disk can be estimated from thermal continuum emission measurements in the (sub-)millimetre range (Hildebrand, 1983; Miotello et al., 2022). Dust mass estimates of many YSOs in different star forming regions reveal a strong dependence of dust mass with time. The youngest objects, corresponding to class 0/I, are more than an order of magnitude more massive than

the older class II objects (Andrews et al., 2013; Ansdell et al., 2016; Barenfeld et al., 2016; Pascucci et al., 2016; Ansdell et al., 2018; Tychoniec et al., 2018). The typical dust mass reduces from a few hundred Earth masses to ~ 50 M_E for class II YSOs (van der Marel and Mulders, 2021). Comparing these dust mass estimates to the observed mass of exoplanetary systems, suggests that planet formation likely initiates earlier than classically assumed, before the disk is fully assembled, or that planet formation is more efficient than currently thought (Drazkowska et al., 2022). However, it has been recently demonstrated that median dust masses might be underestimated by a factor of 6 due to the assumed dust properties which could alleviate the mismatch with the masses of exoplanetary systems (Liu et al., 2024). The oldest YSOs, estimated at ∼5-11 Myr, show again a factor of a few lower median dust masses consistent with class III objects. The most obvious interpretation of this trend is that ongoing planet formation is converting the dust into larger bodies which are unobservable in this wavelength range, and some of it is accreted by the star. Evidence for stellar accretion is found in the ultraviolet range of the spectral energy distribution of YSOs. An excess ultraviolet emission, particularly at the Hα spectral line of the hydrogen atom, is indicative of gas temperatures of $\sim 10^4$ K. This is consistent with the expected shock temperatures of disk gas accreting onto the star (Joy, 1945; Hartmann et al., 1994). The stellar accretion rates can be inferred from the ultraviolet excess emission. They are found to be on the order of $\sim 10^{-8}$ $M_{Sun}yr^{-1}$ and are correlated with the disk masses and with the ages of the young systems (Manara et al., 2016; Hartmann et al., 2016; Testi et al., 2022). Reproducing the stellar accretion rates is a further key requirement for models of protoplanetary disks and their time evolution.

Inferring the total disk mass requires some constraint on the gas mass on top of the dust mass. As mentioned before, a natural assumption is that the elemental composition of the star is representative of the composition of the disk. This means that, to first order, stellar metallicity distributions can be used to estimate the typical dust-to-gas ratios in disks. Ratios of about 1% are commonly quoted which results in typical total disk masses of ~ 5000 M_E (~ 0.015 M_{Sun}). Measuring the gas mass of protoplanetary disks directly is much more difficult than measuring dust masses. The main problem stems from the fact that the emission of the main component of the gas, molecular hydrogen (H_2), is very faint (Field et al., 1966). The main tracer molecules that are used instead are the less abundant hydrogen isotopologue hydrogen deuteride (HD), and carbon monoxide (CO). Both methods are associated with large uncertainties but, so far, CO-based observations seem to

indicate dust-to-gas ratios just below of 1% (Miotello et al., 2022). As is the case of dust mass measurements, the uncertainties of YSO ages further complicate the estimation of early class II gas disk masses.
Estimating the radial extend of protoplanetary disks presents a further significant challenge. Since the gas and dust densities diminish at large separations from the central star, it is difficult to measure any emission from these cold and faint regions. A popular approach of defining outer radii of disks is the radius R_{68} which encloses 68% ($\pm$1 standard deviation) of the measured (sub-)millimetre continuum dust emission. Note however, that this radius does not necessarily enclose 68% of the dust mass due to the uncertainties in the density distribution and optical depth of the material (Miotello et al., 2022). Measurements of R_{68} vary from 20 au to over 100 au (Manara et al., 2023). The bright emission of ^{12}CO allows to trace the outer radii of the gas in the disk, which are generally found to be larger than the outer radii of the dust component (Sanchis et al., 2021). Varying optical depths in the different wavelength ranges of these measurements or the growth of dust and subsequent inward drift could both explain the observed differences (Dutrey et al., 1998; Testi et al., 2003; Birnstiel et al., 2016, e.g.). Therefore, the correlation of outer disk radii of the different disk components with disk age is important in order to understand the time evolution of protoplanetary disks. The emerging general physical picture is that young disks extend to the order of $\sim$100 au (Manara et al., 2023).
Infrared observations of the light which is scattered by the smallest grains at the surface of the disk allow us to measure the vertical extent of disks. The aspect ratio, the ratio of a disks representative height at a given radial distance, is found to be increasing with radial separation (Avenhaus et al., 2018). This is consistent with theoretical predictions of flared disks (Kenyon and Hartmann, 1987; Chiang and Goldreich, 1997). Larger dust grains are found to be well-settled in a remarkably thin midplane layer in (sub-)millimetre measurements which provides valuable constraints for the physical processes involved in the disk evolution (Pinte et al., 2016; Villenave et al., 2022).

In the classical picture of protoplanetary disks, the radial disk profile is smooth and devoid of substructures. However, the most recent generation of high resolution (sub-)millimetre observatories, namely the *Atacama Large Millimeter Array* (ALMA), has revealed a remarkable diversity in disk substructures in the last few years. These substructures take the form of dust rings, deep gaps, spirals, and

arcs and are found at essentially all currently observable scales (Andrews, 2020; Benisty et al., 2022). There is a vast amount of possible origins of these substructures ranging from (magneto-)hydrodynamical processes to tidal effects, as well as processes related to the dust evolution (Bae et al., 2022). A particularly intriguing possibility lies in the tidal interaction of massive planets with the disk, forcing a ring-shaped gap in the disk around the planet's orbit. This could provide a way to find young massive exoplanets and to observe them while they are still undergoing formation (Dong et al., 2015). Indeed, some planets have been imaged in gaps of protoplanetary disks and their presence has been inferred by the measurements of planet-induced gas dynamics (Keppler et al., 2018; Teague et al., 2018). However, not all ring-like substructures have lead to the discovery of planets. As such, it is not clear whether these rings are carved by planets or whether rings predate planets and could rather serve as their birthplace. It has been shown that an accumulation of dust in a ring promotes the growth of dust and the rapid formation of planets (Zhang et al., 2015; Jiang and Ormel, 2022; Lau et al., 2022). In the wake of the newly discovered stunning diversity of disks, planet formation in structured disks is currently intensively studied (Drazkowska et al., 2022). Since substructures that are potentially related to planets are also found in very young disks, it is becoming increasingly clear that planet formation initiates already before the disk has fully assembled. In this thesis, however, as is the case in many current studies, the focus lies on the physical processes that take place in fully formed protoplanetary disks that show no initial substructures.

1.4 The core accretion paradigm

To set the context for planet formation, a brief summary of the conditions in the protoplanetary disk is helpful. The protoplanetary disk contains mainly gas and to the order of 1% dust. The dust component has the tendency to settle in the midplane, where the density of the gas disk is the largest. By comparing with dust grain sizes in the interstellar medium, the lower limit of the size of the dust grains in the protoplanetary disk is found to be on the order of micrometres. The fundamental challenge of planet formation is to bridge the size range from micrometre grains up to planets larger than Jupiter with radii of more than 100,000 kilometres. The presence of giant planets which contain hundreds of Earth masses in H-He, implies that their formation must take place before the gas disk dissipates,

typically within a couple million years. A detailed overview of the most important physical processes of planet formation is given in Chapter 2. In the following, a qualitative picture of planet formation is outlined.

There are two paradigms of planet formation which are thought to be possible: *gravitational instability* and *core accretion*. The former considers a planet formation process akin to the formation of stars. Massive disks collapse locally under their own gravity, forming fragments which may condense into planets. Gravitational instability has been initially proposed as a formation mechanism of the Solar System (Kuiper, 1951). Today, this scenario can be ruled out for the formation of the Solar System but it remains an intriguing pathway for massive planets on wide orbits, which is where the conditions for gravitational collapse are most likely to be satisfied. Gravitational instability in massive disks generally yields very massive planets, brown dwarfs, and even stellar companions.
The more popular formation paradigm of core accretion is relevant for planets within tens of au, where most exoplanets are known to exist. As the name suggests, it involves the formation of a planetary core[1] from the refractory material in the protoplanetary disk. If such a core becomes massive enough, gas in it's co-orbital vicinity in the protoplanetary disk can be gravitationally bound to the core, further increasing the mass of the forming planet. At the so-called *critical core mass*, the accretion of gas becomes self-accelerating, commonly referred to as *runaway gas accretion*, resulting in a gas-dominated giant planet. In this picture, terrestrial planets can simply form as cores that are not massive enough to attract large amounts of gas. The next obvious question is how the cores form. Without going into the detailed physics presented in Chapter 2, the growth of cores can be divided into different stages. Initially, the dust grains can grow by coagulation to roughly centimetre sized, so-called *pebbles*. Growth by coagulation beyond this threshold is prevented by the fragmentation in mutual collisions and fast inward drift (Drazkowska et al., 2022). Various proposed mechanisms can lead to the local accumulation of pebbles which gravitationally collapse into much larger and more massive so-called *planetesimals*. This provides a way to skip over several orders of magnitude in size on a short timescale, which is a necessary acceleration in order

[1]In the field of planet formation, the notion of a core simply refers to everything but the planet's envelope. Notably, this convention is not adopted in general planetary science, where a core rather refers to the innermost layers of planetary interiors.

to form giant planets within observed disk lifetimes. However, planetesimal formation remains poorly understood and successful planetesimal formation can not be confidently demonstrated in all current dust evolution models (e.g. Estrada et al., 2016, 2022). The resulting initial size distribution of planetesimals is a crucial question which is not definitively answered yet either. Generally, they are found to be on the order of kilometres to hundreds of kilometres in diameter. Subsequently, planetesimals can grow via mutual collisions in a process called *planetesimal accretion*, or by the accretion of the remaining centimetre sized pebbles which is called *pebble accretion*. Note that the different solid accretion mechanisms are not mutually exclusive, which introduces an interesting interplay. Both mechanisms of solid accretion have different characteristics which influence all other aspects of planet formation, such as the accretion of gas and the planet's interaction with the protoplanetary disk. I investigate the concurrent accretion of planetesimals and pebbles in the context of giant planet formation in Chapter 4 (Kessler and Alibert, 2023).

Conceptually, the planet formation epoch ends after the dispersal of the gas disk. With the lack of gas drag, the remaining solids are quickly scattered and the formed planets are, a priori, isolated.[2] In the absence of the disk and with ceased accretion processes, planets evolve over billions of years. Planetary evolution is mainly characterised by the way planets cool and interact with the incident radiation of the central star. This can lead to loss processes which shape the atmosphere over long timescales, especially for planets close to their host star. Therefore, planetary evolution is crucial in the context of observed exoplanets that are billions of years old, many of which are on short orbits. A brief overview of the most important evolutionary processes is given in Chapter 2.8, however, the focus of this thesis lies on the formation stage.

1.5 Global modelling and population synthesis

Planet formation is inherently stochastic, involving a large number of interconnected processes. The aim of global models of planet formation is to combine all relevant physical process into a self-consistent model – from protoplanetary disk

[2]The planets are still interacting gravitationally which can lead to collisions, reshaping the planets considerably in terms of mass and radius.

to planetary system. This allows to study the importance and interplay of all included processes which are often studied in isolation (Drazkowska et al., 2022). However, it is not straight forward to confidently link initial conditions to the characteristics of the emerging planetary systems. This raises the question of how planet formation theory can be tested in the first place. Looking at the Solar System for instance, a single example of the planet formation process outcome, one might expect that it would be possible for a similar system to emerge from a planet formation model. But when presented with such a fitting model outcome, it is impossible to judge whether the modelled physical processes are necessarily the right ones or whether it is just a randomly fitting outcome of incomplete physics. A way to overcome this problem is to test planet formation theory on a statistical level by comparing synthetic populations of planetary systems, emerging from global models, with the exoplanet population. In order to obtain a meaningful synthetic population, initial condition parameters of the protoplanetary disk must be sampled from distributions that reflect observations. If the population comparison results in a good fit across the whole parameter space, the global model likely contains all the relevant physical processes and provides a good picture of planet formation. If there are mismatches, the nature of the differences and the detailed study of formation pathways can hint at incomplete or inaccurate physics. In this way, *population synthesis* can inform which specific physical processes might be most important to include or understand better in order to progress planet formation theory efficiently.

Planetary population synthesis imposes a number of requirements on a planet formation model. First of all, the model must be global in the sense that it contains the structure and evolution of the protoplanetary disk, accretion processes, planetary structure, planet-planet, as well as planet-disk interactions (Benz et al., 2014). Furthermore, since a large number of simulations[3] must be performed, the model is required to be computationally efficient. In practice, this implies necessary simplifications of the numerical descriptions of the physical processes. Along with significant observational uncertainties associated with the initial conditions of protoplanetary disks, this reduces the predictive power and capability to dismiss certain models (Drazkowska et al., 2022). Nevertheless, population synthesis has

[3] A single population can contain up to a hundred thousand planets (e.g. Emsenhuber et al., 2021a).

revealed and contributed to the understanding of several key planet formation processes. For instance, early syntheses have identified that planets most likely do not form at the same location (*in-situ*) but are subject to *orbital migration* (Ida and Lin, 2008; Mordasini et al., 2009b). This lead to the increasingly in-depth modelling of planetary migration in dedicated studies (e.g. Masset and Casoli, 2010; Kley et al., 2009; Paardekooper et al., 2010) which were in turn again incorporated in improved global models (Dittkrist et al., 2014). Similarly, grain dynamics and opacities of planetary atmospheres have been shown to play a critical role in planet formation (Mordasini et al., 2014) which has subsequently spawned more detailed models of dust dynamics (e.g. Ormel, 2014; Mordasini, 2014; Brouwers and Ormel, 2020; Brouwers et al., 2021). These, and further (see Mordasini, 2018), examples highlight the productive synergy between global and specialised models.

In this thesis, planet formation is investigated in the context of a global planet formation model. By comparing formation outcomes emerging from different assumptions and model setups, the relative impact and interplay of different planet formation processes can be studied. This approach is especially powerful when applied to population synthesis. In a large number of simulations, using different initial conditions, the intricate interplay of the physical processes is probed in a large parameter space. This provides another dimension to the understanding of planet formation as it captures the stochastic nature of the combination of all processes. This approach is applied to the interplay between accretion processes in chapter 4 (Kessler and Alibert, 2023) and to formation pathways of Uranus/Neptune-like planets in chapter 5 (Kessler et al., subm.).

2 The physics of planet formation

Planet formation from protoplanetary disk to planetary system is a complex combination of many physical processes, acting on vastly different length and timescales which presents a significant challenge for modelling. In the following, I provide an overview of the most important physics which constitute a global model of planet formation and at the same time represent the fundamentals of planet formation theory. This overview is inspired by various previous works (Armitage, 2020; Drazkowska et al., 2022; Burn and Mordasini, 2024). The physics introduced here are the foundations of the global model used in chapters 4 and 5, which is described in detail in chapter 3, highlighting the specific model choices.

2.1 Protoplanetary disk evolution

As described in chapter 1.3, protoplanetary disks are not static structures but rather evolve over time. Here, we are interested in the dominant component of the disk which is in the gaseous phase and refer to chapter 2.2 for a discussion of the dust evolution which is coupled to the evolution of the gas disk. The key observational constraint which hints at the time evolution of protoplanetary disks is the stellar accretion of gas. This observation already poses a fundamental and non-trivial problem because in order for gas to flow inward and accrete onto the star, it must lose angular momentum in some way. Since the total angular momentum is conserved, gas somewhere else has to gain angular momentum. There are two main theories that are both currently pursued in order to explain the angular momentum transport in protoplanetary disks. Material could be launched directly from the disk in so-called disk winds, thought to be driven by large-scale magnetic fields, effectively removing angular momentum from the disk. These magnetohydrodynamic disk winds are a recently popularised idea which is able to reconcile with many observed properties of protoplanetary disks. It is beyond the scope of this thesis to discuss this theory and I refer to the detailed review of Pascucci

et al. (2023). The classical approach to the problem is to consider the redistribution of angular momentum within the disk. In contrast to the direct removal of angular momentum, here, some gas in the disk gains angular momentum and moves outwards. In this picture, the disk spreads out over time which facilitates an inward flow of gas onto the star. The mechanism of angular momentum transport is typically described as an *effective viscosity* ν with the idea that parcels of gas exchange angular momentum through turbulent mixing. The amount of turbulence in protoplanetary disks is therefore a key quantity which I will revisit later. Considering thin and axisymmetric disks, it is simplest to describe the disk gas by a surface density Σ_g which is defined as the vertically integrated gas density

$$\Sigma_g = \int_{-\infty}^{\infty} \rho_g(z) dz. \tag{2.1}$$

Note that by assumption, the surface density takes the same value at all azimuthal angles ϕ. The vertical gas density profile $\rho_g(z)$ is obtained by comparing the vertical force balance between gravity and pressure (vertical hydrostatic equilibrium) at cylindrical radius r and height z. In the case of geometrically thin and vertically isothermal disks, and Keplerian orbits, the vertical gas density profile takes the form

$$\rho_g(z) = \rho_{\mathrm{mid,g}} e^{-z^2/(2H_g^2)}, \tag{2.2}$$

where $\rho_{\mathrm{mid,g}}$ is the gas density in the midplane ($z = 0$) given by

$$\rho_{\mathrm{mid,g}} = \frac{\Sigma_g}{\sqrt{2\pi} H_g}. \tag{2.3}$$

H_g is the vertical disk scale-height given by

$$H_g = \frac{c_s}{\Omega_{\mathrm{K}}}, \tag{2.4}$$

depending on the Keplerian frequency

$$\Omega_{\mathrm{K}} = \sqrt{\frac{GM_\star}{r^3}}, \tag{2.5}$$

which is the classic result obtained from the balance of the gravitational and centrifugal force around a star of mass $M_\star$, G being the gravitational constant. The isothermal sound speed c_s at temperature T reads

$$c_s = \sqrt{\frac{k_\mathrm{B} T}{\mu m_p}}, \tag{2.6}$$

where k_B is the Boltzmann constant and μ is the mean molecular weight of the gas in units of the proton mass m_p. Typically, the interstellar gas value of $\mu \approx 2.3$[1] is used (e.g. Emsenhuber et al., 2021a). This means that, given equation (2.4), we are assuming a vertically isothermal disk in order to estimate the thickness of the disk using the midplane temperature $T_\mathrm{mid,g}$.

The governing equation of the temporal evolution of the radial surface density profile $\Sigma_g(r,t)$ can be obtained from radial mass conservation and the conservation of angular momentum (Pringle, 1981). A detailed derivation is given in appendix A, yielding the viscous disk evolution equation (Lüst, 1952; Lynden-Bell and Pringle, 1974)

$$\dot{\Sigma}_g = \frac{3}{r}\frac{\partial}{\partial r}\left[r^{1/2}\frac{\partial}{\partial r}\left(\nu\Sigma_g r^{1/2}\right)\right], \tag{2.7}$$

where the dot signifies the temporal derivative. In this approach, the evolution of the protoplanetary disk is reduced to a one-dimensional problem of a surface density Σ_g with viscosity ν. One can show easily that equation (2.7) has the form of a diffusion equation (see e.g. Armitage, 2020). Therefore, the disk evolution equation is, in full, the 1D axially symmetric viscous diffusion equation of a geometrically thin disk.

In protoplanetary disk conditions, the molecular viscosity of hydrogen is far too low to account for stellar accretion rates and the disk evolution timescale. On the other hand, fluids with low molecular viscosity are highly turbulent in the presence of a physical perturbation. Classically, the magneto-rotational instability (MRI) is invoked as a source of turbulence in protoplanetary disks which appears in ionized rotating fluids in the presence of a magnetic field. However, it is unlikely that

[1] This value is reflective of the fact that the majority of gas is molecular hydrogen (H_2) of mass $2m_p$ with a small contribution of mainly helium of mass $4m_p$.

conditions leading to MRI induced turbulence are equally maintained everywhere in the disk and constant in time. In the interest of brevity, I refrain from discussing further sources of turbulence in this thesis and refer to the detailed review of Lesur et al. (2022).
Assuming protoplanetary disks really are turbulent, the isotropic turbulence leads to macroscopic mixing which acts as an effective or turbulent viscosity. Since the scale of the turbulent flow is smaller than the scale height H_g and the flow must be shock-free and therefore sub-sonic, the magnitude of the turbulent viscosity is typically parametrised as (Shakura and Sunyaev, 1973)

$$\nu = \alpha c_s H_g. \tag{2.8}$$

The dimensionless Shakura-Sunyaev α parameter, measures the efficiency of angular momentum transport due to turbulence. Since viscosity contributes to the temperature in the disk, large values of alpha imply thicker disks and vice-versa. Considering stellar accretion rates and measurements of disk thicknesses, typical values are $\alpha \sim 10^{-4} - 10^{-3}$.

The disk temperature in the midplane $T_{\mathrm{mid,g}}$ is driven by viscous heating and the direct irradiation of the star. Assuming the energy loss due to the viscous torque (A.17) is ultimately converted into heat and radiated away on either of the two surfaces of the disk with temperature T_{surf}, the energy dissipation rate $\dot{E}_\nu$ per unit surface area is (Armitage, 2020)

$$\dot{E}_\nu = \frac{9}{8}\nu\Sigma_g\Omega_{\mathrm{K}}^2 = \sigma_{\mathrm{SB}}T_{\mathrm{surf}}^4, \tag{2.9}$$

where σ_{SB} is the Stefan-Boltzmann constant. Assuming the dissipation is strongly concentrated toward the disk midplane, the disk surface and midplane temperatures are proportional (Armitage, 2020)

$$T_{\mathrm{mid,g}}^4 \propto \tau T_{\mathrm{surf}}^4, \tag{2.10}$$

with the optical depth $\tau = \kappa\Sigma_g$ and the opacity κ. In practice, one has to consider whether the disk is optically thin or thick in the vertical direction in order to link $T_{\mathrm{mid,g}}$ and T_{surf}. In general, the disk opacity stems from both molecular and dust contributions and is a key disk parameter with large associated uncertainties.

In reality, the temperature due to stellar irradiation $T_{\rm irr} = T_{\rm irr}(T_\star, T_{\rm cloud}, T_{\rm irr,mid})$ contributes to the midplane temperature as well. The direct irradiation of the disk surface given a stellar surface temperature $T_\star$ is dependent on the disk geometry (e.g. Hueso and Guillot, 2005). Furthermore, the background temperature $T_{\rm cloud}$ set by the molecular cloud environment can be considered as shown in chapter 3.1. The direct stellar irradiation through the midplane $T_{\rm irr,mid}$ becomes important in the late stages of evolution when the disk midplane becomes optically thin. It depends on the stellar luminosity $L_\star$ and the midplane optical depth $\tau_{\rm mid}$ as

$$T^4_{\rm irr,mid} = \frac{L_\star}{16\pi r^2 \sigma_{\rm SB}} e^{-\tau_{\rm mid}}. \tag{2.11}$$

Without going into detail on the form of $f(\tau)$ here (see e.g. Nakamoto and Nakagawa, 1994), the midplane temperature can be described as

$$\sigma_{\rm SB} T^4_{\rm mid,g} = \sigma_{\rm SB} T^4_{\rm irr} + f(\tau)\dot{E}_\nu. \tag{2.12}$$

The midplane pressure can be obtained by the simple equation of state

$$P_{\rm mid,g} = \rho_{\rm mid,g} c_s^2. \tag{2.13}$$

This radial one dimensional description with the midplane quantities and the associated vertical structure[2] provides the parameters needed for the description of the physics of planet formation. In studies of planet formation in global models, this approach is almost exclusively used since global full (magneto-)hydrodynamical models are not feasible when the evolution of the solid disk component is of interest over millions of years as well. Sometimes, instead of considering the disk evolution according to equation (2.7), analytical evolution models or even static models are used (e.g. Chambers, 2009). In this thesis, I consider results from simulations that always include the viscous disk evolution.
However, to get an idea of the surface density profile Σ_g, it is instructive to look at the steady-state solution derived in appendix A for a constant stellar accretion rate $\dot{M}_\star$ around a star of radius $R_\star$. Considering $r \gg R_\star$, the relation (A.24) is simply

$$\Sigma_g = \frac{\dot{M}_\star}{3\pi\nu} \tag{2.14}$$

[2]Such models are sometimes also called 1+1-dimensional.

and we note that $\Sigma_g(r) \propto \nu^{-1}$ away from the inner disk boundary. Combining the above equations in the simple case of $T_{\rm irr} = 0$, $f(\tau) = \frac{3}{8}\tau$, and assuming a temperature dependent opacity due to icy grains $\kappa = \kappa_0 T^2_{\rm mid,g}$, the steady state surface density simplifies to (Armitage, 2020)

$$\Sigma_g^3 = \frac{64}{81\pi}\frac{\sigma_{\rm SB}}{\kappa_0}\left(\frac{\mu m_p}{k_{\rm B}}\right)^2 \alpha^{-2}\dot{M}_\star. \tag{2.15}$$

For typical values $\dot{M}_\star = 10^{-8}$ $\mathrm{M_{Sun}yr^{-1}}$, $\alpha = 10^{-3}$, and $\kappa_0 = 2.4\times10^{-4}$ $\mathrm{cm^2g^{-1}K^{-2}}$, the surface density is $\Sigma_g \approx 300$ $\mathrm{gcm^{-2}}$. This value is rather an overestimation since disks are expected to be warmer due to stellar irradiation. The viscous timescale $t_\nu \approx r^2/\nu$ at 30 au is ~ 2.8 Myr which is consistent with the significant observed evolution of protoplanetary disks over millions years.

2.1.1 Photo-evaporation

Above, I have considered the internal physics driving the evolution of protoplanetary disks and the stellar accretion. However, loss processes due to stellar irradiation from the host star and the external environment also play a role in the disk evolution and, in particular, in the dispersal of evolved disks. These processes are called *photo-evaporation* and we differentiate between *internal* and *external* energy sources. Due to the heating of the disk surface, gas can escape the stellar gravitational field if the thermal energy is sufficient. The loss rate

$$\dot{\Sigma}_{\rm photo} \sim \rho_{\rm base} c_s \tag{2.16}$$

depends on the gas density $\rho_{\rm base}$ and thermal sound speed c_s at the depth to which photons can penetrate, which is determined by the disk opacity. Since opacities are wavelength dependent, the spectrum of the incident irradiation must be considered. In ascending order of energy per photon, the irradiation is divided into far ultraviolet (FUV), extreme ultraviolet (EUV), and X-rays. Therefore, the critical radius within which the gas stays bound is wavelength dependent and found to be $\lesssim 1-2$ au for EUV-driven evaporation, $\lesssim 2-4$ au for X-ray-driven evaporation, and $\lesssim 3-12$ au for FUV-driven evaporation (Pascucci et al., 2023). Internal photo-evaporation due to the host star is most relevant in the inner disk

where X-rays and EUV radiation drive the loss. The X-ray contribution to internal photo-evaporation has recently been shown to dominate over the EUV-driven wind (e.g. Jennings et al., 2018). FUV radiation from young neighbouring stars can be significant since star formation occurs in clusters of hundreds of thousands of stars. Therefore, FUV-driven external photo-evaporation of the outer disk acts in parallel to the viscous evolution of the disk. Total mass loss rates due to photo-evaporation are found to be on the order of $10^{-9} - 10^{-8}$ $M_{Sun}yr^{-1}$ in radiation hydrodynamical simulations (Wang and Goodman, 2017; Nakatani et al., 2018; Komaki et al., 2021). Due to the impact of grain opacities, the description of the photo-evaporation processes, especially the FUV-driven heating, are coupled to the evolution of dust grains and the disk chemistry. A full physical characterisation of these thermal winds is not yet achieved.

Qualitatively, photo-evaporation expresses in two main ways in the late stages of the evolution of a protoplanetary disk. Internal photo-evaporation can carve an inner cavity as the optical depth increases for an ever thinner disk. On the other hand, external photo-evaporation erodes the outer disk edge which is crucial in the picture of a viscously expanding disk. External photo-evaporation is the main process linked to the dispersal of the gas disk, causing the disk to shrink over time despite its tendency of viscous spreading. For global modelling, this means that the external photo-evaporation rates can be constrained by the observed disk lifetimes (e.g. Emsenhuber et al., 2021a). Considering internal and external photo-evaporation introduces sink terms $\dot{\Sigma}_{\mathrm{photo,int}}$ and $\dot{\Sigma}_{\mathrm{photo,ext}}$ to the disk evolution equation (2.7), yielding

$$\dot{\Sigma}_g = \frac{3}{r}\frac{\partial}{\partial r}\left[r^{1/2}\frac{\partial}{\partial r}\left(\nu\Sigma_g r^{1/2}\right)\right] - \dot{\Sigma}_{\mathrm{photo,int}} - \dot{\Sigma}_{\mathrm{photo,ext}}. \tag{2.17}$$

2.2 Dust evolution

The dynamics and evolution of dust grains in a protoplanetary disk are driven by the interaction with the surrounding gas disk. Dust grains are coupled to the motion of the gas as they experience a drag force F_D. The drag force depends fundamentally on the size of dust grains compared to the mean free path λ_{mfp} of the gas. Considering small spherical dust grains of radius a, two drag regimes are

identified

$$F_D = \begin{cases} \frac{4}{3}\pi a^2 \rho_g \bar{v} v & \text{Epstein,} \quad (2.18) \\ 6\pi a \rho_g \nu_{\text{mol}} v & \text{Stokes.} \quad (2.19) \end{cases}$$

The Epstein regime applies for the smallest grains with $a \lesssim \lambda_{\text{mfp}}$ and the Stokes regime is relevant for $a > \lambda_{\text{mfp}}$ and for Reynolds numbers $Re = \frac{2va}{\lambda_{\text{mfp}}\bar{v}} \lesssim 1$ (Birnstiel et al., 2010). Here, $\bar{v} = \sqrt{\frac{8}{\pi}} c_s$ denotes the mean thermal velocity, v is the relative speed between the gas and the dust grain, and ρ_g is the gas density which is just $\rho_{\text{mid,g}}$ in the context of dust in the midplane of the protoplanetary disk. The viscosity that is relevant for the gas drag at this scale is the molecular viscosity ν_{mol}. Note that even larger bodies like planetesimals and planets obey modified Stokes laws (e.g. Weidenschilling, 1977). In order to quantify how well the dust grains are coupled to the gas motion, the dimensionless coupling constant called the *Stokes number* St

$$\text{St} = \frac{t_{\text{stop}}}{t_{\text{eddy}}} \quad (2.20)$$

is usually used. The stopping time t_{stop} describes the characteristic time it takes for a particle to lose it's momentum under friction. It is defined as

$$t_{\text{stop}} = \frac{m_{\text{grain}} v}{F_D}, \quad (2.21)$$

where we assume that the grains are spherical and have an internal density ρ_{grain} such that their mass is $m_{\text{grain}} = \frac{4}{3}\pi a^3 \rho_{\text{grain}}$. In the two main drag regimes the stopping time is then

$$t_{\text{stop}} = \begin{cases} \frac{\rho_{\text{grain}} a}{\rho_g \bar{v}} & \text{Epstein,} \quad (2.22) \\ \frac{2\rho_{\text{grain}} a^2}{9\nu_{\text{mol}} \rho_g} & \text{Stokes.} \quad (2.23) \end{cases}$$

The eddy turn-over time t_{eddy} describes the characteristic timescale of the turbulent gas motion. Until here, the description of dust-gas coupling is universal and not specific to protoplanetary disks. In the context of protoplanetary disks, the typical assumption is (e.g. Cuzzi et al., 2001; Schräpler and Henning, 2004; Birnstiel et al.,

2010)

$$t_{\rm eddy} = \frac{1}{\Omega_{\rm K}}. \tag{2.24}$$

In this case, the Stokes numbers of particles in the disk midplane are

$$\mathrm{St} = \begin{cases} \dfrac{\pi \rho_{\rm grain} a}{2\Sigma} & \text{Epstein,} \quad (2.25) \\ \dfrac{2\pi \rho_{\rm grain} a^2}{9\lambda_{\rm mfp}\Sigma} & \text{Stokes.} \quad (2.26) \end{cases}$$

If the Stokes number is much smaller than 1, the dust grains are well coupled to the gas motion, and if the Stokes number is much larger than 1, the dust grains are fully decoupled from the gas which increases the relative speed v between the dust and the gas. This has two important consequences for grains of different sizes a. Firstly, it can be demonstrated in a simple calculation that larger grains settle to the disk midplane. Considering Epstein drag and the stellar gravity component in the vertical disk direction at some height z

$$\frac{4}{3}\pi a^2 \rho_g \bar{v} v_z = m_{\rm grain}\Omega_{\rm K}^2 z, \tag{2.27}$$

where v_z is here the terminal speed at which a grain settles in the vertical direction, yields a characteristic settling time

$$t_{\rm settle} = \frac{z}{v_z} = \frac{1}{t_{\rm stop}\Omega_{\rm K}^2}. \tag{2.28}$$

Therefore, larger grains with larger characteristic stopping time $t_{\rm stop}$ settle more quickly. Note that this is neglecting the vertical stirring of dust due to turbulence which can be described as vertical diffusion. The diffusion timescale

$$t_{\rm diff} = \frac{z^2}{D_d} \tag{2.29}$$

over a distance z depends on the dust diffusivity (Youdin and Lithwick, 2007)

$$D_d \approx D_g(1 + \mathrm{St}^2) \approx \nu(1 + \mathrm{St}^2), \tag{2.30}$$

where the gas Diffusivity D_g is often approximated by the viscosity ν. Comparing the diffusion and settling timescale yields the scale height of the dust disk H_d as a function of the gas disk scale height H_g

$$H_d = H_g \sqrt{\frac{\alpha}{\mathrm{St} + \alpha}}. \tag{2.31}$$

The settling and concentration of solid material in the disk midplane is fundamentally important for the formation of planets.

The second important consequence of the decoupling of larger dust grains from the gas is radial drift. Fully decoupled particles are on Keplerian orbits while the gas is slightly non-Keplerian due to the self-support of the gas through the radial pressure gradient. This relative velocity between the gas and decoupled particles leads to drag and accelerates the dust, causing it to gain or lose angular momentum depending on the sign of the pressure gradient. In the radial direction this means particles drift inwards for a negative pressure gradient and outwards for a positive pressure gradient. Following Weidenschilling (1977) and considering the midplane of the disk, the gravitational acceleration on a circular Keplerian orbit is

$$g = \frac{GM_\star}{r^2} = \Omega_\mathrm{K}^2 r = \frac{v_\mathrm{K}^2}{r}, \tag{2.32}$$

where $v_\mathrm{K} = \Omega_\mathrm{K} r$ is the Keplerian velocity. The hydrostatic equilibrium in the co-moving reference frame with the gas reads

$$\Delta g = \frac{1}{\rho_\mathrm{mid,g}} \frac{\partial P}{\partial r}. \tag{2.33}$$

The total azimuthal gas velocity $v_{\phi,g}$ is then

$$\frac{v_{\phi,g}^2}{r} = g + \Delta g. \tag{2.34}$$

We can therefore write the deviation of the gas velocity from the Keplerian velocity Δv as

$$\Delta v = v_\mathrm{K} - v_{\phi,g} = v_\mathrm{K} - v_\mathrm{K} \sqrt{1 + \frac{\Delta g}{g}}, \tag{2.35}$$

which for almost Keplerian orbits ($\frac{\Delta g}{g} \ll 1$) is

$$\Delta v \approx -v_{\mathrm{K}} \frac{\Delta g}{2g} = -\frac{1}{2\rho_{\mathrm{mid,g}}\Omega_{\mathrm{K}}} \frac{\partial P}{\partial r} \equiv \eta v_{\mathrm{K}}, \tag{2.36}$$

where η is a dimensionless parameter of the radial pressure gradient. It is commonly written as

$$\eta = -\frac{r}{2\rho_{\mathrm{mid,g}} v_{\mathrm{K}}^2} \frac{\partial P}{\partial r} = -\frac{1}{2} \left(\frac{H}{r}\right)^2 \frac{\partial \ln P}{\partial \ln r}. \tag{2.37}$$

In unstructured disks, the radial pressure gradient is generally negative ($\eta > 0$), which means that the orbital gas velocity is sub-Keplerian. Therefore, a decoupled particle orbiting at Keplerian velocity is experiencing a headwind which causes it to lose angular momentum and drift inwards. Note that smaller, well-coupled, dust grains also drift inwards. Since they orbit with the gas at sub-Keplerian speed, the centrifugal force is insufficient to balance gravity (Armitage, 2020).
In general, the dust is coupled to the gas according to the Stokes number and does, therefore, not orbit at exactly Keplerian speed. We can write the azimuthal equation of motion of a dust particle as (Weidenschilling, 1977)

$$\frac{\partial}{\partial t} \left(r v_{\phi,d}\right) = -\frac{r}{t_{\mathrm{stop}}} \left(v_{\phi,d} - v_{\phi,g}\right), \tag{2.38}$$

where $v_{\phi,d}$ is the orbital velocity of a dust particle. The specific angular momentum $r v_{\phi,d}$ of a dust grain changes at a rate given by relative orbital velocity of the grain and the gas and the characteristic stopping time $t_{\mathrm{stop}} = \frac{\mathrm{St}}{\Omega_{\mathrm{K}}}$. We assume that the specific angular momentum is always almost Keplerian, leading to spiralling on almost circular Keplerian orbits. This means

$$\frac{\partial}{\partial t} \left(r v_{\phi,d}\right) \approx v_{r,d} \frac{\partial}{\partial r} \left(r v_{\mathrm{K}}\right) = \frac{1}{2} v_{r,d} v_{\mathrm{K}}, \tag{2.39}$$

using $\frac{\partial v_{\mathrm{K}}}{\partial r} = -\frac{v_{\mathrm{K}}}{2r}$. Equation (2.38) yields then the relative azimuthal velocity

$$v_{\phi,d} - v_{\phi,g} = -\frac{t_{\mathrm{stop}} v_{r,d} v_{\mathrm{K}}}{2r}. \tag{2.40}$$

The radial equation of motion of a dust particle is given by (Weidenschilling, 1977)

$$\frac{\partial v_{r,d}}{\partial t} = \frac{v_{\phi,d}^2}{r} - \Omega_{\mathrm{K}}^2 r - \frac{1}{t_{\mathrm{stop}}} \left(v_{r,d} - v_{r,g}\right), \tag{2.41}$$

where $v_{r,d}$ and $v_{r,g}$ are the radial velocities of the dust and the gas, respectively. The radial acceleration is given by the centrifugal contribution due to the orbital velocity $v_{\phi,d}$, the gravity $g = \Omega_{\mathrm{K}}^2 r$, and an advective term given by the relative radial speeds of the dust and gas flow. Using equation (2.35), we can rewrite the second term

$$-\Omega_{\mathrm{K}}^2 r = -\frac{v_{\phi,g}^2}{r(1-2\eta)}. \tag{2.42}$$

In the limits of $(v_{\phi,d} - v_{\mathrm{K}}) \ll 1$, $(v_{\phi,g} - v_{\mathrm{K}}) \ll 1$, and $\frac{\Delta g}{g} = -2\eta \ll 1$, the radial equation of motion reads

$$\frac{\partial v_{r,d}}{\partial t} = -2\eta \frac{v_{\mathrm{K}}^2}{r} + 2\frac{v_{\mathrm{K}}}{r}\left(v_{\phi,d} - v_{\phi,g}\right) - \frac{1}{t_{\mathrm{stop}}}\left(v_{r,d} - v_{r,g}\right). \tag{2.43}$$

Assuming terminal radial velocity ($\dot{v}_{r,d} = 0$) and using equation (2.40), the radial velocity of a dust particle $v_{r,d}$ can be expressed in terms of the Stokes number as

$$v_{r,d} = \frac{1}{\mathrm{St}^2 + 1} v_{r,g} - \frac{\mathrm{St}}{\mathrm{St}^2 + 1} 2\eta v_{\mathrm{K}}. \tag{2.44}$$

The first term is the radial velocity due to advection with the radial gas flow and the second term is the radial velocity induced by the differential orbital velocity of dust and gas. Note that, here, we assume that the gas velocity is unaffected by the dust particles which is feasible in the limit of $\epsilon = \frac{\rho_{\mathrm{mid,d}}}{\rho_{\mathrm{mid,g}}} \ll 1$ (Nakagawa et al., 1986). We can again identify the relative velocity of a Keplerian orbit $\Delta v = \eta v_{\mathrm{K}}$, which is achieved for $\mathrm{St} = 1$, representing the maximal radial drift velocity possible for a given local pressure gradient η. Dust grains which are large enough to drift significantly, typically $0.01 \lesssim \mathrm{St} \lesssim 1$, are called *pebbles*. Depending on the disk conditions and radial distance, pebble sizes range from millimetres to metres. Pebbles are thought to play a key role in the formation of planetesimals and planets as discussed in chapters 2.3 and 2.4.

Similar to the evolution of the gas disk, we are looking for the evolution equation of the dust component of the disk described by the dust surface density Σ_d. Mass conservation reads (Armitage, 2020)

$$\frac{\partial \Sigma_d}{\partial t} = -\frac{\partial \mathcal{F}_d}{\partial r}, \tag{2.45}$$

where $\mathcal{F}_d$ is the dust mass flux. The flux is decomposed into an advective term and a diffusive term

$$\mathcal{F}_d = \Sigma_d v_{r,g} - D_d \Sigma_g \frac{\partial}{\partial r}\left(\frac{\Sigma_d}{\Sigma_g}\right), \tag{2.46}$$

where the subscripts indicate the disk components of dust and gas explicitly. The evolution of the dust surface density is then given by the advection-diffusion equation

$$\frac{\partial \Sigma_d}{\partial t} = \frac{1}{r}\frac{\partial}{\partial r}\left[r D_d \Sigma_g \frac{\partial}{\partial r}\left(\frac{\Sigma_d}{\Sigma_g}\right) - r \Sigma_d v_{r,d}\right]. \tag{2.47}$$

As in the gas disk, the midplane dust density is related to the surface density Σ_d and the scale height H_d by

$$\rho_{\mathrm{mid,d}} = \frac{\Sigma_d}{\sqrt{2\pi} H_d}. \tag{2.48}$$

Since the dust dynamics depend on the size of the dust grains, the next important question is regarding the growth of dust particles. Grains can grow by coagulation in mutual collisions. In detail, dust collisions do not always result in perfect sticking but also bouncing or fragmentation into smaller grains. The collision outcome depends on the relative collision velocities, grain sizes, grain composition, etc. The growth rate due to coagulation is described by the Smoluchowski equation which incorporates collision rates and outcomes depending on the collision parameters (Smoluchowski, 1916). I omit an in-depth look at dust growth and rather focus on the growth timescale and resulting dust sizes.
The relative velocity Δv_{turb} between dust particles with $\mathrm{St} \lesssim 1$ is mainly driven by turbulence and can be approximated as (Ormel and Cuzzi, 2007)

$$\Delta v_{\mathrm{turb}} \approx \sqrt{3\alpha \mathrm{St}} c_s. \tag{2.49}$$

Assuming mono-disperse growth, where a particle doubles its mass in every collision, the growth timescale is

$$t_{\rm grow} \approx \frac{1}{Z\Omega_{\rm K}}, \tag{2.50}$$

where $Z = \frac{\Sigma_d}{\Sigma_g}$ is the (local) dust-to-gas ratio. This reveals that grain growth in a protoplanetary disk operates inside-out. In the context of radial drift, this is important as grains from the outer disk take longer to grow to sizes where they start drifting inwards, supplying the inner disk with material in the form of pebbles. There are a couple of limits to the growth of dust grains, preventing them to grow beyond pebble sizes. Due to the increasing relative velocity between dust and gas as grains grow to pebbles, at some point, they drift inwards on a shorter timescale than they can grow further. Equating the growth and drift timescales, the drift-limited Stokes number is (Klahr and Bodenheimer, 2006; Birnstiel et al., 2012)

$$\mathrm{St}_{\rm drift} = \frac{2Z}{|\eta|}, \tag{2.51}$$

which, assuming Epstein drag, corresponds to a size limit of

$$a_{\rm drift} = \frac{4\Sigma_d}{|\eta|\pi\rho_{\rm grain}}. \tag{2.52}$$

A second important size limit arises due to increasing turbulent relative velocities between pebbles as they grow larger as described in equation (2.49). At some point, the threshold velocity $v_{\rm frag}$ is reached where collisions are too energetic to result in sticking and rather result in fragmentation of the colliding pebbles. Assuming all pebbles have the same size, the fragmentation-limited Stokes number is

$$\mathrm{St}_{\rm frag} = \frac{v_{\rm frag}^2}{3\alpha c_s^2}, \tag{2.53}$$

which, assuming Epstein drag, corresponds to a size limit of

$$a_{\rm frag} = \frac{2\Sigma_g v_{\rm frag}^2}{3\pi\rho_{\rm grain}\alpha c_s^2}. \tag{2.54}$$

Typical values of the fragmentation threshold velocity used in the literature are

$v_{\rm frag} \approx 1 - 10$ ms^{-1}. The fragmentation velocity likely depends on the composition and porosity of the pebbles (Wada et al., 2011; Meru et al., 2013; Blum, 2018). In laboratory experiments, it has been found that pebbles containing water ice stick more easily with $v_{\rm frag} \approx 10$ ms^{-1} and ice-free pebbles consisting of silicate monomers are more easily fragmented with $v_{\rm frag} \approx 1$ ms^{-1} (Aumatell and Wurm, 2014; Gundlach and Blum, 2014). However, there is no clear consensus from laboratory experiments on these values and trends. Some recent studies are not finding a strong dependence of $v_{\rm frag}$ on the composition (Gundlach et al., 2018; Steinpilz et al., 2019; Musiolik and Wurm, 2019).

Given the physical descriptions above, the qualitative picture of dust evolution in a protoplanetary disk is as follows. Micrometre dust grains grow by coagulation and settle in the disk midplane. As they grow to pebble size, they decouple from the gas motion and drift inwards. This happens from the inside-out through the disk, finally resulting in a continuous flux of pebbles fed by the mass reservoir in the outer disk. Generally, pebble sizes are fragmentation-limited in the inner disk and drift-limited in the outer disk beyond ~ 20 au (Birnstiel et al., 2016).
Regarding the composition of the solid material which will later form planets, the disk temperature structure plays a crucial role. The main molecule of interest, both due to its abundance and its significance for life, is water. In the inner, hotter, regions of the disk, water is in the gas phase. At some point further out, defined by the equations of state of water, it can condense onto dust grains as ice. This location is called the *water iceline* and has been identified as a particularly interesting planet formation location (Cuzzi and Zahnle, 2004; Öberg et al., 2011; Ros and Johansen, 2013; Schoonenberg and Ormel, 2017; Drążkowska and Alibert, 2017). Assuming the sublimation of ice is rapid compared to the radial drift, a large fraction of mass is removed from the solid phase inside the iceline and left inaccessible for planets through accretion of solids. Outside of it, however, the surface density of dust is larger. Additionally, the dry pebbles are smaller and drift more slowly which causes a pile-up of pebbles inside the iceline (Birnstiel et al., 2010), whereas the released water vapour can diffuse outwards and re-condensate onto the icy pebbles outside of the iceline, increasing the pebble surface density just outside of the iceline (Cuzzi and Zahnle, 2004). As seen in the next chapter, concentrations of solids are a necessary next step towards the formation of planets. Note that, naturally, the concept of icelines applies to all compounds that are present and experience condensation/sublimation conditions in the protoplanetary

disk.

2.3 Planetesimal formation

As described in the previous chapter, larger objects are not formed in mutual collisions beyond pebble sizes ($\mathrm{St} \lesssim 1$). Another way for larger objects to grow is the local collapse under self-gravity of pebbles, directly forming planetesimals (Goldreich and Ward, 1973). The gravitational stability of a thin particle disk is determined using linear stability analysis where the classical instability criterion is (Toomre, 1964)

$$Q \equiv \frac{c_s \Omega_\mathrm{K}}{\pi G \Sigma_d} < 1. \tag{2.55}$$

Typically, a disk is assumed to be unstable if $Q \lesssim Q_\mathrm{crit}$, where the critical value of Q_crit is of order, but slightly larger than, one (Armitage, 2020). Assuming gravitational collapse occurs on the free-fall timescale, planetesimals form very quickly on the order of years. The resulting planetesimal size distribution is poorly understood, but generally diameters of $\sim 1 - 100$ km are found. The size dependence on orbital distance is also not clear, since although collapsing pebble clouds are larger and more massive at larger distances, the formed planetesimals may simply be more numerous and of the same size as in the inner disk regions (Polak and Klahr, 2022).

In order to locally satisfy the Toomre instability criterion in a protoplanetary disk, pebbles must accumulate significantly. There are multiple proposed processes which can lead to the concentration of dense, potentially unstable, pebble clouds (see e.g. Cuzzi et al., 2008; Klahr et al., 2018; Hartlep and Cuzzi, 2020). The most commonly mentioned effect is the streaming instability which can occur when particles in a fluid interact aerodynamically at a mutual flow velocity (Youdin and Goodman, 2005). It leads to small-scale pebble concentrations of sufficient density to trigger gravitational collapse and is especially efficient for pebble sized particles with $\mathrm{St} \approx 1$ (Johansen et al., 2007). However, effective streaming instability itself also requires a locally increased concentration of pebbles and is typically said to trigger when

$$\frac{\rho_\mathrm{mid,d}}{\rho_\mathrm{mid,g}} \approx 1. \tag{2.56}$$

This condition is not readily met by the settling in the midplane but pebbles can accumulate sufficiently due to the radial drift as a consequence of their interaction with the gas. If pebbles drift slower at some location, faster drifting pebbles from further outside will pile up in a "traffic jam". As described before, this can happen at icelines where the drift velocity changes due to the size difference of dry and icy pebbles and due to the re-condensation of outwards diffusing water vapour (Drążkowska and Alibert, 2017). If, for whatever reason, there is a local pressure trap in the gas disk where the pressure gradient becomes positive ($\eta < 0$), pebbles experience a tailwind at this location. This prevents their inward drift past this point, potentially leading to planetesimal forming conditions. Since pebble accumulations are commonly observed as disk substructures in recent years, planetesimal and subsequent planet formation is increasingly frequently studied in these special locations (Zhang et al., 2015; Guilera and Sándor, 2017; Guilera et al., 2020; Jiang and Ormel, 2022; Lau et al., 2022). Note that the origin and longevity of such pebble traps is poorly constrained and often a free model parameter.

2.4 Accretion of solids

In order to grow planetesimals into planets, some of them must accrete significant amounts of solids. This can occur in mutual collisions of planetesimals and/or by the direct accretion of pebbles. In the formation phase, the most massive planetesimals are called *protoplanets* and in the context of the model described in chapter 3, protoplanets are the seeds for planet formation called *embryos*. I use "planets" and "protoplanets" interchangeably, as it is clear that the objects are still undergoing formation from context.

2.4.1 Planetesimal accretion

Considering mutual collisions of planetesimals, the collisional cross section is enhanced compared to the geometric cross section due to the gravitational attraction between the colliding bodies. Energy and momentum conservation of two colliding planetesimals of mass M and radius R, which are initially at a large separation and approaching at relative velocity δv, yields the gravitationally focused cross

section σ, given by

$$\sigma = 4\pi R^2 \left(1 + \frac{v_{\rm esc}^2}{\delta v^2}\right). \tag{2.57}$$

The escape velocity $v_{\rm esc}$ of one of the planetesimals at a distance R reads

$$v_{\rm esc} = \sqrt{\frac{2GM}{R}}. \tag{2.58}$$

It is apparent, that planets with $\delta v \ll v_{\rm esc}$ are most affected by gravitational focusing. In order to understand when this two-body approach is valid, we compare the gravitational attraction of a test particle around a protoplanet of mass M with the tidal gravitational field of the star of mass $M_\star$. This yields the so-called Hill radius $R_{\rm H}$ at a distance r to the star given by

$$R_{\rm H} = r \left(\frac{M}{3M_\star}\right)^{1/3}, \tag{2.59}$$

within which the two-body system dominates the dynamics. The orbital velocity $v_{\rm H}$ around the protoplanet at the Hill radius is called the Hill velocity

$$v_{\rm H} = \Omega_{\rm K} R_{\rm H}. \tag{2.60}$$

If the random velocity δv is large compared to the Hill velocity ($\delta v > v_{\rm H}$), then the collision is determined by the two body dynamics. This is called the *dispersion dominated* regime (Armitage, 2020). On the other hand, if $\delta v < v_{\rm H}$, then the stellar gravity is non-negligible and three-body effects must be considered. In this regime, the dynamics are said to be *shear dominated*.

Since the numerical task of calculating the gravitational interaction of thousands of planetesimals over millions of years is unfeasible in the context of global models, a statistical approach for the treatment of planetesimal dynamics is useful. Considering a planetesimal surface density $\Sigma_{\rm plan}$, the Keplerian orbital elements e (eccentricity) and i (inclination) of planetesimals of mass M are Rayleigh distributed. The probability distribution $f(e,i)$ is given by (Lissauer, 1993)

$$f(e,i) = \frac{4\Sigma_{\rm plan}}{M} \frac{ei}{\langle e^2\rangle \langle i^2\rangle} \exp\left[-\frac{e^2}{\langle e^2\rangle} - \frac{i^2}{\langle i^2\rangle}\right], \tag{2.61}$$

where $\langle e^2 \rangle$ and $\langle i^2 \rangle$ are the mean square eccentricity and inclination, respectively. The planetesimal velocity relative to the local circular orbit with $i = 0$ is then (Adachi et al., 1976)

$$\delta v = v_{\rm K} \sqrt{\eta^2 + \frac{5}{8} e^2 + \frac{1}{2} i^2}. \tag{2.62}$$

The evolution of the dynamical state of the planetesimals, characterised by e and i, is driven by the interaction of planetesimals with the gas, themselves, and growing protoplanets. Gas drag has a dampening effect on e and i, while the self-stirring and the stirring by protoplanets increase e and i. Avoiding a more detailed mathematical description of these interactions and the evolution of the dynamical state of planetesimals here, I refer to the specific model description in chapter 3.2.

In the dispersion dominated regime, and assuming all collisions are constructive, the planetesimal accretion rate $\dot{M}_{\rm plan}$ of a protoplanet of mass M and radius R is simply

$$\dot{M}_{\rm plan} = \rho_{\rm mid,plan} \delta v 4\pi R^2 \left(1 + \frac{v_{\rm esc}^2}{\delta v^2} \right), \tag{2.63}$$

for a planetesimal midplane density $\rho_{\rm mid,plan}$. Under the basic scaling assumptions of the planetesimal density in the midplane and the planetesimal scale height $H_{\rm plan}$ of

$$\rho_{\rm mid,plan} \sim \frac{\Sigma_{\rm plan}}{H_{\rm plan}}, \tag{2.64}$$

and

$$H_{\rm plan} \sim \frac{\delta v}{\Omega_{\rm K}}, \tag{2.65}$$

a fundamental characteristic of planetesimal accretion is found. The planetesimal accretion rate, given by

$$\dot{M}_{\rm plan} \sim \Sigma_{\rm plan} \Omega_{\rm K} 4\pi R^2 \left(1 + \frac{v_{\rm esc}^2}{\delta v^2} \right), \tag{2.66}$$

falls off with increasing distance to the star. This is because both the orbital frequency $\Omega_{\rm K}$ and the planetesimal surface density $\Sigma_{\rm plan}$ are decreasing with orbital separation. This poses a general challenge for the formation of planets in the outer disk with a steep fall off of planetesimal accretion rates outside of ~ 10 au.

In the early formation limit where $v_{\rm esc} \gg \delta v$, and δv is barely dependent on M, gravitational focusing drives a self-accelerating accretion rate, scaling super-linearly with mass as

$$\dot{M}_{\rm plan} \propto M^{4/3}. \tag{2.67}$$

This is commonly known as the *runaway planetesimal accretion* regime, where the largest planetesimals grow faster than the smaller ones, separating themselves from the population of primordial planetesimals as protoplanets (Greenberg et al., 1978; Wetherill and Stewart, 1989; Kokubo and Ida, 1996, 2000).
As the protoplanets grow more massive, the relative velocities and the planetesimal surface density in the vicinity of a protoplanet are no longer independent of its mass. Protoplanets increasingly stir up the planetesimals, which, in turn, results in a circularisation and planar alignment of the protoplanets in the disk midplane. Furthermore, the relative velocities between protoplanets and planetesimals increase to the point at which they no longer grow in the runaway accretion regime. Numerical simulations including the dynamical stirring rather show a sub-linear mass dependence of the accretion rate of (Ida and Makino, 1993; Kokubo and Ida, 2000)

$$\dot{M}_{\rm plan} \propto M^{2/3}. \tag{2.68}$$

This is known as the *oligarchic planetesimal accretion* regime, where more massive protoplanets grow slower than less massive protoplanets, leading to similarly sized so-called oligarchs. Note that, while growth of the protoplanets slows down, they still grow faster than the planetesimals, resulting in a bi-modal system of large protoplanets and more or less primordial planetesimals (Kokubo and Ida, 2012). This stage is often taken to be the initial state of global models such as the one described in chapter 3.

Since the planetesimal accretion rate strongly depends on the dynamical state of the planetesimal disk, not only the mass of the protoplanet, exciting the planetesimals, but also the mass and size of the planetesimals themselves are crucial. The stirring through gravitational interactions depends on the mass of involved objects, while the counteracting drag forces, scale with the surface of the bodies. Therefore, smaller planetesimals are more affected by the gas drag, dampening their eccentricities and inclinations, leading to lower relative velocities which allows them to be accreted more efficiently than larger planetesimals. Additionally, since the gas density around a growing embedded protoplanet increases in the

proximity of the planetary core, the collision cross section is larger for smaller planetesimals. Instead of narrowly passing the protoplanet, smaller planetesimals can be slowed down and collide with the protoplanet (Inaba and Ikoma, 2003; Mordasini and Burn, 2024). This effect can be significant, since the gas that is gravitationally bound to the protoplanet in the early phases of planet formation extends all the way to radii comparable to the Hill radius.
Note that not all collisions between planetesimals are constructive, but rather ejecting fragments of smaller sizes. In the presence of more massive protoplanets, there is expected to be planetesimal fragmentation induced by the dynamical stirring which changes the planetesimal size distribution. If planetesimals or their fragments get too small, the gas drag becomes so significant that they drift radially much the same as pebbles do. This can have a negative effect on the planetesimal accretion rate if the material is drifting away faster than it can be accreted (Inaba and Ikoma, 2003; Kobayashi et al., 2010, 2011; Ormel and Kobayashi, 2012). For this reason, it is not straight forward to estimate whether planetesimal fragmentation has a net positive or negative effect on planetary growth through planetesimal accretion (Guilera et al., 2014; Kaufmann and Alibert, 2023).

Considering an isolated protoplanet at a fixed distance from the star, it can only accrete planetesimals from its vicinity, a region called the *feeding zone*. The width of the feeding zone depends not only on the mass of the protoplanet but also on the dynamical state of the planetesimals (Pollack et al., 1996). Since planetesimals are not on circular orbits, the feeding zone is wider than a Hill radius and a protoplanet can accrete from a wider region than it is gravitationally dominating. Generally, the feeding zone extends a couple of Hill radii in either radial direction centred around the planet ($\sim CR_{\rm H}$). The mass in the feeding zone $M_{\rm feed}$ of width $CR_{\rm H}(M)$ of a planet of mass M at distance r is

$$M_{\rm feed} = 2\pi r C R_{\rm H}(M) \Sigma_{\rm plan}. \tag{2.69}$$

Therefore, the mass in the feeding zone grows slower than the protoplanet ($M_{\rm feed} \propto M^{1/3}$), which means that, at some mass $M_{\rm iso,plan}$ called the *planetesimal isolation mass*, the feeding zone is depleted and planetesimal accretion seizes. Equating the protoplanet mass with the mass in its feeding zone, the planetesimal isolation

mass is found to be (Armitage, 2020)

$$M_{\mathrm{iso,plan}} = \sqrt{\frac{8}{3M_\star}} \left(\pi C \Sigma_{\mathrm{plan}}\right)^{3/2} r^3. \tag{2.70}$$

Considering a solar mass star and using typical values of $\Sigma_{\mathrm{plan}} = 10$ gcm^{-2} and $C = 4\sqrt{3}$ (Lissauer, 1993), the planetesimal isolation mass at 1 and 5.2 au, are ~ 0.06 M$_\mathrm{E}$ and ~ 9.3 M$_\mathrm{E}$, respectively. Note that the planetesimal isolation mass is not a suitable estimate for the final core mass of the planet, as orbital migration leads to a replenishment of the feeding zone and mutual planet-planet collisions can result in growth as well as described in chapter 2.7.

2.4.2 Pebble accretion

The accretion of pebbles is an attractive idea for several reasons. First of all, it is observationally evident that dust and pebbles are present in all stages of protoplanetary disk evolution and, therefore, planetesimal formation is not efficient enough to convert all solids in the disk into planetesimals. Furthermore, a protoplanet faces a significant flux of inward drifting pebbles, fed by the mass reservoir in the outer disk. This is a fundamental difference to the accretion of planetesimals which are locally sourced. The pebble flux can be estimated by considering the growth timescale of dust to pebbles in the drift limit. Following Lambrechts and Johansen (2014), the growth timescale of pebbles is

$$t_{\mathrm{grow}} = \frac{4}{\sqrt{3}\epsilon_{\mathrm{stick}} Z \Omega_{\mathrm{K}}}, \tag{2.71}$$

where $\epsilon_{\mathrm{stick}} \approx 0.5$ is a sticking efficiency factor and Z the dust-to-gas ratio[3]. Assuming growth is roughly constant in logarithmic size ratio of pebbles with radius R_{peb} and dust with radius R_{dust}, the growth time from dust to pebbles is

$$\Delta t = \ln\left(\frac{R_{\mathrm{peb}}}{R_{\mathrm{dust}}}\right) t_{\mathrm{grow}} \approx 10\, t_{\mathrm{grow}}, \tag{2.72}$$

where the growth over about four orders of magnitude from micrometre dust to $\sim$ 10 mm pebbles is considered. This expression can be rearranged to find the

[3]This is equivalent to the growth timescale given in equation (2.50) up to a constant factor.

growth radius $r_{\mathrm{grow}}(t)$, at which the dust has grown to pebbles at any given time t

$$r_{\mathrm{grow}}(t) = \left(\frac{3GM_\star}{16}\right)^{1/3} \left(\frac{\epsilon_{\mathrm{stick}} Z t}{10}\right)^{2/3}. \tag{2.73}$$

Since this takes longer at larger orbital separations, the growth radius sweeps outwards at a speed

$$v_{\mathrm{grow}} = \frac{\mathrm{d}r_{\mathrm{grow}}}{\mathrm{d}t} = \frac{2}{3}\left(\frac{3GM_\star}{16}\right)^{1/3} \left(\frac{\epsilon_{\mathrm{stick}} Z}{10}\right)^{2/3} t^{-1/3}. \tag{2.74}$$

Given the initial dust surface density $\Sigma_{d,0}$ and assuming the radial drift is faster than the outwards speed of the growth radius, the pebble mass flux $\dot{M}_{\mathcal{F}}$ at a given time is

$$\dot{M}_{\mathcal{F}} = 2\pi r_{\mathrm{grow}} v_{\mathrm{grow}} \Sigma_{d,0}(r_{\mathrm{grow}}). \tag{2.75}$$

From this simple consideration, typical pebble fluxes on the order of $\sim 10^{-5}$ $\mathrm{M_E yr^{-1}}$ are found. This is promising because, if pebbles can be accreted efficiently by a protoplanet, terrestrial planets could form on a $\sim 10^5$ yr timescale and giant planet cores on a $\sim 10^6$ yr timescale, which is a requirement for planet formation from the observed disk lifetimes. Note that equation (2.75) also gives a simple way of modelling the pebble surface density Σ_{peb}. From the initial dust surface density and the dust-to-gas ratio, the known pebble flux $\dot{M}_{\mathcal{F}}$ produces a pebble surface density for $r < r_{\mathrm{grow}}$

$$\Sigma_{\mathrm{peb}}(r) = \frac{\dot{M}_{\mathcal{F}}}{2\pi r v_{\mathrm{peb}}}, \tag{2.76}$$

where v_{peb} is the radial drift velocity of pebbles given by equation (2.44), adopting the drift-limited Stokes number of the pebbles given by equation (2.51).

Since pebbles are strongly affected by gas drag, the collisional cross sections of pebbles colliding with a protoplanet are enhanced over the gravitationally focussed cross section. The potential of such aerodynamically assisted accretion of pebbles was for the first time recognised by Ormel and Klahr (2010). To describe the pebble accretion rate, I follow the approach given in Ormel (2017). Considering a pebble approaching a protoplanet of mass M at an impact parameter b, the

relative velocity δv is

$$\delta v = \Delta v + \frac{3}{2}\Omega_{\rm K} b, \tag{2.77}$$

where $\Delta v = \eta v_{\rm K}$ is the headwind velocity felt by a pebble on a Keplerian orbit as defined in equation (2.36). Two regimes, separated by $b = (2/3)\Delta v \Omega_{\rm K}^{-1}$, are identified. If δv is dominated by the first term (small b), the encounter is in the headwind regime, if the relative velocity is dominated by the second term (large b), the encounter is in the shear regime[4].

For the pebble to be accreted, two conditions must be met. First, the pebble must be sufficiently coupled to the gas such that the gas drag can modify the trajectory while the encounter is taking place. Second, the gravitational pull of the planet must be strong enough to allow the pebbles to settle instead of flowing along with the gas. In terms of timescales, these conditions are equivalent to

$$t_{\rm stop} < t_{\rm enc}, \tag{2.78}$$

and

$$t_{\rm settle} < t_{\rm enc}, \tag{2.79}$$

where $t_{\rm stop}$ is the stopping time according to the particle size and drag regime, $t_{\rm enc}$ is the encounter timescale, and $t_{\rm settle}$ the settling timescale. For the common assumption of Epstein drag, the stopping time is given by equation (2.22). The encounter timescale depends on the relative velocity δv as

$$t_{\rm enc} = \frac{2b}{\delta v}. \tag{2.80}$$

The settling timescale onto a protoplanet of mass M from a distance b is obtained considering the terminal settling velocity $v_{\rm settle}$ of the pebble of mass m where the drag force, given by equation (2.21), is equal to the gravitational force $F_g = GMm/b^2$. The settling timescale is then given by

$$t_{\rm settle} = \frac{b}{v_{\rm settle}} = \frac{b^3}{GMt_{\rm stop}}. \tag{2.81}$$

[4]The headwind and shear regimes are also known as the "Bondi" and "Hill" regimes, respectively.

In the headwind regime ($\delta v \approx \Delta v$), the maximum impact parameter $b_{\rm hw}$ that satisfies the settling condition is

$$b_{\rm hw} = \sqrt{\frac{2GMt_{\rm stop}}{\Delta v}}. \tag{2.82}$$

In this limit, the minimum mass $M_{\rm hw}$ to fulfil $t_{\rm stop} < t_{\rm enc}$ is

$$M_{\rm hw} = \frac{\Delta v^3 t_{\rm stop}}{8G} = \frac{1}{8}\mathcal{M}{\rm St}, \tag{2.83}$$

where $\mathcal{M}$ is the characteristic mass, measuring the relative importance of headwind versus shear given by

$$\mathcal{M} = \frac{\Delta v^3}{G\Omega_{\rm K}}. \tag{2.84}$$

Written in this way, it is clear that the transition into the headwind regime depends on both the mass of the protoplanet and the pebble size. Encounters with $M < M_{\rm hw}$ follow ballistic trajectories, i.e. can be treated the same way as drag-free planetesimals which means pebble accretion is effectively shut off.
In the shear regime ($\delta v \approx (3/2)\Omega_{\rm K} b$), the encounter timescale is on the order of an orbital period

$$t_{\rm enc} \approx \frac{1}{\Omega_{\rm K}}. \tag{2.85}$$

The maximal impact parameter $b_{\rm sh}$ satisfying the settling condition is

$$b_{\rm sh} = \left(\frac{GMt_{\rm stop}}{\Omega_{\rm K}}\right)^{1/3}. \tag{2.86}$$

Since the $b_{\rm sh}$ scales more weakly with mass than $b_{\rm hw}$, the transition mass $M_{\rm hw/sh}$ is the minimum mass to consider in the shear regime to fulfil $t_{\rm stop} < t_{\rm enc}$. Setting $b_{\rm sh} = b_{\rm hw}$ it is given by

$$M_{\rm hw/sh} = \frac{1}{8}\frac{\mathcal{M}}{\rm St}, \tag{2.87}$$

which again depends on the protoplanet mass and the pebble size. For protoplanets with $M > M_{\rm sh}$, the impact cross section for pebbles with ${\rm St} \sim 1$ are significant as $b_{\rm sh}$ becomes comparable to the Hill radius. Therefore, all pebbles on trajectories entering the Hill sphere of a protoplanet are accreted in this limit.

Moving from a single pebble to a disk of pebbles, the accretion rate depends on the scale height $H_{\rm peb}$ of the pebble disk with a surface density $\Sigma_{\rm peb}$ and a midplane density $\rho_{\rm mid,peb}$[5], as well as on the maximum impact parameter $b_{\rm col}$ that still leads to a collision given the mass of the protoplanet and the size of the pebbles. In the limit where the protoplanet is embedded in the pebble disk midplane and does not have a large cross section ($b_{\rm col} \ll H_{\rm peb}$), the pebble accretion rate is said to be in the 3D regime and given by

$$\dot{M}_{\rm 3D} = \pi b_{\rm col}^2 \delta v \rho_{\rm mid,peb}. \tag{2.88}$$

The settling boundary condition $t_{\rm settle} = t_{\rm enc}$ directly yields

$$\dot{M}_{\rm 3D} = 2\pi G M t_{\rm stop} \rho_{\rm mid,peb} = 6\pi R_{\rm H}^3 {\rm St} \Omega_{\rm K} \rho_{\rm mid,peb} \tag{2.89}$$

and there is no transition in the accretion rate between the headwind and shear regime.
If, conversely, the protoplanet is able to accrete from the full vertical extent of the disk ($b_{\rm col} \gg H_{\rm peb}$), the pebble accretion rate is in the 2D regime and given by

$$\dot{M}_{\rm 2D} = 2 b_{\rm col} \delta v \Sigma_{\rm peb}. \tag{2.90}$$

The settling boundary condition $t_{\rm settle} = t_{\rm enc}$ then gives

$$\dot{M}_{\rm 2D} = \frac{4GMt_{\rm stop}}{b_{\rm col}} \Sigma_{\rm peb} = \begin{cases} \sqrt{8GMt_{\rm stop}\Delta v}\Sigma_{\rm peb} & \text{headwind}, \quad (2.91) \\ 2R_{\rm H}^2 \Omega_{\rm K} {\rm St}^{2/3} \Sigma_{\rm peb} & \text{shear}, \quad (2.92) \end{cases}$$

where the headwind and shear regimes are obtained by setting $b_{\rm col} = b_{\rm hw}$ and $b_{\rm col} = b_{\rm sh}$, respectively. The pebble accretion rate $\dot{M}_{\rm peb}$ can be written in the form (Ormel, 2017)

$$\dot{M}_{\rm peb} = \dot{M}_{\rm 2D} \frac{b_{\rm col}}{b_{\rm col} + H_{\rm peb}\sqrt{8/\pi}}, \tag{2.93}$$

which ensure a smooth transition between 3D and 2D accretion and recovers $\dot{M}_{\rm 3D}$

[5]The pebble disk properties $H_{\rm peb}$, $\Sigma_{\rm peb}$, and $\rho_{\rm mid,peb}$ are given by the general descriptions for dust in chapter 2.2. For the accretion, the largest sized dust, the pebbles (St $\lesssim 1$), are the most important.

and $\dot{M}_{\rm 2D}$ in the limits $b_{\rm col} \ll H_{\rm peb}$ and $b_{\rm col} \gg H_{\rm peb}$, respectively.
Although pebble accretion is fast due to the large collision cross sections, the pebble accretion rate is not a runaway process. At best, the accretion rate scales linearly as $\dot{M}_{\rm peb} \propto M, M^{1/2}$, and $M^{2/3}$ in the different regimes given by equations (2.89), (2.91), and (2.92). It is a common misconception that pebble accretion is "efficient", because in fact, the opposite is true. Only a small fraction of the pebble flux crossing the orbit of a protoplanet is accreted. Nevertheless, pebble accretion rates can be considerable depending on the pebble flux, especially if the pebbles are well-settled in a thin disk midplane. This has lead to an ongoing paradigm shift towards pebble accretion, away from planetesimal accretion, especially for the formation of giant planets and planets at larger distances from the star where planetesimal accretion rates are very low. However, it is worth repeating that pebble accretion is essentially inexistent for protoplanet masses below $M_{\rm hw}$. This means that, if planetesimals are formed small, at least an intermediate phase of runaway planetesimal accretion is necessary to allow pebble accretion to take over. Alternatively, the planetesimals in the the tail end of the initial planetesimal size distribution could directly accrete pebbles if they are massive enough. Whether this is the case is still an open question, depending on the disk conditions, the orbital separation, and the stellar mass (Kaufmann et al., subm.).

Pebble accretion stops when the flux of pebbles seizes. This can either be the case if the mass reservoir is exhausted and all pebbles have drifted past the protoplanet, or if pebbles are somehow trapped outside the protoplanets orbit. As planets become more massive, they tidally interact with the gas disk (see chapter 2.6). This can lead to an acceleration of the gas outside a planet's orbit to the extent it revolves at super-Keplerian speeds, opening a gap in the gas disk. This means that there is a pressure maximum ($\eta = 0$) outside of the planet, where pebbles are trapped and do not drift further. The mass where this happens is called the *pebble isolation mass*, beyond which a planet is depriving itself of pebbles by halting the pebble flux. Assuming this happens roughly when the planet's Hill sphere extends beyond the gas disk ($R_{\rm H} > H_g$), the gap opening criterion at a distance r is

$$\frac{M}{M_\star} > \left(\frac{H_g}{r}\right)^3 . \tag{2.94}$$

In numerical simulations, the pebble isolation mass around solar mass stars is found to be approximated by (Lambrechts and Johansen, 2014; Bitsch et al., 2015)

$$M_{\rm iso,peb} \approx 20 \left(\frac{H_g/r}{0.05} \right)^3 \mathrm{M_E}. \tag{2.95}$$

Since disks are flared, the pebble isolation mass increases with distance and typical values are $\sim 2-3$ $\mathrm{M_E}$ at 1 au and ~ 10 $\mathrm{M_E}$ at 10 au (Kessler and Alibert, 2023). As discussed in the next chapter, the accretion of gas is strongly dependent on the accretion of solids. Therefore, the pebble isolation mass, conceptually, plays an important role for the formation of giant planets which must accrete a large amount of gas. Another important aspect of pebble isolation arises in multi-planetary systems, where a massive outer planet can starve the inner planets of pebbles by blocking the flux. In a more detailed recent analysis it was found that, while pebbles are fairly well trapped at the outer edge of such gaps, the smallest dust grains can diffuse through (Stammler et al., 2023). In this way, the inner planets could still be supplied with solid material, albeit at a lower rate.

2.5 Gas accretion

It is unsurprising that as the core mass increases, some of the gas from the disk in which the growing planet is embedded can be gravitationally bound to the planet. A very simple comparison of the thermal velocity of the gas and the escape velocity of the planet reveals that already at very low masses of $\gtrsim 10^{-4}$ $\mathrm{M_E}$, a tenuous atmosphere can be present (Armitage, 2020). To really assess whether a planet can sustain a more substantial gaseous envelope, a one-dimensional approach is again helpful. We consider an envelope in hydrostatic equilibrium described by

$$\frac{\partial P}{\partial r} = -\frac{GM}{r^2}\rho, \tag{2.96}$$

where P is the pressure, $M = M(r)$ is the mass enclosed within a radius r, and $\rho = \rho(r)$ is the density. Conservation of mass yields a second equation

$$\frac{\partial M}{\partial r} = 4\pi r^2 \rho. \tag{2.97}$$

The above equations depend on the temperature T via the pressure $P = P(\rho, T)$. The radial temperature gradient is given by the requirement that the luminosity L must be transported from the surface of the core and the deep interior of the envelope to the surface of the envelope. If this transport occurs via radiative diffusion, the temperature gradient can be derived from Fick's first law, finding

$$\left(\frac{\partial T}{\partial r}\right)_{\text{rad}} = -\frac{3\kappa_{\text{R}}\rho L}{64\pi r^2 \sigma_{\text{SB}} T^3}, \tag{2.98}$$

where κ_{R} is the Rosseland mean opacity. If the luminosity is high, for instance due to the liberation of the gravitational energy of the accreting bodies during the formation of the core, the temperature gradient could be very steep. This suggests that the energy transport by convection might be possible as well. Convection is a buoyancy instability where under-dense blobs of material rise upwards while over-dense material is buried downwards, effectively mixing the envelope and transporting energy very efficiently. Following Kippenhahn and Weigert (1990), the stability against convection can be studied by considering a blob of material being displaced radially from r to $r + \Delta r$. Suppose the displacement takes place in a slow manner, such that the blob of material stays in pressure equilibrium as it moves, and suppose that the displacement takes place adiabatically, where the blob does not exchange energy with the surrounding envelope. The stability against convection comes down to whether the displaced blob at $r + \Delta r$ is more dense or less dense than the surrounding envelope. If it is more dense, the blob will sink back and convection is absent or inefficient. However, if the the displaced blob is less dense than the envelope at $r + \Delta r$, it will keep rising which drives convection. In other words, the envelope is stable against convection if the adiabatic density gradient is larger than the density gradient found in the envelope (which we assume to be radiative)

$$\left(\frac{\partial \rho}{\partial r}\right)_{\text{ad}} > \left(\frac{\partial \rho}{\partial r}\right)_{\text{rad}}. \tag{2.99}$$

As is eloquently put in Armitage (2020): "The fact that both gradients are negative quantities occasions a good deal of confusion, but the physical argument in terms of buoyancy is clear."
Given an equation of state $\rho = \rho(P, T)$, the stability criterion can be reformulated

in terms of the temperature and pressure, finding the so-called Schwarzschild criterion[6]

$$\nabla_{\rm ad} \equiv \left(\frac{\partial \ln T}{\partial \ln P}\right)_{\rm ad} > \left(\frac{\partial \ln T}{\partial \ln P}\right)_{\rm rad} \equiv \nabla_{\rm rad}. \tag{2.100}$$

The explicit radiative temperature gradient given in equation (2.98) combined with equation (2.104) yields

$$\left(\frac{\partial T}{\partial r}\right)_{\rm rad} = \frac{\partial P}{\partial r}\frac{3\kappa_{\rm R} L}{64\pi G M \sigma_{\rm SB} T^3}, \tag{2.101}$$

which can be brought into the same form as in equation (2.100)

$$\nabla_{\rm rad} = \frac{3\kappa_{\rm R} L P}{64\pi\sigma_{\rm SB} G M T^4}. \tag{2.102}$$

According to this treatment in 1D, forming planetary envelopes, typically, have large convective zones with a radiative layer at the outer envelope boundary.
The three equations to solve, called the *planetary structure equations*, are then

$$\frac{\partial M}{\partial r} = 4\pi r^2 \rho, \tag{2.103}$$

$$\frac{\partial P}{\partial r} = -\frac{GM}{r^2}\rho, \tag{2.104}$$

$$\frac{\partial T}{\partial r} = \frac{T}{P}\frac{\partial P}{\partial r}\min(\nabla_{\rm ad}, \nabla_{\rm rad}), \tag{2.105}$$

where the first two equations are again the mass conservation and hydrostatic equilibrium. The third equation describes the energy transport, considering the possibility of convection. Given an equation of state $\rho = \rho(P, T)$, opacities $\kappa_{\rm R}$, and luminosity L, the structure equations can be solved numerically for appropriate boundary conditions (see chapter 3.4).

In the early stages of planet formation, where planetary cores are embedded in the gaseous disk, the planetary envelope is well-described by the hydrostatic

[6] In general, the equation of state also depends on the mean molecular weight μ. The Schwarzschild criterion is found, by assuming μ is uniform in the envelope. If $\frac{\partial \mu}{\partial r} \neq 0$ instead, the so-called Ledoux criterion is recovered.

equilibrium, balancing gravity and pressure considering the transport of energy away from the planet into the surrounding disk. The underlying assumption is that the mass changes on a longer timescale than hydrostatic equilibrium is established. In this case the free-fall time, the timescale on which gravity attempts to contract, and the sound-crossing time, the timescale on which pressure attempts to expand, remain similar. Therefore, hydrostatic equilibrium is re-established quickly and the process is adequately described by a sequence of hydrostatic states.
As the core mass increases due to the accretion of solids, so does the planet's potential to bind an envelope. Ultimately, the accretion rate of gas depends not only on the gas disk and the mass of the planet but also on the luminosity. Large luminosities hinder the accretion of gas and if the planet is able to cool efficiently, gas accretion rates can become large. The luminosity is time dependent, stemming from the accretion of solids and gas, as well as from the contraction of the envelope. The energy released by the accretion of material onto the core is given by

$$L_{\mathrm{acc}} = \frac{G M_{\mathrm{core}} \dot{M}_{\mathrm{core}}}{R_{\mathrm{core}}}, \tag{2.106}$$

where the accretion rate of solids $\dot{M}_{\mathrm{core}}$ onto a core of mass M_{core} and radius R_{core} is assumed to deposit the energy (and material) at the core's surface.
Since the envelope is typically radiative at the envelope-disk boundary, the planet's ability to cool is strongly influenced by the opacities in these envelope regions. If the opacities are high, the planet cannot radiate efficiently and accretes gas at a lower rate and vice-versa. Not only the molecular opacities but also the contribution of suspended grains plays a role. To what extent the accreted material breaks up in the envelope, supplying it with grains, and how efficiently these grains grow and settle to the core, is an important question in order to get the correct opacities in the radiative layer (e.g. Mordasini, 2014; Brouwers et al., 2021). Envelope opacities, especially during formation, are associated with large uncertainties but have a strong influence on the planet formation outcome of gas-accreting planets as shown in Kessler et al. (subm.) in chapter 5. A further influence on the gas accretion rate arises from the enrichment of the envelope by heavy elements. This increases the mean molecular weight in the envelope, making it more dense which allows more gas to be captured by the planet. Due to the large convective zones in planetary envelopes, the envelopes are often assumed to be well mixed with a

radially constant mean molecular weight. It is worth mentioning that this picture has been questioned in the case of giant planets, inspired by measurements of Jupiter's gravitational moments (Bolton et al., 2017). The presence of a dilute core instead of a well-defined core-envelope boundary has been shown to constrain the remaining luminosity after the formation phase and other formation parameters (Vazan et al., 2018; Müller et al., 2020; Stevenson et al., 2022; Polman and Mordasini, 2024).

If the mass of a planetary core increases further, at some point the so-called *critical core mass*[7] is reached. If the core becomes more massive than this critical mass, the additional mass in envelope that would be attracted can no longer be supported by pressure. In other words, past the critical core mass, there is no hydrostatic solution for the envelope structure and hydrodynamic contraction of the envelope ensues, causing it to detach from the surrounding gas disk. Roughly speaking, this happens when the envelope mass exceeds the core mass ($M_{\rm env} \gtrsim M_{\rm core}$) and typical values for the critical core mass are on the order of ~ 10 $\mathrm{M_E}$ (Ikoma et al., 2000). In this phase, the accretion rate of gas onto the planet is limited by the disk's ability to supply it. Giant planets accrete the bulk of their gas mass in this so-called *runaway gas accretion* on comparably short timescales of the order of $\sim 10^5$ yr.
As mentioned before and will be discussed further in the following chapter, massive planets can open up local gaps through tidal interactions with the gas disk. This lowers the gas surface density in the planet's vicinity, hindering the supply of gas to the planet. The accretion of gas finally stops when the gas disk dissipates.

2.6 Planet-disk interactions

As a planet grows in mass, the gravitational interactions with the gas can no longer be neglected. Both the disk and the planet are exerting a torque onto each other, leading to an exchange of angular momentum between the gas in the disk and the planet. Fundamentally, the torques exerted onto the planet are due to asymmetric mass concentrations accelerating or decelerating the planet through their

[7] Recently, in the context of envelopes which are significantly enriched in heavy elements ("metals"), it has been suggested that the better notion is the *critical metal mass* (Ormel et al., 2021).

gravitational interaction. This potentially leads to a change in semi-major axis of the planet in a process called disk-driven *orbital migration*, and for more massive planets the torque onto the disk can be such that the disk gas is pushed away from the co-orbital region, forming a gap. It is beyond the scope of this thesis to reproduce the lengthy derivations of the different torques and I characterise the most important contributions qualitatively instead.

Consider first a planet that is embedded in the gas disk and has not yet opened up a gap in the disk. The classical contributions to the net torque exerted onto an embedded planet are the so-called Lindblad torque and the co-rotation torque. In this case, the planet is said to migrate in the *type-I* regime (Ward, 1997; Tanaka et al., 2002). The Lindblad torque references the torque exerted onto the planet by density waves, launched at so-called Lindblad resonances (Goldreich and Tremaine, 1979). A Lindblad resonance occurs at a radius r_{L} where the perturbations of a planet at orbital radius r excite the gas at the epicyclic frequency or multiples thereof. An illustrative example is when the planet is on a circular orbit with frequency $\Omega_{\mathrm{K}}(r)$ and the disk is Keplerian, where the epicyclic frequency is equal to the orbital frequency. The resonant condition is then

$$n\left[\Omega_{\mathrm{K}}(r_{\mathrm{L}}) - \Omega_{\mathrm{K}}(r)\right] = \pm\Omega_{\mathrm{K}}(r_{\mathrm{L}}), \tag{2.107}$$

where n is an integer, and the Lindblad resonances are located at

$$r_{\mathrm{L}} = \left(1 \pm \frac{1}{n}\right)^{2/3} r. \tag{2.108}$$

The key point here is that there are multiple resonances both inside and outside of the planetary orbit. The Lindblad torques exerted by the density waves launched at the resonances outside the planet's orbit are negative, while the torques from the inner resonances are positive. The magnitude of the torques mainly depends on the distance of the resonances to the orbit of the planet and the surface density of the gas at the resonances. The net Lindblad torque is given by the sum and therefore depends, among other quantities, on the surface density gradient and temperature gradient in the disk. In essentially all disk models, the outer resonances exert a greater negative torque than the inner positive resonances, yielding a negative net Lindblad torque. Therefore, the planet loses angular momentum

and migrates inwards.
The second contribution to the total torque in the type-I regime comes from the gas in the co-orbital region of the planet at orbital distance r. Gas streamlines outside the planetary circulate with a lower orbital speed than the planet, and gas streamlines inside the planetary orbit circulate faster than the planet. The gas kinematics in this region are non-trivial, with gas librating on so-called *horseshoe orbits* where the gas streamlines follow a u-turn from $> r$ to $< r$ in front of the planet and a u-turn from $< r$ to $> r$ behind the planet (Ward, 1991). It is clear that gas performing such a closed horseshoe orbit must lose (in front of the planet) and gain (behind the planet) angular momentum, in exchange with the planet. If the situation is fully symmetrical, the contributions from each u-turn cancels out and only if there is a persistent asymmetry, a non-zero net torque arises from the horseshoe region.
There are a number of effects which can lead to an asymmetry in the density of the gas in the forward and backward horseshoe turns. An illustrative example is the presence of an entropy gradient across the horseshoe region where low-entropy gas moves inwards in front of the planet and high-entropy gas flows outwards behind the planet. This establishes an over-density in front of the planet and an under-density behind the planet if the gas performs the u-turn faster than it can thermally equilibrate. Then the exerted torque on the planet is positive. The stability of the asymmetry requires that the viscous timescale must be lower than the libration timescale of a full horseshoe orbit in order to re-establish the entropy gradient. If this is not the case, this contribution to the co-rotation torque is said to be *saturated* and vanishes. A complete (adiabatic) description of the co-rotation torque contains linear and non-linear contributions (called horseshoe drag) due to the entropy gradient and due to the gradient of the vortensity (e.g. Masset and Casoli, 2010; Paardekooper et al., 2010, 2011; Jiménez and Masset, 2017). The Lindblad and co-rotation torques scale with the planetary mass as M^2, and type-I migration generally sets in as the planets approach ~ 1 $\mathrm{M_E}$. Depending on the radial gradients in the disk and whether the co-rotation torques are saturated, the net type-I torque can be negative or positive, leading to inwards or outwards migration, respectively. However, the picture over the course of formation is dominated by inwards migration. This is one of the main insights in planet formation from recent years, including the works presented in chapters 4 and 5. The "theoretical necessity" of planetary migration as a consequence of angular momentum conservation poses nuanced challenges for the formation of massive planets and

planets in the outer disk beyond ~ 10 au.
A number of further torques have been investigated in order to complete the picture and perhaps remedy the otherwise oppressive efficiency of type-I migration. This includes so-called thermal torques due to the heating of the co-rotation region by the planet (Masset, 2017; Velasco Romero and Masset, 2020; Guilera et al., 2019, 2021), and dynamical torques due to the distortion of the co-rotation region as a planet migrates (Masset and Papaloizou, 2003; Paardekooper, 2014; Yun et al., 2022) which are particularly relevant in low viscosity environments (Weder et al., subm.).

At a certain mass, the planet locally dominates the angular momentum transport in the disk. Whether a planet opens a gap or not can be assessed by comparing the timescale on which the planet opens a gap with the timescale on which the viscosity erases sharp radial gradients in the surface density and closes the gap. A simple estimate can be obtained in the impulse approximation (Lin and Papaloizou, 1979) and by assuming a gap of characteristic size H_g. Then the critical planet to star mass ratio $q_{\rm crit}$ scales as (Armitage, 2020)

$$q_{\rm crit} = \frac{M_{\rm crit}}{M_\star} \propto \left(\frac{H_g}{r}\right)^{5/2} \alpha^{1/2}, \tag{2.109}$$

where a planet starts opening a gap as $M \gtrsim M_{\rm crit}$. Gap opening strongly depends on the aspect ratio H_g/r and it is easier to open a gap if the viscosity is low. For a planet around a solar mass star with $\alpha = 10^{-3}$ and a typical value of $H_g/r = 0.05$, gap opening begins at a mass $M_{\rm crit} \approx 20$ M$_{\rm E}$. Note that a detailed treatment of gap opening should be done in 3D, since planets in the range of $q_{\rm crit}$ have Hill radii comparable to the disk height.
When a planet opens a gap, the co-orbital region and the close Lindblad resonances are severely depleted of mass. Therefore, the type-I torques do not apply any longer and planets are migrating in the slower *type-II* regime. In a simplified view of a gap, most of the angular momentum resides in the gas rather than the planet and the planet only sustains the gap and does not otherwise alter the angular momentum transport. The viscously encroaching gas at the outer gap edge receives angular momentum from the planet and at the inner disk edge the opposite happens, maintaining the gap. Since the inner disk loses angular momentum

(accreting onto the star), the inner gap edge and thus the planet move inward according to the radial gas flow. In reality however, the gap edges have been found to be leaky, allowing a flow of gas to pass the gap. In hydrodynamical simulations, the type-II migration rates appear to be lower than the radial gas velocity (e.g. Kanagawa et al., 2018).

The emerging picture is that planets grow more or less *in-situ* until at least $\sim$ 1 M_E. Type-I migration becomes significant when the migration timescale becomes shorter than the growth timescale (Emsenhuber et al., 2023b). Therefore the accretion rate of solids influences planetary migration. Once type-I migration acts efficiently, the planet either migrates inwards unhindered or grows massive enough to open a gap and transitions to the much slower type-II migration regime. Therefore, in order to retain planets on longer orbits, the accretion mechanism and the timing of runaway gas accretion is important as it allows planets to reach the gap opening mass. Note that planets can be trapped at pre-existing gaps such as, for instance, the inner disk edge where disk-driven orbital migration stops. Obviously, the migration due to planet-disk interactions ultimately stops when the gas disk dissipates.

2.7 Planet-planet interactions

If multiple massive planets are forming in the protoplanetary disk, the dynamics in the system can no longer be treated as a two-body problem for each planet individually. The mutual gravitational interactions of many bodies is a well-known problem without analytic solutions and the numerical integration of the *N-body* problem is computationally expensive with a time complexity of $\mathcal{O}(N^2)$. Practically, the integration of many bodies over a billion year time span is the most restrictive constraint for global models. The mutual gravitational interactions of the forming planets influence the dynamics of the system and are not negligible because they are important for both the orbital configuration of planets as well as their final mass.
Due to the exchange of angular momentum in close encounters, planets can be forced onto highly eccentric orbits to the point they are ejected from the system or sent crashing into the star. The more interesting consequence in the context of the remaining bodies are collisions of planets, called *giant impacts*. The exact

collision outcomes of these extremely energetic events depend on the collision parameters, the composition of the planets, their material strengths, etc. As was likely the case for the formation of the Moon, giant impacts are not guaranteed to result in the perfect merging of the colliding planetary cores (Ida et al., 1997; Jutzi and Asphaug, 2011). Under this assumption however, it has been shown that the inclusion of the mutual gravitational interactions in global models with many protoplanets, results in frequent giant impacts which ultimately promotes the formation of more massive planets (e.g. Emsenhuber et al., 2021a). The frequency of these events depends, apart from the number of gravitating bodies, on the mass of the protoplanets. Therefore, giant impacts tend to be most prevalent in the later stages of the disk lifetime when the protoplanets are more massive and the gas in the disk becomes less dense. The dispersal of the gas disk has been identified as a potential source of dynamical instability since the dampening effect of the gas ceases (Liu et al., 2022). Since there is an enormous amount of energy liberated in such collisions, the envelope structure of the colliding bodies is profoundly affected. Whether any gas can be retained in the collision between gas-bearing protoplanets depends on how quickly the impact energy can be dissipated.
A fundamental property of the gravitational interactions between planets is the presence of resonances. So called mean-motion resonances occur when two planets orbit such that their orbital period ratio is an integer. This can have a stabilising effect for planetary mass objects, synchronising their closest approaches. Mean-motion resonances can, for instance, be seen in the Solar System in the resonant orbits of the moons of Jupiter and Pluto, or in the TRAPPIST-1 planetary system. In the context of planet formation, mean-motion resonances are important because they can lock planets on certain orbits relative to an inner planet, inhibiting their disk-driven migration. The presence of mean-motion resonances in observed systems is strong evidence for orbital migration on at least intermediate scales because the differential inward migration of planets can explain how they end up in the stable mean-motion resonances in the first place.

2.8 Planet evolution

In this chapter, I only give a brief overview of some of the most transformative processes that are important after the dispersal of the gas disk. Once the gas disk is dissipated, the accretion of gas ceases and only growth by giant impacts

is possible since pebbles stop drifting and planetesimals are quickly scattered in the absence of gas drag. Without accretion, planets evolve thermodynamically by releasing the remaining energy from their formation over a long period of time. Gas-rich planets cool and contract on the Kelvin-Helmholtz timescale $t_{\rm KH}$, which is the time it takes a planet of mass M and radius R to radiate away its gravitational energy E_g at a luminosity L

$$t_{\rm KH} = \frac{E_g}{L} = \frac{GM^2}{2RL}. \tag{2.110}$$

This is important in order to link measured planetary radii of evolved planets with predictions from planetary formation models. Note that the Luminosity is not necessarily constant over time and intrinsic heat sources such as radioactive decay in the core are relevant on billion year timescales.

In the absence of accretion, the mass of the planets is not guaranteed to be constant due to atmospheric loss processes. Atmospheric escape is present when gas molecules have enough energy to overcome the escape velocity. The energy source can either be intrinsic, from the remaining luminosity of the core after formation, or from the external radiation of the star. These processes are known as *core-powered mass loss* and *photo-evaporation*[8], respectively. Naturally, the latter is more important the closer the planet orbits the host star due to the higher received flux. The heating of the envelope preferentially removes lighter molecules in thermal *Jeans escape* but if strong thermal winds are driven, mainly by X-rays and EUV radiation, heavier molecules can be dragged with the flow as well in so-called *hydrodynamic escape*. Close to the star, there are many more mechanisms that can contribute to the atmospheric escape and alter the envelope composition and chemistry such as photo-dissociation, photo-ionisation, and the interaction with the ions in the stellar wind.

[8]Note the distinction from the photo-evaporation of the gas disk. Although the energy source is the same as for internal disk photo-evaporation (the star), here, the envelope gas is bound to the planet instead of freely orbiting the star.

"Program received signal
SIGSEGV, Segmentation fault."
gfortran

3 The Bern Model of planet formation and evolution

The Bern Model of planet formation and evolution is a global 1D model considering most of the physical processes introduced in the previous chapter. The Bern Model originates from the model presented in Alibert et al. (2004, 2005), which simulates the formation of single planets from the protoplanetary disk until the gas disk disperses. At the core of this model lie the planetary structure equations and the viscous evolution equation of the protoplanetary disk, which are solved numerically. Inspired by the pioneering work in Ida and Lin (2004a,b), the model was then applied in a population synthesis approach for the first time in Mordasini et al. (2009a,b). Subsequently, the model diverged into an evolution and a formation model. The planetary evolution model follows the thermodynamic cooling and contraction, as well as atmospheric escape on a billion year timescale (Mordasini et al., 2012a,b; Jin et al., 2014). The formation model was developed further to be capable of simulating the formation of multi-planetary systems considering N-body interactions, including improved versions of the gas and planetesimal disks, as well as more advanced migration prescriptions (Fouchet et al., 2012; Alibert et al., 2013; Fortier et al., 2013; Dittkrist et al., 2014). The formation and evolution model was combined into what we call the Bern Model today in Emsenhuber et al. (2021a), linking the formation of multi-planetary systems from the protoplanetary disk to the dispersal of the gas disk with the subsequent billion year thermodynamical evolution. Due to the heritage of the model it remains computationally manageable, capable of performing large-scale population syntheses. The Bern Model has been described in detail and applied extensively in the *Next Generation Planetary Population Synthesis* (NGPPS) paper series (Emsenhuber et al., 2021a,b; Schlecker et al., 2021a; Burn et al., 2021; Schlecker et al., 2021b; Mishra et al., 2021).
The Bern Model has since been developed further to include new physics, such as

planetesimal fragmentation and drift (Kaufmann and Alibert, 2023), the presence of compositional gradients in planetary envelopes in the evolution phase (Polman and Mordasini, 2024), a wind-driven disk evolution module (Weder et al., 2023), the inclusion of the evolution of dust, planetesimal formation, and pebble accretion (Voelkel et al., 2020).

The Bern Model, parts of it, and modified versions, have been used in a number of diverse studies. In order to extend the Bern Model to be able to perform disk population syntheses, it must calculate observable quantities which can be compared with observations. To compare the modelled disks with the measured emissions in millimetre observations, an improved treatment of dust dynamics and the calculation of continuum dust emissions was implemented in Burn et al. (2022). In Emsenhuber et al. (2023a), the best-fitting initial disk conditions have been evaluated in a parameter study, focussing on observed disk masses and lifetimes. Brügger et al. (2020) compared planetesimal and pebble-based planet formation scenarios. Mol Lous et al. (2022) investigated the long-term habitability of planets with primordial H-He envelopes. Voelkel et al. (2022) studied the dynamic formation of planetary embryos and the emerging multiple generations of planets in the same system. Davoult et al. (2024) analysed the architectures of planetary systems emerging from the Bern Model with a focus on systems that are hosting Earth-like planets. Burn et al. (2024) studied the radius valley between super-Earths and sub-Neptunes using an improved treatment of the planetary composition based on new equations of state of water (Haldemann et al., 2020). Shibaike and Mordasini (2024) implemented a simple model of a circumplanetary disk to constrain the planetary properties from the dust emission measurements in the PDS70 system, where two planets have been successfully identified while still undergoing formation (Gaia Collaboration et al., 2018; Müller et al., 2018). Using synthetic populations from the Bern Model, Egger et al. (2024) constrain the formation history and disk conditions of an exoplanet system observed with the CHEOPS telescope. Kaufmann et al., (subm.) investigate the early planet formation phase in a ring of planetesimals, formed from the streaming ability. Gottstein et al., (in prep.) study the planetary temperature-luminosity relationship during the formation and evolution of giant planets. The dynamical co-rotation torque, potentially important in low viscosity disks, is implemented in Weder et al., (in prep.). I used the Bern Model to investigate concurrent pebble and planetesimal accretion in Kessler et al. (2022), and the formation of Uranus/Neptune-like planets in Kessler et al., (subm.).

As is evident from the physical descriptions in chapter 2, a large number of choices must be made in order to build a global model. Note that there are many valid prescriptions implemented for some of the model components. In this chapter, I give an overview of the choices, assumptions, and prescriptions that are used for the work in chapters 4 and 5. The majority of the setup is identical to the one presented and described in detail in Emsenhuber et al. (2021a) and Emsenhuber et al. (2021b). Naturally, most of the following descriptions are a repetition of what can be found there.

3.1 Gas disk evolution

The protoplanetary gas disk is described following the concepts described in chapter 2.1. We solve the 1D radially symmetric viscous diffusion equation (2.7) (Lüst, 1952; Lynden-Bell and Pringle, 1974)

$$\dot{\Sigma}_g = \frac{3}{r}\frac{\partial}{\partial r}\left[r^{1/2}\frac{\partial}{\partial r}\left(\nu\Sigma_g r^{1/2}\right)\right] - \dot{\Sigma}_{\text{photo,int}} - \dot{\Sigma}_{\text{photo,ext}} - \dot{\Sigma}_{\text{acc}}. \tag{3.1}$$

to compute the time evolution of the protoplanetary gas disk surface density Σ_g at an orbital distance r. We consider the sink terms $\dot{\Sigma}_{\text{photo,int}}$ and $\dot{\Sigma}_{\text{photo,ext}}$ due to internal and external photo-evaporation. The removal of gas by gas accreting planets is included by the term $\dot{\Sigma}_{\text{acc}}$. We parametrise the viscosity according to equation (2.8) with a fiducial value of $\alpha = 10^{-3}$. Following the approach of Mordasini et al. (2012b), the FUV-driven external photo-evaporation rate is given by (Matsuyama et al., 2003)

$$\dot{\Sigma}_{\text{photo,ext}}(r) = \begin{cases} 0 & \text{for } r < \beta\, r_{\text{g,I}}, \quad (3.2) \\ \dfrac{\dot{M}_{\text{wind}}}{\pi(r_{\text{max}}^2 - \beta^2 r_{\text{g,I}}^2)} & \text{otherwise}, \quad (3.3) \end{cases}$$

where $r_{\text{max}} = 1000$ au, and we choose $\beta = 0.14$ (similarly to Alexander and Pascucci, 2012). We assume that external photo-evaporation removes mass outside of $r < \beta\, r_{\text{g,I}}$, where

$$r_{\text{g,I}} = \frac{GM_\star}{c_{s,\text{I}}} \tag{3.4}$$

is the gravitational radius for a gas at 10^3 K with a mean molecular weight of 1.35, corresponding to dissociated gas. $\dot{M}_{\rm wind}$ is a parameter scaling the external photo-evaporation rate, which represents different external FUV field strengths. Practically, $\dot{M}_{\rm wind}$ is an initial condition which is essentially determines the disk lifetime.
The internal photo-evaporation rate is given by Clarke et al. (2001)[1]

$$\dot{\Sigma}_{\rm photo,int}(r) = \begin{cases} 0 & \text{for } r < \beta\, r_{\rm g,II}, \quad (3.5) \\ 2 c_{s,\rm II} n_{\rm base} m_p & \text{otherwise.} \quad (3.6) \end{cases}$$

The gas is removed outside of $r < \beta\, r_{\rm g,II}$, where the gravitational radius $r_{\rm g,II}$ is given by equation (3.4) considering gas with thermal sound speed $c_{s,\rm II}$. Internal photo-evaporation removes ionised hydrogen with a sound speed $c_{s,\rm II}$ corresponding to a temperature of 10^4 K with a mean molecular weight of 0.68. m_p is the mass of a proton (ionised hydrogen), and $n_{\rm base}$ is the base number density given by

$$n_{\rm base}(r) = n_{\rm base}(r_{14}) \left(\frac{r}{r_{\rm g,II}} \right)^{-5/2}, \quad (3.7)$$

where $r_{14} = \beta\, r_{\rm g,II}/10^{14}$cm. The base density at the inner evaporation limit $n_{\rm base}(r_{14})$ is estimated by (Hollenbach et al., 1994)

$$n_{\rm base}(r_{14}) = k_{\rm hol} \Phi_{41}^{1/2} (r_{14})^{-3/2}, \quad (3.8)$$

where $k_{\rm hol} = 5.7 \times 10^4$ and the ionising photon luminosity $\Phi_{41} = 0.1 (M_\star / {\rm M_{Sun}})^{1/2}$ in units of $10^{41}\,{\rm s}^{-1}$ are determined from hydrodynamical simulations.

In order to evolve the gas surface density over time, we must choose an initial disk profile. The gas surface density is initialised by (Andrews et al., 2010)

$$\Sigma_g(r) = \Sigma_{\rm g,0} \left(\frac{r}{5.2\ {\rm au}} \right)^{-0.9} \exp \left[- \left(\frac{r}{R_{\rm char}} \right)^{1.1} \right] \left(1 - \sqrt{\frac{R_{\rm in}}{r}} \right), \quad (3.9)$$

where $\Sigma_{\rm g,0}$ is the initial gas surface density at 5.2 au, $R_{\rm char}$ is the characteristic outer disk radius, and $R_{\rm in}$ is the inner disk truncation radius. $R_{\rm in}$ is set as the

[1] Compare with equation (2.16) and note that $n_{\rm base} m_p = \rho_{\rm base}$.

co-rotation radius with respect to the stellar rotation period. $\Sigma_{\mathrm{g},0}$ and R_{char} are then given by the initial gas disk mass. As described in chapter 3.8, The stellar rotation period as well as the initial gas disk mass are initial conditions of the model.

We follow the approach of Nakamoto and Nakagawa (1994) for the vertical disk structure which is equation (2.12) in the explicit form

$$\sigma_{\mathrm{SB}} T_{\mathrm{mid,g}}^4 = \sigma_{\mathrm{SB}} T_{\mathrm{irr}}^4 + \left(\frac{3}{8} \tau_{\mathrm{R}} + \frac{1}{2\tau_{\mathrm{Pl}}} \right) \dot{E}_\nu, \tag{3.10}$$

where τ_{R} and $\tau_{\mathrm{Pl}} = 2.4\,\tau_{\mathrm{R}}$ are the Rosseland and Planck mean optical depths, respectively. In this way, equation (3.10) takes into account both the optically thick (τ_{R}) and the optically thin (τ_{Pl}) regimes. The viscous energy dissipation rate $\dot{E}_\nu$ is given by equation (2.9). The optical depth $\tau_{\mathrm{R}} = \kappa_{\mathrm{R}} \Sigma_g$ depends on the opacities κ_{R} which are given in a simplified approach by the maximum of the grain opacities of Bell and Lin (1994) and the molecular opacities of Freedman et al. (2014). The temperature due to stellar irradiation T_{irr} is given by (Adams et al., 1988; Ruden and Pollack, 1991; Chiang and Goldreich, 1997; Hueso and Guillot, 2005)

$$T_{\mathrm{irr}}^4 = T_\star^4 \left[\frac{2}{3\pi} \left(\frac{R_\star}{r} \right)^3 + \frac{1}{7} \left(\frac{R_\star}{r} \right)^2 \frac{H_g}{r} \right] + T_{\mathrm{irr,mid}}^4 + T_{\mathrm{cloud}}^4, \tag{3.11}$$

where the first term is the contribution due to the stellar heating of the disk surface, $T_{\mathrm{irr,mid}}$ is the direct heating of the midplane according to equation (2.11), and $T_{\mathrm{cloud}} = 10$ K is the background temperature.

3.2 Planetesimals

The planetesimal disk is described following Fortier et al. (2013), where the planetesimals disk is initialised by

$$\Sigma_{\mathrm{plan}}(r) = \Sigma_{\mathrm{plan},0} f_{\mathrm{ice}} \left(\frac{r}{R_{\mathrm{in}}} \right)^{1.5} \exp \left[- \left(\frac{r}{R_{\mathrm{char}}/2} \right)^2 \right], \tag{3.12}$$

where the characteristic radius of the planetesimal disk is half the value of the gas disk (Ansdell et al., 2018) and the the power law index is steeper than in the case of the gas disk (Weidenschilling, 1977). The reference surface density $\Sigma_{\mathrm{plan},0}$ is fixed by the bulk solids-to-gas ratio Z which is given as an initial parameter. The factor f_{ice} is 0.5 inside the water iceline and 1 outside of it.

The dynamical state of the planetesimals is evolved considering the gas drag and the stirring due to protoplanets and planetesimals alike. The mean square eccentricities $\langle e^2 \rangle$ and inclinations $\langle i^2 \rangle$ then change over time as

$$\langle \dot{e^2} \rangle = \langle \dot{e^2} \rangle|_{\mathrm{drag}} + \langle \dot{e^2} \rangle|_{\mathrm{stirr,M}} + \langle \dot{e^2} \rangle|_{\mathrm{stirr,plan}}, \tag{3.13}$$

$$\langle \dot{i^2} \rangle = \langle \dot{i^2} \rangle|_{\mathrm{drag}} + \langle \dot{i^2} \rangle|_{\mathrm{stirr,M}} + \langle \dot{i^2} \rangle|_{\mathrm{stirr,plan}}. \tag{3.14}$$

Considering the relative velocity δv given by equation (2.62), the drag-induced rate of change of the dynamical state is given by (Adachi et al., 1976; Chambers, 2006)

$$\langle \dot{e^2} \rangle|_{\mathrm{drag}} = -\frac{\langle e^2 \rangle}{t_{\mathrm{stop}}} \delta v, \tag{3.15}$$

$$\langle \dot{i^2} \rangle|_{\mathrm{drag}} = -\frac{\langle i^2 \rangle}{2t_{\mathrm{stop}}} \delta v. \tag{3.16}$$

The stopping time t_{stop} depends on the drag regime of the planetesimals which is determined according to Rafikov (2004).
The stirring by protoplanets is following Guilera et al. (2010), which is a modification of the treatment presented in Ohtsuki et al. (2002). The rate of change of the planetesimal dynamical state induced by planets $j = 1, \ldots, n$ with masses M_j is given by

$$\langle e^2 \rangle|_{\mathrm{stirr,M}} = \sum_{j=1}^{n} f_{\Delta j} \left(\frac{\Omega_{\mathrm{K}} M_j}{30 \pi M_\star} \right) P_{\mathrm{stirr}}, \tag{3.17}$$

$$\langle i^2 \rangle|_{\mathrm{stirr,M}} = \sum_{j=1}^{n} f_{\Delta j} \left(\frac{\Omega_{\mathrm{K}} M_j}{30 \pi M_\star} \right) Q_{\mathrm{stirr}}, \tag{3.18}$$

where

$$f_{\Delta j}^{-1} = 1 + \left(\frac{|r - r_j|}{5R_{\mathrm{H}}} \right)^5 . \tag{3.19}$$

Here, r corresponds to the location in which the planetesimal dynamical state is to be evaluated, and r_j are the locations of the protoplanets. The stirring functions P_{stirr} and Q_{stirr} are given by Ohtsuki et al. (2002), containing elliptical integrals which we approximate by the fit given in Chambers (2006). The full form of these can be found explicitly in Emsenhuber et al. (2021a).
Lastly, the self-stirring of the planetesimals is given by (Ohtsuki et al., 2002)

$$\langle \dot{e^2} \rangle|_{\mathrm{stirr,plan}} = \frac{1}{6}\sqrt{\frac{Gr}{M_\star}} \Sigma_{\mathrm{plan}} H_{\mathrm{plan}} P_{\mathrm{stirr}}, \tag{3.20}$$

$$\langle \dot{i^2} \rangle|_{\mathrm{stirr,plan}} = \frac{1}{6}\sqrt{\frac{Gr}{M_\star}} \Sigma_{\mathrm{plan}} H_{\mathrm{plan}} Q_{\mathrm{stirr}}. \tag{3.21}$$

The scale height of the planetesimal disk is given by

$$H_{\mathrm{plan}} = \left(\frac{2m}{3M_\star} \right)^{1/3} \tag{3.22}$$

and the planetesimal mass m of planetesimals with radius R_{plan} and density ρ_{plan} is simply

$$m = \frac{4}{3}\pi R_{\mathrm{plan}}^3 \rho_{\mathrm{plan}}. \tag{3.23}$$

In this setup, the planetesimal radius is a fixed parameter set to 300 metres and planetesimal drag is neglected. This choice is discussed separately in the chapters 4 and 5. A more realistic treatment involves a size distribution and the fragmentation into smaller planetesimals which are more strongly affected by gas drag (Kaufmann and Alibert, 2023).

The planetesimal accretion rate can be expressed as (Chambers, 2006)

$$\dot{M}_{\mathrm{plan}} = \Omega_{\mathrm{K}} \bar{\Sigma}_{\mathrm{plan}} R_{\mathrm{H}}^2 p_{\mathrm{coll}}, \tag{3.24}$$

where $\bar{\Sigma}_{\mathrm{plan}}$ is the mean planetesimal surface density in the feeding zone and p_{coll} is the collision probability, containing the kinematic details. The feeding zone

half-width is set to $5R_{\rm H}$ (Fortier et al., 2013). Following Inaba et al. (2001), the collision probability can be divided into three regimes based on the relative velocities between planetesimals and the protoplanet – the low, mid, and high-velocity regimes. The distinction is based on the reduced planetesimal eccentricity $\tilde{e} = re/R_{\rm H}$ and inclination $\tilde{i} = ri/R_{\rm H}$. The low-velocity regime is given by $\tilde{e}, \tilde{i} \lesssim 0.2$, the mid-velocity regime is given by $\tilde{e} \lesssim 2$ and $\tilde{i} \gtrsim 0.2$, and the high-velocity regime holds for $\tilde{e}, \tilde{i} \gtrsim 2$. The collision probabilities in the different regimes are

$$p_{\rm low} = 11.3 \left(\frac{R_{\rm cap} + R_{\rm plan}}{R_{\rm H}} \right), \tag{3.25}$$

$$p_{\rm mid} = \frac{(R_{\rm cap} + R_{\rm plan})^2}{4\pi R_{\rm H} \tilde{i}} \left(17.3 + \frac{232 R_{\rm H}}{R_{\rm cap} + R_{\rm plan}} \right), \tag{3.26}$$

$$p_{\rm high} = \frac{(R_{\rm cap} + R_{\rm plan})^2}{2\pi R_{\rm H}} \left(I_{\rm F}(i/e) + \frac{6 R_{\rm H} I_{\rm G}(i/e)}{(R_{\rm cap} + R_{\rm plan})\tilde{e}^2} \right), \tag{3.27}$$

and the final collision probability is given by

$$p_{\rm coll} = \min \left(p_{\rm mid}, \left(p_{\rm low}^{-2} + p_{\rm high}^{-2} \right)^{-1/2} \right). \tag{3.28}$$

The functions $I_{\rm F}$ and $I_{\rm F}$ evaluated at i/e are again semi-analytic approximations by Chambers (2006). $R_{\rm cap}$ is the capture radius is larger than simply the core radius if there is an envelope present. It is given by the implicit equation (Inaba and Ikoma, 2003)

$$R_{\rm plan} = \frac{3}{2} \frac{\rho(R_{\rm cap}) R_{\rm cap}}{\rho_{\rm plan}} \left(\frac{\delta v^2 + 2GM(R_{\rm cap})/R_{\rm cap}}{\delta v^2 + 2GM(R_{\rm cap})/R_{\rm H}} \right). \tag{3.29}$$

3.3 Pebbles

The evolution of dust into pebbles and the accretion of pebbles was not included in the model presented in the NGPPS paper series. In my work, I have used two different approaches to integrate pebble accretion into the pre-existing framework.

For the paper presented in chapter 4, I have rewritten and integrated the model presented in Brügger et al. (2018) which was based on Lambrechts and Johansen

(2014); Bitsch et al. (2015). The simple model is outlined in chapter 2.4.2 in equations (2.71) to (2.76), and described in more detail in Kessler and Alibert (2023). It is characterised by a couple of simplifying assumptions: pebble sizes are drift-limited and the drift is faster than the outwards movement of the growth radius – the orbital distance where the dust reaches the local pebble size. Furthermore, we assume that the location and outwards speed of the growth radius are well approximated from the initial state of the disk. Outside the water iceline, this yields a radially constant flux which evolves over time according to the evolved gas disk at the current position of the growth radius. The pebble surface density, which is used to calculate the pebble accretion rate, is then retrieved from the pebble flux (Johansen and Lambrechts, 2017). The flux is halved inside the water iceline, assuming a water ice fraction of 50% for icy pebbles outside the iceline and instantaneous sublimation. Further, assuming pebbles break into their grain components when the water sublimates, the pebble size inside the iceline is set to the interstellar medium grain size. For the formation of giant planets outside the iceline, which was the main application of the model, this assumption is inconsequential. The pebble flux finally ceases when the growth radius reaches the outer disk edge.

A more involved approach was chosen in Kessler et al. (subm.), presented in chapter 5, following the approach of Birnstiel et al. (2012). This was first implemented and applied in the Bern Model framework in Voelkel et al. (2020). In this model the dust surface density evolution is solved in a simplified way. Instead of considering a size distribution, the aptly named *two-population* model solves the problem in a mass-averaged approach, considering only two populations of solids: the small dust grains and the larger pebbles. This is a valid approach since the dust mass is dominated by largest particles (Birnstiel et al., 2010). The dust evolution equation (2.47) is transformed into a single evolution equation for the combined two-population surface density Σ_{tp}

$$\dot{\Sigma}_{\mathrm{tp}} + \frac{1}{r}\frac{\partial}{\partial r}\left[r\left(\Sigma_{\mathrm{tp}}\bar{v} - D_g\Sigma_g\frac{\partial}{\partial r}\left(\frac{\Sigma_{\mathrm{tp}}}{\Sigma_g}\right)\right)\right] = 0, \tag{3.30}$$

where the mass-averaged diffusivity of the two populations is assumed to be equal to the gas diffusivity D_g. The combined surface density Σ_{tp} separates into the

surface densities of the two underlying populations

$$\Sigma_{\rm peb}(r) = \Sigma_{\rm tp}(r) f_m(r), \tag{3.31}$$
$$\Sigma_{\rm grains}(r) = \Sigma_{\rm tp}(r)(1 - f_m(r)). \tag{3.32}$$

The factor $f_m(r)$ is calibrated with full dust evolution simulations in Birnstiel et al. (2010). The initial combined surface density is simply $\Sigma_{\rm tp,0} = Z\Sigma_{g,0}$ where Z is the dust-to-gas ratio. The mass-averaged radial drift speed $\bar{v}$ reads

$$\bar{v} = (1 - f_m) v_{\rm grains} + f_m v_{\rm peb}, \tag{3.33}$$

where $v_{\rm grains}$ and $v_{\rm peb}$ are the drift speeds of the small and the large populations, respectively, given by equation (2.44). The dust grain size is fixed and the size of the pebbles is evaluated by comparing the drift and fragmentation size limits given in equations (2.51) and (2.53), respectively.

There exist many valid models of the pebble accretion rate, given some pebble surface density. The description of Ormel (2017) outlined in chapter 2.4.2 is consistent with other recent works, within orders of unity (e.g. Ormel and Klahr, 2010; Ormel and Kobayashi, 2012; Lambrechts and Johansen, 2012, 2014; Guillot et al., 2014; Ida et al., 2016; Johansen and Lambrechts, 2017). In this thesis, I apply the descriptions of Johansen and Lambrechts (2017) and Ormel (2017) in the first and second paper, respectively.

When considering the formation of giant planets in multi-planetary systems, the pebble isolation mass must be taken into account. A simple approach is the one given in equation (2.95) which is suitable for single planets and used in Kessler and Alibert (2023). Since multi-planetary systems are considered in Kessler et al. (subm.), the pebble flux inside of a planet above the pebble isolation mass must be reduced. This is achieved by applying the tidal gap profile, caused by a massive planet, of Kanagawa et al. (2016, 2017) to the gas disk which is used to calculate the two-population surface density evolution according to equation (3.30). In this way, a planet above the pebble isolation mass will trap pebbles at the outer edge of the induced gap. This simple treatment is not fully self-consistent as the gap is not considered in the further evolution of the gas disk (only the dust can see the gap). In such traps, where multiple protoplanets may be expected

to grow in close vicinity of each other, this approach breaks down and requires a better treatment of the planet-disk interactions. As shown in Stammler et al. (2023), small dust grains can diffuse through pebble traps which is an effect that cannot be captured in the two-population approach.

3.4 Gas accretion

We solve the classical 1D radially symmetric internal structure equations of mass conservation (2.103), hydrostatic equilibrium (2.104), and energy transport (2.105). The density $\rho(P,T)$ and the adiabatic gradient are obtained from the equations of state of Saumon et al. (1995). When a planet is still embedded in the gas disk, called the *attached phase*, the structure equations are integrated over the mass with the outer boundary condition of the radius of the planet R being (Lissauer et al., 2009)

$$\frac{1}{R} = \frac{1}{k_1 R_\mathrm{B}} + \frac{1}{k_2 R_\mathrm{H}}, \tag{3.34}$$

where

$$R_\mathrm{B} = \frac{GM}{c_s^2} \tag{3.35}$$

is the Bondi radius of a planet of mass M, $k_1 = 1$, and $k_2 = 1/4$. The pressure $P(R)$ and temperature $T(R)$ at the outer boundary are given by the gas disk midplane values at the planet's location

$$P(R) = P_\mathrm{mid,g}, \tag{3.36}$$

$$T^4(R) = T^4_\mathrm{mid,g} + \frac{3\tau_\mathrm{out} L(R)}{8\pi\sigma_\mathrm{SB} R^2}. \tag{3.37}$$

The second term in the temperature boundary condition is the internal temperature for a given luminosity L at the boundary, depending on the optical depth at the surface of the planet τ_out (Mordasini et al., 2012b)

$$\tau_\mathrm{out} = \max\left(\kappa(\rho_\mathrm{mid,g}, T_\mathrm{mid,g})\rho_\mathrm{mid,g} R, \frac{2}{3}\right). \tag{3.38}$$

The outer boundary condition, as well as the radiative gradient (2.102) depend on the envelope opacity which, following Mordasini et al. (2014), is given by the

interstellar grain opacities by Bell and Lin (1994) reduced by a factor of 0.003 by default. This value is a fit to numerical simulations of the grain dynamics in protoplanetary atmospheres under the assumption of perfect sticking (Movshovitz and Podolak, 2008; Movshovitz et al., 2010).
The total mass of the planet $M(R) = M$, the quantity we are solving for, is divided into the core mass $M_{\rm core}$ and envelope mass $M_{\rm env}$ such that

$$M = M_{\rm core} + M_{\rm env}. \tag{3.39}$$

Since the accretion rate of solids onto the core is known, an iterative method can be applied to solve the structure equations until $M(R_{\rm core}) = M_{\rm core}$ is fulfilled. This yields the needed envelope mass $M_{\rm env} = M - M_{\rm core}$ given the new core mass in order to satisfy the structure equations. In some time interval Δt, the envelope accretion rate of gas $\dot{M}_{\rm env}$ is then simply

$$\dot{M}_{\rm env} = \frac{M_{\rm env}(t) - M_{\rm env}(t - \Delta t)}{\Delta t}. \tag{3.40}$$

The planetary luminosity is given by the accretion of gas and solids, as well as contraction. Luminosity contributions due to radioactive decay, bloating of close-in planets, and deuterium burning for the most massive planets, are also considered. In order to integrate the structure equations, the luminosity is estimated from the previous iteration. The actual luminosity obtained from the structure equations is used to correct the estimate a posteriori, which is then used for the next iteration (see Emsenhuber et al., 2021a).

The critical core mass is assumed to be reached when the computed gas accretion rate exceeds the disk-limited gas accretion rate given by Bodenheimer et al. (2013). These rates consider the fact that massive planets open up a gap in the gas, reducing the surface density and hence the maximum possible gas accretion rate. The planet is then in the *detached phase*, accreting at the disk-limited rate (runaway gas accretion). Since both the core and envelope accretion rates are known, the structure equations can be iterated over the radius to find the outer radius R. Since the envelope is no longer smoothly transitioning to the disk gas in the detached phase, the outer pressure boundary condition is adapted to

$$P(R) = P_{\rm mid,g} + P_{\rm edd} + P_{\rm ram} + P_{\rm rad}, \tag{3.41}$$

where $P_{\rm edd}$ is the photospheric Eddington pressure, $P_{\rm ram}$ is the ram pressure of the accretion shock due to the freely falling gas, and $P_{\rm rad}$ is the radiation pressure (see Emsenhuber et al., 2021a).

3.5 Orbital migration

The type-I migration of planets is treated according to the approach in Coleman and Nelson (2014) which is a modification of the adiabatic torques of Paardekooper et al. (2011). It has been shown that the eccentricity and inclination of a planet have an attenuating effect on the co-rotation torques (Bitsch and Kley, 2010, 2011), as well as on the Lindblad torques (Cresswell and Nelson, 2008). Therefore, the total type-I torque is

$$\Gamma_{\rm I} = F_{\rm L}\Gamma_{\rm L} + F_e F_i \Gamma_{\rm c}, \tag{3.42}$$

where $\Gamma_{\rm L}$ is the Lindblad torque and $\Gamma_{\rm c}$ is the co-rotation torque given in (Paardekooper et al., 2011). This prescription also includes the saturation of the co-rotation torque. The co-rotation torque consists of the linear and non-linear torques due to both the entropy gradient and the vortensity gradient (see chapter 2.6). The factors $F_{\rm L}$ (Cresswell and Nelson, 2008), F_e (Fendyke and Nelson, 2014), and F_i (Coleman and Nelson, 2014) are the attenuating functions of the different torques due to the eccentricity and inclination of a planet.

In order to determine when a planet starts to open a gap tidally, transitioning into the type-II migration regime, we consider the criterion (Crida et al., 2006)

$$\frac{3H_g}{4R_{\rm H}} + \frac{50\nu M_\star}{Ma^2\Omega_{\rm K}} \leq 1, \tag{3.43}$$

where a is the planet's semi-major axis. If a planet of mass M fulfils this criterion, it is considered to migrate in the type-II regime according to Dittkrist et al. (2014). Here the planet follows the radial velocity of the gas $v_{r,g}$ as described in chapter 2.6. If the planet mass exceeds the local gas disk mass, the migration rate $v_{r,\rm planet}$ is suppressed as (Alexander and Armitage, 2009)

$$v_{r,\rm planet} = v_{r,g} \min\left(1, \frac{2a^2\Sigma_g}{M}\right). \tag{3.44}$$

This simplified prescription results in similar behaviour as the simulation fits obtained in Kanagawa et al. (2018).

3.6 N-body and collisions

The mutual gravitational interactions between planets are modelled using the symplectic N-body integrator code `mercury` (Chambers, 1999). Note that while the rest of the model follows a 1D approach, the N-body is solved in 3D where the contributions from disk-driven migration and gas drag are considered as additional forces (Emsenhuber et al., 2021a). The N-body calculations are performed during the disk stage and after the disk disperses until a simulated time of 20 Myr has elapsed. To reduce the computation time, the N-body integration is stopped at this point, assuming that the planetary system is stable. This is not necessarily the case in the outermost regions of the system but remains a necessary simplification for large-scale populations.

When two planets collide, a simplified treatment of the giant impact is applied. The cores are assumed to merge perfectly, while the envelope of the smaller body (the impactor) is completely expelled. The impact energy E_{imp} between two colliding protoplanets of masses M_1 and M_2 with a relative velocity v_{imp} is

$$E_{\mathrm{imp}} = \max\left(\frac{1}{2}\frac{M_1 M_2}{M_1 + M_2} v_{\mathrm{imp}}^2 - G\frac{M_1 M_{\mathrm{core},2}}{R_{\mathrm{core},1} + R_{\mathrm{core},2}}, 0\right). \tag{3.45}$$

The second term is the centre-of-mass impact energy of the target and the core of the impactor at their mutual escape velocity. Since the accretion of the impactor is considered as a contribution to the core accretion rate, the centre-of-mass energy is subtracted to avoid double counting. The core accretion rate and luminosity contribution due to a giant impactor with $M_{\mathrm{core},2}$ are smoothed out over time by

$$\dot{M}_{\mathrm{imp}} = \frac{M_{\mathrm{core},2}}{t_{\mathrm{imp}}\sqrt{2\pi}} \exp\left[-\frac{1}{2}\left(\frac{t - \mathbf{t}}{t_{\mathrm{imp}}} - 3\right)^2\right], \tag{3.46}$$

$$L_{\mathrm{imp}} = \frac{E_{\mathrm{imp}}}{t_{\mathrm{imp}}\sqrt{2\pi}} \exp\left[-\frac{1}{2}\left(\frac{t - \mathbf{t}}{t_{\mathrm{imp}}} - 3\right)^2\right]. \tag{3.47}$$

Here, t is the current time, $\mathbf{t}$ is the time of the impact, and $t_{\rm imp} = 10^4$ yr is the characteristic impact timescale (Broeg and Benz, 2012). In this approach, the impact energy is considered in the subsequent evaluation of the planetary structure which can lead to significant (short-term) loss of the envelope of the target planet.

3.7 Planet evolution

After 20 Myr, the planetary system is in the evolution phase where we continue to solve the structure equations (Mordasini et al., 2012b). With the termination of gas accretion and in absence of the gas disk, the outer boundary conditions simplify to

$$P(R) = P_{\rm edd} + P_{\rm rad}, \tag{3.48}$$
$$T^4(R) = T^4_{\rm int} + (1-A)T^4_{\rm eq}, \tag{3.49}$$

where the internal temperature $T_{\rm int}$ is simply given by the luminosity L at the surface

$$T^4_{\rm int} = \frac{L}{4\pi\sigma_{\rm SB}R^2}, \tag{3.50}$$

and the equilibrium temperature $T_{\rm eq}$ is

$$T_{\rm eq} = T_\star\sqrt{\frac{R_\star}{2a}}. \tag{3.51}$$

We assume an albedo $A = 0.343$ equal to the value for Jupiter (Guillot, 2005).

In the evolution phase, the photo-evaporative atmospheric escape due to X-ray and EUV irradiation of the star is also considered. The evaporation model is following Jin et al. (2014), using the X-ray flux and EUV luminosity of Ribas et al. (2005). In the low-flux regime ($< 10^4$ erg cm^{-2} s^{-1}), the energy-limited escape rates of Jackson et al. (2012) are used, while in the high-flux regime ($> 10^4$ erg cm^{-2} s^{-1}), the radiation-recombination-limited escape rate is applied (Murray-Clay et al., 2009).

3.8 Initial conditions

The Bern Model requires a number of parameters to initialise a simulation. Some of the most important fixed parameters are the stellar mass, the viscosity parameter α, the planetesimal size, as well as the threshold fragmentation velocity of pebbles. The planetary embryos, which are the N-body objects for which we solve the planetary structure equations and compute their accretion, are inserted at a fixed mass $M = 10^{-2}$ $\mathrm{M_E}$ at $t = 0$ in the works presented here. The parameters which are not fixed but sampled from a statistical distribution for the purpose of population synthesis are the initial disk mass, the inner disk radius, and the external photo-evaporation parameter $\dot{M}_{\mathrm{wind}}$. The characteristic disk radius R_{char} is obtained from the relation (Andrews et al., 2010)

$$\frac{M_g}{2 \times 10^{-3} \mathrm{M_{Sun}}} = \left(\frac{R_{\mathrm{char}}}{10 \text{ au}} \right)^{1.6} . \tag{3.52}$$

The initial gas surface density profile given by equation (3.9) can then be inferred using

$$M_g = \frac{2\pi \Sigma_{\mathrm{g},0}}{1.1} \left(5.2 \text{ au}\right)^{0.9} \left(R_{\mathrm{char}}\right)^{1.1} . \tag{3.53}$$

Finally, we sample the initial bulk dust-to-gas ratio which determines the total mass of available solids and allows for the initialisation of the disk of solids.
The specific distributions used, which are fits to observations of young Sun-like stars and their disks, are listed in Kessler and Alibert (2023) and Kessler et al., (subm.) separately.

4 Paper I

Early global models of planet formation considered the accretion of planetesimals as the main core accretion process (e.g. Pollack et al., 1996). For giant planets, the formation timescale constraint due to the gas disk lifetime poses a significant challenge. With the more recent proposition of pebble accretion (Ormel and Klahr, 2010), planet formation models have undergone a gradual shift towards this core accretion mechanism. The promise of rapidly growing cores, also at moderate orbital distances, is particularly intriguing for the formation of giant planets (Lambrechts and Johansen, 2014). However, as outlined in chapter 2, it is a reasonable scenario that a growing protoplanet can accrete both planetesimals and pebbles concurrently. This motivated the study presented in the following. The main goal is to understand the arising interplay between classical planetesimals accretion and pebble accretion, not to predict the characteristics of a physical population of planets formed from a disk consisting of pebbles and planetesimals. Therefore, a simple pebble accretion model based on Lambrechts and Johansen (2014) and Brügger et al. (2018) is integrated into the Bern Model framework. Simulating a single planet per disk allows us to isolate the key differences in the formation pathway of planets accreting planetesimals and pebbles concurrently. In this way, we can understand whether the inclusion of pebble accretion necessarily brings the hoped for boost to planet formation timescales.

A&A 674, A144 (2023)
https://doi.org/10.1051/0004-6361/202245641

Astronomy & Astrophysics

The interplay between pebble and planetesimal accretion in population synthesis models and its role in giant planet formation

A. Kessler and Y. Alibert

Physikalisches Institut, University of Bern, Gesellschaftsstrasse 6, 3012 Bern, Switzerland
e-mail: andrin.kessler@unibe.ch

Received 7 December 2022 / Accepted 25 April 2023

ABSTRACT

Context. In the core accretion scenario of planet formation, rocky cores grow by first accreting solids until they are massive enough to accrete gas. For giant planet formation, this means that a massive core must form within the lifetime of the gas disk. Inspired by observations of Solar System features such as the asteroid and Kuiper belts, the accretion of roughly kilometre-sized planetesimals is traditionally considered as the main accretion mechanism of solids but such models often result in longer planet formation timescales. The accretion of millimetre- to centimetre-sized pebbles, on the other hand, allows for rapid core growth within the disk lifetime. The two accretion mechanisms are typically discussed separately.

Aims. We investigate the interplay between the two accretion processes in a disk containing both pebbles and planetesimals for planet formation in general and in the context of giant planet formation specifically. The goal is to disentangle and understand the fundamental interactions that arise in such hybrid pebble-planetesimal models laying the groundwork for informed analysis of future, more complex, simulations.

Methods. We combined a simple model of pebble formation and accretion with a global model of planet formation which considers the accretion of planetesimals. We compared synthetic populations of planets formed in disks composed of different amounts of pebbles and 600 metre-sized planetesimals to identify the impact of the combined accretion scenario. On a system level, we studied the formation pathway of giant planets in these disks.

Results. We find that, in hybrid disks containing both pebbles and planetesimals, the formation of giant planets is strongly suppressed, whereas, in a pebbles-only or planetesimals-only scenario, giant planets can form. We identify the heating associated with the accretion of up to 100 kilometre-sized planetesimals after the pebble accretion period to delay the runaway gas accretion of massive cores. Coupled with strong inward type-I migration acting on these planets, this results in close-in icy sub-Neptunes originating from the outer disk.

Conclusions. We conclude that, in hybrid pebble-planetesimal scenarios, the late accretion of planetesimals is a critical factor in the giant planet formation process and that inward migration is more efficient for planets in increasingly pebble-dominated disks. We expect a reduced occurrence rate of giant planets in planet formation models that take the accretion of pebbles and planetesimals into account.

Key words. planets and satellites: formation – protoplanetary disks

1. Introduction

In the core accretion paradigm, the formation of giant planets is inherently constrained by the lifetime of the circumstellar gas disk. A protoplanet core must grow massive enough on the time scale of a few million years in order to accrete significant amounts of gas before the dispersal of the disk (Haisch et al. 2001). Classical planet formation models consider the accretion of planetesimals (e.g. Pollack et al. 1996; Alibert et al. 2005). From the size frequency distribution of Solar System asteroids, the diameter of primordial planetesimals is estimated to be around 100 km (Bottke et al. 2005; Morbidelli et al. 2009). This is supported by simulations of planetesimal formation through the streaming instability (Schäfer et al. 2017). On the other hand, observations of small Kuiper belt objects suggest a larger number of kilometre-sized planetesimals (Arimatsu et al. 2019), which is consistent with small primordial planetesimals (Schlichting et al. 2013). The exact size distribution of primordial planetesimals remains uncertain. Core growth time scales using large planetesimals are long, typically exceeding the disk lifetime (Pollack et al. 1996). However, giant planet formation is shown to be successful in a planetesimals-only setting when sub-kilometre-sized planetesimals are considered (Emsenhuber et al. 2021a, hereafter NGPPS I). Even smaller, roughly millimetre- to centimetre-sized objects called pebbles are more strongly affected by gas drag and can be captured efficiently, forming cores quickly (Ormel & Klahr 2010; Lambrechts & Johansen 2012). Planet formation models considering the accretion of such pebbles typically produce giant planets comparatively easily while disregarding planetesimal-like objects entirely (Lambrechts & Johansen 2014; Bitsch et al. 2015; Brügger et al. 2018).

High-precision measurements of isotopes in meteorites suggest that the early population of small bodies in the Solar System has been separated into two reservoirs for ∼2–3 Myr. The origin of this dichotomy is unknown. The forming Jupiter is theorised to have acted as a radial barrier for planetesimals (Kruijer et al. 2017; Brasser & Mojzsis 2020), whereas, other proposed explanations link the dichotomy to protoplanetary disk effects such as pressure bumps related to silicate and volatile evaporation fronts (Lichtenberg et al. 2021; Izidoro et al. 2021; Morbidelli et al. 2021). In order for proto-Jupiter to separate the drifting pebbles for several millions of years, the core mass must remain

at least around 20 Earth masses. In any standard planet formation model, this is very unlikely to happen. In this mass range, the gravitational pull of the planet triggers rapid gas accretion, quickly forming a Jupiter-like planet. In Alibert et al. (2018), a Jupiter formation scenario using a combination of pebble and planetesimal accretion is suggested to connect the Jovian formation history to the observational constraints. They consider the in situ formation of Jupiter in their proof of concept study. Fast core growth to ∼10–20 Earth masses within ∼1 Myr is facilitated by the accretion of pebbles. At this mass, the further accretion of pebbles is prevented by a pressure bump outside the planetary orbit (Paardekooper & Mellema 2006; Lambrechts & Johansen 2014). Slow planetesimal accretion can sufficiently heat the envelope for the pressure to balance the gravitational pull on the surrounding gas, delaying runaway gas accretion. At some point, Jupiter grows massive enough to quickly accrete large amounts of gas, reaching its present-day mass.

Motivated by this proposed formation scenario of Jupiter, we investigate the consequences of a combined pebble and planetesimal accretion model for the formation of giant planets and planet formation in general. We modify the Bern model of planet formation and evolution (NGPPS I) with a simple model of pebble formation and accretion (Bitsch et al. 2015; Brügger et al. 2018). The Bern model of planet formation and evolution is a global model that self-consistently computes the evolution of the gas disk, the dynamics of the planetesimal disk, the accretion of gas and planetesimals by planetary embryos, the planet-planet N-body interactions, as well as planet-gas interactions such as gas-driven migration.

Population synthesis allows one to probe a large part of the parameter space of planet formation. For this reason, we investigate the effects of the two solid accretion mechanisms on a population level. The primary goal here is to understand the interplay of classical planetesimal accretion and pebble accretion models, not to predict the characteristics of a physical population of planets formed from a disk consisting of pebbles and planetesimals. To remove the chaotic component of multi-planetary systems, we investigate the formation of a single planet per disk. This allows us to isolate the key differences in the formation pathway of planets forming in disks composed of pebbles and planetesimals. A comparison to the observed population of planetary systems would necessarily require the simultaneous modelling of multiple planets per disk. To uncover the interplay of the two accretion mechanisms, we vary the amount of pebbles with respect to planetesimals. We especially focus on giant planet formation as a key topic of interest in the scientific debate about the size of the accreted solids.

In Sect. 2, we give a brief overview of our planet formation and evolution model. The pebble formation and accretion model is described in more detail. In Sect. 3, we present the populations emerging from different solid disk compositions. We compare populations from a pure planetesimal disk, a pebble-poor (30%), a pebble-rich (70%), and a pure pebble disk. We focus on the formation of giant planets in Sect. 4. Particularly, we investigate the onset of rapid gas accretion as well as the impact of orbital migration and the pebble isolation mass. Finally, Sect. 5 is dedicated to a brief summary of the results and conclusions.

2. Theoretical models

We first give a short overview of the model components outlined in Brügger et al. (2020) and described in great detail in NGPPS I. In particular, we detail the gas disk model, the treatment of planetesimals, the gas accretion model, and the planetary migration prescriptions. We then present the pebble formation model, and finally, the pebble accretion model in more detail.

2.1. Gas disk model

The time evolution of the protoplanetary gas disk surface density $\Sigma_{\rm gas}$ is governed by the 1D radially symmetric viscous diffusion equation (Lust 1952; Lynden-Bell & Pringle 1974)

$$\frac{\partial \Sigma_{\rm gas}}{\partial t} = \frac{1}{r}\frac{\partial}{\partial r}\left[3r^{1/2}\frac{\partial}{\partial r}\left(r^{1/2}\nu\Sigma_{\rm gas}\right)\right] - \dot{\Sigma}_{\rm gas,ph} - \dot{\Sigma}_{\rm gas,pl}, \tag{1}$$

where r is the orbital distance, $\dot{\Sigma}_{\rm gas,ph}$ is the sink term related to internal and external photo-evaporation following Mordasini et al. (2012a), and $\dot{\Sigma}_{\rm gas,pl}$ is the sink term due to the accretion of gas by planets. We use the $\nu = \alpha c_{\rm s} H$ viscosity parametrisation of Shakura & Sunyaev (1973), where $c_{\rm s}$ is the isothermal sound speed and $H = c_{\rm s}/\Omega_{\rm K}$ is the vertical scale height at Kepler frequency $\Omega_{\rm K} = \sqrt{GM_\star/r^3}$, G being the gravitational constant and $M_\star$ the stellar mass. In this work we set $\alpha = 0.002$ (Emsenhuber et al. 2021b, hereafter NGPPS II). The initial conditions of the simulations are further described in Sect. 3.

The initial radial surface density profile is given by (Andrews et al. 2010)

$$\Sigma_{\rm gas}(r) = \Sigma_0 \left(\frac{r}{5.2\ {\rm AU}}\right)^{-\beta} \exp\left[-\left(\frac{r}{R_{\rm char}}\right)^{(2-\beta)}\right]\left(1-\sqrt{\frac{R_{\rm in}}{r}}\right). \tag{2}$$

Here, Σ_0 is the initial gas surface density at 5.2 AU, β is fixed to 0.9, $R_{\rm char}$ is the characteristic radius, and $R_{\rm in}$ is the inner radius where the disk is truncated by the stellar magnetic field (see NGPPS II). Typical values of these parameters are $R_{\rm in} = 0.05$ AU and $R_{\rm char} = 70$ AU.

The midplane temperature $T_{\rm mid}$ is calculated in a semi-analytical approach considering viscous heat dissipation and direct stellar irradiation (Nakamoto & Nakagawa 1994; Hueso & Guillot 2005)

$$T_{\rm mid}^4 = \frac{1}{2\sigma_{\rm SB}}\left(\frac{3}{8}\kappa_{\rm R}\Sigma_{\rm gas} + \frac{1}{2\kappa_{\rm P}\Sigma_{\rm gas}}\right)\dot{E}_\nu + T_{\rm irr}^4, \tag{3}$$

where $\sigma_{\rm SB}$ is the Stefan-Boltzmann constant and $\dot{E}_\nu = \frac{9}{4}\Sigma_{\rm gas}\nu\Omega_{\rm K}^2$ is the viscous energy dissipation rate. The Rosseland mean opacity κ_R is obtained from the minimum of the grain-free gas opacities of Freedman et al. (2014) and the full interstellar opacities of Bell & Lin (1994) obtained for a micrometre dust-to-gas ratio of 1%. For the Planck opacity $\kappa_{\rm P}$, we follow Nakamoto & Nakagawa (1994). In reality, the disk opacities are coupled to the evolution of dust which then influences the disk temperature and density evolution. We refer to NGPPS I for a more detailed discussion of disk opacity. The temperature due to stellar irradiation $T_{\rm irr}$ depends on the stellar temperature $T_\star$, radius $R_\star$, and luminosity $L_\star$ via (Adams et al. 1988; Ruden & Pollack 1991; Chiang & Goldreich 1997; Hueso & Guillot 2005)

$$T_{\rm irr}^4 = T_\star^4\left[\frac{2}{3\pi}\left(\frac{R_\star}{r}\right)^3 + \frac{1}{7}\left(\frac{R_\star}{r}\right)^2\frac{H}{r}\right] + \frac{L_\star}{16\pi r^2\sigma_{\rm SB}}{\rm e}^{-\tau_{\rm mid}} + T_{\rm c}^4. \tag{4}$$

The stellar parameters are obtained from the stellar evolution tracks of Baraffe et al. (2015). In this way, the temporal evolution of the star affects the evolution of the disk temperature profile. The stellar luminosity term accounts for the direct irradiation contribution through the midplane, considering the optical depth $\tau_{\rm mid}$ through the midplane (NGPPS I). The term with $T_{\rm c} = 10$ K adds the heating due to the surrounding molecular cloud.

2.2. Planetesimals

We divide the solids in the disk, given by the initial total solids-to-gas ratio $Z_{\rm tot}$, into planetesimals and dust such that $Z_{\rm tot} = Z_{\rm plan} + Z_{\rm dust}$, as well as a 0.01 $M_{\rm E}$ embryo. The planetesimals are described by a surface density with a dynamical state given by their root mean square eccentricity and inclination (Fortier et al. 2013). The planetesimal disk evolves considering the effects of aerodynamic drag (Adachi et al. 1976; Inaba et al. 2001; Rafikov 2004), dynamical stirring by protoplanets (Guilera et al. 2010) and by other planetesimals (Ohtsuki et al. 2002). Initially, the planetesimal surface density profile is steeper than the gas disk profile (Drążkowska & Alibert 2017; Lenz et al. 2019) and the planetesimals are in dynamical equilibrium with respect to their self-stirring. We consider rocky and icy planetesimals inside and outside the water ice line respectively. Due to sublimation in the inner parts of the disk, there is a significant decrease in the planetesimal surface density just inside the ice line. Hence the growth via the accretion of planetesimals is most efficient just outside the ice line. The planetesimal disk is initialised such that $Z_{\rm plan}$ is the total planetesimals-to-gas ratio. In Fig. A.1, we show the initial radial gas and planetesimal surface density profiles of the most and least massive planetesimal disks.

The planetesimal accretion rate $\dot{M}_{\rm plan}$ of a planetary embryo depends on the Kepler frequency $\Omega_{\rm K}$, the embryo mass over stellar mass ration $M/M_\star$, the surface density of planetesimals $\Sigma_{\rm plan}$, as well as the collision probability of planetesimals $p_{\rm coll}$ (Chambers 2006). It is given by

$$\dot{M}_{\rm plan} = \Omega_{\rm K} \bar{\Sigma}_{\rm plan} R_{\rm H}^2 p_{\rm coll}, \tag{5}$$

where $R_{\rm H} = r\left(\frac{M}{3M_\star}\right)^{1/3}$ is the Hill radius and $\bar{\Sigma}_{\rm plan}$ is the mean planetesimal surface density in the planet's feeding zone. The feeding zone is centred around the planet with a radius $R_{\rm feed} = 5R_{\rm H}$ (Fortier et al. 2013) for circular orbits. This is always the case in a single planet system.

The collision probability is a function of the planetesimal dynamical state (Inaba et al. 2001; Chambers 2006) and the capture radius of the protoplanet, which is enhanced by the presence of an envelope (Inaba & Ikoma 2003). The increased capture radius over the physical radius is crucial for the overall planetesimal accretion rate (Podolak et al. 1988; Venturini & Helled 2020). Especially for smaller planetesimals, this means the calculation of gas accretion cannot be omitted at any stage of the simulation.

2.3. Gas accretion model

The gas accretion is calculated by solving the 1D radially symmetric internal structure equations (Bodenheimer & Pollack 1986) which describe mass conservation, hydrostatic equilibrium, and energy transport respectively

$$\frac{\partial M}{\partial r} = 4\pi r^2 \rho, \tag{6}$$

$$\frac{\partial P}{\partial r} = -\frac{GM}{r^2}\rho, \tag{7}$$

$$\frac{\partial T}{\partial r} = \frac{T}{P}\frac{\partial P}{\partial r}\min(\nabla_{\rm ad}, \nabla_{\rm rad}), \tag{8}$$

where M is the mass enclosed in a sphere of radius r, P is the pressure, and T is the temperature. The density $\rho(P,T)$ is obtained from the equations of state of Saumon et al. (1995). In convective zones, the temperature gradient is given by the adiabatic gradient $\nabla_{\rm ad}$ from the equations of state. Otherwise we use the radiative gradient (Kippenhahn & Weigert 1990)

$$\nabla_{\rm rad} = \frac{3\kappa L P}{64\pi\sigma_{\rm SB} G M T^4} \tag{9}$$

depending on the luminosity L of the planet and the envelope opacity κ. Following Mordasini et al. (2014), we reduce the full interstellar opacity (Bell & Lin 1994) by a factor of 0.003. This value is a fit to detailed simulations of the grain dynamics in protoplanetary atmospheres (Movshovitz & Podolak 2008; Movshovitz et al. 2010). The total luminosity includes the energy contribution due to the accretion of solids and gas, as well as the contraction of the envelope (Mordasini et al. 2012a,b; Alibert et al. 2013). Solving the structure equations is crucially important to self-consistently account for the feedback of planetary luminosity and gas accretion.

The accreted gas mass is determined iteratively by comparing the envelope masses between two iterations (Alibert et al. 2005). In the beginning, the gas accretion is limited by the capacity of the planet to cool given its luminosity. As the core mass of the planet increases, the cooling can be so efficient that the gas accretion is limited by the supply of gas from the disk. Once the planet reaches this threshold, the planet is considered to be detached from the surrounding gas disk, accreting gas at the disk-limited gas accretion rate following Bodenheimer et al. (2013). In past iterations of this and similar models, the disk limited gas accretion rate was either constrained by the radial flow of the gas or used a Bondi- or Hill-like accretion scheme (NGPPS I). Both are inconsistent with the expected reduction of gas accretion due to the formation of a gap. This effect could only be ignored assuming eccentric orbits where the planet can efficiently access disk material despite the gap which is not applicable to the circular case of a single forming planet (Lubow et al. 1999; Bryden et al. 1999). In Bodenheimer et al. (2013), this reduction to the gas accretion rate is taken into account.

2.4. Orbital migration

A growing planet excites density waves in the gas disk through the inner- and outer Lindblad resonances as well as the corotation resonances (Goldreich & Tremaine 1979; Korycansky & Pollack 1993). A net torque is exerted on the planet resulting in orbital migration, so-called type-I migration (Ward 1997; Tanaka et al. 2002). The positive torque of the Lindblad resonances inside the planetary orbit and the negative torque of the outer resonances usually result in migration towards the star. The corotation torque can be positive or negative, allowing outward migration for lower mass planets (Dittkrist et al. 2014). The net torque depends on the local gas surface density gradient, the temperature profile, and the entropy. We follow the approach of Coleman & Nelson (2014) based on the torques of Paardekooper et al. (2011) including the attenuation of the corotation torque due to eccentricity and inclination (Bitsch & Kley 2010; Fendyke & Nelson 2014; Coleman & Nelson 2014).

As the planet grows more massive, it tidally interacts with the gas disk, locally decreasing the gas surface density until a gap forms (Lin & Papaloizou 1986). In this so-called type-II migration regime, the orbital migration rate can be significantly lower than in the type-I regime. We use the gap opening criterion of Crida et al. (2006) as the transition threshold from type-I to type-II migration for a planet of mass M orbiting with

semi-major axis a

$$\frac{3H}{4R_{\rm H}} + \frac{50\nu M_\star}{Ma^2\Omega_{\rm K}} \leq 1. \tag{10}$$

We adopt the smooth transition from the type-I to the type-II regime of Dittkrist et al. (2014) and for the type-II migration direction and rate, we follow their approach where the planet moves along with the radial velocity of the gas (Pringle 1981). For even higher mass planets, the migration rate is limited by the disk-to-planet mass ratio corresponding to the fully suppressed case in Alexander & Armitage (2009).

2.5. Pebble formation model

The dust surface density $\Sigma_{\rm dust} = Z_{\rm dust}\,\Sigma_{\rm gas}$ follows the evolution of the gas disk surface density. The dust disk provides the mass reservoir for pebble formation and we identify the fraction $f_{\rm peb} = Z_{\rm dust}/Z_{\rm tot}$ as the initial dust fraction. Since it is the parameter that is varied to change the amount of pebbles in the disk, we call it the pebble fraction. It marks the theoretical maximum fraction of solids that can be converted into pebbles. Because the dust surface density decreases with time following the gas surface density evolution, not all of the initial dust is converted into pebbles. Given the total solids-to-gas ratio $Z_{\rm tot}$ and a fixed value $0 \leq f_{\rm peb} \leq 1$, which are both initial conditions of the model, the planetesimals-to-gas fraction is simply $Z_{\rm plan} = Z_{\rm tot}(1 - f_{\rm peb})$. We note that in this way, the total initial solid mass in the system is independent of the value of $f_{\rm peb}$. However, since the different species of solids do not evolve in the same way, the available solid mass at a later time is strongly impacted by the choice of $f_{\rm peb}$. Most notably, pebbles neither form nor drift in the absence of the gas disk, whereas planetesimal accretion is not directly tied to the lifetime of the disk.

The location of pebble formation $r_{\rm g}$, called growth radius, is defined by equating the pebble formation and drift time scales. Assuming Epstein drag, Lambrechts & Johansen (2014) find

$$r_{\rm g}(t) = \left(\frac{3}{16}GM_\star\right)^{1/3} (\epsilon_{\rm d} Z_{\rm dust}\, t)^{2/3}. \tag{11}$$

Here, $\epsilon_{\rm d} = 0.5$ is a free dust to pebble growth parameter. We use this prescription to determine the location of pebble formation given the initial dust-to-gas ratio $Z_{\rm dust}$. The outward moving growth radius leaves behind inward drifting pebbles, inducing a mass flux

$$\dot{M}_{\rm peb}(r) = 2\pi r_{\rm g} \frac{{\rm d}r_g}{{\rm d}t} \Sigma_{\rm dust}(r_{\rm g}) \tag{12}$$

for $r < r_{\rm g}$. Equation (12) assumes that the pebble flux instantaneously adapts to the conditions at $r_{\rm g}$. The pebble surface density inside the growth radius is then given by

$$\Sigma_{\rm peb} = \frac{\dot{M}_{\rm peb}}{2\pi r v_{\rm r}}, \tag{13}$$

assuming all of the dust converts to pebbles. This means that $\Sigma_{\rm dust}$ vanishes and is replaced by $\Sigma_{\rm peb}$ inside of $r_{\rm g}$. Pebbles drift radially with the velocity $v_{\rm r}$, depending on the Stokes number St (Weidenschilling 1977)

$$v_{\rm r} = -2\frac{\rm St}{{\rm St}^2 + 1}\Delta v, \tag{14}$$

where $\Delta v = \eta v_{\rm K}$ is the sub-Keplerian headwind velocity given by the Kepler velocity $v_{\rm K} = r\Omega_{\rm K}$ and $\eta = -\frac{1}{2}\left(\frac{H}{r}\right)^2 \frac{\partial \ln P}{\partial \ln r}$ for a disk scale height H and a pressure P at a radius r. Lambrechts & Johansen (2014) find a typical pebble Stokes number of

$${\rm St} \approx \frac{\sqrt{3}\epsilon_{\rm p} Z_{\rm dust}}{8\eta}, \tag{15}$$

with a pebble growth efficiency $\epsilon_{\rm p} = 0.5$. We adopt this prescription outside the ice line. We ignore erosive collisions of pebbles for both the pebble formation timescale as well as the resulting pebble size. By assuming pebble growth is only limited by radial drift, the pebble sizes are slightly overestimated in the inner parts of the disk at early times. In more turbulent disks, depending on the fragmentation velocity, the fragmentation of pebbles can be non-negligible resulting in different pebble sizes (Birnstiel et al. 2010). The pebble size and size distributions affect the disk opacity and in turn the disk structure (Savvidou et al. 2020). Smaller pebbles drift more slowly resulting in higher pebble surface densities. The pebble flux, however, does not change in this model as it is directly given by the radial velocity of the growth radius.

The abundance of the dominant volatile species in icy pebbles (only water in this model) is assumed constant over the course of their inward drift up to the ice line in accordance with Eistrup & Henning (2022). After the sublimation of ice at the ice line crossing (Ida & Guillot 2016), the growth and drift timescales do not balance anymore and Eq. (15) does not hold in the rocky pebble region. For the approximately chondrule-sized (Morbidelli et al. 2015; Shibaike et al. 2019) rocky pebbles inside the ice line we use the definition of the Stokes number (Weidenschilling 1977)

$${\rm St} = \frac{t_{\rm stop}\, v_{\rm K}}{r} \tag{16}$$

where $t_{\rm stop}$ is the stopping time due to the gas drag, depending on the particle size and the local gas properties. The Stokes number is calculated in the appropriate drag regime (Rafikov 2004) assuming a particle radius of 1 mm (Friedrich et al. 2015). We model the consequential pebble mass loss with a reduction of the pebble mass flux by a factor of 0.5 inside the ice line.

At $t = 0$, the solids in the disk consist of a planetary embryo, planetesimals, and dust which is forming pebbles. If planetesimals and embryos form from pebble-like objects themselves, we slightly overestimate planetary growth in the first $\sim 10^5$ yr by using this approach. There are models that connect the formation of planetesimals to the pebble disk, for instance by using a pebble flux-regulated approach and invoking the streaming instability in local pebble traps (Lenz et al. 2019; Voelkel et al. 2020). In Voelkel et al. (2021), this approach is extended to the dynamic formation of embryos from the formed planetesimals. However, since the dust is quickly converted into pebbles in anywhere between 10^5 and 10^6 yr depending on the disk and since planetesimal accretion onto $10^{-2}\,M_{\rm E}$ objects is inefficient, the planetary embryo cannot grow significantly by planetesimal accretion in the time needed until the dust is converted into pebbles. This means that the disk quickly consists of planetesimals and a planetary embryo that is mainly accreting pebbles. Hence, the overestimation stemming from using this simplified approach is small and does not impede the main goal of understanding the interplay of the two accretion mechanisms.

2.6. Pebble accretion model

We consider the accretion of pebbles onto planets following Johansen & Lambrechts (2017). The relative velocity δv of a pebble approaching a protoplanet is given by

$$\delta v = \Delta v + \Omega_K R_{acc}, \tag{17}$$

where R_{acc} is the accretion radius of a planet as defined below. For lower mass planets, the pebble approach velocity is dominated by the headwind Δv compared to the Keplerian motion of the planet. This is referred to as the headwind or Bondi regime. For more massive planets, δv is dominated by the shear velocity. We consider this to be the case when the Hill speed $v_H = \Omega_K R_H$ exceeds the headwind velocity Δv, entering the shear or Hill regime. This represents a transition as the planet reaches the mass $M = 3\eta^3 M_\star$. In the strong pebble–protoplanet coupling limit, where friction timescales are short compared to encounter timescales, the accretion radii in the headwind regime (top) and the shear regime (bottom) are given by (Johansen & Lambrechts 2017)

$$R'_{acc} = \begin{cases} \left(\frac{4\tau_f \Delta v}{R_B}\right)^{1/2} R_B, \\ \left(\frac{\Omega_K \tau_f}{0.1}\right)^{1/3} R_H, \end{cases} \tag{18}$$

with $\tau_f = St/\Omega_K$, the Bondi radius $R_B = \frac{GM}{\Delta v^2}$, and the Hill radius R_H. To account for weaker interactions when the friction timescale is longer than the encounter timescale $t_e = GM/(\Delta v + \Omega_K R_H)^3$, the accretion radii are modified by (Ormel & Klahr 2010)

$$R_{acc} = R'_{acc}\, e^{-0.4(\tau_f/t_e)^{0.65}}. \tag{19}$$

We further distinguish between 3D accretion, where the accretion region is fully embedded in the pebble disk, and the more efficient 2D accretion, which occurs when the accretion radius R_{acc} reaches beyond the pebble scale height $H_{peb} = H\left(1 + \frac{St}{\alpha}\frac{1+2St}{1+St}\right)^{-1/2}$ (Youdin & Lithwick 2007). Here $\alpha = 0.002$ is the α-viscosity parameter. The 2D and 3D pebble accretion rates are

$$\dot{M}_{2D} = 2R_{acc}\Sigma_{peb}\delta v, \tag{20}$$

$$\dot{M}_{3D} = \pi R_{acc}^2 \rho_{peb}\delta v, \tag{21}$$

where $\rho_{peb} = \Sigma_{peb}/(\sqrt{2\pi}H_{peb})$ is the midplane pebble density. Inserting the appropriate expression for R_{acc} into Eqs. (20) and (21) respectively, yields four possible pebble accretion rates.

Pebble accretion stops when the pebble flux vanishes. This can be due to the exhaustion of the outside solid mass reservoir. In this model, this corresponds to the growth radius r_g reaching the outer edge of the gas disk. Another mechanism for stopping the pebble flux is the so-called pebble isolation mass (Lambrechts & Johansen 2014; see also Ataiee et al. 2018; Bitsch et al. 2018; Shibaike & Alibert 2020)

$$M_{iso} \approx 20\left(\frac{H/r}{0.05}\right)^3 M_E. \tag{22}$$

At this mass, the planet perturbs the gas disk outside the planet sufficiently in order to create a region of super-Keplerian gas flow. In this zone, the drifting pebbles from further outside encounter a tailwind instead of a headwind. Thus, pebbles stop drifting and pile up outside the planet. This stops the pebble accretion onto the planet responsible for this pressure bump, as well as starving all potential inside planets of pebbles (Paardekooper & Mellema 2006). The value of the pebble isolation mass depends on the particular disk via the scale height H in this prescription but, typically, it is equal to roughly one Earth mass at 0.1 AU and increases to 20–30 M_E at 1 AU due to the flared disk structure. Beyond that distance, planet cores almost never reach the even larger pebble isolation mass because the growth radius reaches the outer disk edge before. This does not imply that core masses do not easily exceed tens of Earth masses outside of 1 AU when pebble accretion stops. Even though planets are exposed to the flux of pebbles for a shorter amount of time, depending on the disk, core growth can be significant up to the maximum of 40 AU considered here.

3. Population synthesis outcomes

We simulate the formation and evolution of 1000 single-planet systems around solar mass stars for different fixed values of f_{peb}. Since we focus on the formation stage rather than the long term evolution of planets, we present populations after 2 Gyr of time evolution which is well beyond the longest gas disk lifetimes of up to 10^7 yr considered here. We compare the planetesimals-only case, where $f_{peb} = 0$, to the pebble-poor ($f_{peb} = 0.3$), the pebble-rich ($f_{peb} = 0.7$), and the pebbles-only ($f_{peb} = 1$) cases. Following NGPPS I, we use planetesimals with a diameter of 600 m, a fixed viscosity $\alpha = 0.002$, and an initial gas disk slope parameter of $\beta = 0.9$ for all populations. For each of the 10^3 systems within a population, the initial gas disk mass, the inner radius R_{in}, and the total solids-to-gas ratio Z_{tot} are varied. In order to compare the populations using different pebble fractions, we choose the same initial conditions for all four sets of simulations.

The solids-to-gas ratio Z_{tot} is given by normally distributed stellar metallicities of Santos et al. (2005) under the assumption of an equal disk and stellar dust-to-gas ratio. We use the gas disk masses of Tychoniec et al. (2018) which are obtained from continuum dust emission spectra assuming a dust-to-gas ratio of 0.01. We assume a log-normal distribution and correct for the actual, not necessarily equal to 0.01, solids-to-gas ratio in our setup. The inner radius R_{in} is given by the corotation radius with respect to the stellar rotation which is obtained from a log-normal distribution of stellar rotation periods of T-Tauri stars (Venuti et al. 2017). Given these parameters, the characteristic radius R_{char} and the initial surface density at 5.2 AU Σ_0 are determined. The external photo-evaporation rate parameter $\dot{M}_{wind}$ (see NGPPS I) is also varied for each system following a log-normal distribution. Note that since the initial stellar mass is fixed to one solar mass, the initial internal photo-evaporation rate is not varied. In Table 1, we list the distribution parameters of the varied quantities. The distributions of the initial gas disk masses and the characteristic disk sizes are shown in Figs. A.2 and A.3. Note that, compared to NGPPS II, the protoplanetary disks are slightly less massive since we now correct the assumed dust-to-gas ratio of 0.01 in Tychoniec et al. (2018) to the actual one in the calculation of the initial gas disk mass. In every disk, a 0.01 M_E embryo is randomly placed at up to 40 AU following a log-uniform distribution at the beginning of the simulation.

The planet masses are displayed in Fig. 1 as a function of semi-major axis for the different populations. The colour shows the constitution of the accreted solid material: the darkest dots

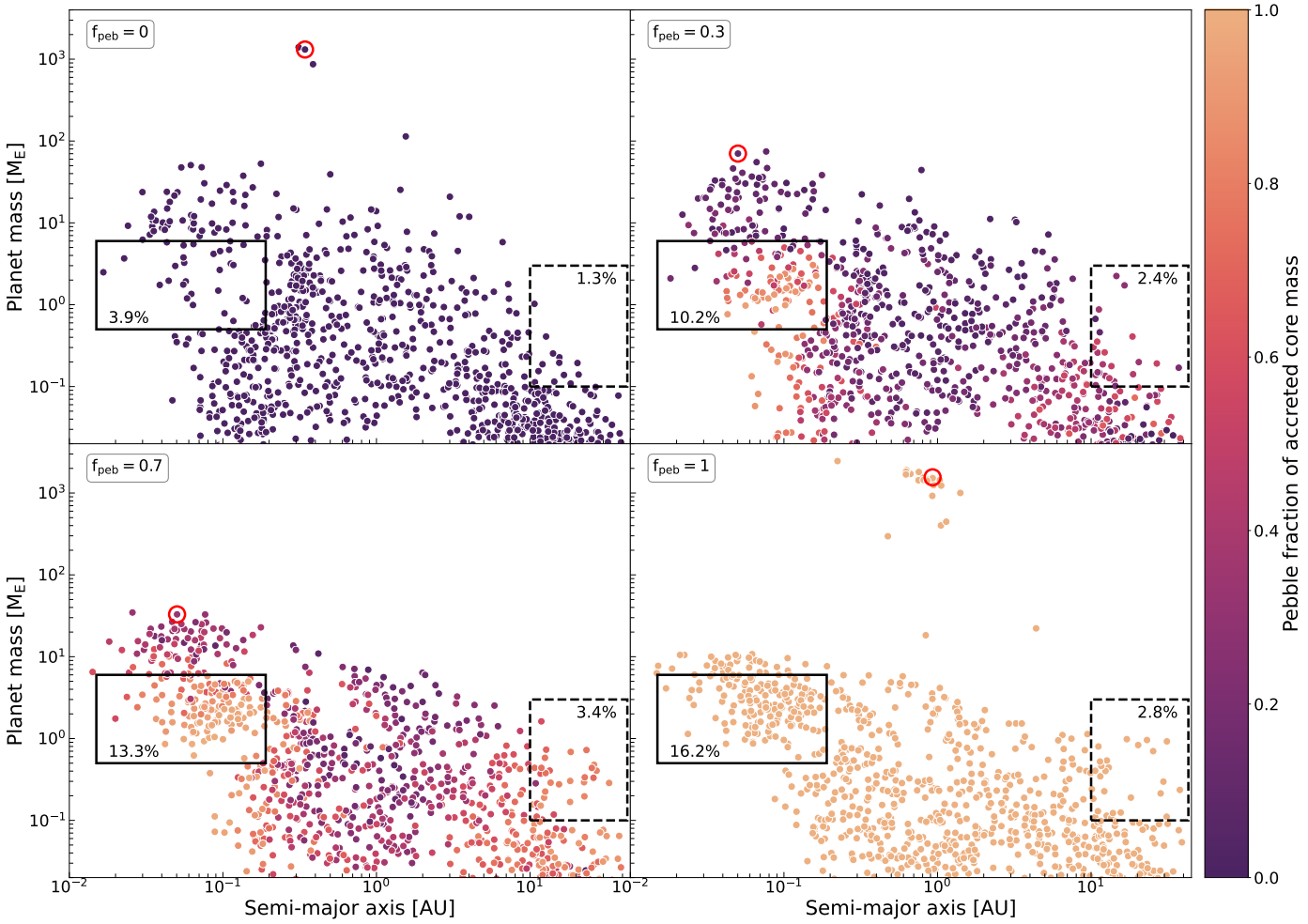

Fig. 1. Planet mass over semi-major axis of one thousand single-planet simulations after 2 Gyr for pebble fractions $f_{\rm peb} = 0$ (planetesimals-only), $f_{\rm peb} = 0.3$ (pebble-poor), $f_{\rm peb} = 0.7$ (pebble-rich), and $f_{\rm peb} = 1$ (pebbles-only). The solid-line boxes highlight planet masses of 0.5–6 $M_{\rm E}$ in the inner disk region up to 0.2 AU. The dashed-line boxes highlight planet masses above 0.1 $M_{\rm E}$ outside of 10 AU. The boxes are labelled with the percentage of planets in these regions. The colour of the points indicates the fraction of accreted pebbles compared to the total mass of accreted solids. The darkest points are fully planetesimal-formed planets and the brightest points are planets formed only by pebbles. The encircled points are planets that formed from the same disk with different pebble fractions. Their formation paths are further examined in Sect. 4.

Table 1. Distributions of varied initial parameters of the population synthesis.

Parameters	Mean	Deviation
$Z_{\rm tot}$	$\mu = -0.02$	$\sigma = 0.22$
$M_{\rm gas}$	$\log_{10}(\mu/M_{\rm sol}) = -1.49$	$\sigma = 0.35$ dex
$P_\star$	$\log_{10}(\mu/d) = 0.676$	$\sigma = 0.306$ dex
$\dot{M}_{\rm wind}$	$\log_{10}(\mu/(M_{\rm sol}{\rm yr}^{-1})) = -4.7$	$\sigma = 1$ dex

have accreted planetesimals only, whereas the lightest dots are dominated by pebble accretion.

The top-left panel shows the synthesis outcome using only planetesimals without any pebbles present. It features a few giant planets above 100 $M_{\rm E}$ around 0.3 AU. The fact that only a few giants form is due to the rather low-mass disks generated here as well as the absence of other planetary embryos (NGPPS I). Nevertheless, this confirms once more that in disks that are massive enough and contain enough small planetesimals, it is possible to form giant planets. Around 0.1 AU, there is a lower number density of roughly Earth mass planets compared to the simulations containing increasing amounts of pebbles, shown in the top-right, bottom-left, and bottom-right panel (see solid-line boxes). This is explained by the fact that inner planets have access to much more mass in the form of drifting pebbles from the whole disk rather than locally available planetesimals. The more massive planets found in the same region are formed further outside, around a few AU, where growth via planetesimal accretion is efficient. These planets start to migrate inwards more quickly once they reach a few Earth masses (see Sect. 2.4) populating the higher-mass demographic of the inner disk. Outside of 10 AU, there are few planets above 0.1 $M_{\rm E}$ as shown by dashed-line box in the top-left panel. Low planetesimal accretion rates of low-mass planets in the outer regions of the disk, even with small 600 metre planetesimals, are expected (NGPPS I). This is due to the low collision probability, large orbital period, and low planetesimal surface density in the outer disk.

In the pebble-poor and pebble-rich populations shown in the top-right and bottom-left panel of Fig. 1, no giant planets are formed. More precisely, there are no planets where the envelope mass exceeds the core mass and the maximal planet mass decreases to about 74 $M_{\rm E}$ ($f_{\rm peb} = 0.3$) and 34 $M_{\rm E}$ ($f_{\rm peb} = 0.7$) as the pebble fraction increases. More planets above

a few Earth masses end up on close orbits compared to the planetesimals-only simulation. While roughly 24% of planets grow more massive than one Earth mass in the planetesimals-only case, this percentage increases up to about 34% with increasing pebble fraction. We find that, as a consequence, in the planetesimals-only case 15% of all planets migrate to closer than half their initial distance, whereas almost 23% of all planets do so in the pebble-rich simulation. The increased number of strongly migrating planets is, however, not only due to the larger number of planets above one Earth mass. Due to the early growth by pebbles, planets are more massive while still inside a more dense gas disk which enhances migration rates. We find that among the planets that grow beyond one Earth mass, 59% migrate significantly (decay more than half their initial separation) in the planetesimals-only case, whereas 70% do so in the pebbles-only case. Such increased migration rates for pebble-formed planets have been reported before (e.g. Brügger et al. 2020). Planets in this mass range normally enter the type-II migration regime due to runaway gas accretion, once pebble accretion stops. But since these planets do not end up rapidly accreting gas due to the continuously heated envelope by planetesimal accretion in our simulations, slower type-II migration is never reached. We investigate the (non-)formation of giant planets more closely in Sect. 4. Compared to the planetesimals-only population, we observe more planets approaching 1 M_E outside of 10 AU (dahsed-line boxes) as well as more planets around a few Earth masses in the inner disk regions (solid-line boxes). These planets are increasingly pebble-dominated with larger pebble fractions, as can be seen from the colour mapping in Fig. 1. In the regions where growth via planetesimal accretion is efficient, many planets still end up accreting more of their mass in the form of planetesimals. This is possible since after pebble accretion stops, by reaching the pebble isolation mass, depletion of pebbles, or due to the dispersal of the gas disk, the planets continue to accrete planetesimals.

In the pebbles-only simulations shown in the bottom-right panel, the before mentioned increased inward migration trend persists. Planets that do not accrete a large envelope never grow more massive than about 10 M_E. However, some of the most massive planets can accumulate a large envelope and slow their migration significantly. Several giant planets of roughly one Jupiter mass and more are formed around and inside of 1 AU. This agrees with the previous findings of more frequent giant formation in pebble accretion models (Lambrechts & Johansen 2012; Bitsch et al. 2015). In the outer disk, planets grow more massive with increasing pebble fractions (see dashed-line box) since planetesimal accretion rates are low in this region. Pebbles on the other hand, can also be accreted at large distances once the growth radius moves past the planet. For $f_{peb} = 1$, the number density of planets above 0.1 M_E in the outer region (dashed-line box) is again lower compared to the pebble-rich case because planets tend to migrate inside of 10 AU. The pebble accretion period ends when all the dust is converted to pebbles, ultimately limiting the core masses that can be reached in the pebbles-only scenario.

4. Giant planet formation

It is not surprising that giants can form from pebbles alone (Lambrechts & Johansen 2012) or from small planetesimals alone (NGPPS I). We do not aim to discuss giant formation pathways in those cases in detail again but use them as a reference for the hybrid setups. We focus on the mechanisms preventing giant formation that arise from the interplay of planetesimal and pebble accretion which can be best understood from the formation history on a system level.

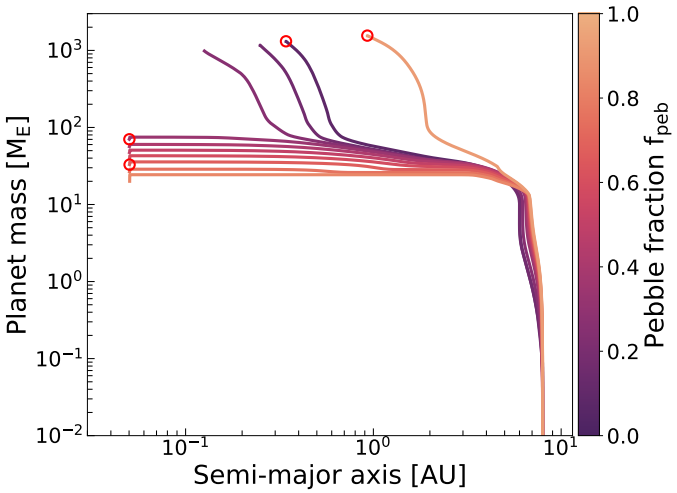

Fig. 2. Formation tracks of a planet during 2 Gyr with pebble fractions f_{peb} from 0 to 1 in increments of 0.1 (colours) using the same disk that gives rise to the encircled planets in Fig. 1. The tracks of the four cases (f_{peb} = 0, 0.3, 0.7, 1) shown in Fig. 1 are again marked by a red circle.

The formation of an envelope due to the accretion of gas is strongly coupled to the accretion of solids. On one hand, the increase of the core mass of a planet positively affects the onset of gas accretion. On the other hand, the liberated gravitational energy of the impacting solids heats the envelope, increasing the pressure, which is counteracting the pull of the planet on the surrounding gas. In addition, the different solid accretion rates due to pebbles or planetesimals strongly impact the migration behaviour of the planet.

Figure 2 shows an example where a giant planet is formed in the strongly planetesimal-dominated cases with f_{peb} = 0, 0.1, and 0.2. As seen before, a giant planet can also form in the pebbles-only simulation (f_{peb} = 1). In all other cases shown in pebble fraction increments of 0.1, no giant planet is formed. The formation paths of the encircled planets in Fig. 1, corresponding to f_{peb} = 0, 0.3, 0.7, 1, are again highlighted with a red circle at the planet mass and location at 2 Gyr. This disk is ideal in order to dissect the differences causing the strongly contrasting formation outcomes for different values of f_{peb}. We note, however, that the effects observed here are general since a similar pattern is observed in other systems that form giant planets in the pebbles-only case but fail to produce giants when a fraction of the solids is in the planetesimals. We hence consider it a representative example when it comes to giant (non-)formation in our simulations. The initial conditions of this particularly giant planet favouring disk are shown in Table 2. Listed are the total solid-to-gas ratio Z_{tot}, the gas surface density at 5.2 AU Σ_0, the inner and characteristic disk radii R_{in} and R_{char}, the external photo-evaporation parameter $\dot{M}_{wind}$, and the initial position of the embryo a_{init}.

After an initial phase of inward migration from its starting location at almost 8 AU, the planet can migrate outwards slightly before significantly migrating inwards in all simulations. The planetesimals-only planet (darkest line) grows massive enough to trigger runaway gas accretion, carving a gap in the gas disk and subsequently migrating slower in the type-II migration regime. The same happens in the 10% and 20% pebble fraction cases but the inward migration is stronger, causing the runaway gas

Table 2. Specific initial parameters of the system of interest in Sect. 4.

System specific parameters	Values
$Z_{\rm tot}$	0.012
Σ_0	237 g cm^{-2}
$R_{\rm in}$	0.049 AU
$R_{\rm char}$	120.8 AU
$\dot{M}_{\rm wind}$	9.1921×10^{-6} $M_{\rm sol}$ yr^{-1}
$a_{\rm init}$	7.97 AU

accretion to happen when the planet is already closer in. This is explained by the increased early core growth rate due to the accretion of pebbles. The outcome is a planet that ends up on a closer in orbit the higher the pebble fraction is. The pebbles-only planet (brightest line), on the other hand, grows so fast that it reaches a higher core mass more quickly, entering type-II migration earlier and on a wider orbit. At 2 Gyr, the mass of the formed giant lies between 3 and 4.9 $M_{\rm J}$ and orbits between 0.15 and 0.9 AU. In all the other simulations with pebbles and planetesimals in the disk, the planet migrates all the way to the inner disk edge at about 0.05 AU and has a mass between 23 and 70 $M_{\rm E}$. Note that they lose a small amount of envelope mass over time due to photo-evaporation close to the star.

It is apparent from the tracks shown in Fig. 2 that even when only a small fraction of the mass is in the planetesimals, the formation of giant planets is suppressed. We find that, in this particular disk, a pebble-dominated giant planet can only form when the fraction of planetesimals is below 2%, that is for $f_{\rm peb} > 0.98$. We further note that, as mentioned already in Sect. 3, the increase of the amount of pebbles with respect to planetesimals does not lead to a higher final mass of the planet. Rather, it leads to smaller final planetary masses in the case of these large planets that almost grow to giant planets.

The formation pathway of the same system is again presented in Fig. 3 in terms of core and envelope mass, core accretion rate, and semi-major axis as a function of time. For the sake of clarity, we only show the simulations using the pebble fraction values $f_{\rm peb} = 0$, 0.3, 0.7, and 1. In all cases, the growth radius $r_{\rm g}$ has not yet reached the embryo's location before 10^4 yr. In this early phase, only planetesimal accretion is possible and the total core accretion rate is equal to the planetesimal accretion rate (the dashed and solid lines in the middle panel overlap). Since the planetesimals are in an equilibrium state with respect to self-stirring at the initialisation of the simulation, the accretion rates can be moderate. Within a few 10^4 yr, the embryo starts exciting the planetesimal dynamical state and the planetesimal accretion rate drops as a result. Unsurprisingly, the rates are lower when less planetesimals are present in the disk.

When $r_{\rm g}$ moves outside of the planet orbit, there is an immediate increase in the total core accretion rate due to the onset of pebble accretion. This happens earlier for higher pebble fractions due to the $Z_{\rm dust}^{2/3}$ dependence of the growth radius. As a result, planet cores are formed earlier the larger the pebble fraction is. The pebble accretion rate is higher for larger values of $f_{\rm peb}$. In disks containing more than 70% pebbles, pebble accretion is always more dominant than planetesimal accretion for planets below the pebble isolation mass. In the pebble-poor case ($f_{\rm peb} = 0.3$), the large amount of planetesimals allows for planetesimal accretion rates to become comparable to the accretion rate of pebbles once the core grows more massive. Note that the initial spike in the total solid accretion rate at the start of pebble accretion is a numerical effect due to the crossing of the growth radius and the planet location, which has an insignificant effect on the planet formation pathway and final outcome. The additional step-like features in the pebble-rich ($f_{\rm peb} = 0.7$) and pebbles-only ($f_{\rm peb} = 1$) cases are due to changes of the pebble accretion regime according to Sect. 2.6.

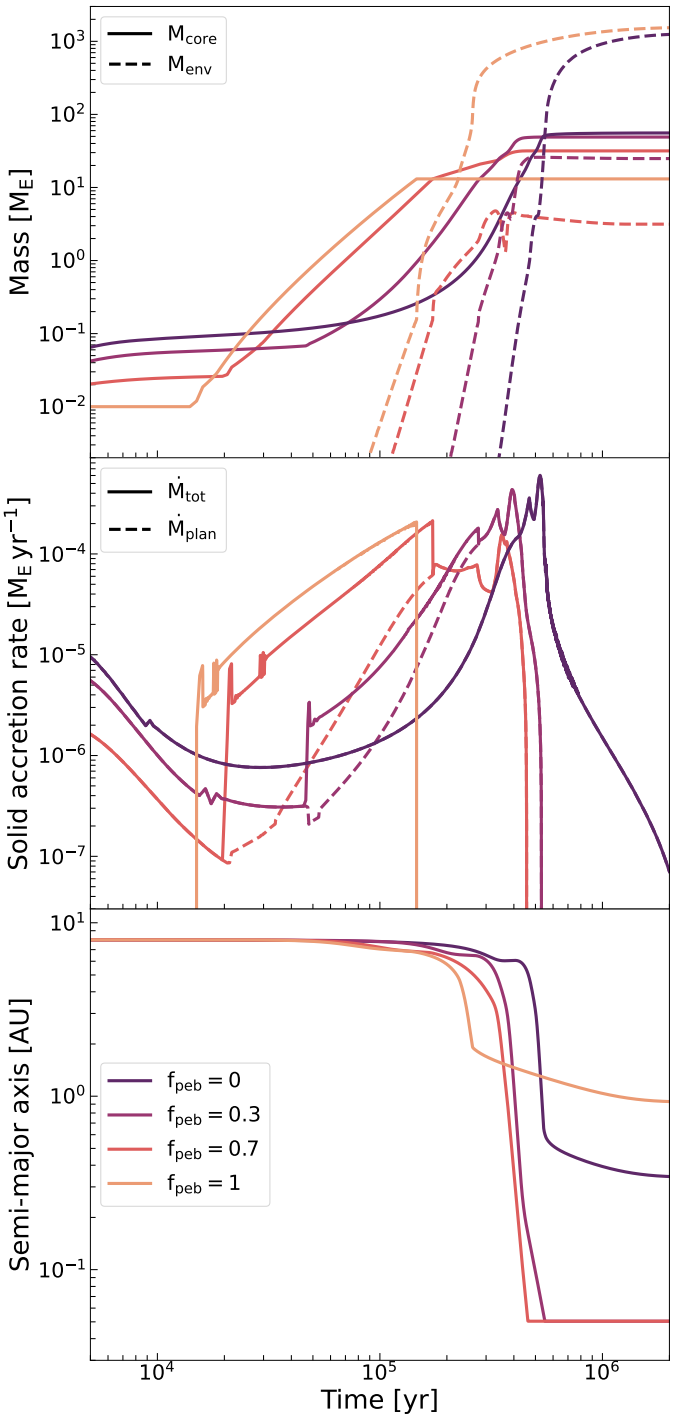

Fig. 3. Time evolution of a planet forming in disks of varying pebble fraction $f_{\rm peb}$ (the four encircled cases in Fig. 2). The top panel shows the core mass (solid lines) and the envelope mass (dashed lines), the middle panel shows the total solid accretion rate (solid lines) and the planetesimal accretion rate for the $f_{\rm peb} = 0.3$ and $f_{\rm peb} = 0.7$ cases (dashed lines). In the bottom panel, the semi-major axis over time is displayed.

The planet stops accreting pebbles between 0.1 and 0.3 Myr depending on the pebble fraction, causing the visible drop in accretion rate (see all lines except the darkest). The value of the pebble isolation mass increases towards greater separations from the star given by Eq. (22). At this point in time, the planet orbits at 7 AU in all simulations that contain pebbles. In this region, $M_{\rm iso}$ is above the 13 $M_{\rm E}$ of the planet in all cases. Hence, the pebble accretion stops because all the dust is converted into pebbles all the way to the outer disk edge. As noted before, the growth radius moves through the disk more rapidly the larger the dust fraction is which results in the pebble accretion phase ending earlier for higher pebble fractions.

After pebble accretion stops, the core can only grow further through planetesimals for the rest of the formation process so the total core accretion rate is again equal to the planetesimal accretion rate. The availability of planetesimals, meaning the value of $f_{\rm peb}$, dictates the core accretion rate. In the $f_{\rm peb} = 1$ case, this means the final core mass is directly limited to the pebble isolation mass or by the mass reached when the pebble flux ceases.

As shown in the top panel of Fig. 3, the planet can already accumulate a small envelope during the pebble accretion phase. When the core accretion rate suddenly drops, the gas accretion rate increases immediately due to the lowered luminosity associated with solid accretion, resulting in a steep increase of the envelope mass. In the $f_{\rm peb} = 1$ case, the planet undergoes runaway accretion of gas as already seen in Fig. 2. In both the hybrid cases, however, the envelope mass never exceeds the core mass and the gas accretion is not sufficient to form a gap which would slow down the inward migration. As a consequence, the planet moves to the inner disk edge in just about 0.2 Myr.

4.1. Delay of runaway gas accretion

The onset of rapid gas accretion is prevented when the planet keeps accreting planetesimals after pebble accretion stops. This suggests that the remaining accretion heating due to planetesimals is responsible for the delay of runaway gas accretion. It begs the question, however, whether this finding is just a result of the small size of the planetesimals chosen. By using large 100 km diameter planetesimals, we test the $f_{\rm peb} = 0.7$ case for lower planetesimal accretion rates and subsequently less envelope heating. The blue lines in Fig. 4 show the equivalent formation pathway in the large planetesimal case as the red lines representing the 600 m simulation. The red lines, shown as a comparison, are identical to the ones in Fig. 3. The general outcome remains the same but the planetesimal accretion rate is reduced by about an order of magnitude. Albeit lower, the heating is still sufficient to prevent runaway gas accretion as the envelope mass does not exceed the core mass and the planet still migrates inwards all the way through the disk. This is compatible with the minimum core accretion rate to prevent runaway gas accretion of roughly 10^{-5}–10^{-6} $M_{\rm E}{\rm yr}^{-1}$ predicted in Alibert et al. (2018).

The green line in Fig. 4 shows the exact same setup but the accretion of planetesimals is disabled. Disregarding the low planetesimal accretion rates early on, these planets follow the same formation path up to the end of pebble accretion as in the blue case, even though there are less available solids in the disk. After pebble accretion stops, the core mass is fixed and no further heating due to the accretion of solids can occur. The planet enters the runaway gas accretion regime shortly after since the envelope cools rapidly in the absence of solid accretion. As before in the planetesimals-only and pebbles-only cases, the planet migrates more slowly in the type-II regime allowing them to halt outside the inner disk edge. Instead of moving all the way inside, as with ongoing planetesimal accretion, a 4.5 $M_{\rm J}$ planet is formed at 0.75 AU.

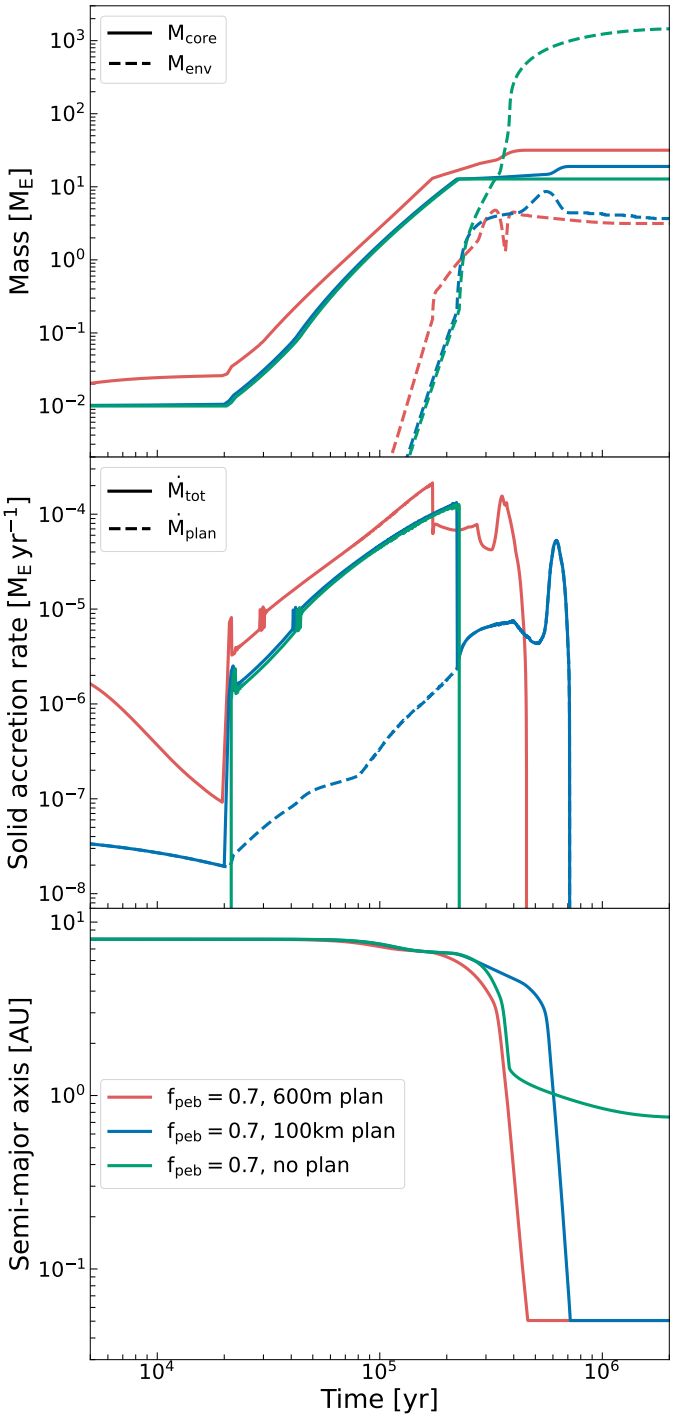

Fig. 4. Time evolution of a planet forming in a $f_{\rm peb}$ = 0.7 disk with 100 km planetesimals (blue) and disabled planetesimal accretion (green). The nominal $f_{\rm peb}$ = 0.7 case using 600 m planetesimals (red) is again shown for comparison. The top panel shows the core mass (solid lines) and the envelope mass (dashed lines), the middle panel shows the total core accretion rate (solid lines) and the planetesimal accretion rate (dashed line). In the bottom panel, the semi-major axis over time is displayed.

Since the remaining accretion of planetesimals after pebble accretion stops is the only difference between the green

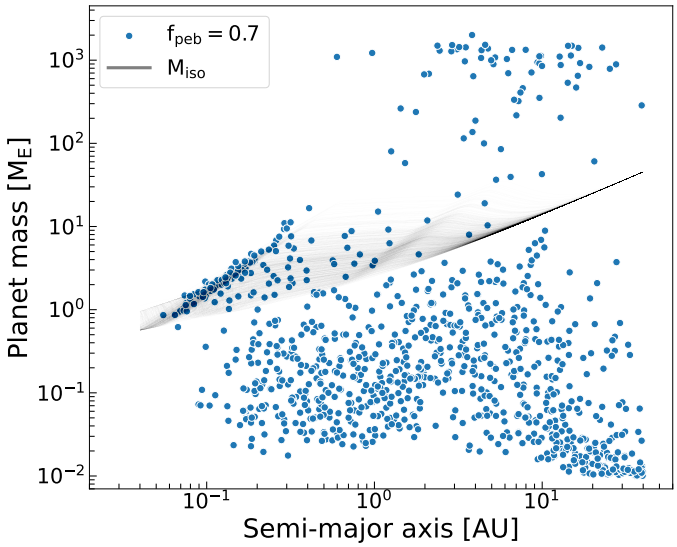

Fig. 5. Planet mass over semi-major axis diagram of the in situ population for $f_{\rm peb} = 0.7$. The opaque black lines are the radial pebble isolation mass profiles of all disks at 10^5 yr.

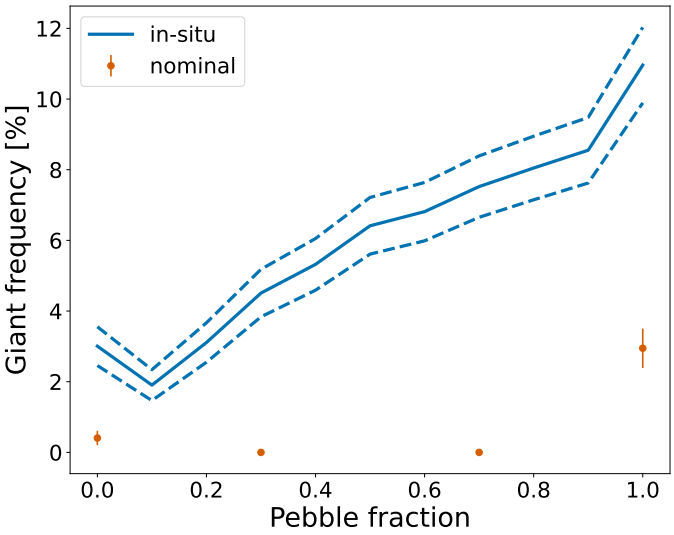

Fig. 6. Frequency of giants formed in the single-planet in situ simulations depending on the fraction of pebbles are shown in blue. For comparison, the giant planet frequencies obtained from the nominal populations in Fig. 1 are shown in orange.

and blue curves, we identify the associated heating as a crucial mechanism that is preventing giant formation in hybrid pebble-planetesimal disks in our model. This has, however, also consequences on the migration of planets. We study the role of migration on giant formation in the following section.

4.2. Inward migration

Since, after pebble accretion stops, the core keeps growing through planetesimal accretion and gas accretion is slowed but not halted entirely, the onset of runaway gas accretion is delayed and not necessarily impossible. The reason why giant formation is prevented altogether in our simulations, is because massive planets that are just about to cross the gas runaway threshold migrate to the inner disk edge within a few 10^5 yr (see bottom panels in Figs. 3 and 4) before they can accrete gas rapidly and carve a gap. We contrast the nominal $f_{\rm peb} = 0.7$ population shown in Fig. 1 with the same population without migration to underline this. While the in situ formation of planets is unlikely, it can give a good impression of the impact migration has. As shown in Fig. 5, there is an abundance of giant planets formed from 1 AU all the way to 40 AU in the $f_{\rm peb} = 0.7$ case without migration. Note that in the inner disk, the pebble isolation mass is too low to allow runaway gas accretion. As a consequence, there is an over-density of planets following the $(H/r)^3$ slope of the isolation mass prescription. These planets correspond to the pebble-dominated planets in the inner disk which exist in every simulation with pebbles shown in Fig. 1 but when also considering migration, the pebble isolation mass slope is washed out in the mass over semi-axis diagram. Since the disk aspect ratios vary and evolve over time, the pebble isolation mass is different for all disks. The opaque black lines in Fig. 5 are the pebble isolation masses as a function of distance for all disks at 10^5 yr. They give an intuition for the value of the pebble isolation mass in the different disk regions at the time when inner planets typically approach this mass range.

In Fig. 6, the frequency of giants forming in situ in increasingly pebble-dominated disks is shown in pebble fraction increments of 0.1 assuming Poisson distributed values for the uncertainty band (blue lines). The giant planet occurrence rate is obtained from in situ populations of 10^3 systems per value of $f_{\rm peb}$ after 2 Gyr. We consider planets to be giants here if the envelope mass exceeds the core mass. There is a general trend of increasing number of giants formed with larger pebble fractions. The frequency increases from 2% to 3% up to about 11% as the disks become more pebble-dominated. This is in clear contrast to the results obtained with migration enabled shown before where, even in the pebbles-only case, the giant planet frequency is below 4% (orange points). The envelope heating effect due to the accretion of planetesimals is easily overpowered when planets, unrealistically, form in situ. We thus identify the delay of runaway gas accretion combined with strong inward migration to be responsible for the observed phenomenon of no giants forming in our nominal simulations of hybrid pebble–planetesimal disks.

4.3. Pebble isolation mass

Another possible influence to giant planet formation comes from the value of the pebble isolation mass. Since this mass sets an upper limit to pebble accretion, it could be too low for significant gas accretion to happen, especially in the inner regions of the disk. As already shown in Fig. 1, giants can form in a pebbles-only setting in the outer disk, where $M_{\rm iso}$ is large, and subsequently migrate closer in. Also in the in situ $f_{\rm peb} = 0.7$ case in Fig. 5, the pebble isolation mass is only reached by planets inside of roughly 0.7 AU. Outside of that, pebble accretion is rather limited by the depletion of pebbles or the disk lifetime. In Fig. 7, the population for $f_{\rm peb} = 0.7$ is shown with a doubled value of the pebble isolation mass. It is qualitatively indistinguishable from the nominal pebble-rich case in the inner disk and identical in the outer disk where planets do not reach pebble isolation anyway. Even an overestimated value of $M_{\rm iso}$ does not assist the formation of giants anywhere in a hybrid pebble–planetesimal disk. Close to the inner edge, where the pebble isolation mass is lowest and a change of $M_{\rm iso}$ shifts planetary masses accordingly (see solid-line box), giant formation is unlikely due to inward migration. For this reason, giant formation models normally focus on initial orbital distances of several

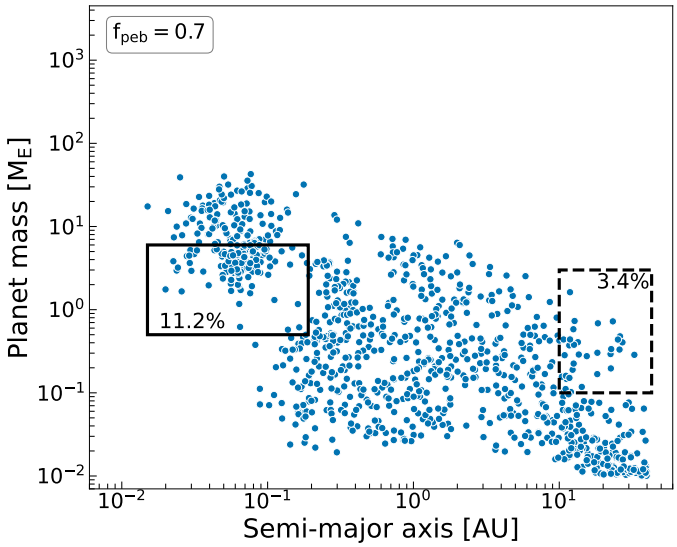

Fig. 7. Planet mass over semi-major axis diagram of the population for $f_{\rm peb} = 0.7$ with a pebble isolation mass that is double the value given in Eq. (22). The solid-line box highlights planet masses of 0.5–6 $M_{\rm E}$ in the inner disk region up to 0.2 AU. The dashed-line box highlights planet masses above 0.1 $M_{\rm E}$ outside of 10 AU. The boxes are labelled with the percentage of planets in these regions.

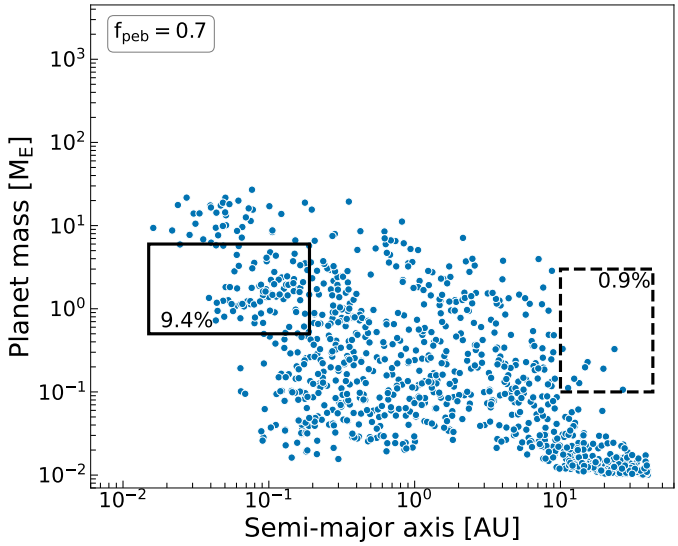

Fig. 8. Planet mass over semi-major axis diagram of the population for $f_{\rm peb} = 0.7$ with a lowered pebble formation efficiency ($\epsilon_{\rm d} = \epsilon_{\rm p} = 0.05$ instead of 0.5). The solid-line box highlights planet masses of 0.5–6 $M_{\rm E}$ in the inner disk region up to 0.2 AU. The dashed-line box highlights planet masses above 0.1 $M_{\rm E}$ outside of 10 AU. The boxes are labelled with the percentage of planets in these regions.

AU where we find the accretion heating of the envelope and inward migration to be the dominant mechanisms at play.

4.4. Pebble flux timing

As mentioned in Sect. 2.5, the pebble growth radius sweeps through the disk within about 1 Myr in this model. There is, however, observational evidence of pebbles in disks that are much older than that which suggests that a flux of pebbles could be present at later times. In Levison et al. (2015), it was shown that a lower pebble flux that is maintained for longer allows for the formation of giant planets. However, these findings were obtained from multi-planet simulations where dynamical interactions remove the smaller embryos, resolving the issue of forming many earth-sized planets and no giants which was found in Kretke & Levison (2014). In our single-planet simulations, this exact interaction cannot be replicated but the pebble flux timing is nevertheless relevant.

We attempt to address the observation of pebbles at later times by arbitrarily reducing the pebble formation efficiency ($\epsilon_{\rm d} = \epsilon_{\rm p} = 0.05$ instead of 0.5, see Sect. 2.5). This results in lower and later pebble fluxes because the pebble growth line moves slower due to the longer pebble growth timescales. The pebble growth radius now reaches the outer disk edge about a factor of 10 times later, extending the presence of pebbles to the order of the gas disk lifetime. In Fig. 8, the $f_{\rm peb} = 0.7$ simulation using the lower pebble formation efficiency is shown. Overall, we find a similar picture to the nominal simulation but with notably less planets that migrate to the inner disk regions (see solid-line box). This is explained by the later onset of pebble accretion and the lower magnitude of the pebble flux due to the lower gas surface densities towards the end of the disk lifetime. This leads to later and slower planet formation. As a consequence, the planet masses are now starting to be limited by the gas disk lifetime in the outer disk (see dashed-line box).

Notably, the late pebble flux in this low efficiency scenario does not resolve the non-formation of giants in the hybrid simulations, even though migration is reduced.

In this model, the lifetime of the pebble flux does not only depend on the pebble formation efficiency but also on the location of the outer disk edge. This is an intrinsic feature of pebble-based planet formation. Since the disk size is a varied quantity in all the presented populations, the pebble flux lifetime is also varied. Within the probed parameter range, even the longest lived pebble fluxes evidently do not result in giant planets in the hybrid scenarios. Nevertheless, disk size is relevant for the formation of giant planets in the pebbles-only case as giant planets only form in disks of sufficient size corresponding to a characteristic radius of at least about 60 AU (see Fig. A.3). This is consistent with the lack of giants formed by pebbles in small disks in Brügger et al. (2020). Unsurprisingly, we also find a positive correlation of higher initial disk masses and the formation of giants (see Fig. A.2).

5. Summary and conclusions

We combine a simple model of pebble formation and accretion with a global model of planet formation considering the accretion of planetesimals. Using a population synthesis approach for single planets, we investigate the effect of hybrid pebble–planetesimal disks on planet formation.

The main results obtained from populations of disks with different pebble fractions can be summarised as follows:

- No giant planets are able to form in hybrid pebble-planetesimal disks, whereas planetesimals alone or pebbles alone form giants;
- Inward migration is more prevalent when more pebbles are available because more planets grow to the point where they are subject to significant type-I migration.

From the closer investigation of giant formation pathways we report the following findings:

- Remaining planetesimal accretion after the pebble accretion phase adds sufficient energy to delay the onset of runaway gas accretion of massive cores in hybrid pebble–planetesimal environments;

– Type-I migration acts strongly on giant planet candidates that do not immediately open a gap in the gas disk;
– The combination of delayed runaway gas accretion and strong inward migration prevents the formation of giant planets in our simulations of hybrid pebble-planetesimal disks.

The simplicity of the pebble model and the use of single-embryo simulations allow us to disentangle the multitude of interdependent mechanisms acting in planet formation at the same time. On the other hand, this also prevents us from making final statements about the outcome of a more true-to-nature description of planet formation from dust all the way to multiple planets. Therefore, the above mentioned results do not imply that giant formation is generally impossible in this setting but they demonstrate the effects arising from the simultaneous accretion of pebbles and planetesimals and how they influence the formation pathway of planets fundamentally. The main conclusion we draw is that, in a combined pebble–planetesimal accretion scenario, planet formation is not necessarily boosted by the avenue of pebble accretion. Specifically for the formation of giant planets, we show that the accretion of pebbles as well as planetesimals can have a hindering effect and that the gap opening and the subsequent shift to the type-II migration regime is necessary for the survival of giant planets. This further underlines the importance of accretion heating for the correct calculation of gas accretion rates and the fact that orbital migration in general is a non-negligible process in planet formation. Note that this is also a consequence of the turbulent viscosity parameter $\alpha = 0.002$ chosen in this work. In disks of lower viscosity, the transport of angular momentum in the disk is less efficient which leads to lower gas driven migration rates and lower gap opening masses. This means that the formation of giant planets might be suppressed less if α is low. Additionally, the prescriptions for orbital migration described in Sect. 2.4 do not include the thermal torque which could allow a higher fraction of planets to stay in the outer disk due to outward migration (Baumann & Bitsch 2020; Guilera et al. 2021).

In their study of the formation of a planetary system considering pebble and planetesimal accretion, apart from not forming any giant planets, Voelkel et al. (2022) find a first generation of pebble-formed terrestrial planets which are accreted by the star due to efficient type-I migration. These hints at a possible detrimental effect of efficient pebble accretion on planet formation are complemented by our results.

Regarding the proposed Jupiter formation scenario in Alibert et al. (2018), our results confirm the plausibility of delayed runaway gas accretion in hybrid disks. However, the notion of a massive planetary core staying at the initial position for multiple millions of years is clearly challenged by this work.

In a more complete model, a number of additional effects are expected to influence the results found in this study. Since pebbles are relatively well coupled to the gas, the structure of the gas disk changes the pebble dynamics strongly. This is especially relevant when progressing from a single-planet scenario to the formation of multi-planetary systems. Planet-gas interactions are important here because massive planets can trap pebbles and effectively shield other growing planets from the pebble flux, leaving them in an accretion environment more akin to the planetesimals-only picture. In Stammler et al. (2023), however, it was recently found that gaps in the disk might not be efficient traps for smaller pebbles and dust. This could still allow pebble accretion inside of massive outer planets. The accumulation of pebbles is also relevant in the context of the N-body interactions between the planets. For example, if a planet moves through a pile-up of pebbles caused by another planet, it can accrete a large amount of pebbles in a short time. The assumption of drift limited pebble formation and evolution is clearly no longer viable under these circumstances. Additionally, the gravitational interactions among multiple planets change the migration behaviour, for instance due to mean motion resonances. As shown in Sect. 4.2, preventing the inward migration of the planet all the way to the inner disk edge can allow massive cores to form giants.

For these reasons, it is impossible to predict the outcome of (giant) planet formation in hybrid pebble–planetesimal disks in multi-planet population syntheses. However, we expect the underlying mechanisms of delayed runaway gas accretion and increased orbital migration to persist.

Acknowledgements. We acknowledge the support from the Swiss National Science Foundation (SNSF) under grant 200020_192038. We would like to thank the anonymous referee for the valuable comments and suggestions that helped us improve the manuscript.

References

Adachi, I., Hayashi, C., & Nakazawa, K. 1976, Progr. Theor. Phys., 56, 1756
Adams, F. C., Lada, C. J., & Shu, F. H. 1988, ApJ, 326, 865
Alexander, R. D., & Armitage, P. J. 2009, ApJ, 704, 989
Alibert, Y., Mordasini, C., Benz, W., & Winisdoerffer, C. 2005, A&A, 434, 343
Alibert, Y., Carron, F., Fortier, A., et al. 2013, A&A, 558, A109
Alibert, Y., Venturini, J., Helled, R., et al. 2018, Nat. Astron., 2, 873
Andrews, S. M., Wilner, D. J., Hughes, A. M., Qi, C., & Dullemond, C. P. 2010, ApJ, 723, 1241
Arimatsu, K., Tsumura, K., Usui, F., et al. 2019, Nat Astron, 3, 301
Ataiee, S., Baruteau, C., Alibert, Y., & Benz, W. 2018, A&A, 615, A110
Baraffe, I., Homeier, D., Allard, F., & Chabrier, G. 2015, A&A, 577, A42
Baumann, T., & Bitsch, B. 2020, A&A, 637, A11
Bell, K. R., & Lin, D. N. C. 1994, ApJ, 427, 987
Birnstiel, T., Dullemond, C. P., & Brauer, F. 2010, A&A, 513, A79
Bitsch, B., & Kley, W. 2010, A&A, 523, A30
Bitsch, B., Lambrechts, M., & Johansen, A. 2015, A&A, 582, A112
Bitsch, B., Morbidelli, A., Johansen, A., et al. 2018, A&A, 612, A30
Bodenheimer, P., & Pollack, J. B. 1986, Icarus, 67, 391
Bodenheimer, P., D'Angelo, G., Lissauer, J. J., Fortney, J. J., & Saumon, D. 2013, ApJ, 770, 120
Bottke, W. F., Durda, D., Nesvorny, D., et al. 2005, Icarus, 175, 111
Brasser, R., & Mojzsis, S. J. 2020, Nat. Astron., 4, 492
Brügger, N., Alibert, Y., Ataiee, S., & Benz, W. 2018, A&A, 619, A174
Brügger, N., Burn, R., Coleman, G., Alibert, Y., & Benz, W. 2020, A&A, 640, A21
Bryden, G., Chen, X., Lin, D. N. C., Nelson, R. P., & Papaloizou, J. C. B. 1999, ApJ, 514, 344
Chambers, J. 2006, Icarus, 180, 496
Chiang, E. I., & Goldreich, P. 1997, ApJ, 490, 368
Coleman, G. A. L., & Nelson, R. P. 2014, MNRAS, 445, 479
Crida, A., Morbidelli, A., & Masset, F. 2006, Icarus, 181, 587
Dittkrist, K.-M., Mordasini, C., Klahr, H., Alibert, Y., & Henning, T. 2014, A&A, 567, A121
Drążkowska, J., & Alibert, Y. 2017, A&A, 608, A92
Eistrup, C., & Henning, T. 2022, A&A, 667, A160
Emsenhuber, A., Mordasini, C., Burn, R., et al. 2021a, A&A, 656, A69
Emsenhuber, A., Mordasini, C., Burn, R., et al. 2021b, A&A, 656, A70
Fendyke, S. M., & Nelson, R. P. 2014, MNRAS, 437, 96
Fortier, A., Alibert, Y., Carron, F., Benz, W., & Dittkrist, K.-M. 2013, A&A, 549, A44
Freedman, R. S., Lustig-Yaeger, J., Fortney, J. J., et al. 2014, ApJS, 214, 25
Friedrich, J. M., Weisberg, M. K., Ebel, D. S., et al. 2015, Chem. Erde Geochem., 75, 419
Goldreich, P., & Tremaine, S. 1979, ApJ, 233, 857
Guilera, O. M., Brunini, A., & Benvenuto, O. G. 2010, A&A, 521, A50
Guilera, O. M., Miller Bertolami, M. M., Masset, F., et al. 2021, MNRAS, 507, 3638
Haisch, Jr., K. E., Lada, E. A., & Lada, C. J. 2001, ApJ, 553, L153
Hueso, R., & Guillot, T. 2005, A&A, 442, 703
Ida, S., & Guillot, T. 2016, A&A, 596, A3
Inaba, S., & Ikoma, M. 2003, A&A, 410, 711

Inaba, S., Tanaka, H., Nakazawa, K., Wetherill, G. W., & Kokubo, E. 2001, Icarus, 149, 235
Izidoro, A., Dasgupta, R., Raymond, S. N., et al. 2021, Nat. Astron., 6, 357
Johansen, A., & Lambrechts, M. 2017, Annu. Rev. Earth Planet. Sci., 45, 359
Kippenhahn, R., & Weigert, A. 1990, Stellar Structure and Evolution (Springer)
Korycansky, D. G., & Pollack, J. B. 1993, Icarus, 102, 150
Kretke, K. A., & Levison, H. F. 2014, AJ, 148, 109
Kruijer, T. S., Burkhardt, C., Budde, G., & Kleine, T. 2017, PNAS, 114, 6712
Lambrechts, M., & Johansen, A. 2012, A&A, 544, A32
Lambrechts, M., & Johansen, A. 2014, A&A, 572, A107
Lenz, C. T., Klahr, H., & Birnstiel, T. 2019, ApJ, 874, 36
Levison, H. F., Kretke, K. A., & Duncan, M. J. 2015, Nature, 524, 322
Lichtenberg, T., Drazkowska, J., Schönbächler, M., Golabek, G. J., & Hands, T. O. 2021, Science, 371, 365
Lin, D. N. C., & Papaloizou, J. 1986, ApJ, 309, 846
Lubow, S. H., Seibert, M., & Artymowicz, P. 1999, ApJ, 526, 1001
Lust, R. 1952, Z. Naturf. A, 7, 87
Lynden-Bell, D., & Pringle, J. E. 1974, MNRAS, 168, 603
Morbidelli, A., Bottke, W. F., Nesvorný, D., & Levison, H. F. 2009, Icarus, 204, 558
Morbidelli, A., Lambrechts, M., Jacobson, S., & Bitsch, B. 2015, Icarus, 258, 418
Morbidelli, A., Baillie, K., Batygin, K., et al. 2021, Nat. Astron., 6, 72
Mordasini, C., Alibert, Y., Georgy, C., et al. 2012a, A&A, 547, A112
Mordasini, C., Alibert, Y., Klahr, H., & Henning, T. 2012b, A&A, 547, A111
Mordasini, C., Klahr, H., Alibert, Y., Miller, N., & Henning, T. 2014, A&A, 566, A141
Movshovitz, N., & Podolak, M. 2008, Icarus, 194, 368
Movshovitz, N., Bodenheimer, P., Podolak, M., & Lissauer, J. J. 2010, Icarus, 209, 616
Nakamoto, T., & Nakagawa, Y. 1994, ApJ, 421, 640
Ohtsuki, K., Stewart, G. R., & Ida, S. 2002, Icarus, 155, 436
Ormel, C. W., & Klahr, H. H. 2010, A&A, 520, A43
Paardekooper, S.-J., & Mellema, G. 2006, A&A, 453, 1129
Paardekooper, S. J., Baruteau, C., & Kley, W. 2011, MNRAS, 410, 293
Podolak, M., Pollack, J. B., & Reynolds, R. T. 1988, Icarus, 73, 163
Pollack, J. B., Hubickyj, O., Bodenheimer, P., et al. 1996, Icarus, 124, 62
Pringle, J. E. 1981, ARA&A, 19, 137
Rafikov, R. R. 2004, AJ, 128, 1348
Ruden, S. P., & Pollack, J. B. 1991, ApJ, 375, 740
Santos, N. C., Israelian, G., Mayor, M., et al. 2005, A&A, 437, 1127
Saumon, D., Chabrier, G., & van Horn, H. M. 1995, ApJ, 99, 713
Savvidou, S., Bitsch, B., & Lambrechts, M. 2020, A&A, 640, A63
Schäfer, U., Yang, C.-C., & Johansen, A. 2017, A&A, 597, A69
Schlichting, H. E., Fuentes, C. I., & Trilling, D. E. 2013, AJ, 146, 36
Shakura, N. I., & Sunyaev, R. A. 1973, Symp. Int. Astron. Union, 55, 155
Shibaike, Y., & Alibert, Y. 2020, A&A, 644, A81
Shibaike, Y., Ormel, C. W., Ida, S., Okuzumi, S., & Sasaki, T. 2019, ApJ, 885, 79
Stammler, S. M., Lichtenberg, T., Drążkowska, J., & Birnstiel, T. 2023, A&A, 670, L5
Tanaka, H., Takeuchi, T., & Ward, W. R. 2002, ApJ, 565, 1257
Tychoniec, Ł., Tobin, J. J., Karska, A., et al. 2018, ApJS, 238, 19
Venturini, J., & Helled, R. 2020, A&A, 634, A31
Venuti, L., Bouvier, J., Cody, A. M., et al. 2017, A&A, 599, A23
Voelkel, O., Klahr, H., Mordasini, C., Emsenhuber, A., & Lenz, C. 2020, A&A, 642, A75
Voelkel, O., Deienno, R., Kretke, K., & Klahr, H. 2021, A&A, 645, A131
Voelkel, O., Klahr, H., Mordasini, C., & Emsenhuber, A. 2022, A&A, 666, A90
Ward, W. R. 1997, ApJ, 482, L211
Weidenschilling, S. J. 1977, MNRAS, 180, 57
Youdin, A. N., & Lithwick, Y. 2007, Icarus, 192, 588

Appendix A: Initial disk properties

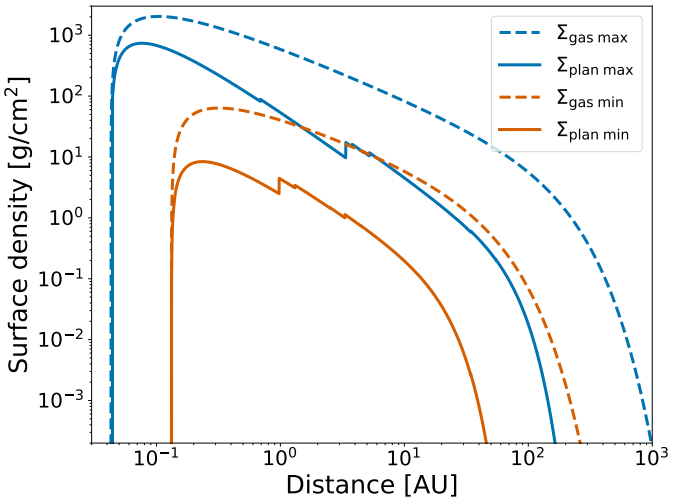

Fig. A.1. Initial radial gas (dashed) and planetesimal (solid) surface density profiles. The blue (orange) lines correspond to the system with the most (least) massive planetesimal disk.

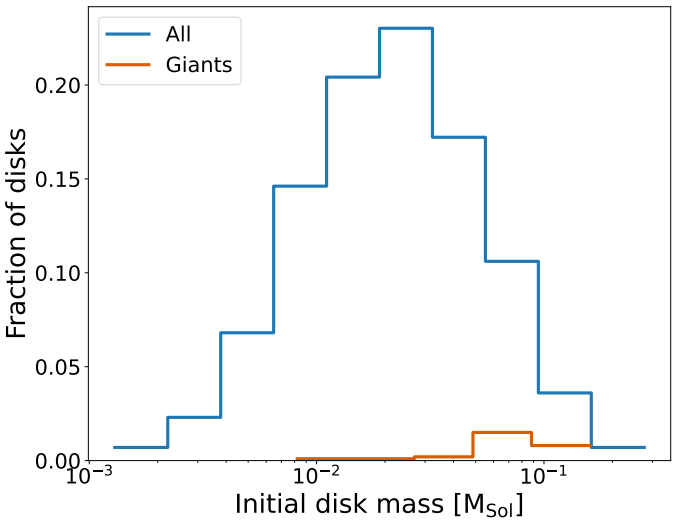

Fig. A.2. Fraction of disks of a given initial gas disk mass. The full set of 1000 disks is shown in blue and the orange line shows the disks that form a giant planet in the f_{peb} = 1 simulations.

The initial radial gas and planetesimal surface density profiles are shown in Fig. A.1. We show the most (blue) and least (orange) massive planetesimal disks. The planetesimal disk mass is a function of the gas disk mass, the size of the gas disk, and the solids-to-gas ratio. Hence, the disks shown here are not necessarily also the most or least massive gas disks.
The distribution of initial gas disk masses is shown in Fig. A.2 (blue). Note that the total number of disks considered in this work is 1000 and that the stellar mass is fixed to one solar mass. We find a positive correlation of high initial disk masses and the formation of giants in the pebbles-only scenario (orange).
As described in Sect. 3, the characteristic gas disk radius is a derived quantity. The resulting distribution of characteristic gas disk sizes is shown in Fig. A.3 (blue). We find no clear correlation of initial disk sizes, and the associated longer pebble flux lifetimes, with the formation of giant planets in the f_{peb} = 1 simulations (orange). However, giant planets only form in disks of sufficient size corresponding to a characteristic radius of at least about 60 AU.

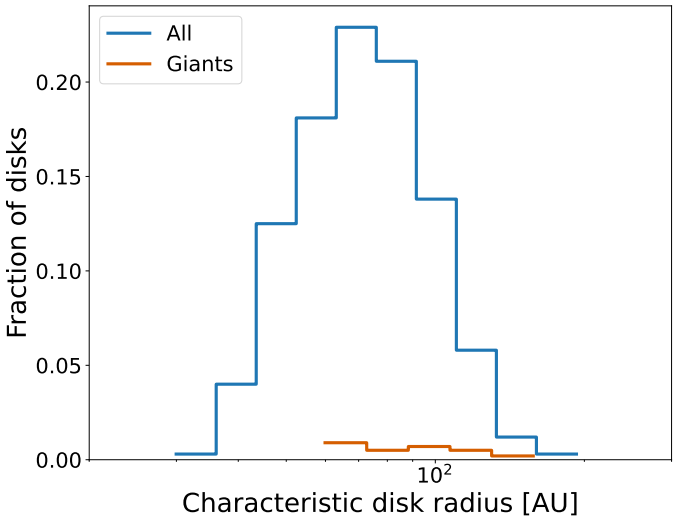

Fig. A.3. Fraction of disks of a given initial characteristic radius.The full set of 1000 disks is shown in blue and the orange line shows the disks that form a giant planet in the f_{peb} = 1 simulations.

5 Paper II

Unlike Jupiter and Saturn, Uranus has been explored only once during the Voyager 2 flyby, leaving substantial gaps in our knowledge about its interior structure, atmospheric composition, and dynamic processes. Acknowledging these gaps in our knowledge of Uranus and ice giants as a whole, the Decadal Survey 2023 has designated Uranus as the highest priority for NASA's next flagship mission. In light of this future mission, formation models are crucial in order to inform instrumentation design choices. This motivated a project to study the formation of Uranus with the hope of providing basic predictions on the bulk elemental abundances of Uranus. The fundamental idea is that, since planetesimal accretion is a quasi-local accretion process and pebble accretion depends on the material supply from the whole outer disk, there might be compositional signatures which could allow us to exclude certain formation scenarios for Uranus once new measurements come in. At the same time, this could provide valuable insights on the most important species to look for with an in-situ probe and inform us about the required precision to do so.
However, after a significant modelling effort, it became clear that the formation of Uranus/Neptune-like ice giants is very challenging – to the point their existence alone is puzzling. This shifted the focus of the study away from tracking composition, a seemingly futile task given the lack of ice giants produced in our simulations, towards a deeper exploration of possible formation scenarios. We deemed this necessary in order to assess the state of current formation theory in the context of ice giant formation. This is something a global model framework is well suited for and by performing population synthesis, a wide range of realistic initial parameters can be explored.

Astronomy & Astrophysics manuscript no. output
December 28, 2024

Formation challenges of Uranus/Neptune-like planets

A. Kessler, Y. Alibert, and A. Vorburger

Space Research & Planetary Sciences, University of Bern, Gesellschaftsstrasse 6, 3012 Bern, Switzerland
e-mail: andrin.kessler@unibe.ch

December 23, 2024

ABSTRACT

Context. The formation of the Solar System ice giants, and of ice giants in general, is a difficult problem of planet formation theory due to their large separation to the host star. Typically, the formation of Uranus and Neptune is studied in isolated in-situ setups or as part of dynamical simulations focusing on the Solar System architecture. At the same time, our knowledge of ice giants remains limited, as neither Neptune nor Uranus have been investigated up close.
Aims. In light of a future mission dedicated to investigating Uranus which would provide measurements that could offer valuable constraints, we assess whether current formation theory is able to provide viable formation pathways of ice giants similar to Uranus and Neptune from a global formation perspective.
Methods. We look for Uranus/Neptune-like planets in planetary populations simulated in a global planet formation and evolution model using expected initial conditions for disks around Solar-mass stars. In particular, we study migrating and non-migrating setups of single and multi-planetary systems in planetesimal and pebble accretion scenarios.
Results. We find that the ice giant parameter space is particularly difficult to populate in scenarios that include planetary migration. In migrating scenarios, single isolated ice giants are never seen while multi-planetary setups can rarely yield planets above 10 $M_{\rm E}$ outside of 10 au. Additionally, the mass and H-He mass fraction constraints for Uranus and Neptune generally require large envelope opacities in pebble accretion scenarios but low envelope opacities in planetesimal accretion scenarios.
Conclusions. We conclude that current formation theory does not support the direct formation of Uranus or Neptune analogues in unstructured disks and does not readily provide the initial conditions of dynamical formation simulations of the Solar System. We conclude that multiple concurrently forming planets need to be considered in order to study the formation of ice giants.

Key words. planets and satellites: formation – protoplanetary disks

1. Introduction

The Solar System planets are, obviously, by far the best characterised known planets, providing an excellent benchmark for our understanding of planet formation. While a single planetary system does not allow for statistical validation of planet formation theories, the well known, most fundamental properties of the Solar System planets such as their mass, radius, and orbital distance, must be reproducible by any good theory of planet formation. Therefore, the study of the formation of the Solar System remains an important test of our knowledge. However, our understanding of the outermost planets in the Solar System, the ice giants Uranus and Neptune, remains limited. Especially the interior structure and bulk composition, which are key to providing crucial constraints on the planet's formation and evolution, are uncertain. Unlike Jupiter and Saturn, Uranus has been explored only once during the Voyager 2 flyby, leaving substantial gaps in our knowledge about its interior structure, atmospheric composition, and dynamic processes. Acknowledging these gaps in our knowledge of Uranus and ice giants as a whole, the Decadal Survey 2023 has designated Uranus as the highest priority for NASA's next flagship mission.

A Uranus probe equipped with advanced instrumentation for atmospheric and interior measurements would provide the much-needed data to deepen our understanding of Uranus. It could provide a comprehensive set of measurements of atmospheric elemental abundances, particularly noble gases and their isotopic ratios which are essential because these elements are minimally affected by chemical and dynamic processes, preserving their original states. In addition, the abundances of volatiles like water (H_2O), methane (CH_4), ammonia (NH_3), and hydrogen sulphide (H_2S) can provide critical insights into the bulk composition of the planet. Disequilibrium species such as carbon monoxide (CO), phosphine (PH_3), and ethane (C_2H_6) in the upper troposphere can reveal vertical mixing and atmospheric dynamics, while the ortho-to-para hydrogen ratio offers further information on atmospheric thermal and mixing processes.
Understanding Uranus's interior structure is a critical but challenging task, as most of the planet's mass lies beyond the reach of remote sensing or atmospheric probes. Microwave sensing, as demonstrated by the Juno mission at Jupiter, can only probe a fraction of the planet's interior, while a traditional entry probe would barely scratch Uranus's outer layers. Overcoming these limitations, high-precision gravity field measurements and tidal dissipation analyses could reveal whether Uranus has a fuzzy core, distinct layering, or compositional gradients, and provide clues to its unusually low heat flux, which suggests inhibited convection in the deep interior due to compositional stratification.
Assessing Uranus's tidal dissipation, including how its gravitational field interacts with its moons, would further illuminate its thermal state, internal mixing, and the evolution of its satellite system. These observations might also uncover evidence of a grazing giant impact, which could explain Uranus's extreme

axial tilt, low luminosity, and unique dynamical characteristics. To complement gravity and tidal measurements, it is also necessary to determine the thermal conductivity of interior materials and the likelihood of internal layering or stable regions. These factors influence how Uranus retains and emits heat, a critical aspect for understanding the planet's energy balance and evolution.

This wealth of possible new information about Uranus offers a unique opportunity to study planetary formation and evolution under conditions distinct from the gas giants. While a dedicated Uranus probe is crucial for advancing our understanding of this enigmatic ice giant, the measurements can only be fully leveraged to understand its role in the formation and evolution of the Solar System if planet formation models are able to provide predictions to compare against. This is crucial in order to, for instance, constrain where in the protosolar nebula Uranus formed.

However, the formation of the Solar System ice giants, Uranus and Neptune, remains a difficult problem since they are located in the outer Solar System at 19.1 and 30 au, respectively. In the core accretion paradigm of planet formation, formation timescales are longer at large orbital separations. With masses of 14.5 and 17.1 $M_{\rm E}$, conceiving formation pathways leading to their current position is challenging as formation timescales can become longer than the expected lifetime of the protoplanetary disk (Safronov 1972).

An additional challenge of the formation of Uranus and Neptune is the fact that planetary cores that become massive enough while still embedded in a gaseous disk, start to accrete vast amounts of gas rapidly, quickly resulting in gas-dominated giant planets akin to Jupiter and Saturn (Pollack et al. 1996; Helled & Bodenheimer 2014). Current Interior structure models constrain the mass of Hydrogen and Helium (H-He) in the envelopes of Uranus and Neptune to 1.25 - 3.53 $M_{\rm E}$ and 1.64 - 4.15 $M_{\rm E}$, respectively (Helled et al. 2011; Nettelmann et al. 2013). This corresponds to H-He mass fractions with respect to the total planetary mass of roughly 8-25% for both Uranus and Neptune. In Lambrechts et al. (2014), the authors suggest an ice giant formation scenario where the energy released due to continued accretion of solids prevents runaway gas accretion. However, the stability of the envelope depends on it's ability to radiate away the heat, which is governed by the opacity. Since molecular opacities are lower in colder environments, ice giant envelopes are either sufficiently opaque due to suspended grains or the runaway gas accretion is cut off by the dispersal of the gas disk (or both). The vaporisation and ablation of accreted solids in the envelope have been shown to lead to elevated envelope opacities, depending on the accreted material, its size, the rate of accretion, and the grain dynamics in the envelope (Brouwers et al. 2021).

While the in-situ formation of Uranus and Neptune is challenging, considering the accretion of planetesimals (Safronov 1972), it has been demonstrated that they could be formed in-situ in sufficiently massive disks from very small planetesimals (Goldreich et al. 2004) or from pebble accretion (Lambrechts et al. 2014; Valletta & Helled 2022). From a theoretical perspective however, prescribed in-situ formation is at odds with the current understanding of disk-planet interactions which lead to (generally inwards) planetary migration (e.g. Paardekooper et al. 2011; Dittkrist et al. 2014; Coleman & Nelson 2014; Jiménez & Masset 2017).

The formation of Uranus and Neptune at shorter orbital distances is an interesting prospect as it could alleviate the formation timescale problem. It has been shown in dynamical simulations that it is possible to reproduce the architecture of the Solar System when Uranus and Neptune are formed inside their current orbits (Tsiganis et al. 2005; Liu et al. 2022). In these scenarios, the planetary masses are fixed and the innermost ice giant is always initially located outside of at least 10 au. In the context of these models, in order to explain the Solar System ice giants, planet formation simulations have to provide formation pathways leading to > 10 $M_{\rm E}$ planets outside of at least 10 au.

In this work, we investigate whether current formation theory is able to provide viable formation pathways of ice giants similar to Uranus and Neptune using the "Bern Model" (Emsenhuber et al. 2021a). It is a global planet formation and evolution model considering a large number of physical processes, the most important of which are outlined in Sect. 2. A global model combining the most important ingredients for ice giant formation – such as the protoplanetary disk evolution, planetary accretion processes, orbital migration, and mutual gravitational interactions of the growing planets – is a powerful tool in order to scan for viable formation pathways and estimate their likelihood in a given scenario. It allows us to couple, according to current understanding, realistic initial disk conditions with the formation outcomes and to compare these with the Solar System ice giants. Complementary to previous studies, this approach offers a bigger picture of the problem of Uranus and Neptune formation.

Since there are currently no extra-solar ice giants known due to their large distance to their host star and comparably small mass, it is not clear how frequent ice giants are and, equivalently, how readily they should form in planet formation simulations. The goal of this work is to assess whether ice giants can or cannot form at all in a given setup and to identify if important physics are still missing in order to understand the formation of these planets in our own Solar System. In light of a future mission potentially providing detailed atmospheric measurements and a characterisation of the interior of Uranus, this question must be addressed in a timely manner.

We employ the following methodology: we simulate different planetary populations using expected initial conditions of unstructured disks around Solar mass stars. We study migrating and in-situ setups of single and multiple planets per disk in both planetesimal and pebble accretion scenarios. Due to their high degree of uncertainty, we consider different envelope opacities. We look for planets that satisfy the conservative requirements of a mass between 10 - 20 $M_{\rm E}$ and a semi-major axis larger than 10 au. We consider such planets that also have a H-He fraction below 25% ice giant candidates.

This work is structured as follows: in Sect. 2, we describe the most important parts of the model. In Sect. 3 we revisit the in-situ formation scenario. In Sect. 4, we present results of simulations of single planets as well as multiple planets per disk including migration. We discuss various aspects of the consequences of migration for the formation outcome in the ice giant parameter space. We discuss model choices and shortcomings, as well as implications of the study in Sect. 5.

2. Model

For this study, we use the Bern model of planetary formation and evolution (Emsenhuber et al. 2021a). It models the formation of planets in a protoplanetary disk, considering a large number of

physical processes such as the viscous evolution of the gas disk, internal and external photo-evaporation of the disk, the accretion of solids and gas by planetary embryos, the gravitational interactions between the growing planets, as well as orbital migration due to the interaction with the gas. The core accretion of planetary embryos is modelled by either planetesimal or pebble accretion. Here, we give a very short overview of the most important model parts for this study and refer to Emsenhuber et al. (2021a) for a much more detailed description.

2.1. Gas disk model

We solve the 1D radially symmetric viscous diffusion equation (Lüst 1952; Lynden-Bell & Pringle 1974)

$$\frac{\partial \Sigma_{\rm gas}}{\partial t} = \frac{1}{r}\frac{\partial}{\partial r}\left[3r^{1/2}\frac{\partial}{\partial r}\left(r^{1/2}\nu\Sigma_{\rm gas}\right)\right] - \dot{\Sigma}_{\rm gas,ph} - \dot{\Sigma}_{\rm gas,pl} \tag{1}$$

to compute the time evolution of the protoplanetary gas disk surface density $\Sigma_{\rm gas}$ at an orbital distance r. The viscosity is given by $\nu = \alpha c_s H$ (Shakura & Sunyaev 1973), where the vertical pressure scale height $H = c_s/\Omega_K$ depends on the isothermal sound speed c_s and the Kepler frequency $\Omega_K = \sqrt{GM_\star/r^3}$. G is the gravitational constant and $M_\star$ is the stellar mass. In this work, we set the turbulent viscosity parameter $\alpha = 10^{-3}$. $\dot{\Sigma}_{\rm gas,ph}$ and $\dot{\Sigma}_{\rm gas,pl}$ are the sink terms related to photo-evaporation (Mordasini et al. 2012) and gas accretion by planets, respectively.
The surface density is initialised by (Andrews et al. 2010)

$$\Sigma_{\rm gas}(r) = \Sigma_0 \left(\frac{r}{5.2\text{ au}}\right)^{-0.9} \exp\left[-\left(\frac{r}{R_{\rm char}}\right)^{1.1}\right]\left(1-\sqrt{\frac{R_{\rm in}}{r}}\right). \tag{2}$$

Σ_0 is the initial gas surface density at 5.2 au, $R_{\rm char}$ is the characteristic outer disk radius, and $R_{\rm in}$ is the inner disk truncation radius (see Emsenhuber et al. 2021b).

The disk temperature in the midplane $T_{\rm mid}$ is governed by the viscous heat dissipation rate $\dot{E}_\nu = \frac{9}{4}\Sigma_{\rm gas}\nu\Omega_K^2$ and the direct stellar irradiation temperature $T_{\rm irr}$ (Nakamoto & Nakagawa 1994; Hueso & Guillot 2005)

$$T_{\rm mid}^4 = \frac{1}{2\sigma_{\rm SB}}\left(\frac{3}{8}\kappa_R\Sigma_{\rm gas} + \frac{1}{2\kappa_P\Sigma_{\rm gas}}\right)\dot{E}_\nu + T_{\rm irr}^4, \tag{3}$$

where $\sigma_{\rm SB}$ is the Stefan-Boltzmann constant. κ_R and κ_P are the Rosseland mean and the Planck opacities, respectively (see Emsenhuber et al. 2021a). $T_{\rm irr}$ is given by (Adams et al. 1988; Ruden & Pollack 1991; Chiang & Goldreich 1997; Hueso & Guillot 2005)

$$T_{\rm irr}^4 = T_\star^4\left[\frac{2}{3\pi}\left(\frac{R_\star}{r}\right)^3 + \frac{1}{7}\left(\frac{R_\star}{r}\right)^2\frac{H}{r}\right] + \frac{L_\star}{16\pi r^2\sigma_{\rm SB}}e^{-\tau_{\rm mid}} + T_{\rm c}^4, \tag{4}$$

where $T_\star$ is the stellar temperature, $R_\star$ the stellar radius, $L_\star$ the stellar luminosity, and $\tau_{\rm mid}$ the optical depth through the midplane. $T_{\rm c} = 10\,$K is the background heating due to the surrounding molecular cloud. We consider the stellar evolution using the evolution tracks of Baraffe et al. (2015).

2.2. Gas accretion model

We solve the classical 1D radially symmetric internal structure equations of mass conservation, hydrostatic equilibrium, and energy transport (Bodenheimer & Pollack 1986)

$$\frac{\partial M}{\partial r} = 4\pi r^2\rho, \tag{5}$$

$$\frac{\partial P}{\partial r} = -\frac{GM}{r^2}\rho, \tag{6}$$

$$\frac{\partial T}{\partial r} = \frac{T}{P}\frac{\partial P}{\partial r}\min(\nabla_{\rm ad}, \nabla_{\rm rad}). \tag{7}$$

M is the enclosed mass in a sphere of radius r, P is the pressure, and T is the temperature. We use the equations of state of Saumon et al. (1995) for the density $\rho(P,T)$ and the adiabatic gradient $\nabla_{\rm ad}$. The radiative gradient is given by (Kippenhahn & Weigert 1990)

$$\nabla_{\rm rad} = \frac{3\kappa LP}{64\pi\sigma_{\rm SB}GMT^4}, \tag{8}$$

depending on the luminosity of the planet L and the envelope opacity κ. In our fiducial runs, we use the full interstellar grain opacities of Bell & Lin (1994) reduced by a factor of $f_\kappa = 0.003$, following Mordasini et al. (2014). The reduction factor is a fit to simulations of grain dynamics in protoplanetary atmospheres (Movshovitz & Podolak 2008; Movshovitz et al. 2010). Due to its high degree of uncertainty, we use the envelope opacity reduction factor f_κ as a parameter to explore ice giant formation pathways. We increase the opacity by two orders of magnitude to $f_\kappa = 0.3$ in our high-opacity setups, following Venturini & Helled (2017).

The accretion of gas is calculated by iteratively comparing the total mass until the integrated structure equations reproduce the core mass (Alibert et al. 2005; Emsenhuber et al. 2021b). The core mass is known from the core accretion rates due to either planetesimals or pebbles as described in Sects. 2.3 and 2.4, respectively. The gas mass is then simply given by the difference of the total mass and the core mass.
Gas accretion of low mass planets is limited by the planet's ability to cool given its luminosity. This is crucially affected by envelope opacities. Lower opacities allow for efficient cooling and thus higher gas accretion rates, whereas higher opacities inhibit cooling and lead to lower gas accretion rates. For increasing core masses, more efficient cooling can result in the gas accretion being limited by the supply of gas from the disk. In this disk-limited regime, we adopt the gas accretion rates of Bodenheimer et al. (2013). The onset mass for this runaway gas accretion depends on the gas accretion rate at a given mass, and therefore on the envelope opacity as well.

2.3. Planetesimals

We use the planetesimal accretion model described in Emsenhuber et al. (2021a) which is based on a planetesimal surface density with a dynamical state defined by their root mean square eccentricity and inclination (Fortier et al. 2013). Aerodynamic drag (Adachi et al. 1976; Inaba et al. 2001; Rafikov 2004), dynamical stirring by protoplanets (Guilera et al. 2010), as well as self-stirring (Ohtsuki et al. 2002) drive the evolution of the planetesimal disk. The initial global dust-to-gas ratio Z fixes the initial planetesimal surface density (Emsenhuber et al. 2021a).

The planetesimal accretion rate of a planet of mass M is given by (Chambers 2006)

$$\dot{M}_{\rm plan} = \Omega_K\bar{\Sigma}_{\rm plan}R_H^2 p_{\rm coll}, \tag{9}$$

where $R_H = r\left(\frac{M}{3M_\star}\right)^{1/3}$ is the Hill radius, $\bar{\Sigma}_{\rm plan}$ is the mean planetesimal surface density in the planet's feeding zone, and $p_{\rm coll}$ is the collision probability. The collision probability depends on the dynamical state of the planetesimal disk (Inaba et al. 2001; Chambers 2006) and the capture radius. The capture radius exceeds the core radius if there is a gaseous envelope (Inaba & Ikoma 2003), which enhances the resulting planetesimal accretion rates, especially for small planetesimals, crucially (Podolak et al. 1988; Venturini & Helled 2020). Planetesimal size is the most important parameter influencing the resulting accretion rates and, therefore, the outcome of the planet formation process. Smaller planetesimals are associated with higher accretion rates, because they are more tightly coupled to the gas. From simulations of collapsing pebble clouds, the initial planetesimal size is expected to be on the order of 100 km (Polak & Klahr 2022). In this study, we fix the planetesimal size at a radius of 1 kilometre which leads to optimistic accretion rates. We discuss this choice further in the following sections.

2.4. Pebbles

We also model the accretion of pebble-sized material instead of planetesimals. In this study, we consider these two accretion channels separately.

Dust grains embedded in the gaseous protoplanetary disk grow by coagulation. As these grains increase in size, they decouple from the gas motion and are typically called pebbles. The dimensionless Stokes number St describes the aerodynamic coupling of a particle to the gas flow, where small values imply tightly coupled grains and larger values imply weakly coupled particles. For particles of radius a near the midplane, it can be simplified to (Cuzzi et al. 2001; Birnstiel et al. 2010)

$$\mathrm{St} = \frac{a\rho_s}{\Sigma_{\rm gas}}\frac{\pi}{2}, \tag{10}$$

where ρ_s is the internal density of the dust aggregate. Larger particles settle to the disk midplane more efficiently than smaller grains. The scale height corresponding to a particle population of Stokes number St embedded in a gaseous disk with turbulent viscosity parameter α is (Dubrulle et al. 1995; Cuzzi et al. 1993; Youdin & Lithwick 2007)

$$H = H_{\rm gas}\sqrt{\frac{\alpha}{\alpha + \mathrm{St}}}. \tag{11}$$

The pressure supported gas disk rotates at sub-Keplerian speed which, from the perspective of an orbiting dust aggregate of non-zero Stokes number, is a headwind. This removes angular momentum from the particle, resulting in a radial drift velocity v given by (Weidenschilling 1977)

$$v = -2\frac{\mathrm{St}}{\mathrm{St}^2 + 1}\Delta v. \tag{12}$$

The drift velocity depends on the headwind speed Δv given by (Weidenschilling 1977; Nakagawa et al. 1986)

$$\Delta v = -\frac{\partial P}{\partial r}\frac{1}{2\rho_{\rm gas}\Omega_K}, \tag{13}$$

where P is the pressure and $\rho_{\rm gas}$ is the midplane gas density. A drifting particle is additionally carrying a velocity $v_{\rm drag}$ induced by drag with respect to the radial component of the gas velocity $v_{\rm gas}$, given by

$$v_{\rm drag} = \frac{1}{1 + \mathrm{St}^2}v_{\rm gas}. \tag{14}$$

Radial drift is particularly dominant for particles approaching St = 1.

In order to describe the dust evolution in the protoplanetary disk, we integrate the two-population model presented in Birnstiel et al. (2012) into the Bern model framework. Instead of calculating the full dust size distribution, we follow the mass-dominating upper end of the distribution (pebbles) as well as the initial small grains. The model parameters are calibrated with full dust evolution simulations of Birnstiel et al. (2010). The model considers dust growth which can be limited by fragmentation induced by turbulence or differential drift. We assume a pebble fragmentation threshold velocity of 10 metres per second. A further size limit arises if particles are removed by drift on a similar timescale as they grow. The size of the large particle population at a given distance is given by the minimum of all size limits. Given the resulting sizes of the large and small particle populations (the pebbles and dust grains, respectively), we solve one advection-diffusion equation for the combined surface density $\Sigma_{\rm solids}$

$$\frac{\partial \Sigma_{\rm solids}}{\partial r} + \frac{1}{r}\frac{\partial}{\partial r}\left[r\left(\Sigma_{\rm solids}\bar{v} - D_{\rm gas}\Sigma_{\rm gas}\frac{\partial}{\partial r}\left(\frac{\Sigma_{\rm solids}}{\Sigma_{\rm gas}}\right)\right)\right] = 0, \tag{15}$$

using the mass averaged radial drift speed

$$\bar{v} = (1 - f_m)v_{\rm grains} + f_m v_{\rm peb}. \tag{16}$$

The drift speeds of the small and the large populations $v_{\rm grains}$ and $v_{\rm peb}$ are given by the sum of Eqs. (12) and (14). The factor $f_m(r)$ is calibrated with the full simulations in Birnstiel et al. (2010). The combined dust surface density $\Sigma_{\rm solids}$ separates into the surface densities of the two underlying populations

$$\Sigma_{\rm peb}(r) = \Sigma_{\rm solids}(r)f_m(r), \tag{17}$$

$$\Sigma_{\rm grains}(r) = \Sigma_{\rm solids}(r)(1 - f_m(r)). \tag{18}$$

The initial combined surface density is simply $\Sigma_{\rm solids,0} = Z\Sigma_{\rm gas,0}$ where Z is the dust-to-gas ratio.

The inward drifting pebbles can be accreted by gravitating bodies, i.e. embryos. In order to calculate the pebble accretion rate, we follow the approach presented in Ormel (2017). The relative encounter velocity $v_{\rm enc}$ between a pebble and an embryo is

$$v_{\rm enc}(b) = \Delta v + \frac{3}{2}\Omega_K b, \tag{19}$$

where b is the impact parameter and Δv is given by Eq. (13). Depending on b, the encounter velocity is dominated by the headwind or the Keplerian shear, which are also called the Bondi and Hill regime, respectively (Lambrechts & Johansen 2012).

We find the maximal impact parameter $b_{\rm acc}$ which still leads to accretion by equating the encounter timescale $t_{\rm enc} = 2b/v_{\rm enc}$ and the settling timescale $t_{\rm settl} = b^3/(GMt_{\rm stop})$, where $t_{\rm stop} = \mathrm{St}/\Omega_K$. When pebbles reside in a thin layer ($H_{\rm peb} \ll b_{\rm acc}$, see Eq. (11)), the accretion geometry is 2-dimensional and the accretion rate is

$$\dot{M}_{\rm 2D} = 2b_{\rm acc}v_{\rm enc}(b_{\rm acc})\Sigma_{\rm peb}. \tag{20}$$

Since the pebble scale height is not necessarily small compared to the accretion radius, especially for low mass embryos, the pebble accretion rate $\dot{M}_{\rm peb}$ contains a scale height correction and reads (Ormel 2017)

$$\dot{M}_{\rm peb} = \dot{M}_{\rm 2D}\frac{b_{\rm acc}}{b_{\rm acc} + \sqrt{8/\pi}H_{\rm peb}}. \tag{21}$$

Note that this description recovers the 3D accretion rate

$$\dot{M}_{\rm 3D} = \pi b_{\rm acc}^2 v_{\rm enc}(b_{\rm acc}) \rho_{\rm peb} \tag{22}$$

in the thick disk limit ($H_{\rm peb} \gg b_{\rm acc}$), where the embryo is embedded in the midplane pebble density $\rho_{\rm peb} = \Sigma_{\rm peb}/(\sqrt{2\pi} H_{\rm peb})$.

Pebble accretion relies on a replenishing influx of pebbles from further out in the disk. When a planet grows massive enough to perturb the gas disk significantly, the orbital velocity of the gas outside the planetary orbit can become super-Keplerian (Lin & Papaloizou 1986). The radial drift of pebbles is halted at the resulting pressure maximum. The planetary mass required to trigger this effect is called the pebble isolation mass (e.g. Lambrechts & Johansen 2014; Ataiee et al. 2018; Bitsch et al. 2018; Shibaike & Alibert 2020). Apart from halting pebble accretion onto massive planets, pebble isolation is an important effect for the formation of multi-planetary systems since embryos inside to the isolating planet are deprived of further pebble supply.
We model this effect by modifying the gas surface density $\Sigma_{\rm gas}$ used in the evolution of the solid disk component $\Sigma_{\rm solids}$ (see Eq. (15)) with the gap profile of Kanagawa et al. (2016, 2017, 2018) for each planet. In this way, the resulting pebble surface density is consistent with the expected gaps induced by massive planets. We recover the reduction and stop of pebble accretion onto massive planets and the depletion of the regions inside an isolating planet. Note that these tidal gaps in the gas are not yet considered in the global evolution of the gas disk. This means that the gas disk "seen" by pebbles locally around massive planets is not the same as the one used for the calculation of gas accretion. The expected reduction of gas accretion onto massive planets due to gap opening is directly included in the accretion rates of Bodenheimer et al. (2013) using the unperturbed gas surface density.
It has been shown recently, that small grains can diffuse through such radial drift barriers to some extent and grow to pebble-size inside of the barrier (Stammler et al. 2023). Due to the mass-averaged approach to the dust evolution, we do not recover this behaviour once the pebble isolation mass is reached. This is most relevant for inner planet formation in the presence of an outer giant planet but since we focus on the formation of ice giants in this work, neglecting leaky dust traps is an acceptable simplification.

2.5. Orbital migration

An embedded planet excites density waves in the gas disk at its inner and outer Lindblad resonances as well as the corotation resonances (Goldreich & Tremaine 1979; Korycansky & Pollack 1993). The resulting differential Lindblad torque is usually negative in standard disks like the ones studies here. Depending on the local radial gas surface density slope, the temperature gradient, and the entropy gradient, the corotation torque can be positive (e.g. Paardekooper et al. 2011; Dittkrist et al. 2014). The planet migrates in the so-called type-I regime (Ward 1997; Tanaka et al. 2002) according to the net torque. In some regions, outward migration is possible when the corotation torque dominates the differential Lindblad torque.
Unless specified otherwise, we use type-I migration rates following Coleman & Nelson (2014) which are based on the torques of Paardekooper et al. (2011) with the addition of the attenuation of the corotation torque due to the eccentricity and inclination of the planet (Bitsch & Kley 2010; Fendyke & Nelson 2014; Coleman & Nelson 2014).

Table 1. Distribution parameters of the sampled initial conditions used in each synthetic population.

Parameter	Mean	Deviation
$Z_\star$	$\mu = -0.02$	$\sigma = 0.22$
$M_{\rm disk}$	$\log_{10}(\mu/{\rm M_{sol}}) = -1.49$	$\sigma = 0.35$ dex
$P_\star$	$\log_{10}(\mu/d) = 0.676$	$\sigma = 0.306$ dex

In Sect. 4.1, we discuss the impact of so-called thermal torques for the formation of Uranus-like planets in pebble accretion scenarios. This additional torque is an effect of the thermal diffusivity of the gas, as opposed to an adiabatic description. It has been studied analytically in Masset (2017) and has been observed in hydro-dynamical simulations (Lega et al. 2014; Benítez-Llambay et al. 2015). Thermal torques become relevant, when the planetary luminosity of a low to intermediate mass planet is significant due to energy released in the process of core accretion. As identified in Guilera et al. (2019) and Guilera et al. (2021), this is most important for pebble accreting planets due to the associated high core accretion rates. The heating of the corotation region results in asymmetric under-dense lobes on either side of the planet's orbit which exert a net positive torque. We adopt the prescription of Guilera et al. (2021) which combines the Lindblad and corotation torques of Jiménez & Masset (2017) with the thermal torques of Velasco Romero & Masset (2020). Thermal torques drop off for planets above the critical mass (Masset & Velasco Romero 2017)

$$M_c = \chi c_s / G, \tag{23}$$

where χ is the thermal diffusivity. We use the expression for the thermal torque $\Gamma_{\rm thermal}$ for a planet of mass M given by Velasco Romero & Masset (2020)

$$\Gamma_{\rm thermal} = \Gamma_{\rm hot} \frac{4M_c}{M + 4M_c} + \Gamma_{\rm cold} \frac{2M_c}{M + 2M_c}, \tag{24}$$

where $\Gamma_{\rm hot}$ and $\Gamma_{\rm cold}$ are the luminosity dependent and independent components of the thermal torque, respectively (Masset 2017).

Planets that grow massive enough to open a local gap in the gas due to tidal interactions (Lin & Papaloizou 1986) migrate in the so-called type-II migration regime. For the transition from type-I to type-II migration, we consider the gap opening criterion of Crida et al. (2006) for a planet of mass M with semi-major axis a

$$\frac{3H}{4R_H} + \frac{50\nu M_\star}{M a^2 \Omega_K} \leq 1. \tag{25}$$

The transition is smoothed according to Dittkrist et al. (2014) and the type-II migration rates are given by the radial gas flow (Pringle 1981).

2.6. Initial conditions

We synthesize populations of planetary systems consisting of 10^3 different protoplanetary disks. In order to have comparable populations, we use an identical set of initial conditions for all runs (see Emsenhuber et al. 2021b; Kessler & Alibert 2023). In table 1, we list the distribution parameters used to sample the initial conditions. The stellar mass is fixed to one Solar mass. We use normally distributed stellar metallicities $Z_\star$ (Santos et al.

2005) for the dust-to-gas ratio of the disks assuming stellar composition. The gas disk masses $M_{\rm disk}$ are obtained from continuum emission observations which assume a dust-to-gas ratio of 0.01 (Tychoniec et al. 2018). We use a log-normal distribution and correct the disk masses according to the used, not necessarily equal to 0.01, dust-to-gas ratio. The inner disk radius $R_{\rm in}$ is set as the corotation radius with respect to the stellar rotation period $P_\star$ obtained from observations of T-Tauri stars using a log-normal distribution (Venuti et al. 2017). The characteristic outer disk radius $R_{\rm char}$ and the initial gas surface density at 5.2 au Σ_0 follow from the disk mass and $R_{\rm in}$ (see (2)). For a fixed viscosity, disk lifetimes are directly constrained by external photo-evaporation. As described in Emsenhuber et al. (2021b), we use external photo-evaporation rates resulting in disk lifetimes clustering around 3 to 4 Myr. This is in agreement with observational estimates of disk lifetimes (Haisch et al. 2001; Fedele et al. 2010; Richert et al. 2018).
In every population, we insert 0.02 $M_{\rm E}$ embryos at the start of the simulations. This is an optimistic assumption for embryo formation which generally leads to over-estimated early growth and needs to be taken into account when looking at final planetary masses in the different populations. Depending on the population, we insert a different number of planetary embryos at different locations in the disk which is detailed in the corresponding Sects. 3 and 4.

3. In-situ formation

First, we consider the in-situ formation of single ice giants where the initial embryo location is identical to the final position of the planet. This means disk-driven migration is neglected and there is no other way for the planet to exchange angular momentum since there are no other planets present in the same disk. Therefore, planets are on circular orbits and the semi-major axis is the orbital distance. We sample the initial embryo location log-uniformly between 5 and 20 au.

In Fig. 1, we show the planetary masses after 5 Gyr as a function of semi-major axis, colour coded by the H-He mass fraction with respect to the total planet mass, for the different in-situ populations. When considering planets formed by planetesimal accretion (left column), it is evident that growth timescales are longer in the outer parts of the disk. In fact, it is only possible to form planets exceeding 10 $M_{\rm E}$ outside of 10 au, if envelope opacities are low enough to allow for sufficient gas accretion. The existence of a gaseous envelope is doubly beneficial in order to grow beyond a couple of Earth masses because an envelope not only adds mass but also increases the planetesimal capture radius (see Sect. 2.3). In the fiducial low-opacity case (top left), there are some giant planets exceeding 100 $M_{\rm E}$ out to about 10 au, as well as some ice giant candidates clustering around the 10 to 20 $M_{\rm E}$ region (orange bar). The H-He mass fractions of these candidates range up to 50% but most of them end up in the 8-25% range (red circles). Although very rarely, it is possible to form an Uranus-like planet around 10 au but not at larger separations in this scenario. In the high-opacity case (bottom left), the resulting lower gas accretion rates leave a strong imprint on the population. There are no planets above 10 $M_{\rm E}$ outside of 8 au and outside of 10 au planets do not even grow beyond three Earth masses. Planets in the 10 to 20 $M_{\rm E}$ region, found inside of 8 au, have H-He fractions below 30%. It is worth repeating here, that the planetesimal size of 1 kilometre is crucial. While planetesimals are not believed to form smaller than 100 km (Polak & Klahr 2022), planetesimal fragmentation to smaller sizes has been shown to be important for the planet formation process (Kaufmann & Alibert 2023). However, the planetesimal size distribution is poorly understood and depends on uncertain descriptions of the material strength and impact energy. We consider the choice of 1 km planetesimals and hence the simulation outcomes to be optimistic with regards to planetary growth in the outer disk. Therefore, we conclude that in-situ formation via planetesimal accretion necessarily requires low opacities but remains unlikely even for these smaller sized planetesimals. Unsurprisingly, forming ice giants in-situ from larger than 1 kilometre planetesimals seems impossible, corroborating previous studies (Safronov 1972; Goldreich et al. 2004).
When considering planets formed by pebble accretion (right column), in-situ formation is more efficient in producing massive planets all the way out to 20 au. Numerous gas-dominated giants, as well as some ice giant candidates in the targeted region of 10 to 20 $M_{\rm E}$, are formed. In the low-opacity case (top right), planets in the ice giant mass range are gas-rich with H-He mass fractions of upwards of 80% and planets in the 8-25% range (red circles) are much less massive. In the high-opacity case (bottom right) H-He mass fractions are below 40% in the 10 to 20 $M_{\rm E}$ region and the planets in the 8-25% range (red circles) cluster just below 10 Earth masses outside of 10 au. Comparing the same disks in the two opacity cases, we find that planets which end up between 10 and 20 $M_{\rm E}$ in the high-opacity case become much more massive gas-dominated giants in the low-opacity case. This is consistent with the results of Valletta & Helled (2022) and Eriksson et al. (2023). These authors also find too large H-He fractions and unrealistically short disk lifetimes to prevent the formation of gas-dominated giants instead of Uranus and Neptune, for lower envelope opacity values.

These results confirm that, especially in the pebble accretion scenario, in-situ formation timescales to grow beyond tens of Earth masses outside of 10 au are overlapping with expected disk lifetimes. In suitable disks, this allows the formation of potential ice giants from 0.01 $M_{\rm E}$ embryos. Note again that the disk lifetime in this model is a result of the viscous disk evolution and external photo-evaporation given the initial disk characteristics. In the explored parameter space, it remains difficult to obtain H-He mass fractions below 25% for planets above 10 Earth masses. The most promising in-situ scenario is pebble accretion when envelope opacities are high, although our simulations hint at even larger opacities being required, as the lowest H-He fractions remain above 30% outside of 10 au.

Since the Solar System hosts two ice giants, an obvious further requirement is the formation of a second planet in this parameter space. Considering the disks that form a planet between 10 and 20 $M_{\rm E}$ outside of 10 au in the high-opacity pebble accretion scenario, we investigate whether a second embryo outside of the first can grow to a similar mass and whether the first embryo is still able to grow above 10 $M_{\rm E}$ in such a scenario. In Liu et al. (2022), the ice giants are proposed to have formed in 2:1 or 3:2 resonant chains. We place the second embryo outside of the first (at t=0 as well) such that they are in 3:2 resonance because it results in a more optimistic setup for the second planet in terms of accretion timescale. Note that since disk-driven migration is not considered in these simulations, the planets necessarily remain in the initial resonance configuration. In Fig. 2, we show the results after 5 Gyr of these runs (circles) and compare them with the planets emerging in the original single-planet case (crosses). It is apparent that the outer planet

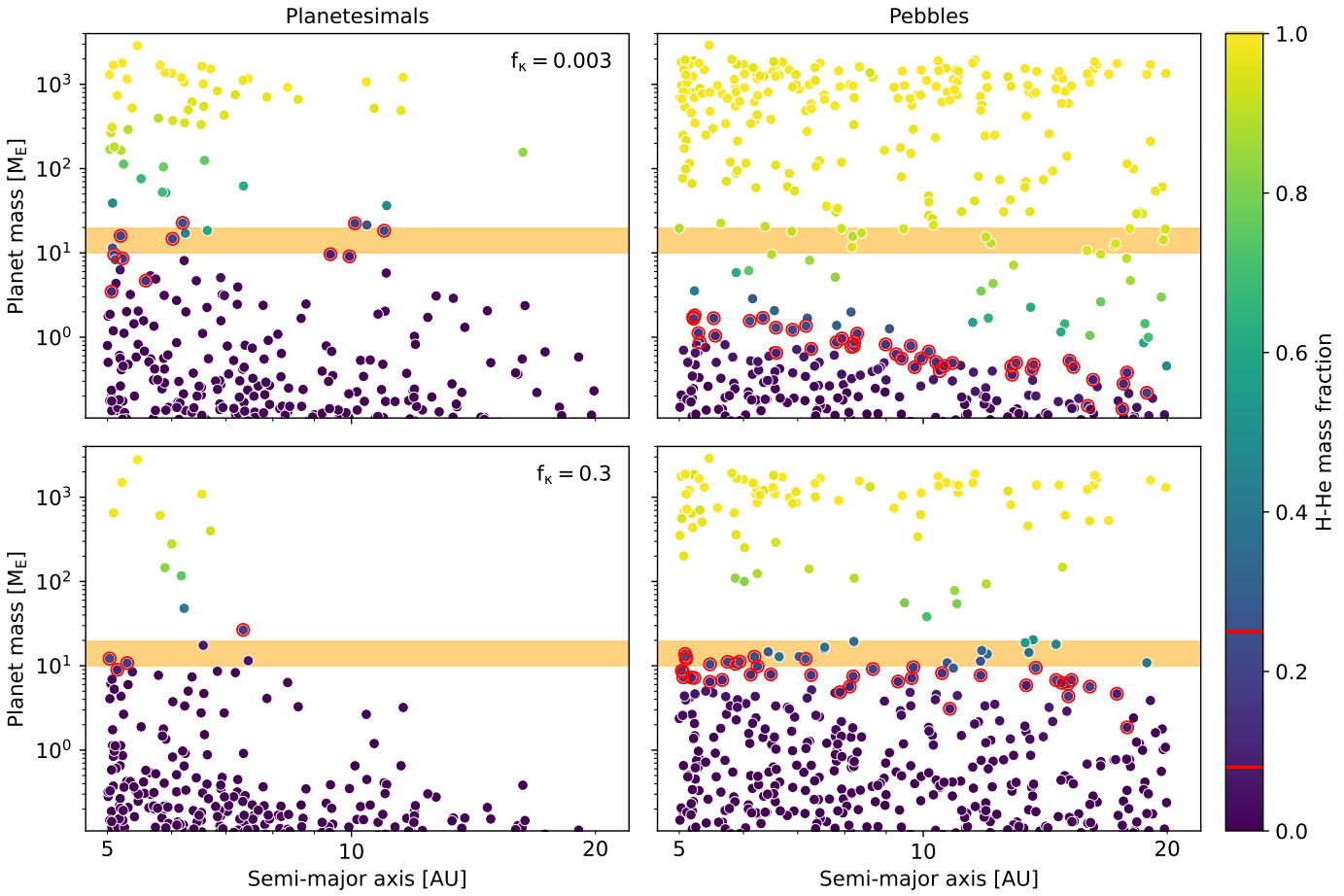

Fig. 1. Planet mass versus semi-major axis of one thousand *in-situ* simulations of single planets after 5 Gyr considering planetesimal accretion (left) or pebble accretion (right) with low (top) or high (bottom) envelope opacity. f_κ is the envelope opacity reduction factor introduced in Sect. 2.2. The colour of the points indicates the fraction of the H-He mass over the total planet mass. The red circles highlight the planets that lie in the 8-25% H-He mass fraction range, indicated by red lines on the colourbar. The orange region highlights the 10 to 20 M_E range.

is always less massive than the inner planet and never grows beyond 5 M_E in these disks. Secondly, the inner planet ends up at a lower mass than in the single-planet case when there is an outer planet present. This is due to the fact that the outer planet accretes some of the inwards drifting pebbles leading to a lower pebble surface density inside it's orbit. However, the inner planet still grows beyond 10 M_E in most cases. This behaviour for a concurrently growing pair of ice giants was also found in the in-situ simulations of Eriksson et al. (2023). We find that the most promising in-situ ice giant candidates in the populations we simulate are likely incompatible with the in-situ formation of a second ice giant.

In summary, while the in-situ paradigm is compatible with the formation of a single ice giant, it is likely not suited to explain an ice giant pair or the outer Solar System. Planetesimal and pebble accretion put opposite requirements on the envelope opacities.

4. Formation with migration

There is no physical reason to neglect the torque exerted onto embedded planets. Given the smooth nature of the radial gas disk profile in this model, the net torque as described in Sect. 2.5 is generally negative in the outer disk regions. Due to the resulting predominantly inward-migrating nature of these formation pathways, we also consider planets that start to grow beyond 20 au. To investigate the imprint of disk-driven migration, we run populations corresponding to the ones discussed in Sect. 3 considering embryos inserted log-uniformly between 5 and 40 au. We refer to Sec. 5 for a discussion on structured disks and possible migration traps. Note that the number of gas giants forming in these setups can not be taken at face value as we are not including embryos forming inside of 5 au. Especially the region around the iceline, where growth is most efficient in both planetesimal and pebble accretion scenarios, is a common birthplace of the most massive planets. Ice giants are unlikely to originate there, particularly when they are accompanied by one or several gas giants as it is the case in the Solar System.

4.1. Single embryo per disk

First, we study again the formation of one single planet per disk. In Fig. 3, we show planetary masses after 5 Gyr as a function of semi-major axis, colour coded by the H-He mass fraction, for the different populations of migrating planets. It is immediately apparent that inward migration acts in all populations and is able to move planets all the way to the inner disk edge from their initial location in the gray shaded region. As in the in-situ case, growth by the accretion of planetesimals (left column) is less efficient in the outer disk. Most remaining embryos are less massive than one Earth mass. Planets that do grow beyond

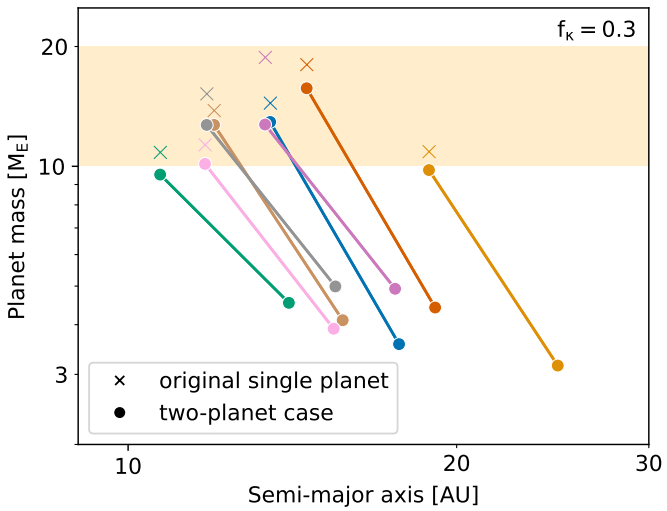

Fig. 2. Mass versus semi-major axis of the eight planets that form planets between 10 and 20 M_E in the high-opacity ($f_\kappa = 0.3$) pebble accretion case after 5 Gyr (bottom right panel in Fig. 1). The crosses are the results from the single-planet run, the connected circles of the same colour are the corresponding two-planet systems in 3:2 resonance. The orange bar highlights the 10 to 20 M_E range.

roughly one Earth mass start to migrate inward, shaping the "inward-leaning" population of planets that do not accrete gas significantly. As planets migrate into the hotter inner disk, gas accretion is inhibited and only the most massive planets can enter runaway gas accretion. In the low-opacity case (top left), some gas giants manage to form before they migrate in the type I regime all the way to the inner disk. This is strongly suppressed in the high-opacity case (bottom left) where no planet exceeds 100 M_E after 5 Gyr. This is again due to the lower gas accretion rates.

When considering pebble accretion (right column), we observe a strong imprint of inward migration in the populations. Compared to the planetesimal accretion cases, more planets grow massive enough to migrate inwards significantly and planets grow earlier, leaving more time to migrate inwards. This leads to a pile up of planets above several Earth masses inside of 0.1 au which is a known consequence of pebble accretion in formation scenarios of single planets (e.g. Kessler & Alibert 2023). Since everything that grows above roughly one Earth mass outside of 10 au is efficiently moved inward, no ice giant candidates are left in the outer disk. As in the planetesimal accretion case, the low-opacity setup (top right) features some massive gas-dominated giants whereas the high-opacity setup (bottom right) does not produce planets above 100 M_E. When envelope opacities are high, gas accretion rates are too low for giant planets to form. We summarise that single planets which are subject to migration do not become ice giants in any of our simulations.

Since accretion rates can be high in pebble accretion scenarios, the resulting heating of the surrounding disk becomes non-negligible for the torque that is exerted on the planet (Benítez-Llambay et al. 2015). Given a sufficiently large accretion luminosity, the net torque can be positive, leading to outward migration (Guilera et al. 2019). This is particularly interesting in the context of forming ice giants without them inevitably migrating inward too far, as is the case with the nominal migration prescription. We adopt the approach of Guilera et al. (2021) to include these so-called thermal torques as described in Sect. 2.5. In Fig. 4, we show the emerging population including thermal torques in the high-opacity case after 5 Gyr. Since we are interested in formation pathways featuring significant outward migration, formation origins inside of 5 au are also considered. Therefore, embryos are placed log-uniformly between 1 and 40 au. The population is similar to the corresponding population using the nominal migration prescription shown in the bottom right panel of Fig. 3. In particular, there are again no ice giant candidates. The main apparent difference lies in the low-mass close-in planets, which are introduced due to some of the embryos that are initialised between 1 and 5 au.

However, looking at the formation paths of planets that grow to 8 to 20 M_E reveals that, although the populations look similar at 5 Gyr, there are formation pathways featuring significant outward migration due to thermal torques. The coloured lines in Fig. 4 show four example pathways. The red and blue lines show planets that are dominated by the hot thermal torque due to rapid pebble accretion. They migrate outwards significantly from their initial locations of less than 3 au. This reproduces the findings in Guilera et al. (2021) well. When the planets approach the critical mass where thermal torques become inefficient, inward migration takes over. In one thousand simulations, the disk never disperses in the precise time to prevent inward migration of planets that have migrated outwards to this extent. The green line shows a planet that also starts growing around 2 au but is not dominated by the thermal torque. It accretes slower than its red and blue counterparts and manages to grow to about 8 M_E before it also migrates inward. This is because this planet is forming in a less massive and lower metallicity disk than in the red and blue examples. Thermal torques are most efficient early and inside of roughly 10 au (Guilera et al. 2019, 2021). Therefore, as shown by the purple line, formation pathways of planets in the outer disk, typically, look the same as they do in the nominal migration prescription where planets that do grow above a couple of Earth masses simply migrate inwards until they reach the inner disk edge or until the disk disperses. This means that, as is the case without thermal torques as well, unless there is something preventing or slowing the inward migration of these planets, they do not become ice giants.

4.2. Multiple embryos per disk

From the results in Sect. 4.1, it is apparent that the formation of ice giants can in all likelihood not be understood from an isolated, single planet perspective when growing planets are allowed to migrate. In such scenarios, inward migration prevents massive planets from ending up in the outer disk. In the following, we investigate planet formation in the outer disk when multiple embryos are growing simultaneously and interacting gravitationally. We insert 35 embryos per disk log-uniformly between 5 and 40 au where neighboring embryos are separated by at least 10 Hill radii. The number of embryos chosen corresponds to the average number of embryos inserted between 5 and 40 au in the largest simulations performed in Emsenhuber et al. (2021a) with 100 embryos. By omitting embryos within 5 au, the computation time due to the N-body calculations is dramatically lower. However, the computational effort remains considerable since planets migrate into the inner regions of the disk as they grow and we are still simulating a thousand disks per population. Mutual embryo collisions are treated in a simplified way (Emsenhuber et al. 2021a). The H-He mass of the less massive impactor is discarded, the core masses are merged, and the remaining impact energy is added

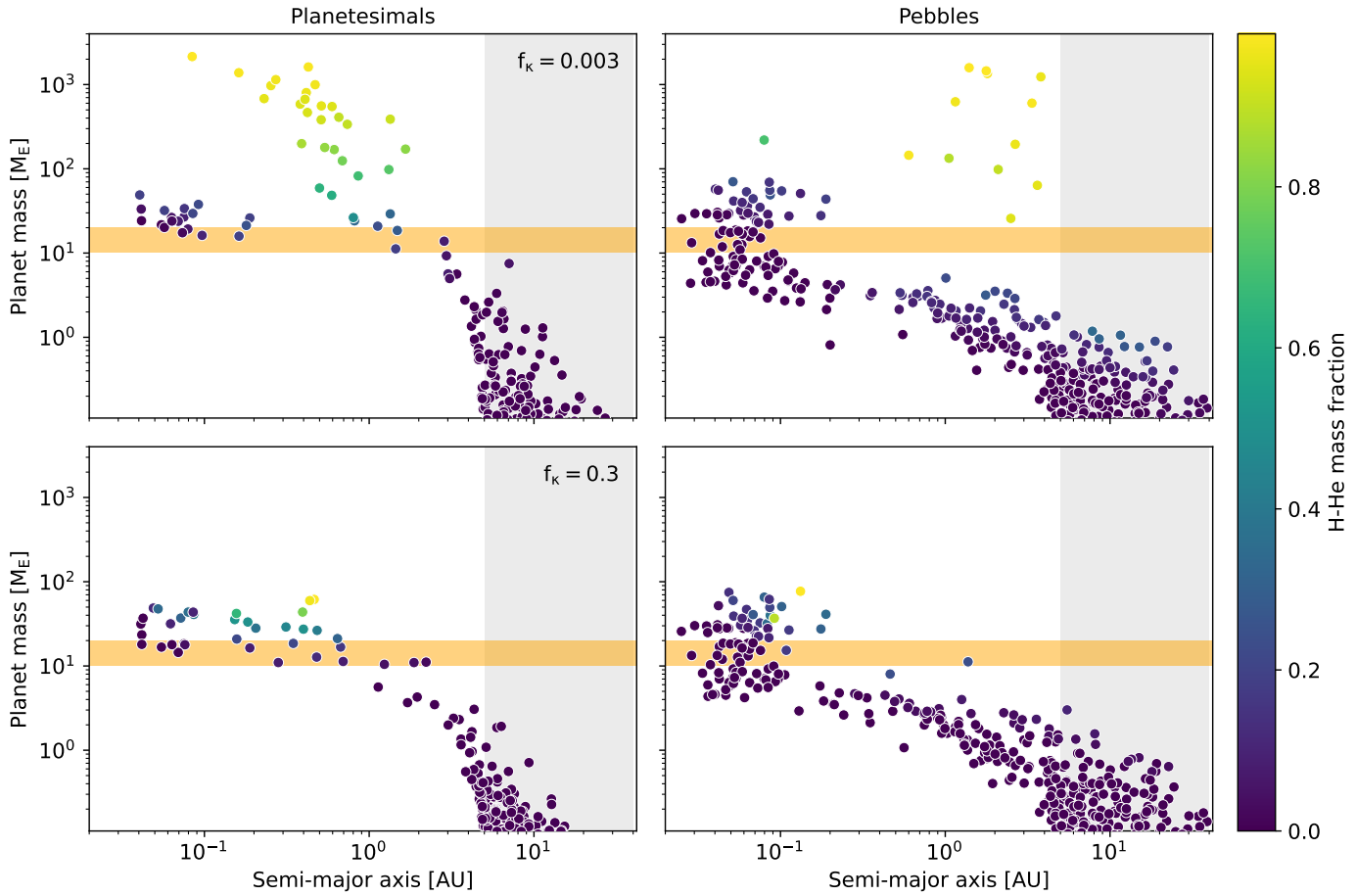

Fig. 3. Planet mass versus semi-major axis of one thousand simulations of *migrating* single planets after 5 Gyr considering planetesimal accretion (left) or pebble accretion (right) with low (top) or high (bottom) envelope opacity. f_κ is the envelope opacity reduction factor introduced in Sect. 2.2. The colour of the points indicates the fraction of the H-He mass over the total planet mass. The orange bar highlights the 10 to 20 M_E range and the gray shaded region shows the range of initial embryo locations.

as a contribution to the luminosity in the structure equations. The additional luminosity from the impact and accretion of the second core typically leads to significant H-He mass loss of the target planet.

In Fig. 5, we show planetary masses after 5 Gyr as a function of semi-major axis, colour coded by the H-He mass fraction, for the different populations of migrating multi-planetary systems (using the nominal migration model). Many of the characteristics of the different single-planet populations in the previous sections are preserved when more embryos are introduced per disk. Planets above a few Earth masses experience inward migration which results in many planets inside of 5 au. The embryo-embryo gravitational interactions cause the general shape of the populations to be scattered around the corresponding single-planet populations. This leads to more massive planets in the outer system in all setups compared to the simulations of single planets. Naturally, since there are 35 embryos present per disk, there are more planets in the whole parameter space.

In the planetesimal accretion scenario (left column), planetary growth outside of 10 au remains insufficient to produce massive planets easily. Compared to the single-planet results shown in Fig. 3 however, there are some more massive planets due to mutual collisions. In the low-opacity case (top left) there are again some gas-dominated planets, mostly inside of 1 au. In contrast to the single-planet case, some gas-dominated planets are on more distant orbits out to about 5 au. This is both due to collisional growth between embryos and outward scattering. When opacities are high (bottom left), the picture remains very similar to the single-planet case and we find no ice giant candidates.

When considering pebble accretion (right column), formation tracks are again strongly dominated by inward migration as planets grow beyond about 1 M_E. Unless planets start accreting gas rapidly and opening a gap, they migrate inwards significantly before growing above 10 to 20 M_E. Although not quantitatively comparable due to the different number of total planets, there are many planets that have acquired a H-He envelope in the low-opacity case (top right), while there are none outside of 10 au in the single-planet simulations in Fig. 3. Embryos growing via pebble accretion in the outer disk can become massive enough to gravitationally interact. This leads to growth of the planetary cores via mutual collisions. Since embryos cool quickly in the low-opacity case, these planets can accrete massive H-He envelopes also outside of 10 au. As observed in the in-situ low-opacity pebble accretion scenario, the planets in the 10 to 20 M_E range outside of a couple of au are typically gas-dominated with H-He mass fractions above 80%. However, there are a few massive planets that barely contain H-He, as seen from the darkest dots outside of a couple of au with masses above 10 M_E. These planets experience a collision

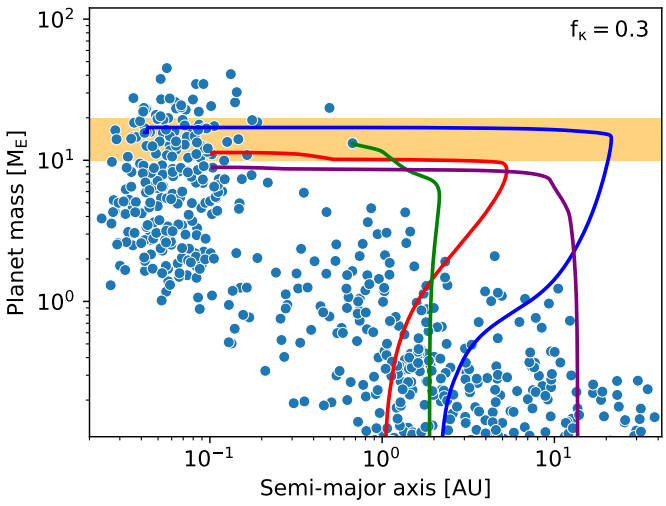

Fig. 4. Planet mass versus semi-major axis of one thousand simulations of migrating single planets after 5 Gyr including thermal torques according to Guilera et al. (2021). The coloured lines correspond to four typical formation pathways, leading to planets of 8 to 20 M_E. f_κ is the envelope opacity reduction factor introduced in Sect. 2.2. The orange bar highlights the 10 to 20 M_E range.

with another embryo at the very end of the disk lifetime. They eject most of their gaseous envelope in the collision and are left without any gas to re-accrete. In our simulations, none of these examples end up in the desired parameter space but it is easily conceivable that candidates can emerge, although rarely, in a larger population. In most cases however, the disk is still present and massive planets that collide with other embryos end up growing well above 100 M_E, with H-He mass fractions above 90%. It is theorised that at least Uranus has experienced a massive collision causing it's axial tilt (Reinhardt et al. 2020). In the high-opacity case (bottom right), there are no planets in the 10 to 20 M_E range outside of 10 au. Compared to the single-planet case however, the planetary cores outside of 10 au are more massive due to mutual collisions. In contrast to the low-opacity case, planets that experience such impacts do not typically start accreting gas readily. Even when they are massive enough to accrete gas, which is about 20 M_E as seen in the in-situ simulations shown in the bottom right panel of Fig. 1, they can not get rid of the impact energy before the gas disk disperses.

We find one out of a thousand systems which harbours a planet between 10 and 20 M_E outside of 10 au in the low-opacity planetesimal accretion scenario. The system is shown in Fig. 6. There is one Jupiter mass gas-dominated giant at 0.8 au and a 17 M_E planet at 2 au. Outside of the candidate (red circle), there is a 8.5 M_E planet at 15 au. From this, we cannot exclude the formation of a second ice-giant candidate in this scenario. The masses of the planets outside of the candidate sum up to 11 M_E but note that they are spread out over a range of 30 au and most are less massive than 0.1 M_E. The total leftover mass, obviously, depends on the number of embryos that are initially inserted but the majority of the leftover embryos do not grow significantly. Most of the leftover mass comes from the two most massive embryos and the formation of the second potential candidate does not rely on the presence of the embryos inserted even further out. We repeat here that this outcome is obtained by inserting embryos at the same time and mass irrespective of their orbital location. This leads to an optimistic outcome in terms of planetary growth.

In the low-opacity pebble accretion case, there are four systems in which a planet between 10 and 20 M_E forms outside of 10 au. In Fig. 7, we show these planetary systems in four panels where the selected planets are highlighted by a red circle. Note that, as found in the single-planet low-opacity pebble accretion simulations before, all of the selected planets are already dominated by H-He and there are no ice giant candidates as defined in Sect. 1. As in the planetesimal accretion case, there are more massive planets inside of the selected planet. In every system there is at least one gas-dominated planet of at least 100 M_E inside of 10 au. None of the selected planets are accompanied by a second similarly massive planet outside of their orbit. The masses of the other remaining planets outside of 10 au sum up to between 6 and 14 M_E. In the pebble accretion scenario, multiple embryos outside the candidate can grow to several Earth masses. As discussed above, large amounts of H-He could be removed from the candidates in collisions with these embryos. This means that, in a multi-planetary setting, the constraints on the envelope opacities become much less strict than what is inferred from simulations of single planets. Given perfect collision timing by chance, it is possible to reproduce Uranus/Neptune-like H-He mass fractions for a wider range of planetary masses. The planets inside of the gas-dominated giant, which is found in all of the selected simulations, must be cautiously appreciated. As mentioned in Sect. 2.4, the diffusion of small grains through the gap induced by a massive planet is not well reproduced by the dust model we use. This could lead to an underestimation of growth for these inner planets. Since we do not insert embryos within 5 au there could be additional massive planets that would grow from embryos starting further inside. However, we know from previous studies that, if planets are allowed to migrate, giant planets that are seeded from embryos starting inside of 5 au typically end up inside of 1 au (Emsenhuber et al. 2021a; Kessler & Alibert 2023).

5. Discussion

There are some limitations to the setups and underlying assumptions in this work. In the following, we discuss some of these choices.

We sample initial conditions according to observations and thus simulate a wide variety of disks. It is, however, possible that due to large uncertainties and oversimplified models that are applied to observations in order to make predictions on disk parameters, we could be missing viable initial conditions. If disks are different in size, metallicity, and lifetime than currently thought, the simulations in this work have to be revisited. For instance, since giant planet formation correlates with more massive and more dust rich disks in planet formation simulations, ice giants can, formally, form more easily at large distances in such disks.
We are considering viscous disks with $\alpha = 10^{-3}$ which is an assumption that, together with the external photo-evaporation rates used, yields disk lifetimes that are in line with observations (Emsenhuber et al. 2021b). We do not consider other α-values, because the disk lifetimes are crucially important for the formation of ice giants. The necessary calibration of external photo-evaporation rates to different viscosities is beyond the scope of this work. Especially the extension to lower viscosity disks and disks driven by magnetic winds is subject of current study and future work (Weder et al. 2023). A lower disk viscos-

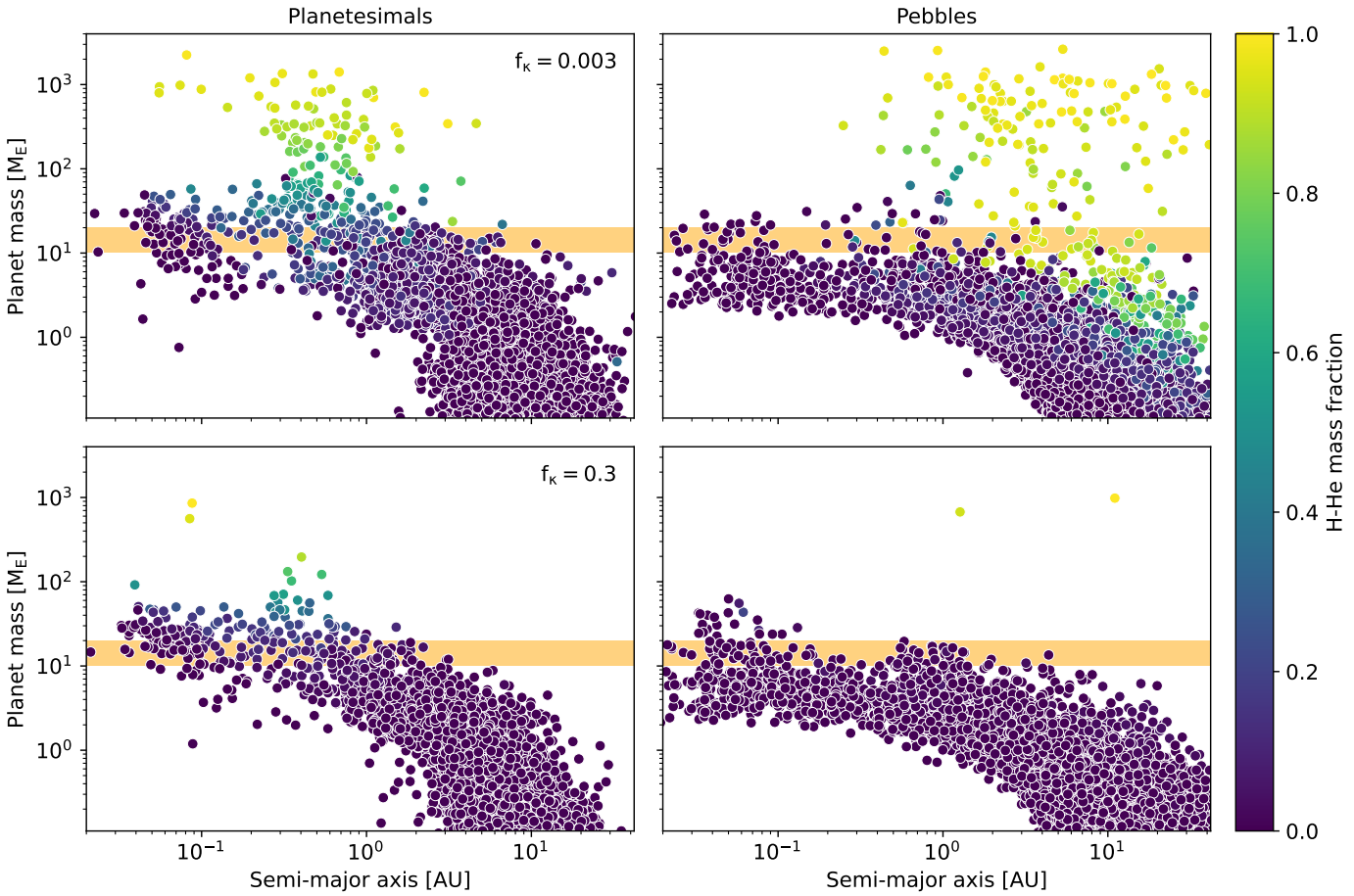

Fig. 5. Planet mass versus semi-major axis of one thousand simulations of 35 planets per disk after 5 Gyr considering planetesimal accretion (left) or pebble accretion (right) with low (top) or high (bottom) envelope opacity. f_κ is the envelope opacity reduction factor introduced in Sect. 2.2. The colour of the points indicates the fraction of the H-He mass over the total planet mass. The orange bar highlights the 10 to 20 M_E range.

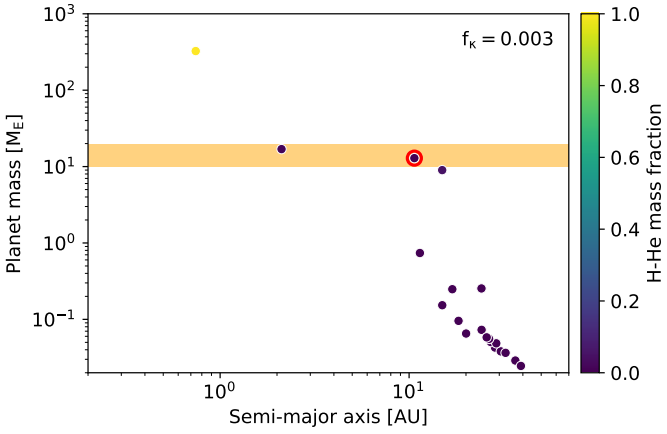

Fig. 6. Planet mass versus semi-major axis of the only system harbouring a planet between 10 and 20 M_E outside of 10 au (red circle) in the low-opacity (f_κ = 0.003) planetesimal accretion setup shown in the top left panel of Fig. 5. The colour of the points indicates the fraction of the H-He mass over the total planet mass. The orange bar highlights the 10 to 20 M_E range.

ity is linked to shorter formation timescales in pebble accretion scenarios because pebbles grow larger as turbulence-driven mutual collisions are less energetic and the pebble scale height becomes smaller (Venturini et al. 2020). How the different disk evolution paradigm influences planet formation generally, and ice giant formation specifically, is still unclear.

Another crucial assumption in this work is the smooth nature of the initial disk structure. Planet formation in structured disks, particularly disks with rings of arbitrary origin, is a currently intensely studied topic (e.g. Jiang & Ormel 2022; Lau et al. 2022; Lee et al. 2022). It is generally found that, given established rings in the disk structure, planet formation can be highly efficient at these locations almost irrespective of distance to the star. Depending on appropriate timing and lifetime of such rings, it appears possible to sculpt virtually any kind of planetary system. Of course, this just moves the fundamental question about the formation history of the planets in such a system to the formation mechanism responsible for the initial rings and their evolution. Nevertheless, planet formation in structured disks allows for otherwise difficult to explain massive planets at large separations and could provide a solution to the challenges of the formation of Uranus and Neptune.

The insertion of the planetary embryos is simple in multiple ways. The embryos are added at the beginning of the simulation no matter where they are and have the same 0.01 M_E mass. This leads to optimistic outcomes in terms of final planetary mass as planets have the maximum amount of time to grow and can do so immediately due to the considerable starting mass. This could also have an adverse effect for the formation of ice giants when considering migration as early growing planets have more time

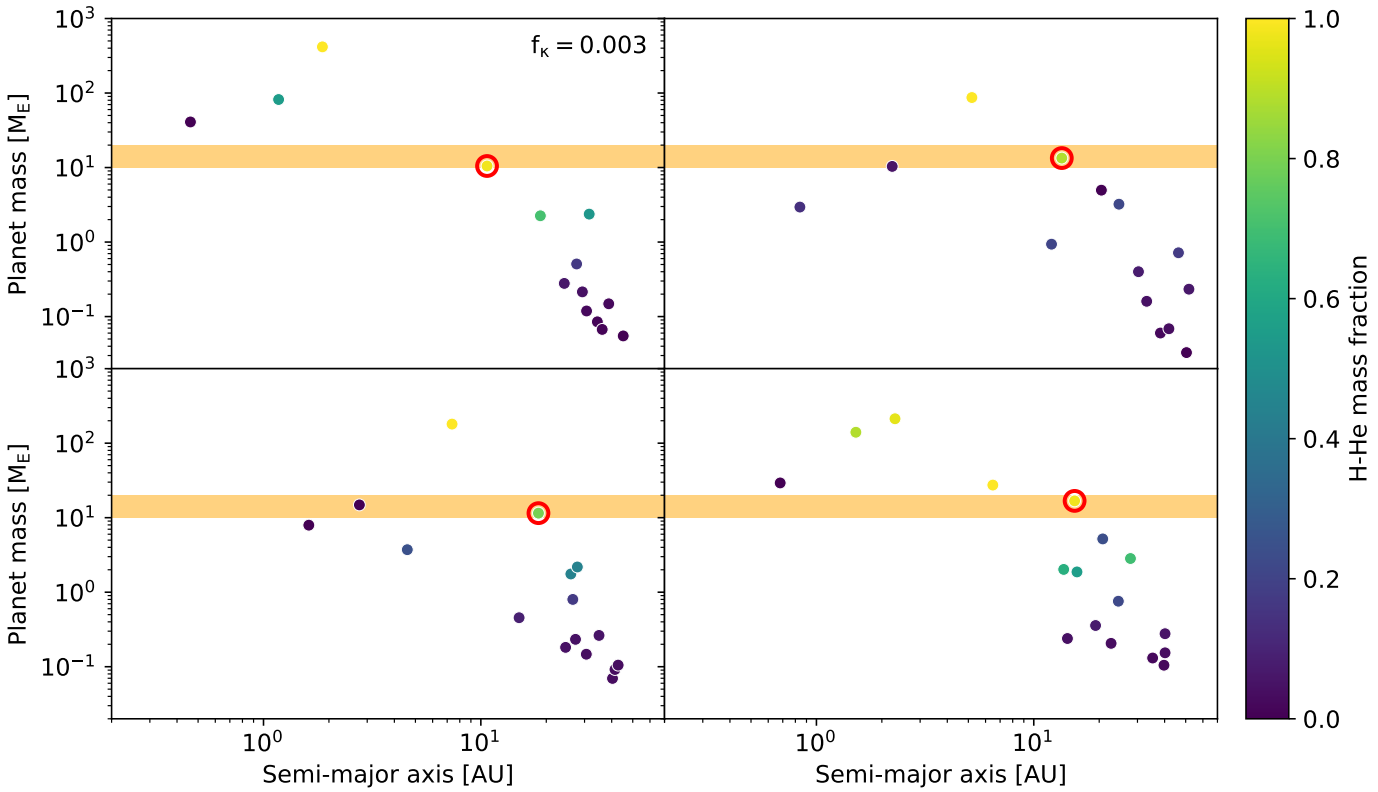

Fig. 7. Planet mass versus semi-major axis of the four systems harbouring a planet between 10 and 20 M_E outside of 10 au (red circles) in the low-opacity (f_κ = 0.003) pebble accretion setup shown in the top right panel of Fig. 5. The colour of the points indicates the fraction of the H-He mass over the total planet mass. The orange bar highlights the 10 to 20 M_E range.

to migrate inwards. However, as seen from all the simulations of migrating planets when opacities are high, simply reaching the ice giant mass regime is difficult in the outer parts of the disk. This problem is accentuated when embryos form later and/or less massive.

We simply scale the grain opacities of Bell & Lin (1994) by a factor f_κ. In reality, the opacity of the envelope depends on the accretion rate, the properties of the accreted material, and the evolution of this material in the envelope. Brouwers et al. (2021) study the envelope opacity considering the evolution of accreted pebbles. They find that the envelope opacity of growing planets can vary by several orders of magnitude for different pebble accretion rates at different distances from the star. Generally, envelope opacities are higher for planets at larger distances and for higher pebble accretion rates. As planets grow beyond 10 M_E beyond 10 au, large opacities can only be achieved for pebble accretion rates above of $10^{-5} M_E$/yr. This highlights that a constant envelope opacity is a simplified approach. They conclude that in the case of Uranus and Neptune, the envelope opacity was unlikely to be elevated sufficiently in order to prevent runaway gas accretion unless these planets formed late rapidly. In our setup, we do not model any late forming planets as embryos are inserted in the beginning, but since, even in that case, reaching the mass range of 10 to 20 M_E is challenging outside of 10 au, a rapid late Uranus and Neptune formation scenario seems unlikely in an unstructured disk when planets are migrating.

The accretion of solids and the heavy-element enrichment of the envelope not only affects the opacity but also increases the mean molecular weight of the envelope. In contrast to an increased opacity, a higher mean molecular weight of the envelope increases a planet's ability to accrete gas (e.g. Stevenson 1982; Hori & Ikoma 2011; Venturini et al. 2015; Venturini & Helled 2017; Valletta & Helled 2020). We do not currently model this effect, therefore, the gas accretion rates may be underestimated, especially in the high-opacity cases where higher heavy-element enrichment could be expected. In order to prevent the onset of runaway gas accretion of potential ice giants, the opacity remains the governing quantity as it controls the cooling ability of the growing planet. As discussed in Sect. 4.2, the opacities can not necessarily be constrained by just looking at final masses and the H-He fraction because the planetary composition can be strongly altered by late impacts. Nevertheless, our approach allows to identify the general dependence of envelope opacity in the Uranus and Neptune parameter space.

In some Solar System formation scenarios, the giants of the outer Solar System can move even closer than we consider in this work. For instance, Walsh et al. (2011) propose that young Uranus and Neptune could have formed at 5 and 8 au, respectively. In this scenario however, the planets begin migrating outwards before they reach their current mass during the lifetime of the disk. The outward migration of the four Solar System giants takes place in resonance, and is driven by a wide gap in the gas disk that is shared by young Jupiter and Saturn. During the outward migration, the planets need to accrete the remaining mass difference to fit the current properties of the Solar System. Our simulations can not be compared to this scenario as a better modelling of the planet gas interactions and gas disk gap structures is necessary. It remains an open question whether the specific initial conditions required for this outward migration mechanism to

work can be naturally obtained in a global formation model and whether the planets are able to accrete the remaining mass when accretion processes are modelled self-sufficiently. This interesting inquiry is subject of future work.

6. Summary and conclusions

We examine populations with respect to the formation of Uranus/Neptune-like planets in in-situ and migrating setups of single and multi-planetary systems in planetesimal and pebble accretion scenarios. The main findings can be summarised as follows:

- The in-situ formation of a single ice giant from planetesimals is challenging. The planetesimals have to be small (on the order of kilometres) and a low envelope opacity is required in order to allow for sufficient planetary growth.
- The in-situ formation of a single ice giant from pebbles is possible, however, the H-He envelopes of planets above 10 $M_{\rm E}$ tend to be too massive, leading to gas-dominated planets. This problem can be alleviated by larger envelope opacities.
- The concurrent in-situ formation of a Uranus/Neptune-like ice giant pair is challenging even in pebble accretion scenarios. In general, the outer planet does not grow sufficiently in disks where the inner planet reaches the 10 to 20 $M_{\rm E}$ range.
- If planets are allowed to migrate, it is not possible to form ice giants from a single growing embryo. Planets migrate inwards efficiently once they grow more massive than a few Earth masses. This finding remains robust when thermal torques leading to temporary outward migration are considered.
- When multiple growing planets per disk are considered, growth in the outer parts of the system is enhanced compared to the single-planet case due to mutual collisions. For planetesimals, the requirements on small sizes and low envelope opacities remain. In the pebble accretion scenario, a large envelope opacity prevents the planets from cooling after mutual collisions and inhibits sufficient gas accretion. Low opacities, on the other hand, rather lead to gas-dominated planets, similarly to the low-opacity in-situ scenario. However, significant amounts of H-He can be stripped from the planets in late collisions which loosens the constraint on the envelope opacity but requires conveniently timed collisions.
- In the multi-planetary systems where a planet forms in the 10 to 20 $M_{\rm E}$ range outside of 10 au, there is always at least one gas-dominated planet in the inner system and the outer system never harbours a second planet above 10 $M_{\rm E}$.

In this work, we study a large number of planets and planetary systems in various planet formation scenarios using realistic initial conditions for Sun-like stars. Yet, the formation of even a single ice giant resembling Uranus or Neptune occurs exceedingly rarely, highlighting the physical challenges that remain in the way of an explanation for the formation of the outer Solar System. This is the case despite the fact that our model is setup for optimistic predictions in terms of planetary growth in multiple ways, as described in Sect. 5. We identify that a pebble accretion scenario of multiple concurrently growing planets is the best suited setup to form ice giants in our model. However, Uranus/Neptune-analogues at 19.1 and 30 au, respectively, are not found at all. We further conclude that planetary migration is a vital ingredient for the outcome of planet formation, especially for planets at larger separations. This highlights that, in all likelihood, the formation of Uranus and Neptune can not be understood without the formation of Jupiter and Saturn and future modelling efforts should reflect that. Lastly, while the envelope opacity plays a central role for ice giant formation, constraints on the opacity can not easily be inferred from current H-He mass estimates of Uranus and Neptune, due to the chaotic nature of inter-planetary collisions which can change H-He mass fractions drastically. Finally, in light of a future mission to Uranus, we identify the need for a significant modelling effort to fully take advantage of a detailed in-situ characterisation of Uranus.

Acknowledgements. This work has been carried out within the framework of the National Centre of Competence in Research PlanetS supported by the Swiss National Science Foundation under grants 51NF40_182901 and 51NF40_205606. The authors acknowledge the financial support of the SNSF. We thank O. M. Guilera for his assistance with the implementation of the thermal torques.

References

2023, Origins, Worlds, and Life: A Decadal Strategy for Planetary Science and Astrobiology 2023-2032 (Washington, D.C.: National Academies Press)
Adachi, I., Hayashi, C., & Nakazawa, K. 1976, Progress of Theoretical Physics, 56, 1756
Adams, F. C., Lada, C. J., & Shu, F. H. 1988, ApJ, 326, 865
Alibert, Y., Mordasini, C., Benz, W., & Winisdoerffer, C. 2005, A&A, 434, 343
Andrews, S. M., Wilner, D. J., Hughes, A. M., Qi, C., & Dullemond, C. P. 2010, ApJ, 723, 1241
Ataiee, S., Baruteau, C., Alibert, Y., & Benz, W. 2018, A&A, 615, A110
Baraffe, I., Homeier, D., Allard, F., & Chabrier, G. 2015, A&A, 577, A42
Bell, K. R. & Lin, D. N. C. 1994, ApJ, 427, 987
Benítez-Llambay, P., Masset, F., Koenigsberger, G., & Szulágyi, J. 2015, Nature, 520, 63
Birnstiel, T., Dullemond, C. P., & Brauer, F. 2010, A&A, 513, A79
Birnstiel, T., Klahr, H., & Ercolano, B. 2012, A&A, 539, A148
Bitsch, B. & Kley, W. 2010, A&A, 523, A30
Bitsch, B., Lambrechts, M., & Johansen, A. 2018, A&A, 609, C2
Bodenheimer, P., D'Angelo, G., Lissauer, J. J., Fortney, J. J., & Saumon, D. 2013, ApJ, 770, 120
Bodenheimer, P. & Pollack, J. B. 1986, Icarus, 67, 391
Brouwers, M. G., Ormel, C. W., Bonsor, A., & Vazan, A. 2021, A&A, 653, A103
Chambers, J. 2006, Icarus, 180, 496
Chiang, E. I. & Goldreich, P. 1997, ApJ, 490, 368
Coleman, G. A. L. & Nelson, R. P. 2014, MNRAS, 445, 479
Crida, A., Morbidelli, A., & Masset, F. 2006, Icarus, 181, 587
Cuzzi, J. N., Dobrovolskis, A. R., & Champney, J. M. 1993, Icarus, 106, 102
Cuzzi, J. N., Hogan, R. C., Paque, J. M., & Dobrovolskis, A. R. 2001, ApJ, 546, 496
Dittkrist, K.-M., Mordasini, C., Klahr, H., Alibert, Y., & Henning, T. 2014, A&A, 567, A121
Dubrulle, B., Morfill, G., & Sterzik, M. 1995, Icarus, 114, 237
Emsenhuber, A., Mordasini, C., Burn, R., et al. 2021a, A&A, 656, A69
Emsenhuber, A., Mordasini, C., Burn, R., et al. 2021b, A&A, 656, A70
Eriksson, L. E. J., Mol Lous, M. A. S., Shibata, S., & Helled, R. 2023, Monthly Notices of the Royal Astronomical Society, 526, 4860
Fedele, D., van den Ancker, M. E., Henning, Th., Jayawardhana, R., & Oliveira, J. M. 2010, Astronomy and Astrophysics, 510, A72
Fendyke, S. M. & Nelson, R. P. 2014, MNRAS, 437, 96
Fortier, A., Alibert, Y., Carron, F., Benz, W., & Dittkrist, K.-M. 2013, A&A, 549, A44
Goldreich, P., Lithwick, Y., & Sari, R. 2004, Annual Review of Astronomy and Astrophysics, 42, 549
Goldreich, P. & Tremaine, S. 1979, ApJ, 233, 857
Guilera, O. M., Brunini, A., & Benvenuto, O. G. 2010, A&A, 521, A50
Guilera, O. M., Cuello, N., Montesinos, M., et al. 2019, MNRAS, 486, 5690
Guilera, O. M., Miller Bertolami, M. M., Masset, F., et al. 2021, MNRAS, 507, 3638
Haisch, Jr., K. E., Lada, E. A., & Lada, C. J. 2001, ApJ, 553, L153
Helled, R., Anderson, J. D., Podolak, M., & Schubert, G. 2011, The Astrophysical Journal, 726, 15
Helled, R. & Bodenheimer, P. 2014, ApJ, 789, 69
Hori, Y. & Ikoma, M. 2011, Monthly Notices of the Royal Astronomical Society, 416, 1419
Hueso, R. & Guillot, T. 2005, A&A, 442, 703
Inaba, S. & Ikoma, M. 2003, A&A, 410, 711
Inaba, S., Tanaka, H., Nakazawa, K., Wetherill, G. W., & Kokubo, E. 2001, Icarus, 149, 235
Jiang, H. & Ormel, C. W. 2022, Efficient Planet Formation by Pebble Accretion in ALMA Rings

Jiménez, M. A. & Masset, F. S. 2017, MNRAS, 471, 4917
Kanagawa, K. D., Muto, T., Tanaka, H., et al. 2016, Publications of the Astronomical Society of Japan, 68, 43
Kanagawa, K. D., Tanaka, H., Muto, T., & Tanigawa, T. 2017, Publications of the Astronomical Society of Japan, 69, 97
Kanagawa, K. D., Tanaka, H., & Szuszkiewicz, E. 2018, ApJ, 861, 140
Kaufmann, N. & Alibert, Y. 2023, The Influence of Planetesimal Fragmentation on Planet Formation
Kessler, A. & Alibert, Y. 2023, A&A, 674, A144
Kippenhahn, R. & Weigert, A. 1990, Stellar Structure and Evolution
Korycansky, D. G. & Pollack, J. B. 1993, Icarus, 102, 150
Lambrechts, M. & Johansen, A. 2012, A&A, 544, A32
Lambrechts, M. & Johansen, A. 2014, A&A, 572, A107
Lambrechts, M., Johansen, A., & Morbidelli, A. 2014, Astronomy and Astrophysics, 572, A35
Lau, T. C. H., Drążkowska, J., Stammler, S. M., Birnstiel, T., & Dullemond, C. P. 2022, A&A, 668, A170
Lee, E. J., Fuentes, J. R., & Hopkins, P. F. 2022, ApJ, 937, 95
Lega, E., Crida, A., Bitsch, B., & Morbidelli, A. 2014, MNRAS, 440, 683
Lin, D. N. C. & Papaloizou, J. 1986, ApJ, 309, 846
Liu, B., Raymond, S. N., & Jacobson, S. A. 2022, Nature, 604, 643
Lüst, R. 1952, Zeitschrift für Naturforschung A, 7, 87
Lynden-Bell, D. & Pringle, J. E. 1974, MNRAS, 168, 603
Masset, F. S. 2017, MNRAS, 472, 4204
Masset, F. S. & Velasco Romero, D. A. 2017, MNRAS, 465, 3175
Mordasini, C., Alibert, Y., Georgy, C., et al. 2012, A&A, 547, A112
Mordasini, C., Klahr, H., Alibert, Y., Miller, N., & Henning, T. 2014, A&A, 566, A141
Movshovitz, N., Bodenheimer, P., Podolak, M., & Lissauer, J. J. 2010, Icarus, 209, 616
Movshovitz, N. & Podolak, M. 2008, Icarus, 194, 368
Nakagawa, Y., Sekiya, M., & Hayashi, C. 1986, Icarus, 67, 375
Nakamoto, T. & Nakagawa, Y. 1994, ApJ, 421, 640
Nettelmann, N., Helled, R., Fortney, J. J., & Redmer, R. 2013, Planetary and Space Science, 77, 143
Ohtsuki, K., Stewart, G. R., & Ida, S. 2002, Icarus, 155, 436
Ormel, C. W. 2017, in Formation, Evolution, and Dynamics of Young Solar Systems, ed. M. Pessah & O. Gressel, Vol. 445 (Cham: Springer International Publishing), 197–228
Paardekooper, S. J., Baruteau, C., & Kley, W. 2011, MNRAS, 410, 293
Podolak, M., Pollack, J. B., & Reynolds, R. T. 1988, Icarus, 73, 163
Polak, B. & Klahr, H. 2022, High Resolution Study of Planetesimal Formation by Gravitational Collapse of Pebble Clouds
Pollack, J. B., Hubickyj, O., Bodenheimer, P., et al. 1996, Icarus, 124, 62
Pringle, J. E. 1981, ARA&A, 19, 137
Rafikov, R. R. 2004, AJ, 128, 1348
Reinhardt, C., Chau, A., Stadel, J., & Helled, R. 2020, Monthly Notices of the Royal Astronomical Society, 492, 5336
Richert, A. J. W., Getman, K. V., Feigelson, E. D., et al. 2018, Monthly Notices of the Royal Astronomical Society, 477, 5191
Ruden, S. P. & Pollack, J. B. 1991, ApJ, 375, 740
Safronov, V. S. 1972, Evolution of the Protoplanetary Cloud and Formation of the Earth and Planets.
Santos, N. C., Israelian, G., Mayor, M., et al. 2005, A&A, 437, 1127
Saumon, D., Chabrier, G., & van Horn, H. M. 1995, ApJ, 99, 713
Shakura, N. I. & Sunyaev, R. A. 1973, Symp. IAU, 55, 155
Shibaike, Y. & Alibert, Y. 2020, A&A, 644, A81
Stammler, S. M., Lichtenberg, T., Drążkowska, J., & Birnstiel, T. 2023, Leaky Dust Traps: How Fragmentation Impacts Dust Filtering by Planets
Stevenson, D. J. 1982, Planetary and Space Science, 30, 755
Tanaka, H., Takeuchi, T., & Ward, W. R. 2002, ApJ, 565, 1257
Tsiganis, K., Gomes, R., Morbidelli, A., & Levison, H. F. 2005, Nature, 435, 459
Tychoniec, Ł., Tobin, J. J., Karska, A., et al. 2018, ApJS, 238, 19
Valletta, C. & Helled, R. 2020, ApJ, 900, 133
Valletta, C. & Helled, R. 2022, ApJ, 931, 21
Velasco Romero, D. A. & Masset, F. S. 2020, MNRAS, 495, 2063
Venturini, J., Alibert, Y., Benz, W., & Ikoma, M. 2015, A&A, 576, A114
Venturini, J., Guilera, O. M., Ronco, M. P., & Mordasini, C. 2020, A&A, 644, A174
Venturini, J. & Helled, R. 2017, The Astrophysical Journal, 848, 95
Venturini, J. & Helled, R. 2020, A&A, 634, A31
Venuti, L., Bouvier, J., Cody, A. M., et al. 2017, A&A, 599, A23
Walsh, K. J., Morbidelli, A., Raymond, S. N., O'Brien, D. P., & Mandell, A. M. 2011, Nature, 475, 206
Ward, W. R. 1997, ApJ, 482, L211
Weder, J., Mordasini, C., & Emsenhuber, A. 2023, A&A, 674, A165
Weidenschilling, S. J. 1977, MNRAS, 180, 57
Youdin, A. N. & Lithwick, Y. 2007, Icarus, 192, 588

6 Conclusions and outlook

6.1 Conclusions

In this thesis, I apply a population synthesis approach using a global model of planet formation and evolution. In both projects, the combination of various physical processes is crucial for the results we present.
In the first paper, we show that the inclusion of pebble accretion does not necessarily provide an easy formation pathway for giant planets. While in planetesimals-only and pebbles-only simulations giants are able to form, the arising interplay between concurrent accretion of planetesimals and pebbles, as well as planetary migration, leads to a suppressed giant planet formation frequency. This highlights the importance of the inclusion of planetary migration, as well as the adequate treatment of the liberated accretion energy in planet formation models.
In the second paper, we explore different ice giant formation scenarios. Considering a wide set of initial conditions and physical mechanisms, we show that there is no straight-forward formation pathway emerging in over 13,000 simulations. This is despite the fact that the models are deliberately set up to favour planetary growth in the outer disk. The removal of growing protoplanets which are candidates to become future ice giants is driven by inward migration. Global models of unstructured disks struggle with this problem as soon as planets grow beyond a couple of Earth masses. We conclude once again that orbital migration is an extremely important aspect of planet formation and not only relevant for the formation of ice giants. In light of a future mission to Uranus, we identify the need for a significant modelling effort to fully take advantage of a detailed in-situ characterisation of Uranus.

In both presented papers, we highlight that due to the many interdependent physical mechanisms acting in planet formation, a priori counter-intuitive results can emerge and planet formation outcomes can not easily be predicted without

performing the simulations. This underlines the fact that, while specialised models are vital in order to understand the specific behaviour of individual processes, global models remain important to be able to make statements about the outcome of planet formation given a multitude of these interlinked processes. I emphasize that this brings significant practical challenges and costly computational requirements which remain a limiting factor with regards to the advance of planet formation theory.

6.2 Outlook

Complementary to the existing telescopes, there are multiple exciting observational facilities coming online in the near future. The *PLATO* space telescope is scheduled to launch in 2026 and will focus on the characterisation of terrestrial exoplanets, providing us with fundamental insights on potentially habitable worlds (Rauer et al., 2024). The *Roman Space Telescope*, scheduled to launch in 2027, will perform a microlensing survey which extends the detectable parameter space of exoplanets towards low-mass planets ($\gtrsim 0.01$ M_E) on orbits of a few au (Penny et al., 2019). The direct imaging capabilities of the *Extremely Large Telescope* (ELT), scheduled to receive first light in 2028, will open the door for atmospheric characterisation in high-contrast direct imaging (Marconi et al., 2024). In 2029, the *Ariel* space mission will again increase our capabilities to characterise exoplanet atmospheres using transmission spectroscopy.
For planet formation and evolution modelling, the current and future measurements of atmospheric abundances are an opportunity to link predicted elemental abundances with observations. In order to be able to disentangle competing formation scenarios, the tracking of bulk composition as well as the modelling of the redistribution of elements in geochemical and geophysical processes within the planets is crucial. These linked models, especially for the evolution of planets over billions of years, are necessary in order to be able to link atmospheric measurements of, for instance, water with the formation history of planets.

With the advent of resolved imaging of protoplanetary disks, a picture of prevalent disk substructures has emerged. Therefore, current and future formation modelling efforts are moving towards disks with ringed substructures due to, for instance, viscosity transitions or infall of cloud material onto the planetary disk.

In order to understand how this new emerging paradigm shapes the planet formation outcome on a population-level, a catalogue of well-characterised disks is needed. Future planetary population synthesis studies where disk substructures can be sampled from said catalogue are an interesting prospect. However, it remains challenging to detect forming planets in these disks and, therefore, it is still unclear whether disk substructures can be seen as an initial condition for planet formation or whether they are a signature of ongoing planet formation. Personally, I find this is one of the most intriguing current questions in the field. Given my experience over the last four years, I suspect that the answer is more complicated than the question might suggest.

A Viscous diffusion equation

The 1D axially symmetric viscous diffusion equation of a surface density Σ of a thin disk can be obtained by considering mass and angular momentum conservation of an annulus extending between r and $r + \Delta r$ of mass $M = 2\pi r \Delta r \Sigma$ (Pringle, 1981; Frank et al., 2002; Armitage, 2020). The rate of change of mass is given by the difference of mass entering at r and exiting at $r + \Delta r$:

$$\frac{\partial M}{\partial t} = \frac{\partial M(r)}{\partial t} - \frac{\partial M(r + \Delta r)}{\partial t}. \tag{A.1}$$

Considering mass flowing with a velocity v_r in the radial direction, mass conservation is given by

$$\frac{\partial}{\partial t}\left(2\pi r \Delta r \Sigma\right) = 2\pi r \Sigma(r) v_r(r) - 2\pi \left[r + \Delta r\right] \Sigma(r + \Delta r) v_r(r + \Delta r). \tag{A.2}$$

For small Δr, the following linear approximations hold for $\Sigma(r+\Delta r)$ and $v_r(r+\Delta r)$

$$\Sigma(r + \Delta r) = \Sigma(r) + \frac{\partial \Sigma(r)}{\partial r}\Delta r, \tag{A.3}$$

$$v_r(r + \Delta r) = v_r(r) + \frac{\partial v_r(r)}{\partial r}\Delta r. \tag{A.4}$$

Therefore, equation (A.2) can be rewritten as

$$\begin{aligned} r\Delta r\frac{\partial\Sigma}{\partial t} &= r\Sigma(r)v_r(r) - [r+\Delta r] \\ &\quad \times \left[\Sigma(r)v_r(r) + \Sigma(r)\frac{\partial v_r(r)}{\partial r}\Delta r + \frac{\partial\Sigma(r)}{\partial r}v_r(r)\Delta r + \mathcal{O}\left(\Delta r^2\right)\right] \\ &= -\left[\Sigma(r)v_r(r)\Delta r + r\frac{\partial\Sigma(r)}{\partial r}v_r(r)\Delta r + r\Sigma(r)\frac{\partial v_r(r)}{\partial r}\Delta r\right. \\ &\quad \left. + \mathcal{O}\left(\Delta r^2\right)\right] \\ &= -\left[\frac{\partial}{\partial r}\Big(r\Sigma(r)v_r(r)\Delta r\Big) + \mathcal{O}\left(\Delta r^2\right)\right]. \end{aligned} \tag{A.5}$$

Dividing by Δr and considering the limit of $\Delta r \to 0$, we finally obtain

$$r\frac{\partial\Sigma}{\partial t} = -\frac{\partial}{\partial r}\Big(r\Sigma v_r\Big). \tag{A.6}$$

The angular momentum of the annulus is $J = jM$, where $j = r^2\Omega$ is the angular momentum per unit mass at orbital frequency Ω. The rate of change of angular momentum is given by the change in mass distribution in the annulus due to a radial mass flow v_r and the net torque. For now we just consider a torque Γ of unspecified origin. In the same form as equation (A.2), angular momentum conservation reads

$$\begin{aligned} \frac{\partial}{\partial t}\left(r^2\Omega r\Delta r\Sigma\right) &= r^3\Omega(r)\Sigma(r)v_r(r) \\ &\quad - [r+\Delta r]^3\,\Omega(r+\Delta r)\Sigma(r+\Delta r)v_r(r+\Delta r) \\ &\quad + \frac{1}{2\pi}\left[\Gamma(r) - \Gamma(r+\Delta r)\right]. \end{aligned} \tag{A.7}$$

As before, and with the additional approximations for $\Omega(r+\Delta r)$ and $\Gamma(r+\Delta r)$

$$\Omega(r+\Delta r) = \Omega(r) + \frac{\partial\Omega(r)}{\partial r}\Delta r, \tag{A.8}$$

$$\Gamma(r+\Delta r) = \Gamma(r) + \frac{\partial\Gamma(r)}{\partial r}\Delta r, \tag{A.9}$$

angular momentum conservation can be rewritten as

$$\frac{\partial}{\partial t}\left(r^2\Omega r\Sigma\right)\Delta r \;=\; \ldots \;= -\frac{\partial}{\partial r}\Big(r^3\Omega(r)\Sigma(r)v_r(r)\Big)\Delta r + \frac{1}{2\pi}\frac{\partial\Gamma(r)}{\partial r}\Delta r + \mathcal{O}\left(\Delta r^2\right). \tag{A.10}$$

Again, dividing by Δr and considering the limit of $\Delta r \to 0$, we finally obtain

$$\frac{\partial}{\partial t}\left(r^2\Omega r\Sigma\right) = -\frac{\partial}{\partial r}\Big(r^2\Omega r\Sigma v_r\Big) + \frac{1}{2\pi}\frac{\partial\Gamma}{\partial r}. \tag{A.11}$$

We can eliminate v_r by assuming $\frac{\partial\Omega}{\partial t} = 0$ combining equations (A.6) and (A.11) as follows

$$\begin{aligned} r^3\Omega\frac{\partial\Sigma}{\partial t} &= -r^2\Omega\frac{\partial}{\partial r}\Big(r\Sigma v_r\Big) - \frac{\partial}{\partial r}\Big(r^2\Omega\Big)r\Sigma v_r + \frac{1}{2\pi}\frac{\partial\Gamma}{\partial r} \\ &= r^3\Omega\frac{\partial\Sigma}{\partial t} - \frac{\partial}{\partial r}\Big(r^2\Omega\Big)r\Sigma v_r + \frac{1}{2\pi}\frac{\partial\Gamma}{\partial r}, \end{aligned} \tag{A.12}$$

therefore we obtain,

$$\frac{\partial}{\partial r}\Big(r^2\Omega\Big)r\Sigma v_r = \frac{1}{2\pi}\frac{\partial\Gamma}{\partial r}, \tag{A.13}$$

and

$$r\Sigma v_r = \left(2\pi\frac{\partial}{\partial r}(r^2\Omega)\right)^{-1}\frac{\partial\Gamma}{\partial r}. \tag{A.14}$$

Finally, combining equations (A.14) and (A.6) yields the general equation for the surface density time evolution

$$\frac{\partial\Sigma}{\partial t} = -\frac{1}{r}\frac{\partial}{\partial r}\left[\left(2\pi\frac{\partial}{\partial r}(r^2\Omega)\right)^{-1}\frac{\partial\Gamma}{\partial r}\right]. \tag{A.15}$$

As described in chapter 2.1, angular momentum is transported due to a viscosity ν. The viscous force F_ϕ between two neighbouring annuli over a full orbit of length $2\pi r$, acting in the azimuthal ϕ-direction is given by

$$F_\phi = 2\pi r\nu\Sigma r\frac{\partial\Omega}{\partial r}, \tag{A.16}$$

where $r\frac{\partial\Omega}{\partial r}$ is the shearing rate caused by the differential orbital frequencies. The net torque Γ at distance r is then simply

$$\Gamma = rF_\phi = 2\pi r^3 \nu\Sigma \frac{\partial\Omega}{\partial r}. \tag{A.17}$$

Assuming a central point mass, a star of mass $M_\star$, the orbital frequency is the Keplerian frequency

$$\Omega_{\rm K} = \sqrt{\frac{GM_\star}{r^3}}, \tag{A.18}$$

with radial derivative

$$\frac{\partial\Omega_{\rm K}}{\partial r} = -\frac{3}{2r}\Omega_{\rm K}. \tag{A.19}$$

In this case, equation (A.15) can be rewritten in terms of Σ, r, and ν

$$\frac{\partial\Sigma}{\partial t} = \frac{3}{r}\frac{\partial}{\partial r}\left[\nu\frac{\partial\Sigma}{\partial r}r + \frac{1}{2}\nu\Sigma\right]. \tag{A.20}$$

This is usually rewritten as (Lüst, 1952; Lynden-Bell and Pringle, 1974)

$$\frac{\partial\Sigma}{\partial t} = \frac{3}{r}\frac{\partial}{\partial r}\left[r^{1/2}\frac{\partial}{\partial r}\left(\nu\Sigma r^{1/2}\right)\right]. \tag{A.21}$$

To estimate the stellar accretion rate, the steady-state solution is useful. Setting the angular momentum equation (A.11) to zero and integrating yields

$$\begin{aligned} const. &= -r^3\Omega\Sigma v_r + \frac{1}{2\pi}\Gamma \\ &= -2\pi r^3\Omega\Sigma v_r + 2\pi r^3\nu\Sigma\frac{\partial\Omega}{\partial r} \\ &= \dot{M}r^2\Omega + 2\pi r^3\nu\Sigma\frac{\partial\Omega}{\partial r}, \end{aligned} \tag{A.22}$$

where $\dot{M} = -2\pi r\Sigma v_r$ and the definition of the viscous torque Γ (A.17) are used[1]. Considering the simple case of the disk extending all the way to a non-rotating

[1]Note that the constant on the left-hand side is multiplied by a (constant) factor of 2π on the second line.

star of radius $R_\star$, the orbital frequency Ω of the gas increases continuously from 0 to Ω_K in a narrow boundary layer of width r_bl. Since Ω_K decreases with distance, there is a transition where $\frac{\partial\Omega}{\partial r} = 0$ which is where Ω becomes Keplerian. Assuming the boundary layer is thin, equation (A.22) simplifies to

$$const. = \dot{M} R_\star^2 \Omega_\mathrm{K}(R_\star) \tag{A.23}$$

and using the definition of Ω_K (A.18), the steady-state surface density Σ of a disk with viscosity ν and a constant accretion rate $\dot{M}$ is

$$\Sigma = \frac{\dot{M}}{3\pi\nu}\left(1 - \sqrt{\frac{R_\star}{r}}\right). \tag{A.24}$$

Bibliography

National Academies Press, Washington, D.C., Oct. 2023. ISBN 978-0-309-47578-5.

I. Adachi, C. Hayashi, and K. Nakazawa. *Progress of Theoretical Physics*, 56: 1756–1771, Dec. 1976. ISSN 0033-06840033-068X.

F. C. Adams, C. J. Lada, and F. H. Shu. *ApJ*, 326:865, Mar. 1988. ISSN 0004-637X.

A. Aguichine, O. Mousis, M. Deleuil, and E. Marcq. *ApJ*, 914(2):84, June 2021. ISSN 0004-637X.

R. D. Alexander and P. J. Armitage. *ApJ*, 704(2):989–1001, Sept. 2009. ISSN 0004-637X.

R. D. Alexander and I. Pascucci. *Monthly Notices of the Royal Astronomical Society*, 422:L82–L86, May 2012. ISSN 0035-8711.

Y. Alibert, C. Mordasini, and W. Benz. *Astronomy and Astrophysics*, 417:L25–L28, Apr. 2004. ISSN 0004-6361.

Y. Alibert, C. Mordasini, W. Benz, and C. Winisdoerffer. *A&A*, 434(1):343–353, Apr. 2005. ISSN 0004-6361.

Y. Alibert, F. Carron, A. Fortier, S. Pfyffer, W. Benz, C. Mordasini, and D. Swoboda. *A&A*, 558:A109, Oct. 2013. ISSN 0004-6361, 1432-0746.

S. M. Andrews. *Annual Review of Astronomy and Astrophysics*, 58:483–528, Aug. 2020. ISSN 0066-4146.

S. M. Andrews, D. J. Wilner, A. M. Hughes, C. Qi, and C. P. Dullemond. *ApJ*, 723(2):1241–1254, Oct. 2010. ISSN 0004-637X.

S. M. Andrews, K. A. Rosenfeld, A. L. Kraus, and D. J. Wilner. *The Astrophysical Journal*, 771:129, July 2013. ISSN 0004-637X.

M. Ansdell, J. P. Williams, N. van der Marel, J. M. Carpenter, G. Guidi, M. Hogerheijde, G. S. Mathews, C. F. Manara, A. Miotello, A. Natta, I. Oliveira, M. Tazzari, L. Testi, E. F. van Dishoeck, and S. E. van Terwisga. *ApJ*, 828(1):46, Aug. 2016. ISSN 0004-637X.

M. Ansdell, J. P. Williams, L. Trapman, S. E. van Terwisga, S. Facchini, C. F. Manara, N. van der Marel, A. Miotello, M. Tazzari, M. Hogerheijde, G. Guidi, L. Testi, and E. F. van Dishoeck. *The Astrophysical Journal*, 859:21, May 2018. ISSN 0004-637X.

P. J. Armitage. Cambridge University Press, Cambridge, 2 edition, 2020. ISBN 978-1-108-42050-1.

G. Aumatell and G. Wurm. *Monthly Notices of the Royal Astronomical Society*,

437(1):690–702, Jan. 2014. ISSN 0035-8711.

H. Avenhaus, S. P. Quanz, A. Garufi, S. Perez, S. Casassus, C. Pinte, G. H.-M. Bertrang, C. Caceres, M. Benisty, and C. Dominik. *ApJ*, 863(1):44, Aug. 2018. ISSN 0004-637X.

J. Bae, A. Isella, Z. Zhu, R. Martin, S. Okuzumi, and S. Suriano. 10.48550/arXiv.2210.13314Structured Distributions of Gas and Solids in Protoplanetary Disks, Oct. 2022.

S. Ballard and J. A. Johnson. *ApJ*, 816(2):66, Jan. 2016. ISSN 0004-637X.

S. A. Barenfeld, J. M. Carpenter, L. Ricci, and A. Isella. *ApJ*, 827(2):142, Aug. 2016. ISSN 0004-637X.

K. R. Bell and D. N. C. Lin. *ApJ*, 427:987, June 1994. ISSN 0004-637X.

M. Benisty, C. Dominik, K. Follette, A. Garufi, C. Ginski, J. Hashimoto, M. Keppler, W. Kley, and J. Monnier. 10.48550/arXiv.2203.09991Optical and Near-infrared View of Planet-forming Disks and Protoplanets, Mar. 2022.

W. Benz, S. Ida, Y. Alibert, D. Lin, and C. Mordasini. eprint: arXiv:1402.7086, Jan. 2014.

T. Birnstiel, C. P. Dullemond, and F. Brauer. *A&A*, 513:A79, Apr. 2010. ISSN 0004-6361, 1432-0746.

T. Birnstiel, H. Klahr, and B. Ercolano. *A&A*, 539:A148, Mar. 2012. ISSN 0004-6361, 1432-0746.

T. Birnstiel, M. Fang, and A. Johansen. *Space Science Reviews*, 205:41–75, Dec. 2016. ISSN 0038-6308.

B. Bitsch and W. Kley. *A&A*, 523:A30, Nov. 2010. ISSN 0004-6361.

B. Bitsch and W. Kley. *Astronomy and Astrophysics*, 530:A41, June 2011. ISSN 0004-6361.

B. Bitsch, M. Lambrechts, and A. Johansen. *A&A*, 582:A112, Oct. 2015. ISSN 0004-6361, 1432-0746.

J. Blum. *Space Science Reviews*, 214:52, Mar. 2018. ISSN 0038-6308.

P. Bodenheimer, G. D'Angelo, J. J. Lissauer, J. J. Fortney, and D. Saumon. *ApJ*, 770(2):120, June 2013. ISSN 0004-637X.

S. J. Bolton, A. Adriani, V. Adumitroaie, M. Allison, J. Anderson, S. Atreya, J. Bloxham, S. Brown, J. E. P. Connerney, E. DeJong, W. Folkner, D. Gautier, D. Grassi, S. Gulkis, T. Guillot, C. Hansen, W. B. Hubbard, L. Iess, A. Ingersoll, M. Janssen, J. Jorgensen, Y. Kaspi, S. M. Levin, C. Li, J. Lunine, Y. Miguel, A. Mura, G. Orton, T. Owen, M. Ravine, E. Smith, P. Steffes, E. Stone, D. Stevenson, R. Thorne, J. Waite, D. Durante, R. W. Ebert, T. K.

Greathouse, V. Hue, M. Parisi, J. R. Szalay, and R. Wilson. *Science*, 356: 821–825, May 2017. ISSN 0036-8075.

C. H. Broeg and W. Benz. *Astronomy and Astrophysics*, 538:A90, Feb. 2012. ISSN 0004-6361.

M. G. Brouwers and C. W. Ormel. *A&A*, 634:A15, Feb. 2020. ISSN 0004-6361, 1432-0746.

M. G. Brouwers, C. W. Ormel, A. Bonsor, and A. Vazan. *A&A*, 653:A103, Sept. 2021. ISSN 0004-6361, 1432-0746.

N. Brügger, Y. Alibert, S. Ataiee, and W. Benz. *A&A*, 619:A174, Nov. 2018. ISSN 0004-6361, 1432-0746.

N. Brügger, R. Burn, G. Coleman, Y. Alibert, and W. Benz. *A&A*, 640:A21, Aug. 2020. ISSN 0004-6361, 1432-0746.

M. L. Bryan, H. A. Knutson, E. J. Lee, B. J. Fulton, K. Batygin, H. Ngo, and T. Meshkat. *The Astronomical Journal*, 157:52, Feb. 2019. ISSN 0004-6256.

R. Burn and C. Mordasini. 10.48550/arXiv.2410.00093Planetary population synthesis, Sept. 2024.

R. Burn, M. Schlecker, C. Mordasini, A. Emsenhuber, Y. Alibert, T. Henning, H. Klahr, and W. Benz. *A&A*, 656:A72, Dec. 2021. ISSN 0004-6361, 1432-0746.

R. Burn, A. Emsenhuber, J. Weder, O. Völkel, H. Klahr, T. Birnstiel, B. Ercolano, and C. Mordasini. *A&A*, 666:A73, Oct. 2022. ISSN 0004-6361, 1432-0746.

R. Burn, C. Mordasini, L. Mishra, J. Haldemann, J. Venturini, A. Emsenhuber, and T. Henning. *Nat Astron*, 8(4):463–471, Apr. 2024. ISSN 2397-3366.

J. Chambers. *Icarus*, 180(2):496–513, Feb. 2006. ISSN 0019-1035.

J. E. Chambers. *Monthly Notices of the Royal Astronomical Society*, 304(4):793–799, Apr. 1999. ISSN 0035-8711.

J. E. Chambers. *The Astrophysical Journal*, 705:1206–1214, Nov. 2009. ISSN 0004-637X.

D. Charbonneau, T. M. Brown, D. W. Latham, and M. Mayor. *The Astrophysical Journal*, 529:L45–L48, Jan. 2000. ISSN 0004-637X.

A. Chau, C. Reinhardt, R. Helled, and J. Stadel. *ApJ*, 865(1):35, Sept. 2018. ISSN 0004-637X.

E. I. Chiang and P. Goldreich. *ApJ*, 490:368–376, Nov. 1997. ISSN 0004-637X.

C. J. Clarke, A. Gendrin, and M. Sotomayor. *Monthly Notices of the Royal Astronomical Society*, 328:485–491, Dec. 2001. ISSN 0035-8711.

G. A. L. Coleman and R. P. Nelson. *MNRAS*, 445(1):479–499, Nov. 2014. ISSN 0035-8711.

P. Cresswell and R. P. Nelson. *Astronomy and Astrophysics*, 482:677–690, May 2008. ISSN 0004-6361.

A. Crida, A. Morbidelli, and F. Masset. *Icarus*, 181:587–604, Apr. 2006. ISSN 0019-1035.

A. Cumming, R. P. Butler, G. W. Marcy, S. S. Vogt, J. T. Wright, and D. A. Fischer. *Publications of the Astronomical Society of the Pacific*, 120:531, May 2008. ISSN 0004-6280.

J. N. Cuzzi and K. J. Zahnle. *ApJ*, 614(1):490, Oct. 2004. ISSN 0004-637X.

J. N. Cuzzi, R. C. Hogan, J. M. Paque, and A. R. Dobrovolskis. *ApJ*, 546(1):496, Jan. 2001. ISSN 0004-637X.

J. N. Cuzzi, R. C. Hogan, and K. Shariff. *ApJ*, 687(2):1432, Nov. 2008. ISSN 0004-637X.

J. Davoult, Y. Alibert, and L. Mishra. *A&A*, Aug. 2024. ISSN 0004-6361, 1432-0746.

K.-M. Dittkrist, C. Mordasini, H. Klahr, Y. Alibert, and T. Henning. *A&A*, 567: A121, July 2014. ISSN 0004-6361.

R. Dong, Z. Zhu, and B. Whitney. *ApJ*, 809(1):93, Aug. 2015. ISSN 0004-637X.

J. Drążkowska and Y. Alibert. *A&A*, 608:A92, Dec. 2017. ISSN 0004-6361.

J. Drazkowska, B. Bitsch, M. Lambrechts, G. D. Mulders, D. Harsono, A. Vazan, B. Liu, C. W. Ormel, K. Kretke, and A. Morbidelli. 10.48550/arXiv.2203.09759Planet Formation Theory in the Era of ALMA and Kepler: From Pebbles to Exoplanets, Oct. 2022.

C. D. Dressing and D. Charbonneau. *The Astrophysical Journal*, 767:95, Apr. 2013. ISSN 0004-637X.

C. D. Dressing and D. Charbonneau. *The Astrophysical Journal*, 807:45, July 2015. ISSN 0004-637X.

X. Dumusque. *A&A*, 593:A5, Sept. 2016. ISSN 0004-6361, 1432-0746.

A. Dutrey, S. Guilloteau, L. Prato, M. Simon, G. Duvert, K. Schuster, and F. Menard. *Astronomy and Astrophysics*, 338:L63–L66, Oct. 1998. ISSN 0004-6361.

J. A. Egger, H. P. Osborn, D. Kubyshkina, C. Mordasini, Y. Alibert, M. N. Günther, M. Lendl, A. Brandeker, A. Heitzmann, A. Leleu, M. Damasso, A. Bonfanti, T. G. Wilson, S. G. Sousa, J. Haldemann, L. Delrez, M. J. Hooton, T. Zingales, R. Luque, R. Alonso, J. Asquier, T. Bárczy, D. B. Navascues, S. C. C. Barros, W. Baumjohann, W. Benz, N. Billot, L. Borsato, C. Broeg, M. Buder, A. Castro-González, A. C. Cameron, A. C. M. Correia, D. Cortes, Sz. Csizmadia,

P. E. Cubillos, M. B. Davies, M. Deleuil, A. Deline, O. D. S. Demangeon, B. O. Demory, A. Derekas, B. Edwards, D. Ehrenreich, A. Erikson, A. Fortier, L. Fossati, M. Fridlund, D. Gandolfi, K. Gazeas, M. Gillon, M. Güdel, Ch. Helling, K. G. Isaak, L. L. Kiss, J. Korth, K. W. F. Lam, J. Laskar, B. Lavie, A. L. des Etangs, C. Lovis, A. Luntzer, D. Magrin, P. F. L. Maxted, B. Merín, M. Munari, V. Nascimbeni, G. Olofsson, R. Ottensamer, I. Pagano, E. Pallé, G. Peter, D. Piazza, G. Piotto, D. Pollacco, D. Queloz, R. Ragazzoni, N. Rando, H. Rauer, I. Ribas, J. Rodrigues, N. C. Santos, G. Scandariato, D. Ségransan, A. E. Simon, A. M. S. Smith, M. Stalport, S. Sulis, Gy. M. Szabó, S. Udry, V. Van Grootel, J. Venturini, E. Villaver, and N. A. Walton. *Astronomy and Astrophysics*, 688: A223, Aug. 2024. ISSN 0004-6361.

A. Emsenhuber, C. Mordasini, R. Burn, Y. Alibert, W. Benz, and E. Asphaug. *A&A*, 656:A69, Dec. 2021a. ISSN 0004-6361, 1432-0746.

A. Emsenhuber, C. Mordasini, R. Burn, Y. Alibert, W. Benz, and E. Asphaug. *A&A*, 656:A70, Dec. 2021b. ISSN 0004-6361, 1432-0746.

A. Emsenhuber, R. Burn, J. Weder, K. Monsch, G. Picogna, B. Ercolano, and T. Preibisch. *Astronomy and Astrophysics*, 673:A78, May 2023a. ISSN 0004-6361.

A. Emsenhuber, C. Mordasini, and R. Burn. *European Physical Journal Plus*, 138: 181, Feb. 2023b.

P. R. Estrada, J. N. Cuzzi, and D. A. Morgan. *ApJ*, 818(2):200, Feb. 2016. ISSN 0004-637X.

P. R. Estrada, J. N. Cuzzi, and O. M. Umurhan. *ApJ*, 936(1):42, Aug. 2022. ISSN 0004-637X.

N. J. Evans, II, M. M. Dunham, J. K. Jørgensen, M. L. Enoch, B. Merín, E. F. van Dishoeck, J. M. Alcalá, P. C. Myers, K. R. Stapelfeldt, T. L. Huard, L. E. Allen, P. M. Harvey, T. van Kempen, G. A. Blake, D. W. Koerner, L. G. Mundy, D. L. Padgett, and A. I. Sargent. *The Astrophysical Journal Supplement Series*, 181:321–350, Apr. 2009. ISSN 0067-0049.

S. M. Fendyke and R. P. Nelson. *MNRAS*, 437(1):96–107, Jan. 2014. ISSN 0035-8711.

R. B. Fernandes, G. D. Mulders, I. Pascucci, C. Mordasini, and A. Emsenhuber. *The Astrophysical Journal*, 874:81, Mar. 2019. ISSN 0004-637X.

G. B. Field, W. B. Somerville, and K. Dressler. *Annual Review of Astronomy and Astrophysics*, 4:207, Jan. 1966. ISSN 0066-4146.

D. A. Fischer and J. Valenti. *The Astrophysical Journal*, 622:1102–1117, Apr.

2005. ISSN 0004-637X.

A. Fortier, Y. Alibert, F. Carron, W. Benz, and K.-M. Dittkrist. *A&A*, 549:A44, Jan. 2013. ISSN 0004-6361.

L. Fouchet, Y. Alibert, C. Mordasini, and W. Benz. *A&A*, 540:A107, Apr. 2012. ISSN 0004-6361, 1432-0746.

J. Frank, A. King, and D. J. Raine. Jan. 2002.

R. S. Freedman, J. Lustig-Yaeger, J. J. Fortney, R. E. Lupu, M. S. Marley, and K. Lodders. *ApJS*, 214(2):25, Oct. 2014. ISSN 0067-0049.

F. Fressin, G. Torres, J. F. Rowe, D. Charbonneau, L. A. Rogers, S. Ballard, N. M. Batalha, W. J. Borucki, S. T. Bryson, L. A. Buchhave, D. R. Ciardi, J.-M. Désert, C. D. Dressing, D. C. Fabrycky, E. B. Ford, T. N. Gautier III, C. E. Henze, M. J. Holman, A. Howard, S. B. Howell, J. M. Jenkins, D. G. Koch, D. W. Latham, J. J. Lissauer, G. W. Marcy, S. N. Quinn, D. Ragozzine, D. D. Sasselov, S. Seager, T. Barclay, F. Mullally, S. E. Seader, M. Still, J. D. Twicken, S. E. Thompson, and K. Uddin. *Nature*, 482(7384):195–198, Feb. 2012. ISSN 1476-4687.

F. Fressin, G. Torres, D. Charbonneau, S. T. Bryson, J. Christiansen, C. D. Dressing, J. M. Jenkins, L. M. Walkowicz, and N. M. Batalha. *The Astrophysical Journal*, 766:81, Apr. 2013. ISSN 0004-637X.

B. J. Fulton and E. A. Petigura. *The Astronomical Journal*, 156:264, Dec. 2018. ISSN 0004-6256.

B. J. Fulton, E. A. Petigura, A. W. Howard, H. Isaacson, G. W. Marcy, P. A. Cargile, L. Hebb, L. M. Weiss, J. A. Johnson, T. D. Morton, E. Sinukoff, I. J. M. Crossfield, and L. A. Hirsch. *The Astronomical Journal*, 154:109, Sept. 2017. ISSN 0004-6256.

B. J. Fulton, L. J. Rosenthal, L. A. Hirsch, H. Isaacson, A. W. Howard, C. M. Dedrick, I. A. Sherstyuk, S. C. Blunt, E. A. Petigura, H. A. Knutson, A. Behmard, A. Chontos, J. R. Crepp, I. J. M. Crossfield, P. A. Dalba, D. A. Fischer, G. W. Henry, S. R. Kane, M. Kosiarek, G. W. Marcy, R. A. Rubenzahl, L. M. Weiss, and J. T. Wright. *The Astrophysical Journal Supplement Series*, 255:14, July 2021. ISSN 0067-0049.

Gaia Collaboration, A. G. A. Brown, A. Vallenari, T. Prusti, J. H. J. de Bruijne, C. Babusiaux, C. A. L. Bailer-Jones, M. Biermann, D. W. Evans, L. Eyer, F. Jansen, C. Jordi, S. A. Klioner, U. Lammers, L. Lindegren, X. Luri, F. Mignard, C. Panem, D. Pourbaix, S. Randich, P. Sartoretti, H. I. Siddiqui,

C. Soubiran, F. van Leeuwen, N. A. Walton, F. Arenou, U. Bastian, M. Cropper, R. Drimmel, D. Katz, M. G. Lattanzi, J. Bakker, C. Cacciari, J. Castañeda, L. Chaoul, N. Cheek, F. De Angeli, C. Fabricius, R. Guerra, B. Holl, E. Masana, R. Messineo, N. Mowlavi, K. Nienartowicz, P. Panuzzo, J. Portell, M. Riello, G. M. Seabroke, P. Tanga, F. Thévenin, G. Gracia-Abril, G. Comoretto, M. Garcia-Reinaldos, D. Teyssier, M. Altmann, R. Andrae, M. Audard, I. Bellas-Velidis, K. Benson, J. Berthier, R. Blomme, P. Burgess, G. Busso, B. Carry, A. Cellino, G. Clementini, M. Clotet, O. Creevey, M. Davidson, J. De Ridder, L. Delchambre, A. Dell'Oro, C. Ducourant, J. Fernández-Hernández, M. Fouesneau, Y. Frémat, L. Galluccio, M. García-Torres, J. González-Núñez, J. J. González-Vidal, E. Gosset, L. P. Guy, J. L. Halbwachs, N. C. Hambly, D. L. Harrison, J. Hernández, D. Hestroffer, S. T. Hodgkin, A. Hutton, G. Jasniewicz, A. Jean-Antoine-Piccolo, S. Jordan, A. J. Korn, A. Krone-Martins, A. C. Lanzafame, T. Lebzelter, W. Löffler, M. Manteiga, P. M. Marrese, J. M. Martín-Fleitas, A. Moitinho, A. Mora, K. Muinonen, J. Osinde, E. Pancino, T. Pauwels, J. M. Petit, A. Recio-Blanco, P. J. Richards, L. Rimoldini, A. C. Robin, L. M. Sarro, C. Siopis, M. Smith, A. Sozzetti, M. Süveges, J. Torra, W. van Reeven, U. Abbas, A. Abreu Aramburu, S. Accart, C. Aerts, G. Altavilla, M. A. Álvarez, R. Alvarez, J. Alves, R. I. Anderson, A. H. Andrei, E. Anglada Varela, E. Antiche, T. Antoja, B. Arcay, T. L. Astraatmadja, N. Bach, S. G. Baker, L. Balaguer-Núñez, P. Balm, C. Barache, C. Barata, D. Barbato, F. Barblan, P. S. Barklem, D. Barrado, M. Barros, M. A. Barstow, S. Bartholomé Muñoz, J. L. Bassilana, U. Becciani, M. Bellazzini, A. Berihuete, S. Bertone, L. Bianchi, O. Bienaymé, S. Blanco-Cuaresma, T. Boch, C. Boeche, A. Bombrun, R. Borrachero, D. Bossini, S. Bouquillon, G. Bourda, A. Bragaglia, L. Bramante, M. A. Breddels, A. Bressan, N. Brouillet, T. Brüsemeister, E. Brugaletta, B. Bucciarelli, A. Burlacu, D. Busonero, A. G. Butkevich, R. Buzzi, E. Caffau, R. Cancelliere, G. Cannizzaro, T. Cantat-Gaudin, R. Carballo, T. Carlucci, J. M. Carrasco, L. Casamiquela, M. Castellani, A. Castro-Ginard, P. Charlot, L. Chemin, A. Chiavassa, G. Cocozza, G. Costigan, S. Cowell, F. Crifo, M. Crosta, C. Crowley, J. Cuypers, C. Dafonte, Y. Damerdji, A. Dapergolas, P. David, M. David, P. de Laverny, F. De Luise, R. De March, D. de Martino, R. de Souza, A. de Torres, J. Debosscher, E. del Pozo, M. Delbo, A. Delgado, H. E. Delgado, P. Di Matteo, S. Diakite, C. Diener, E. Distefano, C. Dolding, P. Drazinos, J. Durán, B. Edvardsson, H. Enke, K. Eriksson, P. Esquej, G. Eynard Bontemps, C. Fabre, M. Fabrizio, S. Faigler, A. J.

Falcão, M. Farràs Casas, L. Federici, G. Fedorets, P. Fernique, F. Figueras, F. Filippi, K. Findeisen, A. Fonti, E. Fraile, M. Fraser, B. Frézouls, M. Gai, S. Galleti, D. Garabato, F. García-Sedano, A. Garofalo, N. Garralda, A. Gavel, P. Gavras, J. Gerssen, R. Geyer, P. Giacobbe, G. Gilmore, S. Girona, G. Giuffrida, F. Glass, M. Gomes, M. Granvik, A. Gueguen, A. Guerrier, J. Guiraud, R. Gutiérrez-Sánchez, R. Haigron, D. Hatzidimitriou, M. Hauser, M. Haywood, U. Heiter, A. Helmi, J. Heu, T. Hilger, D. Hobbs, W. Hofmann, G. Holland, H. E. Huckle, A. Hypki, V. Icardi, K. Janßen, G. Jevardat de Fombelle, P. G. Jonker, Á. L. Juhász, F. Julbe, A. Karampelas, A. Kewley, J. Klar, A. Kochoska, R. Kohley, K. Kolenberg, M. Kontizas, E. Kontizas, S. E. Koposov, G. Kordopatis, Z. Kostrzewa-Rutkowska, P. Koubsky, S. Lambert, A. F. Lanza, Y. Lasne, J. B. Lavigne, Y. Le Fustec, C. Le Poncin-Lafitte, Y. Lebreton, S. Leccia, N. Leclerc, I. Lecoeur-Taibi, H. Lenhardt, F. Leroux, S. Liao, E. Licata, H. E. P. Lindstrøm, T. A. Lister, E. Livanou, A. Lobel, M. López, S. Managau, R. G. Mann, G. Mantelet, O. Marchal, J. M. Marchant, M. Marconi, S. Marinoni, G. Marschalkó, D. J. Marshall, M. Martino, G. Marton, N. Mary, D. Massari, G. Matijevič, T. Mazeh, P. J. McMillan, S. Messina, D. Michalik, N. R. Millar, D. Molina, R. Molinaro, L. Molnár, P. Montegriffo, R. Mor, R. Morbidelli, T. Morel, D. Morris, A. F. Mulone, T. Muraveva, I. Musella, G. Nelemans, L. Nicastro, L. Noval, W. O'Mullane, C. Ordénovic, D. Ordóñez-Blanco, P. Osborne, C. Pagani, I. Pagano, F. Pailler, H. Palacin, L. Palaversa, A. Panahi, M. Pawlak, A. M. Piersimoni, F. X. Pineau, E. Plachy, G. Plum, E. Poggio, E. Poujoulet, A. Prša, L. Pulone, E. Racero, S. Ragaini, N. Rambaux, M. Ramos-Lerate, S. Regibo, C. Reylé, F. Riclet, V. Ripepi, A. Riva, A. Rivard, G. Rixon, T. Roegiers, M. Roelens, M. Romero-Gómez, N. Rowell, F. Royer, L. Ruiz-Dern, G. Sadowski, T. Sagristà Sellés, J. Sahlmann, J. Salgado, E. Salguero, N. Sanna, T. Santana-Ros, M. Sarasso, H. Savietto, M. Schultheis, E. Sciacca, M. Segol, J. C. Segovia, D. Ségransan, I. C. Shih, L. Siltala, A. F. Silva, R. L. Smart, K. W. Smith, E. Solano, F. Solitro, R. Sordo, S. Soria Nieto, J. Souchay, A. Spagna, F. Spoto, U. Stampa, I. A. Steele, H. Steidelmüller, C. A. Stephenson, H. Stoev, F. F. Suess, J. Surdej, L. Szabados, E. Szegedi-Elek, D. Tapiador, F. Taris, G. Tauran, M. B. Taylor, R. Teixeira, D. Terrett, P. Teyssandier, W. Thuillot, A. Titarenko, F. Torra Clotet, C. Turon, A. Ulla, E. Utrilla, S. Uzzi, M. Vaillant, G. Valentini, V. Valette, A. van Elteren, E. Van Hemelryck, M. van Leeuwen, M. Vaschetto, A. Vecchiato, J. Veljanoski,

Y. Viala, D. Vicente, S. Vogt, C. von Essen, H. Voss, V. Votruba, S. Voutsinas, G. Walmsley, M. Weiler, O. Wertz, T. Wevers, Ł. Wyrzykowski, A. Yoldas, M. Žerjal, H. Ziaeepour, J. Zorec, S. Zschocke, S. Zucker, C. Zurbach, and T. Zwitter. *Astronomy and Astrophysics*, 616:A1, Aug. 2018. ISSN 0004-6361.

G. J. Gilbert and D. C. Fabrycky. *AJ*, 159(6):281, May 2020. ISSN 1538-3881.

M. Gillon, E. Jehin, S. M. Lederer, L. Delrez, J. de Wit, A. Burdanov, V. Van Grootel, A. J. Burgasser, A. H. M. J. Triaud, C. Opitom, B.-O. Demory, D. K. Sahu, D. Bardalez Gagliuffi, P. Magain, and D. Queloz. *Nature*, 533(7602):221–224, May 2016. ISSN 1476-4687.

M. Gillon, A. H. M. J. Triaud, B.-O. Demory, E. Jehin, E. Agol, K. M. Deck, S. M. Lederer, J. de Wit, A. Burdanov, J. G. Ingalls, E. Bolmont, J. Leconte, S. N. Raymond, F. Selsis, M. Turbet, K. Barkaoui, A. Burgasser, M. R. Burleigh, S. J. Carey, A. Chaushev, C. M. Copperwheat, L. Delrez, C. S. Fernandes, D. L. Holdsworth, E. J. Kotze, V. Van Grootel, Y. Almleaky, Z. Benkhaldoun, P. Magain, and D. Queloz. *Nature*, 542(7642):456–460, Feb. 2017. ISSN 1476-4687.

S. Ginzburg, H. E. Schlichting, and R. Sari. *ApJ*, 825(1):29, June 2016. ISSN 0004-637X.

P. Goldreich and S. Tremaine. *ApJ*, 233:857–871, Nov. 1979. ISSN 0004-637X.

P. Goldreich and W. R. Ward. *The Astrophysical Journal*, 183:1051–1062, Aug. 1973. ISSN 0004-637X.

R. Greenberg, J. F. Wacker, W. K. Hartmann, and C. R. Chapman. *Icarus*, 35 (1):1–26, July 1978. ISSN 0019-1035.

O. M. Guilera and Zs. Sándor. *Astronomy and Astrophysics*, 604:A10, July 2017. ISSN 0004-6361.

O. M. Guilera, A. Brunini, and O. G. Benvenuto. *A&A*, 521:A50, Oct. 2010. ISSN 0004-6361.

O. M. Guilera, G. C. de Elía, A. Brunini, and P. J. Santamaría. *A&A*, 565:A96, May 2014. ISSN 0004-6361, 1432-0746.

O. M. Guilera, N. Cuello, M. Montesinos, M. M. Miller Bertolami, M. P. Ronco, J. Cuadra, and F. S. Masset. *MNRAS*, 486(4):5690–5708, July 2019. ISSN 0035-8711.

O. M. Guilera, Z. Sándor, M. P. Ronco, J. Venturini, and M. M. M. Bertolami. *A&A*, 642:A140, Oct. 2020. ISSN 0004-6361, 1432-0746.

O. M. Guilera, M. M. Miller Bertolami, F. Masset, J. Cuadra, J. Venturini, and M. P. Ronco. *MNRAS*, 507(3):3638–3652, Nov. 2021. ISSN 0035-8711.

T. Guillot. *Annual Review of Earth and Planetary Sciences*, 33:493–530, Jan. 2005. ISSN 0084-6597.

T. Guillot, S. Ida, and C. W. Ormel. *A&A*, 572:A72, Dec. 2014. ISSN 0004-6361, 1432-0746.

B. Gundlach and J. Blum. *ApJ*, 798(1):34, Dec. 2014. ISSN 0004-637X.

B. Gundlach, K. P. Schmidt, C. Kreuzig, D. Bischoff, F. Rezaei, S. Kothe, J. Blum, B. Grzesik, and E. Stoll. *Monthly Notices of the Royal Astronomical Society*, 479(1):1273–1277, Sept. 2018. ISSN 0035-8711.

A. Gupta and H. E. Schlichting. *Monthly Notices of the Royal Astronomical Society*, 487(1):24–33, July 2019. ISSN 0035-8711.

J. Haldemann, Y. Alibert, C. Mordasini, and W. Benz. *A&A*, 643:A105, Nov. 2020. ISSN 0004-6361, 1432-0746.

T. Hartlep and J. N. Cuzzi. *ApJ*, 892(2):120, Apr. 2020. ISSN 0004-637X.

L. Hartmann, R. Hewett, and N. Calvet. *The Astrophysical Journal*, 426:669, May 1994. ISSN 0004-637X.

L. Hartmann, G. Herczeg, and N. Calvet. *Annual Review of Astronomy and Astrophysics*, 54:135–180, Sept. 2016. ISSN 0066-4146.

M. Y. He, E. B. Ford, and D. Ragozzine. *Monthly Notices of the Royal Astronomical Society*, 490(4):4575–4605, Dec. 2019. ISSN 0035-8711.

M. Y. He, E. B. Ford, and D. Ragozzine. *The Astronomical Journal*, 161:16, Jan. 2021. ISSN 0004-6256.

R. Helled. On the mass of gas giant planets: Is Saturn a failed gas giant?, June 2023.

R. Helled, J. D. Anderson, M. Podolak, and G. Schubert. *The Astrophysical Journal*, 726:15, Jan. 2011. ISSN 0004-637X.

G. W. Henry, G. Marcy, R. P. Butler, and S. S. Vogt. *International Astronomical Union Circular*, 7307:1, Nov. 1999. ISSN 0081-0304.

R. H. Hildebrand. *Quarterly Journal of the Royal Astronomical Society*, 24:267–282, Sept. 1983. ISSN 0035-8738.

C. S. K. Ho and V. Van Eylen. *Monthly Notices of the Royal Astronomical Society*, 519(3):4056–4073, Mar. 2023. ISSN 0035-8711.

D. Hollenbach, D. Johnstone, S. Lizano, and F. Shu. *The Astrophysical Journal*, 428:654, June 1994. ISSN 0004-637X.

A. W. Howard, G. W. Marcy, S. T. Bryson, J. M. Jenkins, J. F. Rowe, N. M. Batalha, W. J. Borucki, D. G. Koch, E. W. Dunham, T. N. Gautier, III, J. Van Cleve, W. D. Cochran, D. W. Latham, J. J. Lissauer, G. Torres,

T. M. Brown, R. L. Gilliland, L. A. Buchhave, D. A. Caldwell, J. Christensen-Dalsgaard, D. Ciardi, F. Fressin, M. R. Haas, S. B. Howell, H. Kjeldsen, S. Seager, L. Rogers, D. D. Sasselov, J. H. Steffen, G. S. Basri, D. Charbonneau, J. Christiansen, B. Clarke, A. Dupree, D. C. Fabrycky, D. A. Fischer, E. B. Ford, J. J. Fortney, J. Tarter, F. R. Girouard, M. J. Holman, J. A. Johnson, T. C. Klaus, P. Machalek, A. V. Moorhead, R. C. Morehead, D. Ragozzine, P. Tenenbaum, J. D. Twicken, S. N. Quinn, H. Isaacson, A. Shporer, P. W. Lucas, L. M. Walkowicz, W. F. Welsh, A. Boss, E. Devore, A. Gould, J. C. Smith, R. L. Morris, A. Prsa, T. D. Morton, M. Still, S. E. Thompson, F. Mullally, M. Endl, and P. J. MacQueen. *The Astrophysical Journal Supplement Series*, 201:15, Aug. 2012. ISSN 0067-0049.

D. C. Hsu, E. B. Ford, D. Ragozzine, and K. Ashby. *AJ*, 158(3):109, Aug. 2019. ISSN 1538-3881.

D. C. Hsu, E. B. Ford, and R. Terrien. *Monthly Notices of the Royal Astronomical Society*, 498(2):2249–2262, Sept. 2020. ISSN 0035-8711.

C. Huang, Y. Wu, and A. H. M. J. Triaud. *The Astrophysical Journal*, 825:98, July 2016. ISSN 0004-637X.

R. Hueso and T. Guillot. *A&A*, 442(2):703–725, Nov. 2005. ISSN 0004-6361.

S. Ida and D. N. C. Lin. *The Astrophysical Journal*, 604:388–413, Mar. 2004a. ISSN 0004-637X.

S. Ida and D. N. C. Lin. *The Astrophysical Journal*, 616:567–572, Nov. 2004b. ISSN 0004-637X.

S. Ida and D. N. C. Lin. *The Astrophysical Journal*, 673:487–501, Jan. 2008. ISSN 0004-637X.

S. Ida and J. Makino. *Icarus*, 106(1):210–227, Nov. 1993. ISSN 0019-1035.

S. Ida, R. M. Canup, and G. R. Stewart. *Nature*, 389:353–357, Sept. 1997. ISSN 0028-0836.

S. Ida, T. Guillot, and A. Morbidelli. *A&A*, 591:A72, July 2016. ISSN 0004-6361, 1432-0746.

M. Ikoma, K. Nakazawa, and H. Emori. *The Astrophysical Journal*, 537:1013–1025, July 2000. ISSN 0004-637X.

S. Inaba and M. Ikoma. *A&A*, 410:711, Nov. 2003. ISSN 0004-6361.

S. Inaba, H. Tanaka, K. Nakazawa, G. W. Wetherill, and E. Kokubo. *Icarus*, 149 (1):235–250, Jan. 2001. ISSN 0019-1035.

A. Izidoro, M. Ogihara, S. N. Raymond, A. Morbidelli, A. Pierens, B. Bitsch, C. Cossou, and F. Hersant. *Monthly Notices of the Royal Astronomical Society*,

470(2):1750–1770, Sept. 2017. ISSN 0035-8711.

A. P. Jackson, T. A. Davis, and P. J. Wheatley. *Monthly Notices of the Royal Astronomical Society*, 422(3):2024–2043, May 2012. ISSN 0035-8711.

J. Jennings, B. Ercolano, and G. P. Rosotti. *Monthly Notices of the Royal Astronomical Society*, 477(3):4131–4141, July 2018. ISSN 0035-8711, 1365-2966.

H. Jiang and C. W. Ormel. Efficient planet formation by pebble accretion in ALMA rings, July 2022.

M. A. Jiménez and F. S. Masset. *MNRAS*, 471(4):4917–4929, Nov. 2017. ISSN 0035-8711.

S. Jin, C. Mordasini, V. Parmentier, R. van Boekel, T. Henning, and J. Ji. *The Astrophysical Journal*, 795:65, Nov. 2014. ISSN 0004-637X.

A. Johansen and M. Lambrechts. *Annu. Rev. Earth Planet. Sci.*, 45(1):359–387, Aug. 2017. ISSN 0084-6597, 1545-4495.

A. Johansen, J. S. Oishi, M.-M. M. Low, H. Klahr, T. Henning, and A. Youdin. *Nature*, 448(7157):1022–1025, Aug. 2007. ISSN 1476-4687.

J. A. Johnson, K. M. Aller, A. W. Howard, and J. R. Crepp. *PASP*, 122(894):905, July 2010. ISSN 1538-3873.

A. H. Joy. *The Astrophysical Journal*, 102:168, Sept. 1945. ISSN 0004-637X.

M. Jutzi and E. Asphaug. *Nature*, 476(7358):69–72, Aug. 2011. ISSN 1476-4687.

K. D. Kanagawa, T. Muto, H. Tanaka, T. Tanigawa, T. Takeuchi, T. Tsukagoshi, and M. Momose. *Publications of the Astronomical Society of Japan*, 68(3):43, June 2016. ISSN 0004-6264.

K. D. Kanagawa, H. Tanaka, T. Muto, and T. Tanigawa. *Publications of the Astronomical Society of Japan*, 69(6):97, Dec. 2017. ISSN 0004-6264.

K. D. Kanagawa, H. Tanaka, and E. Szuszkiewicz. *ApJ*, 861(2):140, July 2018. ISSN 0004-637X.

N. Kaufmann and Y. Alibert. 10.48550/arXiv.2305.16952The influence of planetesimal fragmentation on planet formation, May 2023.

S. J. Kenyon and L. Hartmann. *The Astrophysical Journal*, 323:714, Dec. 1987. ISSN 0004-637X.

M. Keppler, M. Benisty, A. Müller, Th. Henning, R. van Boekel, F. Cantalloube, C. Ginski, R. G. van Holstein, A. L. Maire, A. Pohl, M. Samland, H. Avenhaus, J. L. Baudino, A. Boccaletti, J. de Boer, M. Bonnefoy, G. Chauvin, S. Desidera, M. Langlois, C. Lazzoni, G. D. Marleau, C. Mordasini, N. Pawellek, T. Stolker, A. Vigan, A. Zurlo, T. Birnstiel, W. Brandner, M. Feldt, M. Flock, J. Girard, R. Gratton, J. Hagelberg, A. Isella, M. Janson, A. Juhasz, J. Kemmer, Q. Kral,

A. M. Lagrange, R. Launhardt, A. Matter, F. Ménard, J. Milli, P. Mollière, J. Olofsson, L. Pérez, P. Pinilla, C. Pinte, S. P. Quanz, T. Schmidt, S. Udry, Z. Wahhaj, J. P. Williams, E. Buenzli, M. Cudel, C. Dominik, R. Galicher, M. Kasper, J. Lannier, D. Mesa, D. Mouillet, S. Peretti, C. Perrot, G. Salter, E. Sissa, F. Wildi, L. Abe, J. Antichi, J. C. Augereau, A. Baruffolo, P. Baudoz, A. Bazzon, J. L. Beuzit, P. Blanchard, S. S. Brems, T. Buey, V. De Caprio, M. Carbillet, M. Carle, E. Cascone, A. Cheetham, R. Claudi, A. Costille, A. Delboulbé, K. Dohlen, D. Fantinel, P. Feautrier, T. Fusco, E. Giro, L. Gluck, C. Gry, N. Hubin, E. Hugot, M. Jaquet, D. Le Mignant, M. Llored, F. Madec, Y. Magnard, P. Martinez, D. Maurel, M. Meyer, O. Möller-Nilsson, T. Moulin, L. Mugnier, A. Origné, A. Pavlov, D. Perret, C. Petit, J. Pragt, P. Puget, P. Rabou, J. Ramos, F. Rigal, S. Rochat, R. Roelfsema, G. Rousset, A. Roux, B. Salasnich, J. F. Sauvage, A. Sevin, C. Soenke, E. Stadler, M. Suarez, M. Turatto, and L. Weber. *Astronomy and Astrophysics*, 617:A44, Sept. 2018. ISSN 0004-6361.

A. Kessler and Y. Alibert. *A&A*, 674:A144, June 2023. ISSN 0004-6361, 1432-0746.

A. Kessler, Y. Alibert, C. Mordasini, A. Emsenhuber, and R. Burn. Technical Report EPSC2022-114, Copernicus Meetings, July 2022.

R. Kippenhahn and A. Weigert. Jan. 1990.

E. S. Kite, B. F. Jr, L. Schaefer, and E. B. Ford. *ApJL*, 887(2):L33, Dec. 2019. ISSN 2041-8205.

H. Klahr and P. Bodenheimer. *ApJ*, 639(1):432, Mar. 2006. ISSN 0004-637X.

H. Klahr, T. Pfeil, and A. Schreiber. In H. J. Deeg and J. A. Belmonte, editors, *Handbook of Exoplanets*, pages 2251–2286. Springer International Publishing, Cham, 2018. ISBN 978-3-319-55333-7.

W. Kley, B. Bitsch, and H. Klahr. *Astronomy and Astrophysics*, 506:971–987, Nov. 2009. ISSN 0004-6361.

H. Kobayashi, H. Tanaka, A. V. Krivov, and S. Inaba. *Icarus*, 209:836–847, Oct. 2010. ISSN 0019-1035.

H. Kobayashi, H. Tanaka, and A. V. Krivov. *The Astrophysical Journal*, 738:35, Sept. 2011. ISSN 0004-637X.

E. Kokubo and S. Ida. *Icarus*, 123:180–191, Sept. 1996. ISSN 0019-1035.

E. Kokubo and S. Ida. *Icarus*, 143:15–27, Jan. 2000. ISSN 0019-1035.

E. Kokubo and S. Ida. 10.48550/arXiv.1212.1558Dynamics and Accretion of Planetesimals, Dec. 2012.

A. Komaki, R. Nakatani, and N. Yoshida. *ApJ*, 910(1):51, Mar. 2021. ISSN 0004-637X.

G. P. Kuiper. *Proceedings of the National Academy of Science*, 37:1–14, Jan. 1951. ISSN 0027-8424.

M. Kunimoto and J. M. Matthews. *AJ*, 159(6):248, May 2020. ISSN 1538-3881.

T. Kutra, Y. Wu, and Y. Qian. *AJ*, 162(2):69, July 2021. ISSN 1538-3881.

M. Lambrechts and A. Johansen. *A&A*, 544:A32, Aug. 2012. ISSN 0004-6361, 1432-0746.

M. Lambrechts and A. Johansen. *A&A*, 572:A107, Dec. 2014. ISSN 0004-6361, 1432-0746.

M. Lambrechts, A. Johansen, and A. Morbidelli. *Astronomy and Astrophysics*, 572:A35, Dec. 2014. ISSN 0004-6361.

T. C. H. Lau, J. Drążkowska, S. M. Stammler, T. Birnstiel, and C. P. Dullemond. *A&A*, 668:A170, Dec. 2022. ISSN 0004-6361, 1432-0746.

G. Lesur, B. Ercolano, M. Flock, M.-K. Lin, C.-C. Yang, J. A. Barranco, P. Benitez-Llambay, J. Goodman, A. Johansen, H. Klahr, G. Laibe, W. Lyra, P. Marcus, R. P. Nelson, J. Squire, J. B. Simon, N. Turner, O. M. Umurhan, and A. N. Youdin. 10.48550/arXiv.2203.09821Hydro-, Magnetohydro-, and Dust-Gas Dynamics of Protoplanetary Disks, Mar. 2022.

D. N. C. Lin and J. Papaloizou. *Monthly Notices of the Royal Astronomical Society*, 186:799–812, Mar. 1979. ISSN 0035-8711.

J. J. Lissauer. *Annual Review of Astronomy and Astrophysics*, 31:129–174, Jan. 1993. ISSN 0066-4146.

J. J. Lissauer, O. Hubickyj, G. D'Angelo, and P. Bodenheimer. *Icarus*, 199:338–350, Feb. 2009. ISSN 0019-1035.

J. J. Lissauer, D. C. Fabrycky, E. B. Ford, W. J. Borucki, F. Fressin, G. W. Marcy, J. A. Orosz, J. F. Rowe, G. Torres, W. F. Welsh, N. M. Batalha, S. T. Bryson, L. A. Buchhave, D. A. Caldwell, J. A. Carter, D. Charbonneau, J. L. Christiansen, W. D. Cochran, J.-M. Desert, E. W. Dunham, M. N. Fanelli, J. J. Fortney, T. N. Gautier III, J. C. Geary, R. L. Gilliland, M. R. Haas, J. R. Hall, M. J. Holman, D. G. Koch, D. W. Latham, E. Lopez, S. McCauliff, N. Miller, R. C. Morehead, E. V. Quintana, D. Ragozzine, D. Sasselov, D. R. Short, and J. H. Steffen. *Nature*, 470(7332):53–58, Feb. 2011. ISSN 1476-4687.

B. Liu, S. N. Raymond, and S. A. Jacobson. *Nature*, 604(7907):643–646, Apr. 2022. ISSN 1476-4687.

Y. Liu, H. Roussel, H. Linz, M. Fang, S. Wolf, F. Kirchschlager, T. Henning, H. Yang, F. Du, M. Flock, and H. Wang. 10.48550/arXiv.2411.00277Dust mass in protoplanetary disks with porous dust opacities, Nov. 2024.

E. D. Lopez and J. J. Fortney. *The Astrophysical Journal*, 776:2, Oct. 2013. ISSN 0004-637X.

R. Luque and E. Pallé. *Sci*, 377(6611):1211–1214, Sept. 2022.

R. Lüst. *Zeitschrift für Naturforschung A*, 7(1):87–98, Jan. 1952. ISSN 1865-7109.

D. Lynden-Bell and J. E. Pringle. *MNRAS*, 168:603–637, Sept. 1974. ISSN 0035-8711.

E. E. Mamajek. *AIP Conference Proceedings*, 1158(1):3–10, Aug. 2009. ISSN 0094-243X.

C. F. Manara, G. Rosotti, L. Testi, A. Natta, J. M. Alcalá, J. P. Williams, M. Ansdell, A. Miotello, N. van der Marel, M. Tazzari, J. Carpenter, G. Guidi, G. S. Mathews, I. Oliveira, T. Prusti, and E. F. van Dishoeck. *Astronomy and Astrophysics*, 591:L3, June 2016. ISSN 0004-6361.

C. F. Manara, M. Ansdell, G. P. Rosotti, A. M. Hughes, P. J. Armitage, G. Lodato, and J. P. Williams. 534:539, July 2023.

A. Marconi, M. Abreu, V. Adibekyan, V. Alberti, S. Albrecht, J. Alcaniz, M. Aliverti, C. Allende Prieto, J. D. Alvarado-Gomez, C. S. Alves, P. J. Amado, M. Amate, M. I. Andersen, S. Antoniucci, E. Artigau, C. Bailet, C. Baker, V. Baldini, A. Balestra, S. A. Barnes, F. Baron, S. C. C. Barros, S. M. Bauer, M. Beaulieu, O. Bellido-Tirado, B. Benneke, T. Bensby, E. A. Bergin, P. Berio, K. Biazzo, L. Bigot, A. Bik, J. L. Birkby, N. Blind, O. Boebion, I. Boisse, E. Bolmont, J. S. Bolton, M. Bonaglia, X. Bonfils, L. Bonhomme, F. Borsa, J. C. Bouret, A. Brandeker, W. Brandner, C. H. Broeg, M. Brogi, D. Brousseau, A. Brucalassi, J. Brynnel, L. A. Buchhave, D. F. Buscher, L. Cabona, A. Cabral, G. Calderone, R. Calvo-Ortega, F. Cantalloube, B. L. Canto Martins, L. Carbonaro, Y. Caujolle, G. Chauvin, B. Chazelas, A. L. Cheffot, Y. S. Cheng, A. Chiavassa, L. Christensen, R. Cirami, M. Cirasuolo, N. J. Cook, R. J. Cooke, I. Coretti, S. Covino, N. Cowan, G. Cresci, S. Cristiani, V. Cunha Parro, G. Cupani, V. D'Odorico, K. Dadi, I. de Castro Leão, A. De Cia, J. R. De Medeiros, F. Debras, M. Debus, A. Delorme, O. Demangeon, F. Derie, M. Dessauges-Zavadsky, P. Di Marcantonio, S. Di Stefano, F. Dionies, A. Domiciano de Souza, R. Doyon, J. Dunn, S. Egner, D. Ehrenreich, J. P. Faria, D. Ferruzzi, C. Feruglio, M. Fisher, A. Fontana, B. S. Frank, C. Fuesslein, M. Fumagalli, T. Fusco, J. Fynbo, O. Gabella, W. Gaessler, E. Gallo, X. Gao, L. Genolet, M. Genoni, P. Giacobbe, E. Giro, R. S. Gonçalves, O. A. Gonzalez, J. I. González-Hernández, C. Gouvret, F. Gracia Témich, M. G. Haehnelt, C. Haniff, A. Hatzes, R. Helled, H. J. Hoeijmakers, I. Hughes, P. Huke, Y. Ivanisenko,

A. S. Järvinen, S. P. Järvinen, A. Kaminski, J. Kern, J. Knoche, A. Kordt, H. Korhonen, A. J. Korn, D. Kouach, G. Kowzan, L. Kreidberg, M. Landoni, A. A. Lanotte, A. Lavail, B. Lavie, D. Lee, M. Lehmitz, J. Li, W. Li, J. Liske, C. Lovis, S. Lucatello, D. Lunney, M. J. MacIntosh, N. Madhusudhan, L. Magrini, R. Maiolino, J. Maldonado, L. Malo, A. W. S. Man, T. Marquart, C. M. J. Marques, E. L. Marques, P. Martinez, A. Martins, C. J. A. P. Martins, J. H. C. Martins, P. Maslowski, C. Mason, E. Mason, R. A. McCracken, M. A. F. Melo e Sousa, P. Mergo, G. Micela, D. Milaković, P. Mollière, M. A. Monteiro, D. Montgomery, C. Mordasini, J. Morin, A. Mucciarelli, M. T. Murphy, M. N'Diaye, N. Nardetto, B. Neichel, N. Neri, A. T. Niedzielski, E. Niemczura, B. Nisini, L. Nortmann, P. Noterdaeme, N. J. Nunes, L. Oggioni, F. Olchewsky, E. Oliva, H. Önel, L. Origlia, G. Östlin, N. N. Q. Ouellette, E. Pallé, P. Papaderos, G. Pariani, and L. Pasquini. 13096:1309613, July 2024.

F. S. Masset. *MNRAS*, 472(4):4204–4219, Dec. 2017. ISSN 0035-8711.

F. S. Masset and J. Casoli. *The Astrophysical Journal*, 723:1393–1417, Nov. 2010. ISSN 0004-637X.

F. S. Masset and J. C. B. Papaloizou. *The Astrophysical Journal*, 588:494–508, May 2003. ISSN 0004-637X.

I. Matsuyama, D. Johnstone, and L. Hartmann. *ApJ*, 582:893–904, Jan. 2003. ISSN 0004-637X.

M. Mayor and D. Queloz. *Nature*, 378(6555):355–359, Nov. 1995. ISSN 1476-4687.

M. Mayor, M. Marmier, C. Lovis, S. Udry, D. Ségransan, F. Pepe, W. Benz, J.-L. Bertaux, F. Bouchy, X. Dumusque, G. L. Curto, C. Mordasini, D. Queloz, and N. C. Santos. 10.48550/arXiv.1109.2497The HARPS search for southern extra-solar planets XXXIV. Occurrence, mass distribution and orbital properties of super-Earths and Neptune-mass planets, Sept. 2011.

F. Meru, R. J. Geretshauser, C. Schäfer, R. Speith, and W. Kley. *Monthly Notices of the Royal Astronomical Society*, 435(3):2371–2390, Nov. 2013. ISSN 1365-2966, 0035-8711.

A. Michel, N. van der Marel, and B. C. Matthews. *ApJ*, 921(1):72, Nov. 2021. ISSN 0004-637X.

S. Millholland, S. Wang, and G. Laughlin. *ApJL*, 849(2):L33, Nov. 2017. ISSN 2041-8205.

A. Miotello, I. Kamp, T. Birnstiel, L. I. Cleeves, and A. Kataoka. 10.48550/arXiv.2203.09818Setting the Stage for Planet Formation: Measurements and Implications of the Fundamental Disk Properties, Mar. 2022.

L. Mishra, Y. Alibert, A. Leleu, A. Emsenhuber, C. Mordasini, R. Burn, S. Udry, and W. Benz. *A&A*, 656:A74, Dec. 2021. ISSN 0004-6361, 1432-0746.

M. Mol Lous, R. Helled, and C. Mordasini. *Nat Astron*, pages 1–9, June 2022. ISSN 2397-3366.

C. Mordasini. *A&A*, 572:A118, Dec. 2014. ISSN 0004-6361, 1432-0746.

C. Mordasini. 10.48550/arXiv.1804.01532Planetary population synthesis, Apr. 2018.

C. Mordasini and R. Burn. *Reviews in Mineralogy and Geochemistry*, 90:55–112, July 2024.

C. Mordasini, Y. Alibert, and W. Benz. *A&A*, 501(3):1139–1160, July 2009a. ISSN 0004-6361, 1432-0746.

C. Mordasini, Y. Alibert, W. Benz, and D. Naef. *Astronomy and Astrophysics*, 501:1161–1184, July 2009b. ISSN 0004-6361.

C. Mordasini, Y. Alibert, C. Georgy, K.-M. Dittkrist, H. Klahr, and T. Henning. *A&A*, 547:A112, Nov. 2012a. ISSN 0004-6361, 1432-0746.

C. Mordasini, Y. Alibert, H. Klahr, and T. Henning. *A&A*, 547:A111, Nov. 2012b. ISSN 0004-6361, 1432-0746.

C. Mordasini, H. Klahr, Y. Alibert, N. Miller, and T. Henning. *A&A*, 566:A141, June 2014. ISSN 0004-6361, 1432-0746.

T. D. Morton and J. Swift. *ApJ*, 791(1):10, July 2014. ISSN 0004-637X.

O. Mousis, M. Deleuil, A. Aguichine, E. Marcq, J. Naar, L. A. Aguirre, B. Brugger, and T. Gonçalves. *ApJL*, 896(2):L22, June 2020. ISSN 2041-8205.

N. Movshovitz and M. Podolak. *Icarus*, 194:368–378, Mar. 2008. ISSN 0019-1035.

N. Movshovitz, P. Bodenheimer, M. Podolak, and J. J. Lissauer. *Icarus*, 209: 616–624, 2010.

G. D. Mulders, I. Pascucci, and D. Apai. *The Astrophysical Journal*, 814:130, Dec. 2015a. ISSN 0004-637X.

G. D. Mulders, I. Pascucci, and D. Apai. *The Astrophysical Journal*, 798:112, Jan. 2015b. ISSN 0004-637X.

G. D. Mulders, I. Pascucci, D. Apai, A. Frasca, and J. Molenda-Żakowicz. *AJ*, 152 (6):187, Nov. 2016. ISSN 1538-3881.

G. D. Mulders, I. Pascucci, D. Apai, and F. J. Ciesla. *The Astronomical Journal*, 156:24, July 2018. ISSN 0004-6256.

A. Müller, M. Keppler, T. Henning, M. Samland, G. Chauvin, H. Beust, A.-L. Maire, K. Molaverdikhani, R. vanBoekel, M. Benisty, A. Boccaletti, M. Bonnefoy, F. Cantalloube, B. Charnay, J.-L. Baudino, M. Gennaro, Z. C.

Long, A. Cheetham, S. Desidera, M. Feldt, T. Fusco, J. Girard, R. Gratton, J. Hagelberg, M. Janson, A.-M. Lagrange, M. Langlois, C. Lazzoni, R. Ligi, F. Menard, D. Mesa, M. Meyer, P. Molliere, C. Mordasini, T. Moulin, A. Pavlov, N. Pawellek, S. P. Quanz, J. Ramos, D. Rouan, E. Sissa, E. Stadler, A. Vigan, Z. Wahhaj, L. Weber, and A. Zurlo. 10.1051/0004-6361/201833584Orbital and atmospheric characterization of the planet within the gap of the PDS 70 transition disk. https://arxiv.org/abs/1806.11567v2, June 2018.

S. Müller, R. Helled, and A. Cumming. *A&A*, 638:A121, June 2020. ISSN 0004-6361, 1432-0746.

R. A. Murray-Clay, E. I. Chiang, and N. Murray. *ApJ*, 693(1):23, Feb. 2009. ISSN 0004-637X.

G. Musiolik and G. Wurm. *ApJ*, 873(1):58, Mar. 2019. ISSN 0004-637X.

Y. Nakagawa, M. Sekiya, and C. Hayashi. *Icarus*, 67:375–390, Sept. 1986. ISSN 0019-1035.

T. Nakamoto and Y. Nakagawa. *ApJ*, 421:640, Feb. 1994. ISSN 0004-637X.

R. Nakatani, T. Hosokawa, N. Yoshida, H. Nomura, and R. Kuiper. *ApJ*, 865(1): 75, Sept. 2018. ISSN 0004-637X.

N. Nettelmann, R. Helled, J. J. Fortney, and R. Redmer. *Planetary and Space Science*, 77:143–151, Mar. 2013. ISSN 0032-0633.

H. Ngo, H. A. Knutson, S. Hinkley, M. Bryan, J. R. Crepp, K. Batygin, I. Crossfield, B. Hansen, A. W. Howard, J. A. Johnson, D. Mawet, T. D. Morton, P. S. Muirhead, and J. Wang. *The Astrophysical Journal*, 827:8, Aug. 2016. ISSN 0004-637X.

D. Ni. *A&A*, 632:A76, Dec. 2019. ISSN 0004-6361, 1432-0746.

E. L. Nielsen, R. J. D. Rosa, B. Macintosh, J. J. Wang, J.-B. Ruffio, E. Chiang, M. S. Marley, D. Saumon, D. Savransky, S. M. Ammons, V. P. Bailey, T. Barman, C. Blain, J. Bulger, A. Burrows, J. Chilcote, T. Cotten, I. Czekala, R. Doyon, G. Duchêne, T. M. Esposito, D. Fabrycky, M. P. Fitzgerald, K. B. Follette, J. J. Fortney, B. L. Gerard, S. J. Goodsell, J. R. Graham, A. Z. Greenbaum, P. Hibon, S. Hinkley, L. A. Hirsch, J. Hom, L.-W. Hung, R. I. Dawson, P. Ingraham, P. Kalas, Q. Konopacky, J. E. Larkin, E. J. Lee, J. W. Lin, J. Maire, F. Marchis, C. Marois, S. Metchev, M. A. Millar-Blanchaer, K. M. Morzinski, R. Oppenheimer, D. Palmer, J. Patience, M. Perrin, L. Poyneer, L. Pueyo, R. R. Rafikov, A. Rajan, J. Rameau, F. T. Rantakyrö, B. Ren, A. C. Schneider, A. Sivaramakrishnan, I. Song, R. Soummer, M. Tallis, S. Thomas, K. Ward-Duong, and S. Wolff. *AJ*, 158(1):13, June 2019. ISSN 1538-3881.

K. I. Öberg, R. Murray-Clay, and E. A. Bergin. *The Astrophysical Journal*, 743: L16, Dec. 2011. ISSN 0004-637X.

S. S. R. Offner, M. Moe, K. M. Kratter, S. I. Sadavoy, E. L. N. Jensen, and J. J. Tobin. 10.48550/arXiv.2203.10066The Origin and Evolution of Multiple Star Systems, Dec. 2022.

K. Ohtsuki, G. R. Stewart, and S. Ida. *Icarus*, 155(2):436–453, Feb. 2002. ISSN 0019-1035.

C. Ormel, A. Vazan, and M. Brouwers. *A&A*, 647:A175, Mar. 2021. ISSN 0004-6361, 1432-0746.

C. W. Ormel. *The Astrophysical Journal*, 789:L18, July 2014. ISSN 0004-637X.

C. W. Ormel. In M. Pessah and O. Gressel, editors, *Formation, Evolution, and Dynamics of Young Solar Systems*, volume 445, pages 197–228. Springer International Publishing, Cham, 2017. ISBN 978-3-319-60608-8 978-3-319-60609-5.

C. W. Ormel and J. N. Cuzzi. *Astronomy and Astrophysics*, 466:413–420, May 2007. ISSN 0004-6361.

C. W. Ormel and H. H. Klahr. *A&A*, 520:A43, Sept. 2010. ISSN 0004-6361.

C. W. Ormel and H. Kobayashi. *The Astrophysical Journal*, 747:115, Mar. 2012. ISSN 0004-637X.

J. E. Owen. *Annual Review of Earth and Planetary Sciences*, 47:67–90, May 2019. ISSN 0084-6597.

S.-J. Paardekooper. *Monthly Notices of the Royal Astronomical Society*, 444(3): 2031–2042, Nov. 2014. ISSN 0035-8711, 1365-2966.

S. J. Paardekooper, C. Baruteau, A. Crida, and W. Kley. *Monthly Notices of the Royal Astronomical Society*, 401:1950–1964, Jan. 2010. ISSN 0035-8711.

S. J. Paardekooper, C. Baruteau, and W. Kley. *MNRAS*, 410:293–303, Jan. 2011. ISSN 0035-8711.

I. Pascucci, L. Testi, G. J. Herczeg, F. Long, C. F. Manara, N. Hendler, G. D. Mulders, S. Krijt, F. Ciesla, T. Henning, S. Mohanty, E. Drabek-Maunder, D. Apai, L. Szűcs, G. Sacco, and J. Olofsson. *ApJ*, 831(2):125, Nov. 2016. ISSN 0004-637X.

I. Pascucci, G. D. Mulders, A. Gould, and R. Fernandes. *ApJL*, 856(2):L28, Mar. 2018. ISSN 2041-8205.

I. Pascucci, S. Cabrit, S. Edwards, U. Gorti, O. Gressel, and T. K. Suzuki. 534: 567, July 2023.

M. T. Penny, B. S. Gaudi, E. Kerins, N. J. Rattenbury, S. Mao, A. C. Robin, and S. C. Novati. *ApJS*, 241(1):3, Feb. 2019. ISSN 0067-0049.

E. A. Petigura, G. W. Marcy, J. N. Winn, L. M. Weiss, B. J. Fulton, A. W. Howard, E. Sinukoff, H. Isaacson, T. D. Morton, and J. A. Johnson. *The Astronomical Journal*, 155:89, Feb. 2018. ISSN 0004-6256.

C. Piaulet-Ghorayeb, B. Benneke, M. Radica, E. Raul, L.-P. Coulombe, E.-M. Ahrer, D. Kubyshkina, W. S. Howard, J. Krissansen-Totton, R. MacDonald, P.-A. Roy, A. Louca, D. Christie, M. Fournier-Tondreau, R. Allart, Y. Miguel, H. E. Schlichting, L. Welbanks, C. Cadieux, C. Dorn, T. M. Evans-Soma, J. J. Fortney, R. Pierrehumbert, D. Lafreniere, L. Acuna, T. Komacek, H. Innes, T. G. Beatty, R. Cloutier, R. Doyon, A. Gagnebin, C. Gapp, and H. A. Knutson. 10.48550/arXiv.2410.03527JWST/NIRISS reveals the water-rich "steam world" atmosphere of GJ 9827 d, Oct. 2024.

C. Pinte, W. R. F. Dent, F. Ménard, A. Hales, T. Hill, P. Cortes, and I. de Gregorio-Monsalvo. *The Astrophysical Journal*, 816:25, Jan. 2016. ISSN 0004-637X.

B. Polak and H. Klahr. 10.48550/arXiv.2211.13318High Resolution Study of Planetesimal Formation by Gravitational Collapse of Pebble Clouds, Nov. 2022.

J. B. Pollack, O. Hubickyj, P. Bodenheimer, J. J. Lissauer, M. Podolak, and Y. Greenzweig. *Icarus*, 124:62–85, Nov. 1996. ISSN 0019-1035.

J. Polman and C. Mordasini. 10.48550/arXiv.2411.18686Convective mixing in distant and close-in giant planets – Dependences on the initial composition, luminosity, bloating and semi-convection, Nov. 2024.

J. E. Pringle. *ARA&A*, 19:137, 1981. ISSN 0066-4146.

R. R. Rafikov. *AJ*, 128:1348–1363, Sept. 2004. ISSN 0004-6256.

H. Rauer, C. Aerts, J. Cabrera, M. Deleuil, A. Erikson, L. Gizon, M. Goupil, A. Heras, J. Lorenzo-Alvarez, F. Marliani, C. Martin-Garcia, J. M. Mas-Hesse, L. O'Rourke, H. Osborn, I. Pagano, G. Piotto, D. Pollacco, R. Ragazzoni, G. Ramsay, S. Udry, T. Appourchaux, W. Benz, A. Brandeker, M. Güdel, E. Janot-Pacheco, P. Kabath, H. Kjeldsen, M. Min, N. Santos, A. Smith, J.-C. Suarez, S. C. Werner, A. Aboudan, M. Abreu, L. A. a, M. Adams, V. Adibekyan, L. Affer, F. Agneray, C. Agnor, V. A. Børsen-Koch, S. Ahmed, S. Aigrain, A. Al-Bahlawan, M. d. l. A. A. Gil, E. Alei, S. Alencar, R. Alexander, J. Alfonso-Garzón, Y. Alibert, C. A. Prieto, L. Almeida, R. A. Sobrino, G. Altavilla, C. Althaus, L. A. A. Trujillo, A. Amarsi, M. A.-v. Eiff, E. Amôres, L. Andrade, A. Antoniadis-Karnavas, C. António, B. A. del Moral, M. Appolloni, C. Arena, D. Armstrong, J. A. Aliaga, M. Asplund, J. Audenaert, N. Auricchio, P. Avelino, A. Baeke, K. Baillié, A. Balado, P. B. Balagueró, A. Balestra,

W. Ball, H. Ballans, J. Ballot, C. Barban, G. Barbary, M. Barbieri, S. B. Forteza, A. Barker, P. Barklem, S. Barnes, D. B. Navascues, O. Barragan, C. Baruteau, S. Basu, F. Baudin, P. Baumeister, D. Bayliss, M. Bazot, P. G. Beck, T. Bedding, K. Belkacem, E. Bellinger, S. Benatti, O. Benomar, D. Bérard, M. Bergemann, M. Bergomi, P. Bernardo, K. Biazzo, A. Bignamini, L. Bigot, N. Billot, M. Binet, D. Biondi, F. Biondi, A. C. Birch, B. Bitsch, P. V. B. Ceballos, A. Bódi, Z. Bognár, I. Boisse, E. Bolmont, A. Bonanno, M. Bonavita, A. Bonfanti, X. Bonfils, R. Bonito, A. S. Bonomo, A. Börner, S. B. Saikia, E. B. Martín, F. Borsa, L. Borsato, D. Bossini, F. Bouchy, G. Boué, R. Boufleur, P. Boumier, V. Bourrier, D. M. Bowman, E. Bozzo, L. Bradley, J. Bray, A. Bressan, S. Breton, D. Brienza, A. Brito, M. Brogi, B. Brown, D. J. A. Brown, A. S. Brun, G. Bruno, M. Bruns, L. A. Buchhave, L. Bugnet, G. Buldgen, P. Burgess, A. Busatta, G. Busso, D. Buzasi, J. A. Caballero, A. Cabral, J.-F. C. Gomez, F. Calderone, R. Cameron, A. Cameron, T. Campante, N. C. Gestal, B. L. C. Martins, C. Cara, L. Carone, J. M. Carrasco, L. Casagrande, S. L. Casewell, S. Cassisi, M. Castellani, M. Castro, C. Catala, I. C. Fernández, M. Catelan, H. Cegla, C. Cerruti, V. Cessa, M. Chadid, W. Chaplin, S. Charpinet, C. Chiappini, S. Chiarucci, A. Chiavassa, S. Chinellato, G. Chirulli, J. Christensen-Dalsgaard, R. Church, A. Claret, C. Clarke, R. Claudi, L. Clermont, H. Coelho, J. Coelho, F. Cogato, J. Colomé, M. Condamin, F. C. García, S. Conseil, T. Corbard, A. C. M. Correia, E. Corsaro, R. Cosentino, J. Costes, A. Cottinelli, G. Covone, O. L. Creevey, A. Crida, S. Csizmadia, M. Cunha, P. Curry, J. da Costa, F. da Silva, S. Dalal, M. Damasso, C. Damiani, F. Damiani, M. L. das Chagas, M. Davies, G. Davies, B. Davies, G. Davison, L. de Almeida, F. de Angeli, S. C. C. de Barros, I. d. C. Leão, D. B. de Freitas, M. C. de Freitas, D. D. Martino, J. R. de Medeiros, L. A. de Paula, Á. d. P. Gómez, J. de Plaa, J. D. Ridder, M. Deal, L. Decin, H. Deeg, S. D. Innocenti, S. Deheuvels, C. del Burgo, F. D. Sordo, E. Delgado-Mena, O. Demangeon, T. Denk, A. Derekas, J.-M. Desert, S. Desidera, M. Dexet, M. D. Criscienzo, A. M. D. Giorgio, M. P. D. Mauro, F. J. D. Rial, J.-J. Díaz-García, M. Dima, G. Dinuzzi, O. Dionatos, E. Distefano, J.-D. d. N. Jr, A. Domingo, V. D'Orazi, C. Dorn, L. Doyle, E. Duarte, F. Ducellier, L. Dumaye, X. Dumusque, M.-A. Dupret, P. Eggenberger, D. Ehrenreich, P. Eigmüller, J. Eising, M. Emilio, K. Eriksson, M. Ermocida, R. I. E. Giribaldi, Y. Eschen, L. E. Y. ez, I. s Estrela, D. W. Evans, D. Fabbian, M. Fabrizio, J. P. Faria, M. Farina, J. Farinato, D. Feliz, S. Feltzing, T. Fenouillet, M. Fernández, L. Ferrari, S. Ferraz-Mello, F. Fialho, A. Fienga,

P. Figueira, L. Fiori, E. Flaccomio, M. Focardi, S. Foley, J. Fontignie, D. Ford, K. Fornazier, T. Forveille, L. Fossati, R. d. M. Franca, L. F. da Silva, A. Frasca, M. Fridlund, M. Furlan, S.-M. Gabler, M. Gaido, A. Gallagher, P. I. G. Sempere, E. Galli, R. A. García, A. G. Hernández, A. G. Munoz, H. García-Vázquez, R. G. Haba, P. Gaulme, N. Gauthier, C. Gehan, M. Gent, I. Georgieva, M. Ghigo, E. Giana, S. Gill, L. Girardi, S. G. Winter, G. Giusi, J. G. da Silva, L. J. G. Zazo, J. M. Gomez-Lopez, J. I. G. Hernández, K. G. Murillo, A. G. Melchor, N. Gorius, P.-V. Gouel, D. Goulty, V. Granata, J. L. Grenfell, D. G. bach, E. Grolleau, S. Grouffal, S. Grziwa, M. G. Guarcello, L. c Gueguen, E. W. Guenther, T. Guilhem, L. Guillerot, T. Guillot, P. Guiot, P. Guterman, A. Gutiérrez, F. Gutiérrez-Canales, J. Hagelberg, J. Haldemann, C. Hall, R. Handberg, I. Harrison, D. L. Harrison, J. Hasiba, C. A. Haswell, P. Hatalova, A. Hatzes, R. Haywood, G. Hébrard, F. Heckes, U. Heiter, S. Hekker, R. Heller, C. Helling, K. Helminiak, S. Hemsley, K. Heng, K. Herbst, A. Hermans, J. J. Hermes, N. H. Torres, N. Hinkel, D. Hobbs, S. Hodgkin, K. Hofmann, S. Hojjatpanah, G. Houdek, D. Huber, J. Huesler, A. Hui-Bon-Hoa, R. Huygen, D.-D. Huynh, N. Iro, J. Irwin, M. Irwin, A. Izidoro, S. Jacquinod, N. E. Jannsen, M. Janson, H. Jeszenszky, C. Jiang, A. J. J. Mancebo, P. Jofre, A. Johansen, C. Johnston, G. Jones, T. Kallinger, S. Kálmán, T. Kanitz, M. Karjalainen, R. Karjalainen, C. Karoff, S. Kawaler, D. Kawata, A. Keereman, D. Keiderling, T. Kennedy, M. Kenworthy, F. Kerschbaum, M. Kidger, F. Kiefer, C. Kintziger, K. Kislyakova, L. Kiss, P. Klagyivik, H. Klahr, J. Klevas, O. Kochukhov, U. Köhler, U. Kolb, A. Koncz, J. Korth, N. Kostogryz, G. Kovács, J. Kovács, O. Kozhura, N. Krivova, A. Kucinskas, I. Kuhlemann, F. Kupka, W. Laauwen, A. Labiano, N. Lagarde, P. Laget, G. Laky, K. W. F. Lam, M. Lambrechts, H. Lammer, A. F. Lanza, A. Lanzafame, M. L. Martiz, J. Laskar, H. Latter, T. Lavanant, A. Lawrenson, C. Lazzoni, A. Lebre, Y. Lebreton, A. L. des Etangs, K. Lee, Z. Leinhardt, A. Leleu, M. Lendl, G. Leto, Y. Levillain, A.-S. Libert, T. Lichtenberg, R. Ligi, F. Lignieres, J. Lillo-Box, J. Linsky, J. S. Liu, D. Loidolt, Y. Longval, I. Lopes, A. Lorenzani, H.-G. Ludwig, M. Lund, M. S. Lundkvist, X. Luri, C. Maceroni, S. Madden, N. Madhusudhan, A. Maggio, C. Magliano, D. Magrin, L. Mahy, O. Maibaum, L. Malac-Allain, J.-C. Malapert, L. Malavolta, J. Maldonado, E. Mamonova, L. Manchon, A. Manjón, A. Mann, G. Mantovan, L. Marafatto, M. Marconi, R. Mardling, P. Marigo, S. Marinoni, r. Marques, J. P. Marques, P. M. Marrese, D. Marshall, S. M. Perales, D. Mary, F. Marzari, E. Masana, A. Mascher, S. Mathis, S. Mathur,

I. M. Vodopivec, A. C. M. Figueiredo, P. F. L. Maxted, T. Mazeh, S. Mazevet, F. Mazzei, J. McCormac, P. McMillan, L. Menou, T. Merle, F. Meru, D. Mesa, S. Messina, S. Mészáros, N. Meunier, J.-C. Meunier, G. Micela, H. Michaelis, E. Michel, M. Michielsen, T. Michtchenko, A. Miglio, Y. Miguel, D. Milligan, G. Mirouh, M. Mitchell, N. Moedas, F. Molendini, L. Molnár, J. Mombarg, J. Montalban, M. Montalto, M. J. P. F. G. Monteiro, F. M. Sánchez, J. C. Morales, M. Morales-Calderon, A. Morbidelli, C. Mordasini, C. Moreau, T. Morel, G. Morello, J. Morin, A. Mortier, B. t Mosser, D. Mourard, O. Mousis, C. Moutou, N. Mowlavi, A. Moya, P. Muehlmann, P. Muirhead, M. Munari, I. Musella, A. J. Mustill, N. Nardetto, D. Nardiello, N. Narita, V. Nascimbeni, A. Nash, C. Neiner, R. P. Nelson, N. Nettelmann, G. Nicolini, M. Nielsen, S.-M. Niemi, L. Noack, A. Noels-Grotsch, A. Noll, A. Norazman, A. J. Norton, B. Nsamba, A. Ofir, G. Ogilvie, T. Olander, C. Olivetto, G. Olofsson, J. Ong, S. Ortolani, M. Oshagh, H. Ottacher, R. Ottensamer, R.-M. Ouazzani, S.-J. Paardekooper, E. Pace, M. Pajas, A. Palacios, G. Palandri, E. Palle, C. Paproth, V. Parro, H. Parviainen, J. P. Granado, V. M. Passegger, C. Pastor-Morales, M. Pätzold, M. G. Pedersen, D. P. Hidalgo, F. Pepe, F. Pereira, C. M. Persson, M. Pertenais, G. Peter, A. C. Petit, P. Petit, S. Pezzuto, G. Pichierri, A. Pietrinferni, F. Pinheiro, M. Pinsonneault, E. Plachy, P. Plasson, B. Plez, K. Poppenhaeger, E. Poretti, E. Portaluri, J. Portell, G. F. P. de Mello, J. Poyatos, F. J. Pozuelos, P. G. P. Moroni, D. Pricopi, L. Prisinzano, M. Quade, A. Quirrenbach, J. A. R. Reina, M. C. R. Soares, G. Raimondo, M. Rainer, J. R. Rodón, A. Ramón-Ballesta, G. R. Zapata, S. Rätz, C. Rauterberg, B. Redman, R. Redmer, D. Reese, S. Regibo, A. Reiners, T. Reinhold, C. Renie, I. Ribas, S. Ribeiro, T. P. Ricciardi, K. Rice, O. Richard, M. Riello, M. Rieutord, V. Ripepi, G. Rixon, S. Rockstein, J. R. R. Ortiz, M. T. R. Rodríguez, A. R. Amor, L. F. R. Díaz, J. P. R. Garcia, J. Rodriguez-Gomez, Y. Roehlly, F. Roig, B. Rojas-Ayala, T. Rolf, J. L. Rørsted, H. Rosado, G. Rosotti, O. Roth, M. Roth, A. Rousseau, I. Roxburgh, F. Roy, P. Royer, K. Ruane, S. R. Mastropasqua, C. R. de Galarreta, A. Russi, S. Saar, M. Saillenfest, M. Salaris, S. Salmon, I. Saltas, R. Samadi, A. Samadi, D. Samra, T. S. da Silva, M. A. S. Carrasco, A. Santerne, A. S. Pé, F. Santoli, n. R. G. Santos, R. S. Mesa, L. M. Sarro, G. Scandariato, M. Schäfer, E. Schlafly, F.-X. Schmider, J. Schneider, J. Schou, H. Schunker, G. J. Schwarzkopf, A. Serenelli, D. Seynaeve, Y. Shan, A. Shapiro, R. Shipman, D. Sicilia, M. A. S. sanmartin, A. Sigot, K. Silliman, R. Silvotti, A. E. Simon, R. S. Napoli, M. Skarka, B. Smalley, R. Smiljanic, S. Smit,

A. Smith, L. Smith, I. Snellen, Á. Sódor, F. Sohl, S. K. Solanki, F. Sortino, S. Sousa, J. Southworth, D. Souto, A. Sozzetti, D. Stamatellos, K. Stassun, M. Steller, D. Stello, B. Stelzer, U. Stiebeler, A. Stokholm, T. Storelvmo, K. Strassmeier, P. A. Strøm, A. Strugarek, S. Sulis, M. vanda, L. Szabados, R. Szabó, G. M. Szabó, E. Szuszkiewicz, G. J. Talens, D. Teti, T. Theisen, F. Thévenin, A. Thoul, D. Tiphene, R. Titz-Weider, A. Tkachenko, D. Tomecki, J. Tonfat, N. Tosi, R. Trampedach, G. Traven, A. Triaud, R. Trønnes, M. Tsantaki, M. Tschentscher, A. Turin, A. Tvaruzka, B. Ulmer, S. Ulmer-Moll, C. Ulusoy, G. Umbriaco, D. Valencia, M. Valentini, A. Valio, Á. L. V. Guijarro, V. V. Eylen, V. V. Grootel, T. A. van Kempen, T. V. Reeth, I. V. Zelst, B. Vandenbussche, K. Vasiliou, V. Vasilyev, D. V. de Mascarenhas, A. Vazan, M. V. Nunez, E. N. Velloso, R. Ventura, P. Ventura, J. Venturini, I. V. Trallero, D. Veras, E. Verdugo, K. Verma, D. Vibert, T. V. Martinez, K. Vida, A. Vigan, A. Villacorta, E. Villaver, M. V. Aparicio, V. Viotto, E. Vorobyov, S. Vorontsov, F. W. Wagner, T. Walloschek, N. Walton, D. Walton, H. Wang, R. Waters, C. Watson, S. Wedemeyer, A. Weeks, J. Weingrill, A. Weiss, B. Wendler, R. West, K. Westerdorff, P.-A. Westphal, P. Wheatley, T. White, A. Whittaker, K. Wickhusen, T. Wilson, J. Windsor, O. Winter, M. L. Winther, A. Winton, U. Witteck, V. Witzke, P. Woitke, D. Wolter, G. Wuchterl, M. Wyatt, D. Yang, J. Yu, R. Z. Sanchez, M. R. Z. Osorio, M. Zechmeister, Y. Zhou, C. Ziemke, and K. Zwintz. 10.48550/arXiv.2406.05447The PLATO Mission, Nov. 2024.

I. Ribas, E. F. Guinan, M. Güdel, and M. Audard. *ApJ*, 622(1):680, Mar. 2005. ISSN 0004-637X.

A. J. W. Richert, K. V. Getman, E. D. Feigelson, M. A. Kuhn, P. S. Broos, M. S. Povich, M. R. Bate, and G. P. Garmire. *Monthly Notices of the Royal Astronomical Society*, 477:5191–5206, July 2018. ISSN 0035-8711.

J. G. Rogers, A. Gupta, J. E. Owen, and H. E. Schlichting. *Monthly Notices of the Royal Astronomical Society*, 508(4):5886–5902, Dec. 2021. ISSN 0035-8711.

L. A. Rogers. *ApJ*, 801(1):41, Mar. 2015. ISSN 0004-637X.

K. Ros and A. Johansen. *A&A*, 552:A137, Apr. 2013. ISSN 0004-6361, 1432-0746.

L. J. Rosenthal, H. A. Knutson, Y. Chachan, F. Dai, A. W. Howard, B. J. Fulton, A. Chontos, J. R. Crepp, P. A. Dalba, G. W. Henry, S. R. Kane, E. A. Petigura, L. M. Weiss, and J. T. Wright. *ApJS*, 262(1):1, Aug. 2022. ISSN 0067-0049.

S. P. Ruden and J. B. Pollack. *ApJ*, 375:740, July 1991. ISSN 0004-637X.

E. Sanchis, L. Testi, A. Natta, S. Facchini, C. F. Manara, A. Miotello, B. Ercolano, T. Henning, T. Preibisch, J. M. Carpenter, I. de Gregorio-Monsalvo,

R. Jayawardhana, C. Lopez, K. Mužić, I. Pascucci, A. Santamaría-Miranda, S. van Terwisga, and J. P. Williams. *A&A*, 649:A19, May 2021. ISSN 0004-6361, 1432-0746.

N. C. Santos, G. Israelian, and M. Mayor. *A&A*, 415(3):1153–1166, Mar. 2004. ISSN 0004-6361, 1432-0746.

D. Saumon, G. Chabrier, and H. M. van Horn. *ApJ*, 99:713, Aug. 1995. ISSN 0067-0049.

M. Schlecker, C. Mordasini, A. Emsenhuber, H. Klahr, T. Henning, R. Burn, Y. Alibert, and W. Benz. *A&A*, 656:A71, Dec. 2021a. ISSN 0004-6361, 1432-0746.

M. Schlecker, D. Pham, R. Burn, Y. Alibert, C. Mordasini, A. Emsenhuber, H. Klahr, T. Henning, and L. Mishra. *A&A*, 656:A73, Dec. 2021b. ISSN 0004-6361, 1432-0746.

D. Schoonenberg and C. W. Ormel. *A&A*, 602:A21, June 2017. ISSN 0004-6361, 1432-0746.

R. Schräpler and T. Henning. *ApJ*, 614(2):960, Oct. 2004. ISSN 0004-637X.

N. I. Shakura and R. A. Sunyaev. *Symp. IAU*, 55:155–164, 1973. ISSN 0074-1809.

Y. Shibaike and C. Mordasini. *Astronomy and Astrophysics*, 687:A166, July 2024. ISSN 0004-6361.

M. V. Smoluchowski. *Zeitschrift fur Physik*, 17:557–585, Jan. 1916.

S. M. Stammler, T. Lichtenberg, J. Drążkowska, and T. Birnstiel. Leaky Dust Traps: How Fragmentation impacts Dust Filtering by Planets, Jan. 2023.

T. Steinpilz, J. Teiser, and G. Wurm. *ApJ*, 874(1):60, Mar. 2019. ISSN 0004-637X.

D. J. Stevenson, P. Bodenheimer, J. J. Lissauer, and G. D'Angelo. *The Planetary Science Journal*, 3:74, Apr. 2022. ISSN 2632-3338.

H. Tanaka, T. Takeuchi, and W. R. Ward. *ApJ*, 565:1257–1274, Feb. 2002. ISSN 0004-637X.

R. Teague, J. Bae, E. A. Bergin, T. Birnstiel, and D. Foreman-Mackey. *ApJL*, 860 (1):L12, June 2018. ISSN 2041-8205.

L. Testi, A. Natta, D. S. Shepherd, and D. J. Wilner. *A&A*, 403(1):323–328, May 2003. ISSN 0004-6361, 1432-0746.

L. Testi, A. Natta, C. F. Manara, I. de Gregorio Monsalvo, G. Lodato, C. Lopez, K. Muzic, I. Pascucci, E. Sanchis, A. S. Miranda, A. Scholz, M. De Simone, and J. P. Williams. *Astronomy and Astrophysics*, 663:A98, July 2022. ISSN 0004-6361.

A. Toomre. *The Astrophysical Journal*, 139:1217–1238, May 1964. ISSN 0004-637X.

K. Tsiganis, R. Gomes, A. Morbidelli, and H. F. Levison. *Nature*, 435(7041): 459–461, May 2005. ISSN 1476-4687.

Ł. Tychoniec, J. J. Tobin, A. Karska, C. Chandler, M. M. Dunham, R. J. Harris, K. M. Kratter, Z.-Y. Li, L. W. Looney, C. Melis, L. M. Pérez, S. I. Sadavoy, D. Segura-Cox, and E. F. van Dishoeck. *ApJS*, 238(2):19, Oct. 2018. ISSN 0067-0049.

N. van der Marel and G. D. Mulders. *AJ*, 162(1):28, June 2021. ISSN 1538-3881.

A. Vazan, R. Helled, and T. Guillot. *A&A*, 610:L14, Feb. 2018. ISSN 0004-6361, 1432-0746.

D. A. Velasco Romero and F. S. Masset. *MNRAS*, 495(2):2063–2074, June 2020. ISSN 0035-8711.

J. Venturini, O. M. Guilera, J. Haldemann, M. P. Ronco, and C. Mordasini. *A&A*, 643:L1, Nov. 2020. ISSN 0004-6361, 1432-0746.

A. Vigan, C. Fontanive, M. Meyer, B. Biller, M. Bonavita, M. Feldt, S. Desidera, G.-D. Marleau, A. Emsenhuber, R. Galicher, K. Rice, D. Forgan, C. Mordasini, R. Gratton, H. L. Coroller, A.-L. Maire, F. Cantalloube, G. Chauvin, A. Cheetham, J. Hagelberg, A.-M. Lagrange, M. Langlois, M. Bonnefoy, J.-L. Beuzit, A. Boccaletti, V. D'Orazi, P. Delorme, C. Dominik, T. Henning, M. Janson, E. Lagadec, C. Lazzoni, R. Ligi, F. Menard, D. Mesa, S. Messina, C. Moutou, A. Müller, C. Perrot, M. Samland, H. M. Schmid, T. Schmidt, E. Sissa, M. Turatto, S. Udry, A. Zurlo, L. Abe, J. Antichi, R. Asensio-Torres, A. Baruffolo, P. Baudoz, J. Baudrand, A. Bazzon, P. Blanchard, A. J. Bohn, S. B. Sevilla, M. Carbillet, M. Carle, E. Cascone, J. Charton, R. Claudi, A. Costille, V. D. Caprio, A. Delboulbé, K. Dohlen, N. Engler, D. Fantinel, P. Feautrier, T. Fusco, P. Gigan, J. H. Girard, E. Giro, D. Gisler, L. Gluck, C. Gry, N. Hubin, E. Hugot, M. Jaquet, M. Kasper, D. L. Mignant, M. Llored, F. Madec, Y. Magnard, P. Martinez, D. Maurel, O. Möller-Nilsson, D. Mouillet, T. Moulin, A. Origné, A. Pavlov, D. Perret, C. Petit, J. Pragt, P. Puget, P. Rabou, J. Ramos, E. L. Rickman, F. Rigal, S. Rochat, R. Roelfsema, G. Rousset, A. Roux, B. Salasnich, J.-F. Sauvage, A. Sevin, C. Soenke, E. Stadler, M. Suarez, Z. Wahhaj, L. Weber, and F. Wildi. *A&A*, 651:A72, July 2021. ISSN 0004-6361, 1432-0746.

M. Villenave, K. R. Stapelfeldt, G. Duchêne, F. Ménard, M. Lambrechts, A. Sierra, C. Flores, W. R. F. Dent, S. Wolff, Á. Ribas, M. Benisty, N. Cuello, and C. Pinte.

ApJ, 930(1):11, Apr. 2022. ISSN 0004-637X.

O. Voelkel, H. Klahr, C. Mordasini, A. Emsenhuber, and C. Lenz. *A&A*, 642:A75, Oct. 2020. ISSN 0004-6361, 1432-0746.

O. Voelkel, H. Klahr, C. Mordasini, and A. Emsenhuber. *A&A*, 666:A90, Oct. 2022. ISSN 0004-6361, 1432-0746.

K. Wada, H. Tanaka, T. Suyama, H. Kimura, and T. Yamamoto. *ApJ*, 737(1):36, July 2011. ISSN 0004-637X.

K. J. Walsh, A. Morbidelli, S. N. Raymond, D. P. O'Brien, and A. M. Mandell. *Nature*, 475(7355):206–209, July 2011. ISSN 0028-0836, 1476-4687.

J. Wang and D. A. Fischer. *AJ*, 149(1):14, Dec. 2014. ISSN 1538-3881.

L. Wang and J. Goodman. *The Astrophysical Journal*, 847:11, Sept. 2017. ISSN 0004-637X.

W. R. Ward. 22:1463, Mar. 1991.

W. R. Ward. *ApJ*, 482(2):L211–L214, June 1997. ISSN 0004-637X.

J. Weder, C. Mordasini, and A. Emsenhuber. *A&A*, 674:A165, June 2023. ISSN 0004-6361, 1432-0746.

S. J. Weidenschilling. *MNRAS*, 180:57–70, July 1977. ISSN 0035-8711.

L. M. Weiss, G. W. Marcy, E. A. Petigura, B. J. Fulton, A. W. Howard, J. N. Winn, H. T. Isaacson, T. D. Morton, L. A. Hirsch, E. J. Sinukoff, A. Cumming, L. Hebb, and P. A. Cargile. *The Astronomical Journal*, 155:48, Jan. 2018. ISSN 0004-6256.

G. W. Wetherill and G. R. Stewart. *Icarus*, 77:330–357, Feb. 1989. ISSN 0019-1035.

J. P. Williams and L. A. Cieza. *Annual Review of Astronomy and Astrophysics*, 49:67–117, Sept. 2011. ISSN 0066-4146.

J. T. Wright, G. W. Marcy, A. W. Howard, J. A. Johnson, T. D. Morton, and D. A. Fischer. *The Astrophysical Journal*, 753:160, July 2012. ISSN 0004-637X.

Y. Wu. *ApJ*, 874(1):91, Mar. 2019. ISSN 0004-637X.

A. N. Youdin. *The Astrophysical Journal*, 742:38, Nov. 2011. ISSN 0004-637X.

A. N. Youdin and J. Goodman. *ApJ*, 620(1):459, Feb. 2005. ISSN 0004-637X.

A. N. Youdin and Y. Lithwick. *Icarus*, 192(2):588–604, Dec. 2007. ISSN 00191035.

H.-G. Yun, W.-T. Kim, J. Bae, and C. Han. *ApJ*, 938(2):102, Oct. 2022. ISSN 0004-637X.

L. Zeng, S. B. Jacobsen, D. D. Sasselov, M. I. Petaev, A. Vanderburg, M. Lopez-Morales, J. Perez-Mercader, T. R. Mattsson, G. Li, M. Z. Heising, A. S. Bonomo, M. Damasso, T. A. Berger, H. Cao, A. Levi, and R. D. Wordsworth. *Proceedings of the National Academy of Science*, 116:9723–9728, May 2019. ISSN 0027-8424.

K. Zhang, G. A. Blake, and E. A. Bergin. *ApJL*, 806(1):L7, June 2015. ISSN 2041-8205.

W. Zhu, C. Petrovich, Y. Wu, S. Dong, and J. Xie. *The Astrophysical Journal*, 860:101, June 2018. ISSN 0004-637X.

Erklärung

gemäss Art. 18 PromR Phil.-nat. 2019

Name/Vorname: Kessler Andrin

Matrikelnummer: 14-121-305

Studiengang: PhD in Physics

Bachelor ☐ Master ☐ Dissertation ☑

Titel der Arbeit: Challenges of Planet Formation: Insights from Global Modelling and Population Synthesis

LeiterIn der Arbeit: Prof. Dr. Yann Alibert

Ich erkläre hiermit, dass ich diese Arbeit selbständig verfasst und keine anderen als die angegebenen Quellen benutzt habe. Alle Stellen, die wörtlich oder sinngemäss aus Quellen entnommen wurden, habe ich als solche gekennzeichnet. Mir ist bekannt, dass andernfalls der Senat gemäss Artikel 36 Absatz 1 Buchstabe r des Gesetzes über die Universität vom 5. September 1996 und Artikel 69 des Universitätsstatuts vom 7. Juni 2011 zum Entzug des Doktortitels berechtigt ist. Für die Zwecke der Begutachtung und der Überprüfung der Einhaltung der Selbständigkeitserklärung bzw. der Reglemente betreffend Plagiate erteile ich der Universität Bern das Recht, die dazu erforderlichen Personendaten zu bearbeiten und Nutzungshandlungen vorzunehmen, insbesondere die Doktorarbeit zu vervielfältigen und dauerhaft in einer Datenbank zu speichern sowie diese zur Überprüfung von Arbeiten Dritter zu verwenden oder hierzu zur Verfügung zu stellen.

Bern, 8.1.2025

Ort/Datum

A. Kessl

Unterschrift